Neutron Electric Dipole Moment measurement: simultaneous spin analysis and preliminary data analysis

V. Helaine

Université de Caen Basse-Normandie

U.F.R Sciences

École doctorale: SIMEM

Thèse de doctorat

Présentée et soutenue le 8 Septembre 2014

par

Monsieur Victor Hélaine

pour obtenir le

Doctorat de l'Université de Caen Basse-Normandie

Spécialité : Constituants Élémentaires et Physique Théorique

Mesure du moment dipolaire électrique du neutron: analyse simultanée de spin et analyse préliminaire de données.

Directeur de thèse : Monsieur Gilles Ban

Jury:

P. Harris	-	Pr. University of Sussex (UK)	Rapporteur
O. Zimmer	-	Pr. TUM, Institut Laue-Langevin (Grenoble)	Rapporteur
G. Ban	-	Pr. Ensicaen, LPC (Caen)	Directeur de thèse
K. Kirch	-	Pr. ETH Zürich, Paul Scherrer Institute (Suisse)	Examinateur
L. Serin	-	Directeur de Recherche LAL (Orsay)	Président du jury
G. Quéméner	-	Dr. Chargé de Recherche LPC	Encadrant
T. Lefort	-	Dr. MdC Universié de Caen Basse-Normandie, LPC	Encadrant

Résumé

Dans le cadre de la mesure du moment dipolaire électrique du neutron (nEDM) au Paul Scherrer Institut (Suisse), cette thèse traite du développement d'un nouveau système d'analyse de spin. L'objectif est ici de détecter simultanément les deux composantes de spin de neutrons ultra froids dans le but de diminuer l'erreur statistique sur l'EDM du neutron. Un tel système a été conçu à l'aide de simulations GEANT4-UCN, puis testé en tant que partie intégrante de l'appareillage nEDM. En parallèle de ce travail, les données nEDM de 2013 ont été analysées. Finalement, des méthodes de détermination d'observables magnétiques de premier intérêt pour le contrôle des erreurs systématiques sur l'EDM du neutron ont été testées et de possibles améliorations sont proposées.

Abstract

In the framework of the neutron Electric Dipole Moment (nEDM) experiment at the Paul Scherrer Institut (Switzerland), this thesis deals with the development of a new system of spin analysis. The goal here is to simultaneously detect the two spin components of ultra cold neutrons in order to increase the number of detected neutrons and therefore lower the nEDM statistical error. Such a system has been designed using GEANT4-UCN simulations, built at LPC Caen and then tested as part of the experiment. In parallel to this work, the 2013 nEDM data taken at PSI have been analysed. Finally, methods to recover magnetic observables of first interest to control nEDM systematic errors have been studied and possible improvements are proposed.

Remerciements

Je souhaite remercier tout d'abord les deux directeurs du LPC m'ayant accueilli durant ma thèse: Jean-Claude Steckmeyer et Dominique Durand. Ensuite, mes pensées se tournent vers Gilles Ban, mon directeur de thèse "officiel" qui a toujours été de bon conseil lors de choix stratégiques et dont la parole franche m'a beaucoup apporté. Merci à un mes rapporteurs, particulièrement Phil Harris, pour ses questions intéressantes et critiques constructives sur mon travail. Merci aussi à Laurent Serin et Klaus Kirch pour le temps consacré à la lecture du manuscrit.

Vient ensuite le tour de mes encadrants. Un grand merci tout d'abord à ceux-ci pour m'avoir ravitaillé en camembert et beurre salé pendant mon séjour à PSI. Ce soutient moral a été pour moi des plus précieux... Plus sérieusement, je souhaite remercier Thomas, que j'ai eu tout d'abord comme enseignant quand j'étais tout petit et qui m'a bien aiguillé dès ma première année d'université. C'est un peu grâce à lui si je suis dans ce groupe maintenant. Ses conseils en terme de physique et sa bonne humeur (papy n'est pas encore trop accariâtre) aidèrent beaucoup dans l'avancée de cette thèse. Et que dire de Gilles (dit "Gillounet Clooney"), sinon que mes petites discussions avec lui m'ont permis d'avoir un regard quasi clair sur toutes ces histoires de champ magnétique, si importantes dans cette expérience qu'est nEDM. Pour finir, un grand merci à Yves, encadrant un peu spécial, qui, malgré sa trentaine dépassée maintenant, est resté un ptit jeunot parmi les thésards. Il m'a été de très bon conseil quand il s'agissait de programmer et les conversations que nous avons eu ensemble en shift ou en voiture en rentrant de Suisse ont toujours été des plus agréables.

Je souhaite aussi adresser un grand merci à Damien Goupillière qui a dessiné le USSA et qui a fait un super bon boulot avec toute la team méca. Bien entendu, l'équipe FASTER a toujours été réactive dans les quelques moments tendus où nous avions besoin d'eux. Merci à eux.

Pour continuer au LPC, je me dois de remercier mon collègue de bureau, Xavier, qui m'a supporté avant et après mon séjour à PSI. S'il n'en tenait qu'à moi, je remercierais beaucoup de monde au labo, mais je vais me contenter des "jeunes": Benoît, Greg et Sam pour les moments que nous avons partagés, soit en TP, soit au wake, soit au Trappiste.

Toujours en France, je souhaite remercier Steph, Guillaume, Dominique et Yoann pour les discussions, réunions d'analyse et les shifts que nous avons partagés ainsi que pour leur participation aux premiers tests du détecteur à l'ILL.

Du côté de PSI, après une année et demi passée là-bas, je souhaite remercier en tout premier lieu Klaus Kirch, qui a permis que le travail que j'ai fait à PSI se déroule dans des conditions on ne peut plus agréables. Vient ensuite le tour de tous mes autres collègues à PSI qui m'ont permis une bonne intégration dans l'équipe en Suisse (désolé de ne pas tous vous citer, mais vous êtes nombreux). Merci à Michi qui m'a beaucoup aidé pour l'installation du détecteur et m'a permis de passer un peu de temps dans l'atelier à bricoler. Bien entendu, Philipp est sans aucun doute la personne qui m'a permis le plus de me sentir bien dans cette équipe par ailleurs très accueillante. Merci à toi, Stéphanie et les bouts d'choux pour ces après-midi, soirées jeux partagées qui m'ont permis de m'évader du travail et passer des moments agréables avec vous, tout en parlant français! Je n'oublies pas non plus tous les thésards de PSI dont je citerai quelques noms: Johannes, Martin, Bea, Dieter et Lenny avec lesquels j'ai passé de bons moments.

En parlant de thésards, je n'oublie pas non plus ceux que j'ai côtoillés au LPC ou dans les environs: Edgard, Claire, Matthieu, Xavier, Arnaud et Nono... avec lesquels j'ai passé "quelques" soirées. Spéciale dédicace pour les mousquetaires: Guillaume, Diego et Jérém, mes amis depuis le début de l'université et avec lesquels j'ai fêté la fin de la grippe pour la dernière fois.

Bien sûr, je remercie ma famille pour son soutien dans les choix que j'ai effectués jusqu'ici et avoir contribué à me faire tel que je suis maintenant.

Pour finir, je souhaite remercier mon pupitre de rédaction de thèse pour quelques nuits. Malgré de qu'on pourrait en penser, ce n'était pas l'histoire de quelques soirs, mais plutôt pour la vie. Mon ptit nécureuil, tu m'as rendu la vie tellement plus facile pendant ces années de thèse en m'apportant ta légèreté, ta joie de vivre et ton amour. Merci à toi.

Acknowledgments

I would like first to acknowledge the two directors of the LPC who have welcomed me for my PhD: J.C. Steckmeyer and D. Durand. Then, my thoughts go to Gilles BAN, my official supervisor whose advice has always been good for strategic choices and whose outspokenness brought me a lot. Thanks to my referees, particularly to Phil Harris for his many interesting questions and his constructive criticism on my work. I would also like to acknowledge Laurent Serin and Klaus Kirch for the time they consecrated to the manuscript reading.

This is now the turn of my supervisors. First of all thanks for bringing me back some "camembert" and salt butter during my stay at PSI. This moral support was of great help to me. More seriously, I would like to acknowledge Thomas Lefort for his physics advice and his good mood which helped me a lot during the PhD. My discussions with Gilles Quéméner allowed me to get a quasi clear look on all these magnetic field questions which are so important for the nEDM experiment. To finish, a big thank to Yves, the youngest of the oldest, who adviced me for programming and for the pleasant conversations during shifts or coming back from Switzerland.

A big thank too to Damien Goupillière, the LPC engineer who designed the USSA. Together with the LPC workshop people, they made a great job. Of course, I would like to acknowledge the FASTER team, who was always reactive when we needed their help. To continue at LPC, I would like to thank my office colleague, Xavier Fléchard, who welcomed me before and after my stay at PSI.

Still in France, I would like to acknowledge S. Roccia, G. Pignol, D. Rebreyend and Y. Kermaïdic for the analysis discussions and shifts we shared and for their participation to the first detector tests at ILL.

From the PSI side, after spending there one year and half, I would like first to acknowledge Klaus Kirch, who allowed me to work in very pleasant conditions at PSI. Then comes the turn of all my PSI colleagues who allowed me to be well integrated in the nEDM group and learnt me a lot about the experiment (sorry for not citing all of you but you are a lot). Thanks to Michi who helped me for the USSA installation below the nEDM spectrometer and for allowing me to spend some time in the workshop and teach me some tricks. Of course, Philipp is likely the person who made me feeling good in this welcoming team. Thanks to you, Stéphanie and the kids for these afternoons, game evenings who allowed me to think to something else than work during my stay at PSI, speaking French! I don't forget all the PSI PhD students whose I cite some names: Johannes, Martin, Bea, Dieter and Lenny with whom I spent good moments.

Speaking about PhD students, I don't forget those of the LPC or close to: Edgard, Claire, Arnaud and Nono... with whom I spent "some" parties. Special dedication to the "mouquetaires": Guillaume, Diego and Jérḿie, my friends since the beginning of the university with whom I celebrated the flu ending for the last time.

Of course, I am thankfull to my family who supported me in all the choices I have made until now and for contributing to make me as I am now.

To finish, I would like to ackonwledge my PhD writting desk lying close to me for some nights. In spite of one could think, it was not a some-nights story, but rather for the whole

life. My small squirrel, you made my life so easier during these PhD years through your lightness, your joie de vivre and your love. Thanks to you.

Asimov a dit: En science, la phrase la plus excitante que l'on peut entendre, celle qui annonce les grandes découvertes, ce n'est pas "Eureka" mais "c'est drôle". Je le dis souvent, mais rien de bien neuf jusqu'à maintenant...

Contents

Première partie

Les grandes lignes : en français...

Chapitre 1

Introduction

La recherche du moment dipolaire électrique du neutron (nEDM pour neutron Electric Dipole Moment) est une ambitieuse expérience de précision à basse énergie. Elle est motivée par la découverte potentielle d'une nouvelle source de violation des symétries discrètes de Conjugaison de charge et de Parité (CP) au delà du modèle standard (MS) de la physique des particules, contribuant à la compréhension de la prédominance de la matière sur l'antimatière dans l'Univers. En effet, le modèle standard n'explique pas cette asymétrie matière-antimatière, au contraire de ses extensions, qui de plus, prédisent naturellement un EDM du neutron non nul. Déjà, la meilleure limite expérimentale sur le moment dipolaire électrique du neutron posée par la collaboration RAL-Sussex-ILL - $|d_n| < 2.9 \times 10^{-26}$ e.cm [1] - contraint fortement l'espace des paramètres de ces théories. L'objectif de plusieurs collaborations en compétition autour du monde est maintenant d'abaisser cette limite supérieure sur l'EDM du neutron à $10^{-28} - 10^{-27}$ e.cm. Une telle amélioration de la sensibilité sur l'EDM du neutron est requise pour exclure les modèles modernes au delà du modèle standard, ou pour mener à la découverte de nouvelle physique, dans le cas où une valeur non nulle de l'EDM du neutron serait mesurée.

Cette thèse s'est déroulée dans le cadre de l'expérience nEDM qui se déroule au Paul Scherrer Institute (PSI), en Suisse, utilisant sa nouvelle source de neutrons ultra froids. La première phase du projet se base sur l'ancien spectromètre de la collaboration RAL-Sussex-ILL. Celui-ci est maintenant associé à de nouveaux développements du dispositif expérimental. Le but de cette première phase est d'atteindre un niveau de sensibilité sur l'EDM du neutron de l'ordre de 10^{-26} e.cm et de préparer la seconde phase du projet : n2EDM. Dans cette deuxième étape, la collaboration a pour but d'améliorer le niveau de contrôle des erreurs systématiques et d'augmenter la précision statistique sur l'EDM, en utilisant un nouveau spectromètre.

Le travail présenté ici se place dans le contexte global de l'expérience, entre prise de données nEDM pour la première phase du projet et efforts de R & D pour la phase n2EDM.

Dans le premier chapitre, les motivations théoriques pour mesurer l'EDM du neutron sont présentées, suivies d'une description de la technique de mesure.

Le second chapitre décrit le dispositif expérimental de mesure, ainsi que ses composants et leur utilisation dans l'expérience.

Le troisième chapitre est dédié aux simulations Geant4-UCN d'analyseurs de spin, utilisées pour la conception d'un système d'analyse simultanée de spin pour neutrons ultra froids.

Le quatrième chapitre traite ensuite de la description et des tests expérimentaux de ce nouvel analyseur de spin. Les tests du système d'analyse simultanée sont divisés en deux parties : la caractérisation des modules de l'analyseur sur la ligne faisceau West-2 à PSI, puis la démonstration de ses performances en tant qu'élément du dispositif expérimental de l'expérience nEDM.

Dans le cinquième chapitre, les données nEDM de 2013 sont analysées, représentant une partie de l'effort de l'équipe française travaillant sur l'analyse.

Finalement, dans le dernier chapitre, des méthodes d'estimation d'observables magnétiques basées sur les données de magnétomètres césium, sont caractérisées à l'aide de données simulées. Il est primordial de déterminer précisement la valeur de ces observables puisqu'elles sont utilisées pour corriger des erreurs systématiques ayant une contribution parmi les plus importantes à l'erreur systématique globale sur la mesure de l'EDM du neutron.

Chapitre 2

Le moment dipolaire électrique du neutron

Motivations théoriques

Pour un neutron, un moment dipolaire électrique (EDM) permanent peut être défini quantiquement comme une observable vectorielle intrinsèque. Parce que le neutron a un spin 1/2, son EDM doit être aligné sur celui-ci, qui est la seule quantité vectorielle intrinsèque pour cette particule - selon le théorème de Wigner-Eckart. L'EDM du neutron est l'analogue du moment magnétique, mais il est couplé à un champ électrique au lieu d'un champ magnétique :

$$\hat{H} = -\hat{\vec{d_n}}.\vec{E} - \hat{\vec{\mu_n}}.\vec{B} \tag{2.1}$$

Cependant, il existe une différence fondamentale entre ces deux interactions, leur comportement vis-à-vis des symétries fondamentales de conjugaison de charge C et de renversement du temps T :

$$\begin{aligned} -\hat{\vec{d_n}}.\vec{E} &\xrightarrow{\text{P}} \hat{\vec{d_n}}.\vec{E} \qquad & -\hat{\vec{\mu_n}}.\vec{B} &\xrightarrow{\text{P}} -\hat{\vec{\mu_n}}.\vec{B} \\ -\hat{\vec{d_n}}.\vec{E} &\xrightarrow{\text{T}} \hat{\vec{d_n}}.\vec{E} \qquad & -\hat{\vec{\mu_n}}.\vec{B} &\xrightarrow{\text{P}} -\hat{\vec{\mu_n}}.\vec{B} \end{aligned} \tag{2.2}$$

Ainsi, un EDM non-nul serait la signature d'une violation des symétries P et T et donc d'une nouvelle source de violation de CP. Ceci est une des motivations principales de la recherche des EDMs, intimement liée à l'explication de l'asymétrie matière-antimatière de l'Univers.

Le problème de l'asymétrie baryonique de l'Univers

Selon la théorie du Big-Bang [2], l'Univers devrait être fait aujourd'hui d'un reliquat de lumière après l'annihilation de la majorité de la matière et de l'antimatière présentes à ses débuts. Mais la composition actuelle de l'Univers montre qu'un processus asymétrique a eu lieu, puisque l'antimatière en est presque absente et que nous vivons dans un monde fait de matière.

Sakharov proposa en 1967 un scénario pour expliquer une telle asymétrie [3]. Ce scénario requiert trois conditions. La première est une violation du nombre baryonique B afin d'autoriser un système à aller d'un état $B = 0$ à un état $B \neq 0$. Ensuite, la violation des symétries C et CP sont requises afin de favoriser légèrement la disparition d'antimatière par rapport à la matière. Pour finir, ce processus doit avoir lieu pendant une phase de non-équilibre thermique, afin que tout excès de matière ou antimatière ne soit pas compensé par le processus inverse.

L'EDM du neutron commence ici à jouer un rôle important puisque le modèle standard de la physique des particules ne peut pas expliquer une telle asymétrie avec les violations de CP qui y sont intégrées. Ainsi, une motivation forte des extensions du modèle stantard est de prédire de nouvelles sources de violations de CP. Dans ce contexte, les recherches de l'EDM du neutron sont importantes puisqu'elles pourraient révéler de nouvelles sources de violation de CP.

L'EDM du neutron dans le modèle standard et ses extensions

Le modèle standard prédit une valeur très faible de l'EDM. La contribution majeure provient du secteur électrofaible, de l'ordre de $10^{-31} - 10^{-32}$ e.cm alors que la limite actuelle est $|d_{\mathrm{n}}| < 3 \times 10^{-26}$ e.cm [1]. Dans le secteur fort, une partie du Lagrangien QCD violant la symÃ©trie CP est reliée à l'EDM du neutron via la variable $\bar{\theta}$:

$$|d_{\mathrm{n}}| \sim \bar{\theta} \times 10^{-16} e.\mathrm{cm} \tag{2.3}$$

Aujourd'hui, l'EDM du neutron est la plus forte contrainte sur l'angle θ. Le meilleure limite expérimentale sur l'EDM du neutron [1] se traduit directement en une limite de $\bar{\theta} < 10^{-10}$, constituant le "strong CP problem", puisque l'échelle naturelle pour $\bar{\theta}$ est l'unité. Peccei et Quinn ont essayé de résoudre ce problème en introduisant une nouvelle symétrie [4]. Dans ce modèle, la valeur de $\bar{\theta}$ est 0 et une nouvelle particule, l'axion apparaît lors de la brisure de cette nouvelle symétrie. Cette nouvelle particule n'a toujours pas été observée et le "strong CP problem" reste non résolu aujourd'hui.

Même si le secteur électrofaible du modèle standard reste hors d'atteinte par les mesures expérimentales de l'EDM du neutron, certaines de ses extensions prédisent un EDM du neutron proche des limites de sensibilité actuelles entre $10^{-26} - 10^{-28}$ e.cm. Certaines de ces théories prédisent aussi une transition de phase électrofaible du premier ordre, jouant le rôle de non équilibre thermodynamique dans les critères de Sakharov, transition qui n'est plus autorisée dans le modèle standard suite à la mesure de la masse de la particule correspondant au boson de Higgs au LHC [5, 6]. De telles théories pourraient être exclues par la prochaine génération d'expériences visant à abaisser la limite sur l'EDM en dessous de 10^{-27} e.cm.

Principe de la mesure

Le principe de la mesure de l'EDM du neutron est visible via le hamiltonien d'interaction du neutron avec des champs magnétiques et électriques :

$$H = -\vec{d_n}.\vec{E} - \vec{\mu_n}.\vec{B} \tag{2.4}$$

En présence de champs magnétique et électrique, on a la levée de dégénérescence présentée en Fig. 2.1.

L'EDM du neutron est mesuré via la différence de fréquences de Larmor $\nu_{\parallel}$ et $\nu_{\nparallel}$ dans des champs électrique et magnétique parallèles et anti-parallèles :

$$d_{\mathrm{n}} = \frac{-h(\nu_{\parallel} - \nu_{\nparallel}) - 2\mu_n(B_{\parallel} - B_{\nparallel})}{2(E_{\parallel} + E_{\nparallel})} \tag{2.5}$$

Technique expérimentale

Une dizaine de projets dans le monde ont pour objectif d'améliorer la sensibilité sur l'EDM du neutron. Parmi ces projets, sept utiliseront des neutrons ultra-froids (UCN) pour mesurer la différence de fréquences de Larmor du neutron en présence de champ électrique. Ces neutrons font partie des neutrons dits optiques, qui peuvent être réfléchis sur des parois matérielles. L'énergie des UCNs est si basse qu'ils peuvent être stockés pendant quelques centaines de secondes dans des bouteilles matérielles. De plus, ils peuvent être polarisés à l'aide de champs magnétiques de quelques teslas.

La technique utilisée pour mesurer la fréquence de Larmor des neutrons est la méthode des champs oscillants séparés de Ramsey. Son principe est décrit en Fig. 2.2.

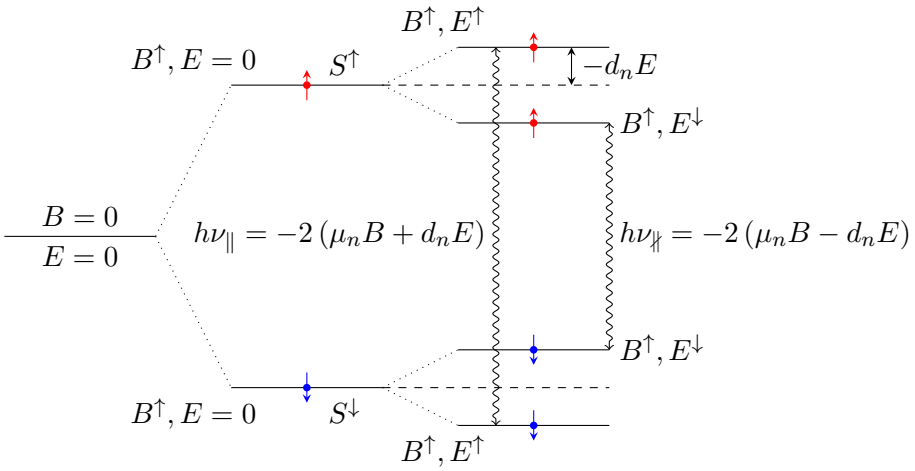

FIGURE 2.1 – Schéma de séparation des niveaux d'énergie d'un neutron possédant un EDM non nul dans des champ électrique et magnétique. Les indices $\parallel$ et $\nparallel$ correspondent respectivement à des configurations de champ électrique et magnétique parallèles et anti-parallèles.

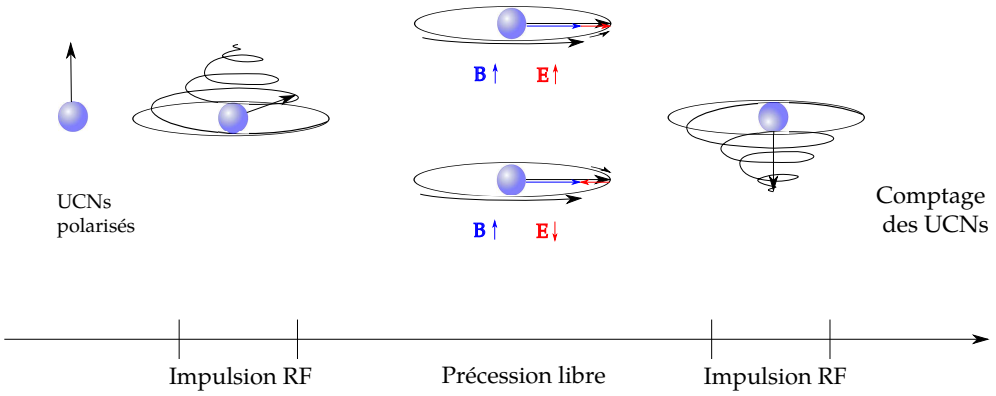

FIGURE 2.2 – Principe de la méthode des champs oscillants séparés de Ramsey.

Des neutrons polarisés sont stockés dans une chambre de précession où des champs électriques et magnétiques sont appliqués. Le spin des neutrons est initialement orienté le long du champ magnétique. Lorsqu'un champ radio-fréquence (RF) à la fréquence de Larmor des neutrons est appliqué pendant un temps τ_{RF}, le spin des neutrons bascule dans le plan orthogonal au champ magnétique et précesse librement pendant un temps T. Un second champ RF est appliqué à la fin de la précession. Si $d_{\mathrm{n}} \neq 0$, une phase est accumulée pendant le précession libre et conduit à une différence de fréquence.

En fait, la fréquence de Larmor est déterminée en dérèglant légèrement la fréquence appliquée pour le champ RF afin de se placer sur quatre points de la frange centrale de la figure d'interférences de Ramsey présentée en Fig. 2.3.

La fréquence de Larmor est récupérée via le nombre de neutrons détectés pour chaque état de spin. Pour une population d'UCNs avec un spin up, le nombre de neutrons est donné par :

$$N^{\uparrow/\downarrow} = N_0^{\uparrow/\downarrow}\left(1 \mp \alpha^{\uparrow/\downarrow}\cos\left[\frac{(f_n - f_{RF})}{\Delta\nu}\pi\right]\right) \tag{2.6}$$

où $\Delta\nu = 1/\left[2\,(T + 4\tau_{\mathrm{RF}}/\pi)\right]$ est la largeur de la frange Ramsey, $N_0^{\uparrow/\downarrow}$ le nombre de neutrons détectés pour chaque état de spin à la moitié de la résonance avec les signes + et - correspondant respectivement aux neutrons avec spin bas et spin haut. $\alpha^{\uparrow/\downarrow}$ est la visibilité (contraste) de la

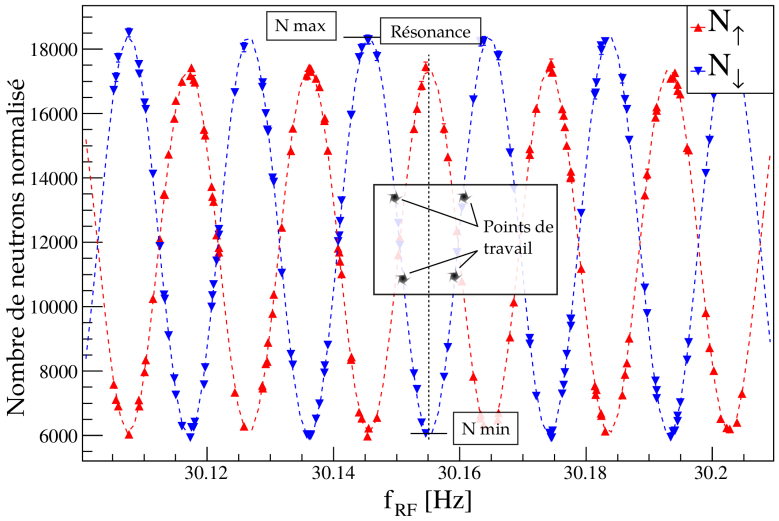

FIGURE 2.3 – Figure d'interférences de Ramsey obtenue en août 2012 après 50 s de précession libre à PSI.

frange centrale de la figure de Ramsey :

$$\alpha^{\uparrow/\downarrow} = \frac{N_{max}^{\uparrow/\downarrow} - N_{min}^{\uparrow/\downarrow}}{N_{max}^{\uparrow/\downarrow} + N_{min}^{\uparrow/\downarrow}} \tag{2.7}$$

La fréquence neutron est extraite via l'ajustement de la courbe de Ramsey avec la précision :

$$\sigma_{f_n}^{\uparrow/\downarrow} \simeq \frac{\Delta\nu}{\pi\alpha^{\uparrow/\downarrow}\sqrt{N^{\uparrow/\downarrow}}} \tag{2.8}$$

Cette erreur statistique se reporte ensuite sur la mesure de l'EDM du neutron :

$$\sigma_{d_n} \simeq \frac{\hbar}{2\alpha T E\sqrt{N_{\text{tot}}}} \tag{2.9}$$

Cette dernière équation fait apparaître les paramètres clés de la mesure. Tout d'abord l'intensité du champ électrique appliqué E ainsi que la durée de la précession libre T. Ensuite, la visibilité de la frange centrale, dépendant de la polarisation initiale des UCNs ainsi que de l'homogénéité du champ magnétique à l'intérieur du volume de précession. Finalement, le nombre de neutrons détectés doit être aussi grand que possible.

Chapitre 3

L'expérience nEDM à PSI

La collaboration européenne nEDM a repris en main le spectromètre oILL, utilisé auparavant pour poser la limite la plus précise sur l'EDM du neutron [1], après l'avoir déplacé au Paul Scherrer Institute, auprès de sa nouvelle source de neutrons ultra froids. Celle-ci utilise un cristal de deutérium solide pour refroidir les neutrons produits par spallation à l'aide du faisceau de protons de 2.2 mA du PSI, après modération dans de l'eau lourde. Les neutrons ultra froids produits dans le cristal sont ensuite guidés vers le dispositif expérimental présenté en Fig. 3.1.

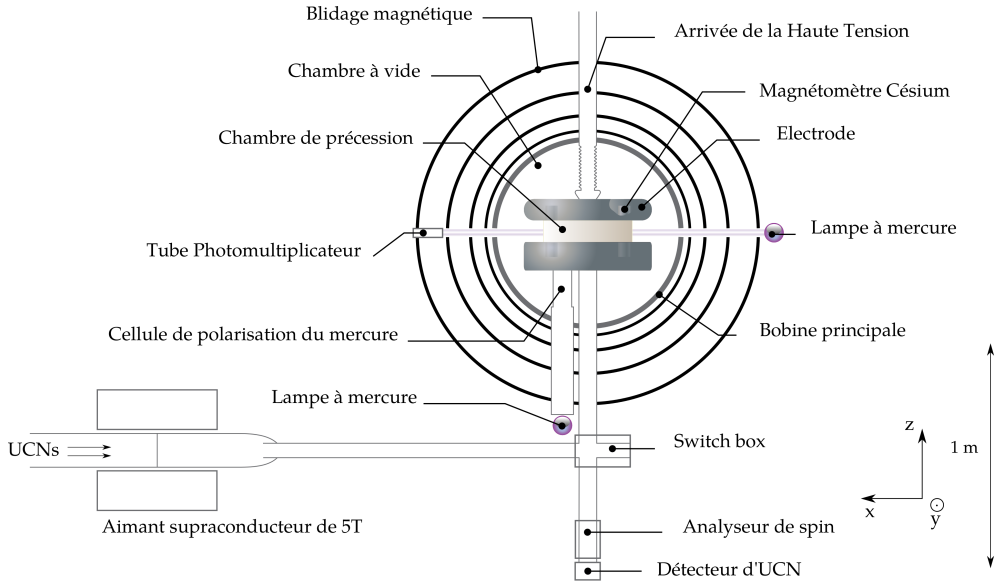

Figure 3.1 – Schéma de l'appareillage expérimental nEDM. Les grosses bobines de compensation du champ magnétique ambiant, englobant le système, ne sont pas montrées.

Transport et polarisation des UCNs

Tout d'abord, les UCNs sont polarisés à leur passage à travers l'aimant supraconducteur de 5 T. La polarisation obtenue a été estimée à près de 100% dans [7]. Ils sont ensuite guidés jusqu'à la chambre de précession via des guides en verre avec un revêtement en NiMo (alliage de Nickel et Molybdène) : son potentiel de Fermi est assez haut (220 neV) et sa faible probabilité de dépolarisation par rebond ($\sim 10^{-5}$) est appropriée pour conserver une bonne polarisation des UCNs le long du trajet.

Sans champ magnétique de maintien pour le spin des neutrons, la polarisation obtenue grâce à l'aimant supraconducteur serait perdue. Pour y remédier, un jeu de bobines a été installé sur le trajet des UCNs, produisant un champ suffisant pour prévenir les dépolarisations dûes à des zones où le champ magnétique serait trop faible.

Les neutrons sont guidés de l'aimant supraconducteur jusqu'à la chambre de précession via la "switch box". Cette pièce non magnétique est centrale, puisqu'elle distribue les neutrons d'une partie de l'appareillage à une autre, au cours d'un cycle de mesure. Elle est constituée d'un disque rotatif sur lequel sont fixés différents guides utilisés pour les différentes phases du cycle : remplissage de la chambre, monitorage et finalement vidage de la chambre vers le détecteur.

La chambre de précession où sont stockés les UCNs est constituée de deux électrodes avec un revêtement en Diamond Like Carbon (DLC) ainsi que d'un anneau isolant. La haute tension est appliquée sur l'électrode du haut. Cet anneau a été amélioré en passant du quartz avec un potentiel de Fermi $V_F = 90\,\text{neV}$ (plus le potentiel de Fermi d'un matériau est élevé, meilleure est sa capacité à stocker des UCNs de haute énergie) à du polystyrène avec un revêtement de polystyrène deutéré ($V_F = 160\,\text{neV}$), augmentant le nombre d'UCNs stockés de 80%.

Contrôle du champ magnétique

Comme le montre l'équation (2.5), le contrôle du champ magnétique est primordial pour mesurer l'EDM du neutron. Les parties de l'appareillage contribuant au contrôle du champ magnétique dans le volume de précession sont présentées dans cette section.

Production du champ magnétique

Le champ magnétique principal ($B_0 \simeq 1\,\mu\text{T}$) est produit le long de l'axe z de l'expérience par une bobine enroulée autour de la chambre à vide. Cette bobine produit un champ aussi homogène que possible, bien qu'ayant une contribution d'environ 40% provenant du blindage magnétique. Cette contribution est cependant limitée par une procédure de démagnétisation du blindage, dont dépend l'homogénéité du champ.

33 bobines correctrices sont installées pour compenser les asymétries du dispositif expérimental et ainsi obtenir une homogénéité relative du champ magnétique de l'odre de $10^{-4} - 10^{-3}$.

Enfin, deux paires de bobines sont utilisées afin de produire des champ RF : l'un pour basculer les spins des UCNs, l'autre pour l'utilisation du co-magnétomètre mercure.

Stabilisation du champ magnétique

Un blindage magnétique fait de quatre couches cylindriques de Mumetal (alliage de nickel et de fer) est utilisé pour réduire les contributions de l'environnement extérieur. Son facteur de blindage a été mesuré et vaut entre 10^3 et 10^4 selon l'axe de mesure.

En plus du blindage statique, une compensation dynamique du champ est effectuée à l'aide de 3 paires de bobines englobant l'appareillage nEDM.

Monitorage du champ magnétique

Deux sortes de magnétomètres scalaires sont installées dans le spectromètre : le co-magnétomètre mercure et un ensemble de magnétomètres césium à l'extérieur du volume de précession.

Le co-magnétomètre mercure moyenne le champ magnétique dans le volume de précession en même temps que les neutrons, permettant de normaliser la fréquence de Larmor extraite pour les neutrons et ainsi de compenser les variations de champ magnétique avec une précision de 300 à 400 fT lors de la prise de données EDM 2013. Cependant, l'utilisation du co-magnétomètre induit des erreurs systématiques comme l'effet de phase géométrique [8], lié au gradient de champ magnétique. Le but du système de magnétométrie externe césium est d'utiliser différents points de mesure du champ magnétique à l'extérieur du volume de précession pour récupérer le gradient moyen sur le volume de la chambre afin de corriger ces erreurs systématiques.

Analyse de spin et détection des UCNs

A la fin de chaque cycle de mesure, les UCNs tombent sur le détecteur NANOSC, développé au LPC Caen. Il utilise un système de scintillateurs en verre collés par adhérence moléculaire. Les UCNs traversent une première couche sans interagir dedans. Ils interagissent dans la deuxième, dopée au ^{6}Li via le processus de capture :

$$^6\mathrm{Li} + \mathrm{n} \rightarrow \alpha +^3 \mathrm{T} + 4.78\mathrm{MeV} \tag{3.1}$$

Toute l'énergie des produits de réaction est convertie en lumière dans les deux couches de scintillateurs qui sera ensuite détectée par un photomultiplicateur. Combiné à l'acquisition FASTER, cette double couche de scintillateurs permet une discrimination des signaux neutrons du bruit de fond composé de γ ou de radiations Čerenkov dans les guides de lumière en PMMA.

L'analyse séquentielle de spin

Les neutrons de spin haut et bas sont comptés indépendemment pour extraire la fréquence de Larmor des UCNs. Cette sélection de spin est faite de manière séquentielle à l'aide de deux dispositifs : l'analyseur et le spin-flipper. L'analyseur est une feuille d'aluminium de 25 µm d'épaisseur avec un dépôt de fer magnétisé de 200-400 nm ne laissant passer qu'un état de spin. Le spin-flipper sert à inverser l'état de spin des UCNs arrivant sur la feuille d'analyse afin de laisser passer les UCNs de l'autre état de spin. Il est constitué d'une bobine dans laquelle circule un courant sinusoïdal, produisant un champ RF de 30-40 µT d'amplitude effective à des fréquences de 20-25 kHz. Dans un premier temps, les neutrons avec un état de spin donné passent à travers la feuille d'analyse et sont détectés pendant 8 s. Ensuite, le spin-flipper est mis en marche et les UCNs de l'autre état de spin peuvent être détectés pendant 25 s. Enfin, le spin-flipper est de nouveau arrêté et l'état de spin initial est détecté pendant 17 s. Le chapitre suivant, dédié aux simulations GEANT4-UCN [9] met en exergue les défauts d'un tel système d'analyse et propose une solution à ces problèmes basée sur l'analyse simultanée du spin des UCNs.

Chapitre 4

Simulations de systèmes d'analyse de spin

L'inconvénient de l'analyse de spin séquentielle est que pendant qu'une des deux composantes de spin est analysée, l'autre est stockée au-dessus de la feuille d'analyse et les UCNs peuvent être perdus ou dépolarisés pendant ce laps de temps. En effet, à cause de rapides pertes de neutrons au-dessus de la feuille d'analyse, il est possible d'estimer le nombre de neutrons perdus à 50% du nombre initial [10]. Cette perte de neutrons contribue donc à la réduction de la sensibilité sur l'EDM du neutron. De plus, par définition, chaque état de spin est traité différemment parce que les deux composantes de spin ne sont pas traitées au même moment et ne sont pas soumis aux mêmes pertes ni aux mêmes dépolarisations.

Cette dernière remarque a conduit à l'idée d'élaborer un système d'analyse simultanée de spin. Une telle technique a ainsi été explorée dans les premières expériences nEDM utilisant des UCNs au LNPI [11]. Ceci peut être réalisé en utilisant un analyseur de spin dans deux bras analysant chacun une composante de spin. En conséquence, il n'y a pas de stockage complet d'un état de spin et les deux composantes sont traitées symétriquement. De tels systèmes d'analyse de spin ont déjà été suggérés [12] puis testés [13].

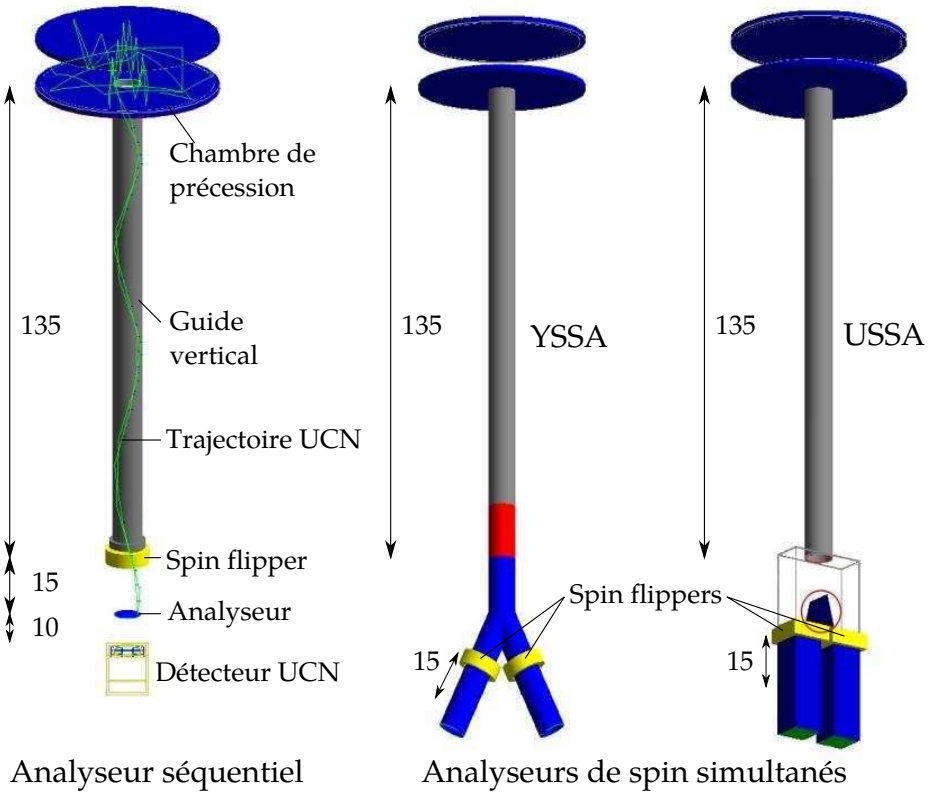

Figure 4.1 – Systèmes d'analyse de spin simulés. A gauche, l'analyseur séquentiel. A droite, les deux analyseurs simultanés : le YSSA et le USSA. Les dimensions sont en cm.

Le paquet GEANT4-UCN est adapté à la physique des neutrons ultra-froids et intègre la majorité des processus d'interaction des UCNs avec la matière. Il a été utilisé pour simuler trois systèmes d'analyse de spin présentés en Fig. 4.1 et pour comparer leurs performances. Les deux critères de comparaison principaux sont l'efficacité de détection des UCNs ainsi que l'asymétrie :

$$\mathcal{A} = \left| \frac{N^{\uparrow} - N^{\downarrow}}{N^{\uparrow} + N^{\downarrow}} \right| \tag{4.1}$$

où $N^{\uparrow/\downarrow}$ est le nombre de neutrons avec un spin haut/bas. L'asymétrie représente l'efficacité d'analyse de spin du dispositif étudié : pour des neutrons non polarisés, elle doit valoir 0 alors que pour des neutrons complètement polarisés, elle doit valoir 100% idéalement.

Analyseur séquentiel

La première géométrie à avoir été simulée est l'analyseur séquentiel utilisé initialement dans l'expérience. L'efficacité de détection obtenue avec ce système est en moyenne de 74.2%. Cette efficacité diffère de 1% selon la polarisation initiale (100% haut ou 100% bas) et provient des différents stockages de chaque composante de spin. De même, l'asymétrie obtenue n'est pas la même selon la polarisation initiale, à 1% près. Ceci est dû à l'analyse séquentielle et provoqué par deux mécanismes différents selon la polarisation initiale. Le premier est dû au temps de vol des UCNs entre le spin-flipper et le détecteur lors de la mise en marche du spin-flipper, pour lequel des UCNs d'un état de spin arrivent pendant le comptage de l'autre composante. L'autre mécanisme est une dépolarisation artificielle d'UCNs stockés entre le spin-flipper et la feuille d'analyse lors de la mise en marche du spin-flipper. Dans le cas d'UCNs polarisés ou non polarisés, l'asymétrie obtenue n'est pas parfaite et diffère en moyenne de 3% avec le cas idéal.

Analyseurs simultanés

Les deux autres géométries à avoir été simulées sont des systèmes d'analyse simultanée de spin, l'un en "Y" inversé : le YSSA, le second en "U" inversé : le USSA. Les dimensions de chacun des systèmes d'analyse ont été optimisés avec les deux critères de comparaison principaux que sont l'efficacité de détection et l'asymétrie.

Il a ensuite été montré que pour les deux systèmes d'analyse simultanée, le biais dû à la mise en marche du spin-flipper en cours de détection n'est plus présent, comme attendu. En même temps, l'efficacité de détection des UCNs a été améliorée d'environ 5% avec l'utilisation de l'analyse simultanée, que ce soit avec le YSSA ou le USSA. Il faut noter que les simulations ont été effectuées avec un système parfait et sans fuite au-dessus de l'analyseur, minimisant ainsi les fuites d'UCNs. Il est donc probable que l'effet bénéfique de l'analyse simultanée de spin ait été minimisé par rapport à l'analyse séquentielle. De plus, il a été montré que cet effet pourrait être encore augmenté en utilisant un revêtement avec un potentiel de Fermi plus élevé. L'asymétrie obtenue avec l'analyse simultanée est proche de l'asymétrie idéale, à moins de 0.5%, ce qui est meilleur qu'avec l'analyse séquentielle.

Il a donc été décidé de construire et de tester un tel système d'analyse de spin, en l'occurrence le USSA, pratique de par sa modularité avec ses parois planes remplaçables, autorisant une amélioration du système. La partie suivante a pour objet les tests de ce système.

Chapitre 5

Tests expérimentaux du USSA

Design du USSA

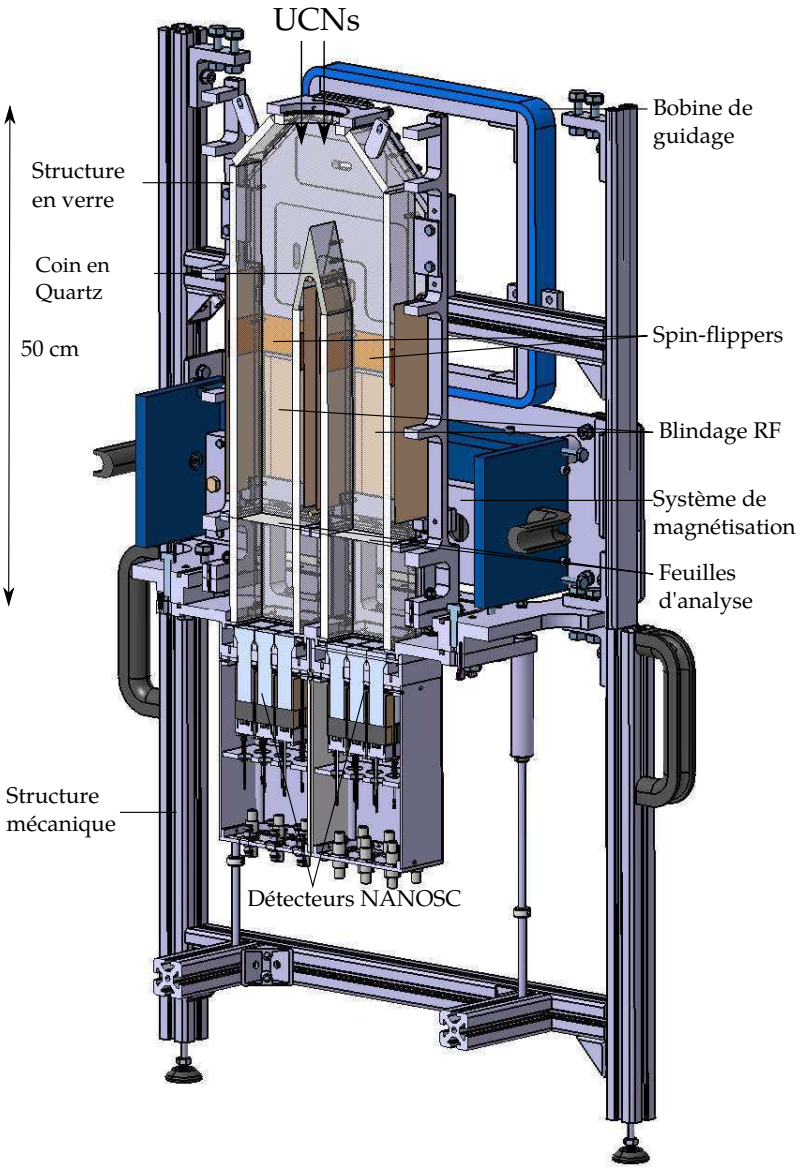

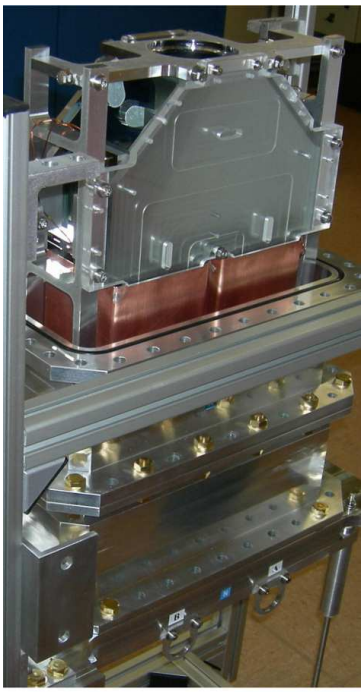

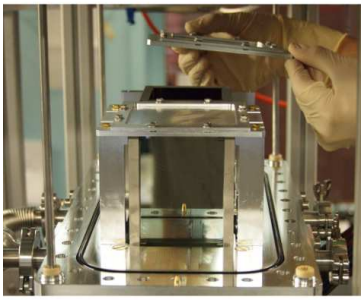

(a) (b)

Figure 5.1 – A gauche : Vue en coupe d'un dessin mécanique du USSA. En haut à droite : vue ouverte du USSA avec le blindage RF ainsi que le bas de la chambre à vide visibles. En bas à droite : installation des feuilles d'analyse du USSA.

Le concept mécanique du USSA ainsi que certaines parties du système une fois réalisé sont montrés en Fig. 5.1a et Fig. 5.1b. Ses parois sont faites de verre flotté avec un revêtement de NiMo (alliage contenant 85% de nickel et 15% de molybdène en proportion massique). Ces parois sont tenues par un exo-squelette en aluminium sur lequel les feuilles d'analyse sont aussi fixées. Le système est enfermé dans une chambre à vide en aluminium. Le système de magnétisation des feuilles d'analyse, un retour de champ en fer avec son jeu de 40 aimants permanents, est situé à l'extérieur de l'ensemble.

Transport et détection des UCNs

Afin d'avoir une transmission des UCNs aussi bonne que possible, du verre flotté a été utilisé pour fabriquer les parois du USSA. En effet, la planéïté de ce matériau est très bonne et il possède une faible rugosité, de l'ordre de quelques nanomètres, qui est importante pour garder des réflexions spéculaires à l'intérieur du USSA. Pour le moment, les parois sont recouvertes d'une couche de NiMo de 300-400 nm mais des techniques pour permettre d'utiliser d'autres revêtements supposés plus performants (diamant, ^{58}NiMo) sont à l'étude.

Pour la partie centrale du USSA, du quartz avec une fine couche de NiMo a été utilisé. Ce matériau aux propriétés proches du verre pour le guidage des UCNs a été utilisé afin de pouvoir tailler une arête fine sur le dessus et de le "creuser" en dessous pour laisser de la place au blindage RF.

Enfin, un second détecteur NANOSC a été construit, et a montré une efficacité de détection similaire à 3% près au premier détecteur, déjà utilisé pour l'expérience. Cet ajout a été accompagné de la modernisation de l'acquisition FASTER et de l'ajout de nouvelles voies d'acquisition.

Manipulation du spin

Dans chaque bras du USSA, un spin-flipper, une feuille d'analyse et un blindage RF sont utilisés pour analyser le spin des UCNs. De plus une paire de bobines produisant un champ de maintien d'environ 100 µT a été ajoutée afin de conserver la polarisation des UCNs lors de leur passage dans le USSA.

Les spin-flippers adiabatiques sont des bobines carrées de 10 cm de côté et de 4.4 cm de long, basés sur le même principe que les spin-flippers solénoïdaux utilisés habituellement. Dans ce cas, le champ RF généré a une amplitude effective de l'ordre de la centaine de µT, avec une fréquence d'environ 25 kHz.

Afin d'éviter tout effet d'un spin-flipper sur les UCNs allant dans l'autre bras, des blindages RF ont été testés puis installés autour de chaque spin-flipper. Ces blindages sont constitués d'une couche de 1 mm de cuivre entourant chaque bras. Il a été montré que l'amplitude du champ RF résiduel est inférieure à 0.3 µT, avec une probabilité de spin-flip associée inférieure à 0.01%.

Les feuilles d'analyse sont fabriquées de la même manière que pour le système d'analyse séquentiel : un support de 25 µm d'aluminium avec une couche de fer magnétisé de quelques centaines de nanomètres. Les deux analyseurs sont faits dans la même feuille afin de garder les deux bras du USSA les plus symétriques possible.

Les feuilles sont magnétisées à saturation grâce à un retour de champ ainsi qu'à un jeu de 40 aimants permanents en néodyme. Le champ magnétique minimum au niveau des feuilles d'analyse est de 80 mT. Le champ de fuite du système de magnétisation est aussi utilisé pour le spin-flipper adiabatique, afin de créer un gradient de champ magnétique le long du spin-flipper.

Tests du USSA sur la ligne faisceau West-2 à PSI

Après deux semaines de tests préliminaires du USSA à l'ILL [1], les performances de chaque sous-sytème du USSA ont été mesurées sur la ligne d'UCNs West-2 à PSI dans le but de montrer que le nouvel analyseur de spin était prêt a être utilisé en dessous du spectromètre nEDM.

La ligne de test utilisée pour les mesures est montrée en Fig. 5.2.

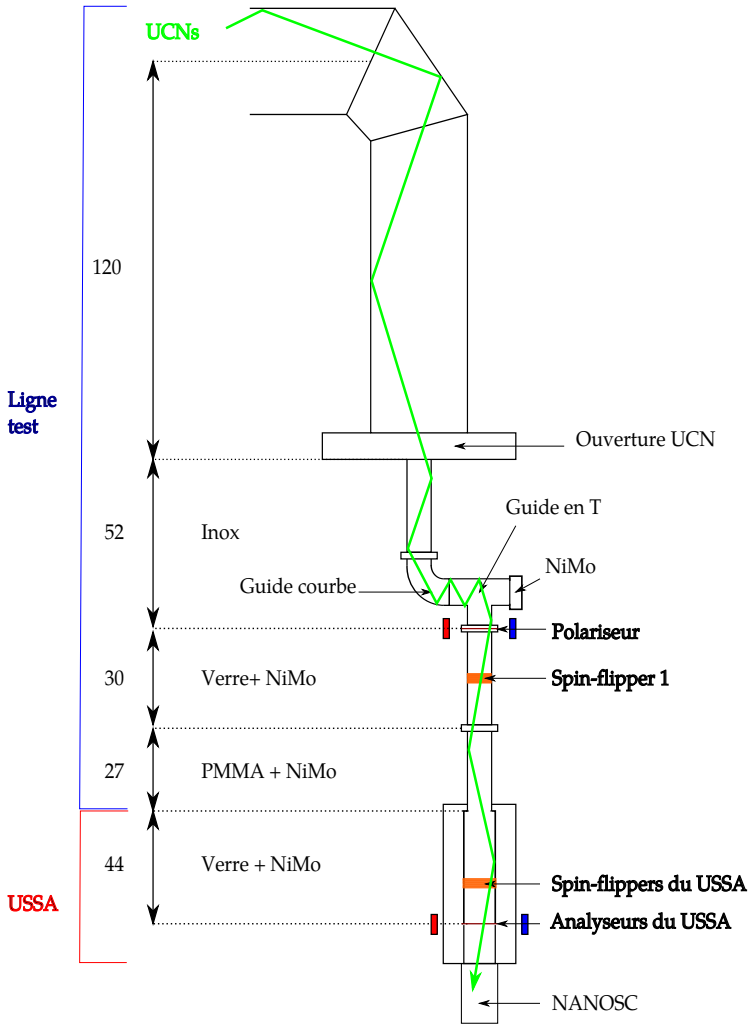

FIGURE 5.2 – Dispositif de mesure sur la ligne faisceau West-2. Le USSA est en bas de la ligne. Les dimensions sont en cm.

Tout d'abord, l'asymétrie entre les deux bras a été mesurée sans feuille d'analyse dans le USSA avec des UCNs non polarisés. Cela signifie que l'asymétrie mesurée est uniquement dûe aux différences de guidage et de détection des UCNs dans chaque bras d'analyse. Cette asymétrie est estimée à $0.43 \pm 0.07\%$.

Dans un second temps, les feuilles d'analyse ont été rajoutées et l'asymétrie entre les deux bras a été de nouveau mesurée avec des UCNs non polarisés. Cette asymétrie vaut $0.40 \pm 0.11\%$. La conclusion de cette mesure est que la seule asymétrie entre les deux bras n'est pas induite par une asymétrie dans le traitement du spin des UCNs.

[1] Merci à P. Geltenbort et à Th. Brenner pour le temps faisceau et leur accueil chaleureux.

La transmission du système a ensuite été mesurée à $80.8 \pm 0.6\%$, avec un spectre en énergie des UCNs plus élevé que ce qui est attendu en dessous du spectromètre nEDM (une limite basse de 250 neV ainsi qu'une proportion de 10% des UCNs avec plus de 330 neV au niveau des feuilles d'analyse). Dans de telles conditions, la proportion d'UCNs récupérés grâce aux rebonds d'un bras à l'autre a été estimée à $33.6 \pm 3.1\%$. Cette valeur est bien en dessous de la valeur attendue d'après les simulations (84.8%). Elle peut cependant être expliquée du fait que les UCNs arrivant avec la mauvaise composante de spin dans un bras ont une grande probabilité de retourner vers la souce s'ils ne sont pas réfléchis vers l'autre bras.

Le système d'analyse de spin a ensuite été caractérisé. Tout d'abord, l'efficacité des spin-flippers a été mesurée pour chacun à 97%, ce qui n'est pas parfait. Cette imperfection pourrait provenir de dépolarisations de la mauvaise composante de spin à cause de multiples réflections dans le mauvais bras. La probabilité de spin-flip dans le bras avec le spin-flipper non actif dûe au spin-flipper de l'autre bras a été mesurée à $0.15 \pm 0.62\%$ et est donc exclue à mieux que 1% de précision. Le pouvoir d'analyse du USSA a été mesuré à environ 80%, dans les mêmes conditions que pour la transmission, c'est-à-dire avec un spectre des UCNs très dur.

Finalement, les mesures effectuées sous la ligne West-2 ont montré que tous les sous-systèmes du USSA fonctionnaient correctement et qu'il était donc possible de l'installer en dessous du spectromètre nEDM.

Tests du USSA en dessous du spectromètre

L'objectif lors de ces mesures sous le spectromètre était de quantifier le gain possible lié à l'utilisation du USSA par rapport à l'analyseur séquentiel.

Il a tout d'abord été montré lors de mesures de polarisation avec des temps de stockage différents dans la chambre de précession que la position basse du USSA par rapport au centre de la chambre (-2.1 m) n'avait pas d'effet sur le pouvoir d'analyse du USSA, grâce à l'adoucissement du spectre en énergie des UCNs pendant le stockage.

Ensuite, la proportion d'UCNs récupérés après être entrés dans le mauvais bras d'analyse à été mesurée à $52.8 \pm 2.8\%$. Bien qu'inférieure aux prédictions des simulations (84.8%), cette valeur est tout de même supérieure à celle obtenue sur la ligne West-2 ($33.6 \pm 3.1\%$), ce qui montre qu'une proportion non négligeable des UCNs ($46.4 \pm 6.8\%$) retourne vers la chambre de précession avant qu'ils ne soient détectés.

Finalement, une comparaison entre le USSA et l'analyseur séquentiel a été effectuée en conditions de prises de données nEDM. La première courbe d'interférences de Ramsey obtenue avec le USSA est montrée en Fig. 5.3.

La visibilité de la frange centrale ainsi que le nombre total d'UCNs détectés sont améliorés respectivement de $6.2 \pm 4.9\%$ et de $23.9 \pm 1.0\%$ par rapport à l'analyse séquentielle. Il en résulte une amélioration de la sensibilité sur l'EDM du neutron de $18.2 \pm 6.1\%$. Finalement, le USSA est maintenant partie intégrante du dispositif de mesure de l'EDM du neutron à PSI.

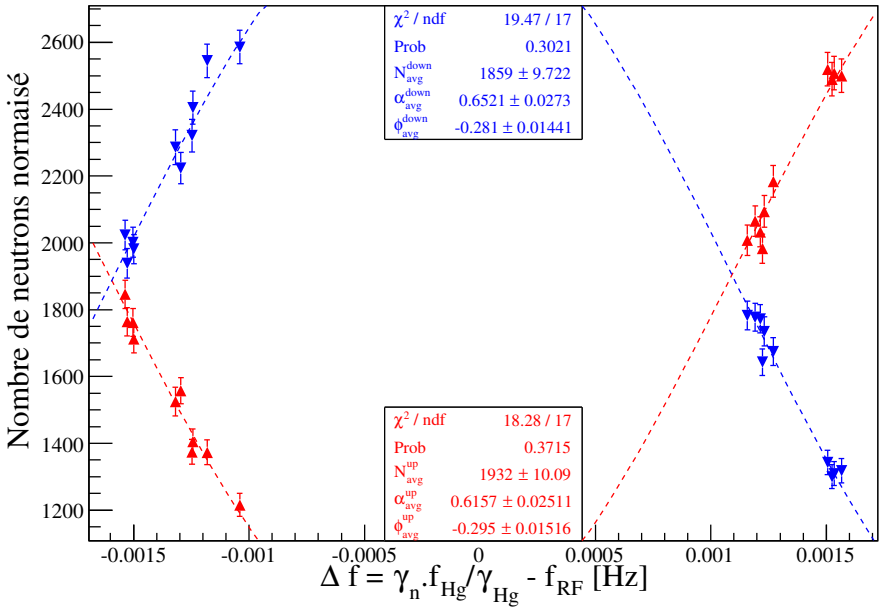

FIGURE 5.3 – Frange centrale de la figure d'interférences de Ramsey obtenue lors du premier run nEDM pris avec le USSA en octobre 2013.

Chapitre 6

Analyse de données nEDM

L'EDM du neutron est mesuré via la méthode des champs oscillants séparés de Ramsey. Elle est utilisée pour extraire la fréquence de précession des UCNs dans différentes configurations de champ magnétique et électrique. La fréquence est obtenue par le biais de l'ajustement de la frange centrale de la figure d'interférences de Ramsey avec la fonction :

$$N^{\uparrow\downarrow} = N_a^{\uparrow\downarrow}\left[1 \mp \alpha_a^{\uparrow\downarrow}\cos\left(\pi\frac{\Delta f}{\Delta\nu} - \phi_a^{\uparrow\downarrow}\right)\right] \tag{6.1}$$

où $\Delta\nu = \frac{1}{2(T+4\tau_{\mathrm{RF}}/\pi)}$ est la largeur de la frange centrale avec un temps de précession T et une durée de l'impulsion RF pour les neutrons de 2 s.

Une nouvelle méthode utilisant l'asymétrie $\mathcal{A}$ est maintenant utilisée :

$$\mathcal{A} = A_a - \alpha_a\cos\left(\pi\frac{\Delta f}{\Delta\nu} - \phi_a\right) + \delta\cos^2\left(\pi\frac{\Delta f}{\Delta\nu} - \phi_a\right) \tag{6.2}$$

L'avantage principal de cette observable est qu'elle s'auto-normalise et qu'elle n'est donc pas dépendante des variations de la source UCN. En Fig. 6.1, un exemple d'ajustement de l'asymétrie pour une polarité de champ électrique est visible.

Afin de tester le programme d'analyse utilisé pour récupérer la fréquence de Larmor des neutrons à partir des données, des données simulées ont été analysées. Plusieurs conditions réelles de prise de données ont été implémentées. Par exemple, la séquence de changement des différentes polarités électriques, des variations de champ magnétique de cycle à cycle, une décroissance exponentielle des performances de la source UCN au cours du temps et des variations de gradient vertical du champ magnétique sont inclus dans les données simulées. Avec l'ajustement de l'asymétrie ou du nombre de neutrons, la précision (au sens exactitude) obtenue sur la fréquence neutron est de 3.2 ± 2.9 nHz, avec toutes les conditions citées précédemment.

Cependant, le χ^2 réduit obtenu avec une variation journalière de gradient de 2 pT/cm, n'est pas de 1, mais de 1.15. Cette mauvaise qualité de l'ajustement a aussi été observée pendant l'analyse de données réelles. Une variation de gradient de 2 pT/cm a aussi été observée dans les données expérimentales. Ainsi, la variation du gradient pourrait entraîner une modification des paramètres de l'ajustement au cours du temps, d'où sa mauvaise qualité.

L'analyse des données nEDM 2013 a montré que la précision statistique obtenue sur la fréquence neutron est cohérente avec la valeur attendue. Un important point est que la fréquence mercure, utilisée comme normalisation des variations de champ magnétique, contribue significativement à l'erreur sur la fréquence neutron normalisée, de l'ordre de 15%. Ceci est dû aux mauvaises performances du co-magnétomètre pendant la prise de données.

Lors de l'extraction de l'EDM du neutron mesuré via l'ajustement linéaire de la quantité $R = f_{\mathrm{n}}/f_{\mathrm{Hg}}$ en fonction de la haute tension appliquée, la mauvaise qualité de l'ajustement ($\chi^2 > 5$ pour plus de la moitié des runs) signifie certainement qu'un effet lié à l'application du champ électrique n'est pas pris en compte et fausse sans doute l'extraction de l'EDM du neutron.

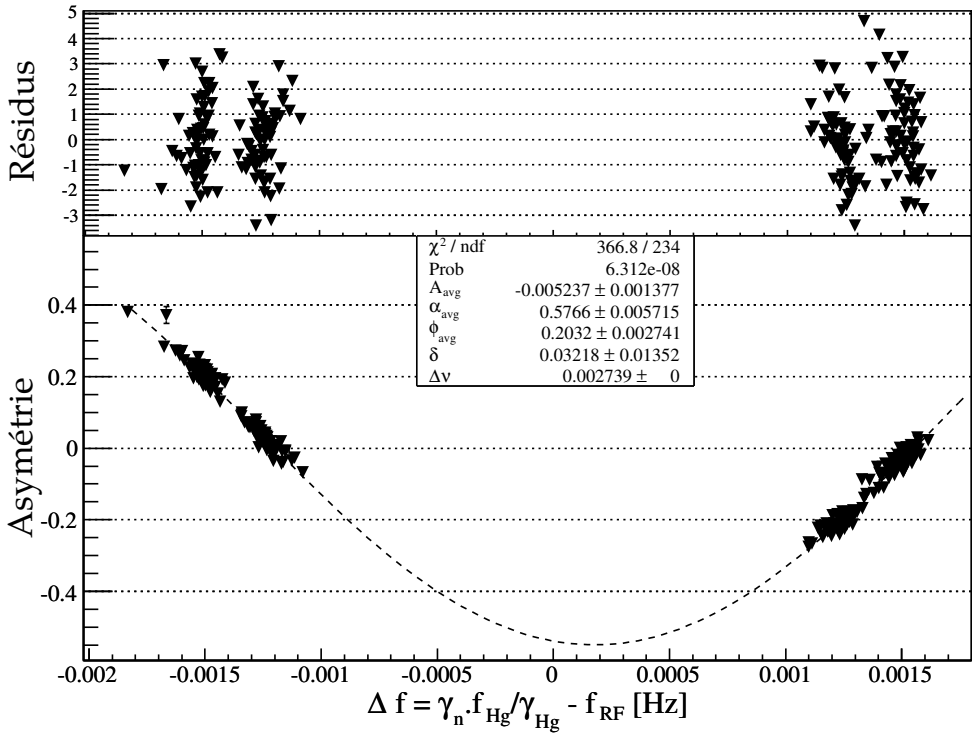

FIGURE 6.1 – Ajustement de l'asymétrie pour extraire la fréquence de Larmor des neutrons. Dans le but de compenser des variations de champ magnétique, la fréquence de l'impulsion RF est normalisée par la fréquence mercure.

Néanmoins, la détermination finale de l'EDM du neutron a été effectuée (voir Fig. 6.2), sans correction de l'effet de phase géométrique. Le résultat obtenu $d_{\mathrm{n}} = (-0.50 \pm 0.83) \times 10^{-25}\, e.\mathrm{cm}$ présente une précision statistique en accord avec celle attendue.

La correction de l'effet de phase géométrique a ensuite été effectué. Pour ce faire, la quantité $R_a - 1 = \frac{f_{\mathrm{n}}\gamma_{\mathrm{Hg}}}{f_{\mathrm{Hg}}\gamma_{\mathrm{n}} - 1}$ est utilisée. Au point de croisement des courbes pour B_0 pointant vers le haut et pointant vers le bas, l'erreur systématique provenant de l'effet de phase géométrique du mercure est nulle. Cette procédure a été appliquée aux données EDM 2013 et est montrée en Fig. 6.3.

Au point de croisement, l'EDM obtenu avec correction de l'effet de phase géométrique est :

$$d_{\mathrm{n}} = (-2.3 \pm 3.4) \times 10^{-25}\, e.\mathrm{cm} \tag{6.3}$$

Du fait que deux points pour B_0 pointant vers le haut sont en dehors de la courbe, la précision sur la pente n'est pas très bonne et se propage sur la précision sur l'EDM. Ce problème est probablement lié à la mauvaise qualité de l'ajustement effectué lors de la détermination de l'EDM mesuré.

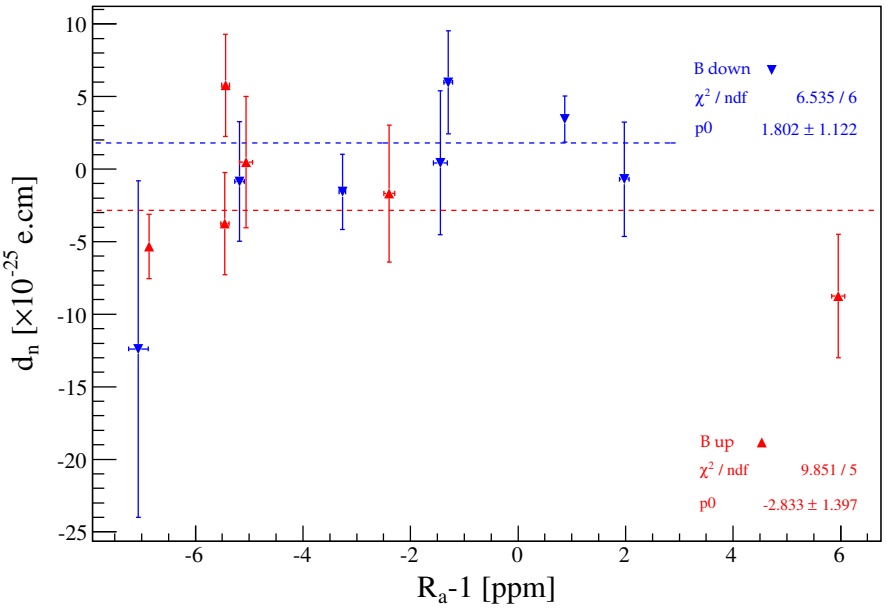

FIGURE 6.2 – Ajustement des données nEDM 2013 sans correction de l'effet de phase géométrique. Les configurations avec B_0 up sont représentées par les triangles rouges pointant vers le haut. Les configurations avec B_0 down sont représentées par les triangles bleus pointant vers le bas.

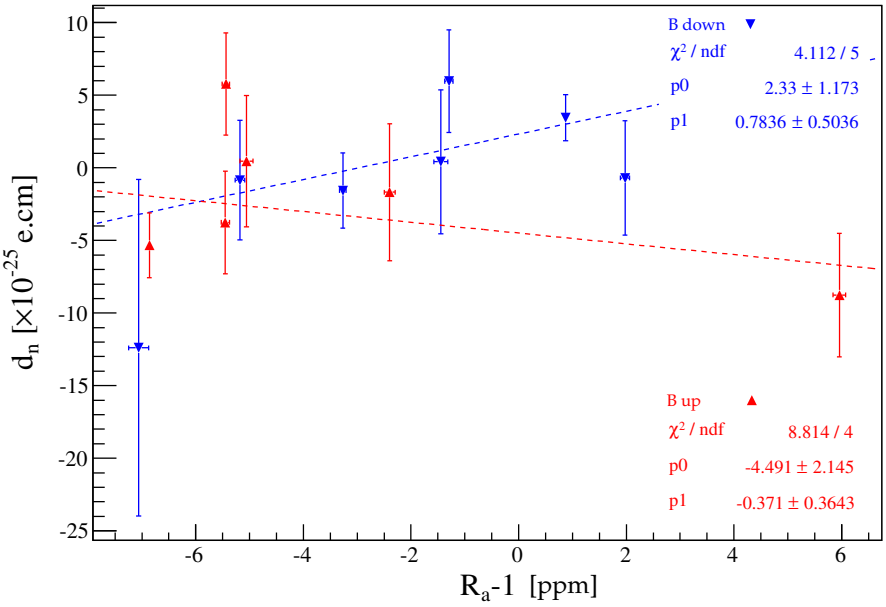

FIGURE 6.3 – Analyse du point de croisement avec les données nEDM de 2013. Les triangles rouges/bleus pointant vers le haut/bas représentent les mesures effectuées pour le champ magnétique pointant vers le haut/bas.

Chapitre 7

Test d'estimateurs d'observables magnétiques

Dans le but de corriger différentes erreurs systématiques liées à l'utilisation du co-magnétomètre mercure, deux observables magnétiques sont de première importance : le gradient vertical de champ magnétique moyen sur le volume de précession $\langle \partial_z B_z \rangle$ et le champ transverse carré $\langle B_\perp^2 \rangle$. Le champ magnétique mesuré par les magnétomètres césium à l'extérieur de la chambre est utilisé pour estimer le gradient de champ.

Pour le moment, seuls des magnétomètres scalaires sont utilisés, n'autorisant que la détermination du gradient vertical. Cependant, le développement de magnétomètres césium vectoriels pourrait permettre d'estimer en plus du gradient le champ transverse carré moyen.

Afin d'estimer l'exactitude de plusieurs méthodes utilisées pour récupérer le gradient à partir des données césium, des "fausses" données ont été générées, basées sur des données réelles recueillies pendant la mesure de cartes du champ magnétique à l'intérieur du volume de précession.

A partir de ces données simulées dont le gradient est connu, il est possible de comparer le gradient estimé par différentes méthodes et ainsi de trouver la plus précise. Cette procédure a été effectuée et il a été montré que l'utilisation d'un ajustement d'une fonction de polynômes harmoniques cartésiens est la meilleure. Elle permet une détermination du gradient avec une erreur proche de $4\,\mathrm{pT/cm}$, pour des gradients allant jusqu'à $150\,\mathrm{pT/cm}$. Une amélioration de cette méthode a aussi été proposée, permettant de diviser le niveau d'erreur par un facteur 2.

En plus de ce test, les données simulées ont été utilisées pour étudier la possibilité d'un ajustement harmonique similaire, mais en 3 dimensions, sur des données provenant de magnétomètres césium vectoriels. La précision atteinte sur le gradient est du même ordre de grandeur qu'avec des magnétomètres césium scalaires, avec un nombre de magnétomètres limité à 20. Cependant, l'utilisation de magnétomètres vectoriels rend possible la détermination en ligne du champ transverse carré moyen sur le volume de la chambre. L'erreur sur sa détermination est de l'ordre de $0.01\text{-}0.05\,\mathrm{nT}^2$. En supposant une précision suffisante des magnétomètres, l'erreur systématique associée sur l'EDM du neutron serait alors proche de $10^{-28}\,e.\mathrm{cm}$, c'est-à-dire diminuée d'un facteur 10 par rapport à maintenant. Ceci montre que l'utilisation de tels magnétomètres vectoriels pourrait rendre possible la correction très précise de l'effet quadrupolaire, l'un des effets systématiques les plus importants.

Chapitre 8

Conclusions et perspectives

Le travail présenté dans cette thèse représente le statut de l'expérience nEDM à PSI. D'abord, l'expérience est dans un état permettant la prise de données nEDM. En même temps, l'appareillage actuel est un parfait banc d'essai pour de nouveaux dispositifs de mesure et permet à la collaboration de préparer le futur de l'expérience nEDM à PSI : la phase n2EDM.

Le USSA, un nouvel analyseur de spin simultané, a été testé. Il a été conçu à l'aide de simulations Geant4-UCN et ensuite construit au LPC. Un des buts initiaux du USSA était de traiter symétriquement chaque état de spin. Lors des tests des sous-systèmes du USSA sur la ligne West-2, il a été montré que cet objectif est rempli. Le USSA a ensuite été installé en-dessous du spectromètre nEDM pour tester ses performances en conditions de prises de données nEDM. Là aussi c'est un succès, puisque le nombre de neutrons détectés est augmenté de $23.9 \pm 1.0\%$ et la visibilité de la frange centrale de $6.2 \pm 4.9\%$, lors de l'utilisation du USSA au lieu de l'analyseur séquentiel. Ces deux améliorations induisent donc un gain en sensibilité sur l'EDM du neutron de $18.2 \pm 6.1\%$. Cette amélioration devrait être confirmée avec les données de 2014, puisque le USSA fait maintenant partie de l'appareillage nEDM.

Ce gain en sensibilité peut être encore augmenté en utilisant un meilleur revêtement dans le USSA, conduisant à une meilleure transmission, comme le suggèrent les simulations Geant4-UCN. Il est donc plannifié de couvrir les parois du USSA avec du ^{58}NiMo. Les efforts de R&D pour réaliser ce type de revêtement vont aussi profiter à d'autres parties de guidage du système. Une autre option initiale utilisant du diamant est à l'étude, bien que techniquement plus difficile. Quelques échantillons ont déjà été produits avec un potentiel de Fermi mesuré à environ 305 neV. D'autres tests des propriétés de stockage du diamant seront effectués car il pourrait être utilisé dans le volume de précession. Son utilisation permettrait de stocker des UCNs avec de plus grandes énergies et donc d'augmenter la sensibilité sur l'EDM du neutron.

Pendant les tests préliminaires du USSA en août 2013, des données EDM ont été mesurées. Pendant cette courte période, les paramètres clés pour une haute sensibilité sur l'EDM du neutron étaient réunis. Une partie de cette thèse est dédiée à l'analyse préliminaire de ces données, afin de contrôler leur qualité ainsi que pour préparer l'analyse finale.

Dans un premier temps, l'estimation de la fréquence de Larmor des neutrons a été étudiée. Pendant cette étude, une technique alternative pour estimer cette fréquence - utilisant l'asymétrie - a été testée avec des données expérimentales et simulées. Pendant la sélection des données brutes, il a été montré que l'ajustement de la courbe de Ramsey utilisant l'asymétrie est plus robuste qu'avec le nombre de neutrons normalisé. Ceci suggère qu'il peut exister un problème dû à un mauvais positionnement du switch, qui n'est pas encore pris en compte dans l'analyse. C'est pourquoi il est nécessaire de pousser l'étude des conditions de prise de données.

L'étude de la qualité de l'ajustement de la courbe Ramsey a aussi permis de choisir la meilleure méthode pour estimer la fréquence mercure, qui est d'une importance primordiale pour le bon déroulement de l'estimation de la fréquence neutron. Une nouvelle méthode revisitant la méthode utilisé par la collaboration RAL-Sussex-ILL a été choisie. Il reste cependant nécessaire de continuer le travail au sein de la collaboration sur l'estimation de la fréquence mercure.

En relation avec l'estimation de la fréquence mercure, le faible temps de dépolarisation transverse du mercure a conduit à une faible erreur statistique sur la fréquence mercure, de l'ordre de

3 µHz. Cette erreur contribue à hauteur de 15% sur le ratio R utilisé pour normaliser les variations de champ magnétique. Cette erreur se répercute ensuite sur la mesure de l'EDM du neutron. C'est pourquoi la collaboration travaille activement pour augmenter le T_2 du mercure.

Dans le but de contrôler le programme d'analyse, des données simulées ont été générées. Il a ainsi été montré que dans des conditions habituelles de prise de données, l'analyse donne des résultats fiables. De plus, à l'aide de ces données simulées, une explication possible au problème du χ^2 réduit de 1.15 observé dans les données a été trouvée. En effet, des variations du gradient de champ magnétique observées dans les données expérimentales ont été simulées et l'effet résultant sur l'ajustement de la fréquence de Larmor des neutrons est en accord avec les observations. Parce que des variations de température pourraient être à l'origine de telles variations du gradient de champ magnétique, une meilleure isolation thermique de la zone expérimentale pourrait résoudre ce problème.

L'étape suivante était de contrôler les données EDM avec une analyse préliminaire. Même si la précision statistique mesurée est en accord avec celle attendue, l'analyse a montré que l'ajustement permettant d'obtenir l'EDM brut du neutron ne se déroule pas correctement dans plus de 50% des cas. Ce problème, peut-être lié à des décharges électriques, doit être investigué et résolu avant la prochaine prise de données.

Sans correction de l'effet de phase géométrique effectué, le résultat obtenu avec cette analyse est $d_\mathrm{n} = (-0.50 \pm 0.83) \times 10^{-25}\, e.\mathrm{cm}$, soit une sensibilité par cycle d'environ $4 \times 10^{-24}\, e.\mathrm{cm}$. Une telle sensibilité journalière permettrait à la collaboration d'atteindre un niveau de sensibilité d'environ $2 \times 10^{-26}\, e.\mathrm{cm}$ après 3 ans de prise de données.

Pour la dernière étape de l'analyse, la correction de l'effet de phase géométrique n'est pas satisfaisant puisque deux points se situent à plus de 3σ de la courbe attendue pour B_0 pointant vers le haut. Néanmoins, la technique a fonctionné correctement pour B_0 pointant vers le bas. Le résultat final après correction de l'effet de phase géométrique est $d_\mathrm{n} = (-2.3 \pm 3.4) \times 10^{-25}\, e.\mathrm{cm}$.

Dans la dernière partie de ce travail de thèse, des estimateurs du gradient vertical de champ magnétique utilisant les données de magnétomètres césium scalaires ont été étudiés en utilisant des données simulées. Cette étude, s'appuyant sur une simulation réalistique du champ magnétique à partir de cartes de champ mesurées, a montré que la méthode la mieux adaptée est l'ajustement harmonique de Taylor, fiable à quelques pT/cm. Une amélioration de cette méthode a été proposée, en sélectionnant les harmoniques contribuant le plus au champ dans la fonction d'ajustement. Une telle amélioration pourrait permettre d'améliorer l'erreur sur le gradient vertical du champ magnétique de plus d'un facteur 2, jusqu'à 1-2 pT/cm. Cette étude a été effectuée dans le cadre de la mesure du ratio des moments gyromagnétiques du neutron et du mercure $\gamma_\mathrm{n}/\gamma_\mathrm{Hg}$, dont l'incertitude a été diminuée à 1 ppm, en utilisant les données des courbes R [14].

Dans la phase n2EDM, des magnétomètres césium vectoriels seront disposés autour de la chambre de précession et devraient être capables de mesurer le champ magnétique au niveau du pT. Ils sont actuellement en développement à PSI et un prototype a été installé sur le "mapper" fabriqué au LPC et utilisé pendant les campagnes de cartographie magnétique de 2013 et 2014. En plus de l'étude précédente, les données simulées ont été utilisées pour prospecter une récupération en ligne du champ magnétique transverse carré en utilisant de tels magnétomètres. La technique utilisée pour estimer le champ transverse carré est l'ajustement harmonique en 3 dimensions, combinée à la sélection des harmoniques ayant la plus grande contribution. Avec une telle technique, le gradient de champ magnétique est mesuré avec une erreur de 1-2 pT/cm et le champ magnétique transverse carré avec une erreur de l'ordre de quelques $0.01\,\mathrm{nT}^2$. Avec une telle erreur sur la détermination du champ trasnverse carré moyen, l'effet quadrupolaire pourrait être corrigé avec une erreur améliorée d'un facteur 10 par rapport à la méthode actuelle, jusqu'à $10^{-28}\, e.\mathrm{cm}$. Cela donne ainsi une perspective vers le contrôle d'une des erreurs systématiques principale sur

l'EDM du neutron pendant la phase n2EDM.

Pour cette dernière phase du projet nEDM, le but est double. D'une part, la collaboration a pour objectif d'améliorer la statistique neutron, et d'autre part de s'occuper avec soin des conditions de champ magnétique à l'intérieur de la chambre. Afin que la mesure de l'EDM soit effectuée dans les mêmes conditions de champ magnétique pour les deux polarités de champ électrique, la précession libre sera effectuée dans une chambre de stockage double, avec des champs électriques plus hauts. Ainsi, le nombre d'UCNs détectés sera aussi doublé par rapport à une chambre simple. Le contrôle du champ magnétique sera atteint par le biais d'un nouveau blindage magnétique multi-couches avec un facteur de blindage d'environ $5 \times 10^4 - 1 \times 10^5$, pour abaisser le gradient de champ magnétique jusqu'à $1\,\mathrm{pT/cm}$. De plus, la bobine B_0 de n2EDM est en train d'être développé de manière à ne pas induire de magnétisation du blindage, produisant une meilleure homogénéïté du champ. Le volume de précession sera monitoré par un co-magnétomètre utilisant un laser pour mesurer le signal mercure. En plus des magnétomètres cesium externes vectoriels, deux "couches" de magnétomètres ^{3}He au-dessus et en dessous du volume de stockage des UCNs seront utilisés comme gradiomètres pour contrôler les erreurs systématiques liées au gradient de champ magnétique.

Grâce à ces améliorations sur l'erreur statistique et les erreurs systématiques, il est prévu d'améliorer la limite sur l'EDM du neutron jusqu'à 4×10^{-27} e.cm dans environ 10 ans avec les performances actuelles de la source d'UCNs. Si la source atteint ses performances nominales, la gamme des 10^{-28} e.cm sera explorée, permettant des tests décisifs de scénarios de nouvelle physique.

Part II

The English part.

Chapter 1

Introduction

The neutron Electric Dipole Moment (nEDM) search is a challenging high precision experiment at low energy. It is motivated by the potential discovery of new CP violation sources beyond the Standard Model (SM) of particle physics. Such a discorvery would contribute to the understanding of the matter predominance over antimatter in the Universe. Indeed, new CP violation mechanisms are required in order to fulfil one of the three Sakharov conditions which are necessary to produce the baryon asymmetry in the early Universe [3]. Contrary to the SM, several of its extensions proposed scenarios able to explain the matter-antimatter asymmetry. Such models naturally predict a non zero value for the nEDM in the 10^{-28}-10^{-26} e.cm range. Already, the best experimental limit on the nEDM, set by the RAL-Sussex-ILL collaboration - $|d_n| < 2.9 \times 10^{-26}$ e.cm (90% CL) [1] - strongly constrains the parameters space of such theories [15, 16]. More generally, global searches for EDMs of fundamental particles or compound systems are worldwide pursued, since EDM is one of the most sensitive probes for new physics beyond the SM [17].

The objective of several international collaborations in a worldwide competition is to push the nEDM upper limit down to the $10^{-28} - 10^{-27}$ e.cm range. Such an improvement of the nEDM sensitivity is required to rule out models beyond the SM, or to lead to the discovery of new physics, in case a non zero nEDM would be measured. Most of nEDM projects use ultra cold neutrons (UCN) to perform the measurement except a few using cold neutron diffraction in crystal (see for instance [18]). Because the current limiting factors for a large sensitivity improvement is the statistic, most of the projects are closely related to the development of new highly intense UCN sources. These new sources are expected to overcome the current UCN density of about $10\,\mathrm{cm}^{-3}$ by a factor 10 to 100.

Around the world, about ten projects aim at measuring the nEDM. They are at very different stage.

The ILL is one of the most active centre for the nEDM search [19]. For instance, the last nEDM measurement was performed by the PNPI group at ILL. They recently published a limit of $|d_\mathrm{n}| < 5.5 \times 10^{-26}$ e.cm (90% CL) [20]. The data taking has been stopped in August 2013 due to the reactor shut-down and will likely not be restarted before end of 2015.

On the other hand, one of the most important nEDM projects, the CryoEDM experiment [21], has recently been stopped due to funding cutoff.

In the next few years, the other UCN projects should be able to start taking data. A project held by the Munich collaboration is ongoing with the development of a new UCN source at FRM-II [22]. The detector progress is going fast. However, the UCN source commissioning has been postpone for a few years. The move of the experiment to the ILL is not excluded. The RCNP-TRIUMF project located in Japan seems to make progresses. They should be able to start soon taking nEDM data [23]. Another project based at Los Alamos is also ongoing [24]. Its goal is to prove that within 3 years the apparatus will be ready to take nEDM data.

On a longer time scale, *i.e.* not before 2020, future projects are planned. They are often the second phase of ongoing projects. The goal for these experiments is to reach at least the 10^{-27} e.cm level. This is the case for the PNPI project which should move to the "old" WWMR reactor in Gatchina where a new UCN source should be constructed. The experiment based at RCNP is planned to move to the new UCN source at TRIUMF in 3 to 5 years. Finally, the SNS

collaboration [25] plans to build and test the critical parts of the apparatus over the next 4 years and will therefore not start taking nEDM data before at least 2020 [26].

Currently, the only experiment taking nEDM data is located at the Paul Scherrer Institute (PSI) in Switzerland. The work presented in this thesis has been performed in the framework of this experiment. The PSI project has two phases. The first phase is based on the upgraded spectrometer of the RAL-Sussex-ILL collaboration (which set the current nEDM upper limit at ILL). After 3 years, a nEDM sensitivity of a few 10^{-26} e.cm could be reached with the current UCN source performances, assuming 4 months of data taking per year. Such a goal is achievable with the current apparatus performances, but efforts are required in order to improve its reliability. The current experiment is also used to prepare the second phase of the project (n2EDM): the building of a new spectrometer. In this second stage, the collaboration aims at improving the control of systematic errors and at lowering the statistical precision below the 10^{-27} e.cm level.

This thesis takes place between nEDM data taking with the former spectrometer and R&D efforts for the n2EDM phase. A new simultaneous spin analyser has been designeed, built and tested, 2013 nEDM data have been analysed and a study of estimators of magnetic observables used to correct for systematic effects has been carried out.

In chapter II, the theoretical motivations for the nEDM measurement are given, followed by the description of the nEDM measurement technique. Furthermore, properties of Ultra Cold Neutrons, used to measure the nEDM, are summarised.

Chapter III describes the spectrometer, as well as its components and their use in the nEDM measurement.

Chapter IV is dedicated to GEANT4-UCN simulations, used to design the simultaneous spin analyser. The new spin analyser has been developed to replace the current sequential analyser. The simultaneous spin analysis is required to symmetrically treat the two spin components and avoid possible spurious effects on the nEDM measurement. At the same time, due to a faster detection, an increase of the number of detected UCNs is expected.

Chapter V concerns the description and the experimental tests of the newly constructed USSA. The study of the simultaneous spin analyser is divided into two parts: the subsystems characterisation on the West-2 beam line at PSI and its performances measurement below the nEDM spectrometer.

The 2013 nEDM data has been analysed. Chapter VI reports on the study of an analysis software used to extract the neutron Larmor frequency using simulated and experimental data. These tests are presented as well as the nEDM extraction with the 2013 data.

Finally, in the last chapter, estimators of the vertical gradient based on scalar caesium magnetometers are characterised using a "toy model". In addition, a study to prospect the online recovery of the square transverse magnetic field from vector caesium magnetometers is presented. This average square transverse field has to be accurately determined as it is needed to correct for the so-called quadrupole effect, one of the main current systematic errors on the nEDM.

Chapter 2

The neutron Electric Dipole Moment

Contents

2.1 Motivations

A permanent electric dipole moment (EDM) $\vec{d}$ is usually defined when two opposite charges $\pm q$ are separated by a distance r as $\vec{d} = q\vec{r}$. Such an EDM is observed in systems for which the barycentres of negative and positive charges do not coincide as for instance in the H_2O molecule.

For a neutron, a permanent EDM can be quantumly defined as a vectorial intrinsic observable. Because neutrons have a 1/2 spin, this EDM has to be aligned along their spin $\vec{S}$ - the solely intrinsic vectorial quantity for this particle - according to the Wigner-Eckart theorem. Such EDM reads $\vec{d_{\mathrm{n}}} = d_{\mathrm{n}}\vec{S}/S$. In fact, the neutron EDM is the analogue of the magnetic moment $\vec{\mu_{\mathrm{n}}}$, but instead of coupling to a magnetic field $\vec{B}$, it couples to an electric field $\vec{E}$. The overall Hamiltonian reads:

$$\hat{H} = -\hat{\vec{d_{\mathrm{n}}}}.\vec{E} - \hat{\vec{\mu_{\mathrm{n}}}}.\vec{B} \tag{2.1}$$

However, these two dipole moments interactions behave differently with respect to the discrete symmetries: charge conjugation symmetry C, parity symmetry P and time reversal symmetry T. Tab. 2.1 summarises the transformation of usual physical observables under P and T. According to transformations of $\left(\hat{\vec{d_n}},\ \vec{E}\right)$ and $\left(\hat{\vec{\mu_n}},\vec{B}\right)$ under these P and T operators, depicted in Fig. 2.1, one has:

$$\begin{aligned} -\hat{\vec{d_{\mathrm{n}}}}.\vec{E} &\xrightarrow{\mathrm{P}} \hat{\vec{d_{\mathrm{n}}}}.\vec{E} \qquad & -\hat{\vec{\mu_{\mathrm{n}}}}.\vec{B} &\xrightarrow{\mathrm{P}} -\hat{\vec{\mu_{\mathrm{n}}}}.\vec{B} \\ -\hat{\vec{d_{\mathrm{n}}}}.\vec{E} &\xrightarrow{\mathrm{T}} \hat{\vec{d_{\mathrm{n}}}}.\vec{E} \qquad & -\hat{\vec{\mu_{\mathrm{n}}}}.\vec{B} &\xrightarrow{\mathrm{P}} -\hat{\vec{\mu_{\mathrm{n}}}}.\vec{B} \end{aligned} \tag{2.2}$$

This also applies to other particles with a non-zero spin, which can have an EDM. Thus, a non-zero EDM would be a signature of P and T violation and assuming the CPT theorem, a new CP violation source.

Observable/Symmetry	P	T
Position $\vec{r}$	$-\vec{r}$	$\vec{r}$
Time t	t	$-t$
Momentum $\vec{p}$	$-\vec{p}$	$-\vec{p}$
Spin, Angular momentum $\vec{S}$	$\vec{S}$	$-\vec{S}$
Magnetic Dipole Moment $\vec{\mu}$	$\vec{\mu}$	$-\vec{\mu}$
Magnetic field $\vec{B}$	$\vec{B}$	$-\vec{B}$
Electric Dipole Moment $\vec{d}$	$\vec{d}$	$-\vec{d}$
Electric field $\vec{E}$	$-\vec{E}$	$\vec{E}$

Table 2.1: Transformation of usual physical observables under P and T symmetries.

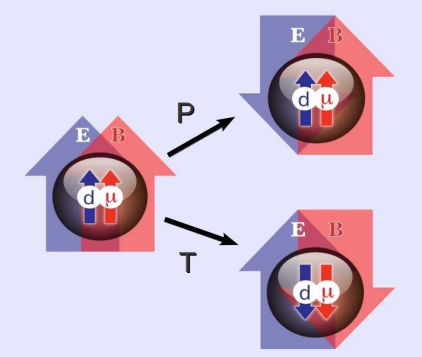

Figure 2.1: $\left(\hat{\vec{d_{\mathrm{n}}}},\ \vec{E}\right)$ and $\left(\hat{\vec{\mu_{\mathrm{n}}}},\vec{B}\right)$ transformation under P and T symmetries.

2.1.1 History of symmetry breaking and nEDM

Purcell and Ramsey first had the idea to experimentally test discrete symmetries in 1950 [27] by measuring the neutron Electric Dipole Moment (nEDM). This pioneering measurement gave the first upper limit on the nEDM in 1957 [28]:

$$|d_{\mathrm{n}}| < 5 \times 10^{-20}\, e.\mathrm{cm} \tag{2.3}$$

This measurement was carried out during a key period for particle physics, when the idea of parity violation in weak processes was discussed by Lee and Yang in 1956 in order to solve the θ-τ puzzle [29]. One year after, the first parity violation in a weak process was experimentally discovered by

Mrs Wu[30]. In this context, the neutron EDM limit reinforced the idea of T and CP conservation [31, 32].

But in 1964, the interest for the neutron EDM measurement grew up with the first observed CP violation in the K^0 decay [33]. Indeed, particle physics theories including CP violation made naturally appear the nEDM, which was one of the main constrain for these models. Today, discovered sources of P and CP violations (K^0, B^0 [34, 35] and D^0 [36] decays) are included in the SM (through the δ phase in the CKM matrix) but the situation remains unchanged for the role played by the nEDM to constrain theories beyond the SM [16, 37]. Those models propose explanations for unexplained points by the SM. For instance, the SM does not answer a crucial question: why the visible Universe is mostly made of matter?

2.1.2 The Universe Baryon Asymmetry problem

In the early Universe, antimatter and matter would have annihilated to produce photons, according to the Big Bang theory [2]. Starting from the same amount of matter and antimatter, the Universe should now be made of a small equal amount of matter and antimatter. The current Universe composition is a proof that an asymmetric process occurred in the past since the antimatter is nearly absent in the Universe [38].

In 1967, Sakharov[1] proposed a scenario to explain this Baryon Asymmetry of the Universe (BAU) [3], requiring three criteria to be fulfilled. First, a small violation of the baryon number B is needed to allow a system to go from a $B = 0$ state to a $B \neq 0$ state. Then, C and CP violations are required in order to slightly favour antimatter disappearance with respect to matter. Finally, these processes have to occur during a non thermal equilibrium phase, otherwise, the reverse processes would smooth out any matter or antimatter excess. In particle physics models, a first order electroweak phase transition plays this role.

The matter-antimatter asymmetry in the universe can be estimated by the ratio:

$$\eta = \frac{n_B - n_{\bar{B}}}{n_\gamma} \tag{2.4}$$

where $n_B/n_{\bar{B}}$ are respectively the number of baryons/anti-baryons and n_γ is the number of photons.

From satellite observations of the Cosmic Microwave Background, this ratio has been estimated to be $\eta = (6.18 \pm 0.15) \times 10^{-10}$ [39]. This ratio is also an input for the Big Bang Nucleosynthesis model which predicts the light nuclei abundances. In order to match measured abundances, the η ratio is constrained to $\eta = (5.80 \pm 0.27) \times 10^{-10}$ [40], which is consistent with the previous η value.

There, the CP violation condition from the three Sakharov criteria becomes very important. With all the CP violating processes found in the electroweak sector and incorporated in the SM, the predicted matter-antimatter asymmetry $\eta_{SM} \sim 10^{-19}$ is 9 orders of magnitude smaller than the experimental one. Thus, a strong motivation of SM extensions is to predict new CP violation sources to get a baryonic asymmetry consistent with observations. In this context, the nEDM searches are important since they may reveal new CP violation sources.

2.1.3 The nEDM in the SM

A neutron EDM could arise from two CP violation sources in the SM: one from the electroweak sector and another one from the strong sector.

In the electroweak sector, a contribution to the nEDM can be calculated in a two quarks model with a spectator quark [41]. This contribution of the electroweak sector to the nEDM amounts

[1] Peace Nobel price in 1975.

to: $|d_n| \sim 10^{-32-31}\,e$.cm. Using the link between the CP violating phase in the CKM matrix and the quarks EDM, another calculation has been performed, based on the fact that there is no quark EDM contribution before 3 loops diagrams [42]. This contribution has been estimated to $|d_n| \sim 10^{-34}\,e$.cm [43].

In the strong sector, the quantum chromodynamics Lagrangian can be split in two parts: one concerning the quark-gluon interactions and the other one related to the interaction of gluons with the quantum vacuum [44]. This latter, violating the CP symmetry, is related to the neutron EDM via a theory-free angle θ. The parameter $\bar{\theta}$ related to this angle θ is linked to the neutron EDM through [15]:

$$|d_{\mathrm{n}}| \sim \bar{\theta} \times 10^{-16}\,e.\mathrm{cm} \tag{2.5}$$

Today, the neutron EDM is the strongest constrain on the θ angle (through the $\bar{\theta}$ parameter). The best experimental limit on the nEDM [1] directly translates to a limit for $\bar{\theta} < 10^{-10}$. This constitutes the strong CP problem, as the natural range for $\bar{\theta}$ is the unity. Peccei and Quinn have tried to solve this problem by introducing an additional symmetry ($U(1)_{PQ}$) [4]. In this model, the $\bar{\theta}$ value is 0 and a new particle, the axion, is involved during the spontaneous break of this additional symmetry. This potential new particle has not been found yet. Thus, the strong CP problem remains unsolved.

Up to now, the nEDM has already brought stringent constrains on the SM in the strong sector. In the electroweak sector, SM predictions are currently out of reach. But extensions of the Standard Model, including other CP violation sources, predict larger values for the nEDM, in the $10^{-28} - 10^{-26}\,e$.cm domain. As a result, it is possible to constrain these SM extensions by measuring the nEDM (and other particles EDMs).

2.1.4 The nEDM in extensions of the SM

The Higgs search at LHC [5, 6] has confirmed what was hinted since about 20 years by EDM measurements: no squark, predicted by supersymmetric (SUSY) models, have been found below the TeV scale. This hint was triggered by the so-called SUSY CP problem: the upper limits brought by the neutron, Tl and Hg EDMs have constrained the CP-odd SUSY phases θ_A and θ_μ to $\simeq 10^{-2}$, for SUSY particle masses M_{SUSY} at the 500 GeV level. These phases are (roughly) constrained by EDMs d as follow [15]:

$$d \times M_{SUSY}^2 = a_\mu \sin\theta_\mu + a_A \sin\theta_A \tag{2.6}$$

For a given EDM value and constant a_μ and a_A, the larger the SUSY mass scale, the larger the θ_A and θ_μ free parameter space. By pushing mass limits of SUSY particles above the TeV scale, LHC results have thus "resolved" this problem, as shown in Fig. 2.2. At the same time, several SUSY models have been excluded.

The first order electroweak phase transition playing the role of the thermodynamic non-equilibrium Sakharov criterion (see 2.1.2) is not allowed anymore in the SM [45]. On the contrary, models of Electroweak Baryogenesis (EWBG) beyond the SM still allow this kind of transition [46]. EDMs vary like $1/\Lambda^2$, where Λ is the new physics mass scale [15]. The power of EDMs can be demonstrated by means of the following example: Fig. 2.3 shows the new physics particle mass range excluded by EDMs in the framework of a minimal EWBG scenario [47]. Today, this kind of scenarios has almost been excluded by the new limits set on the electron EDM and the Hg EDM (see 2.1.5). However, an improvement of the nEDM limit below $10^{-27}\,e$.cm in the next experiments generation has the potential to rule out more elaborated models.

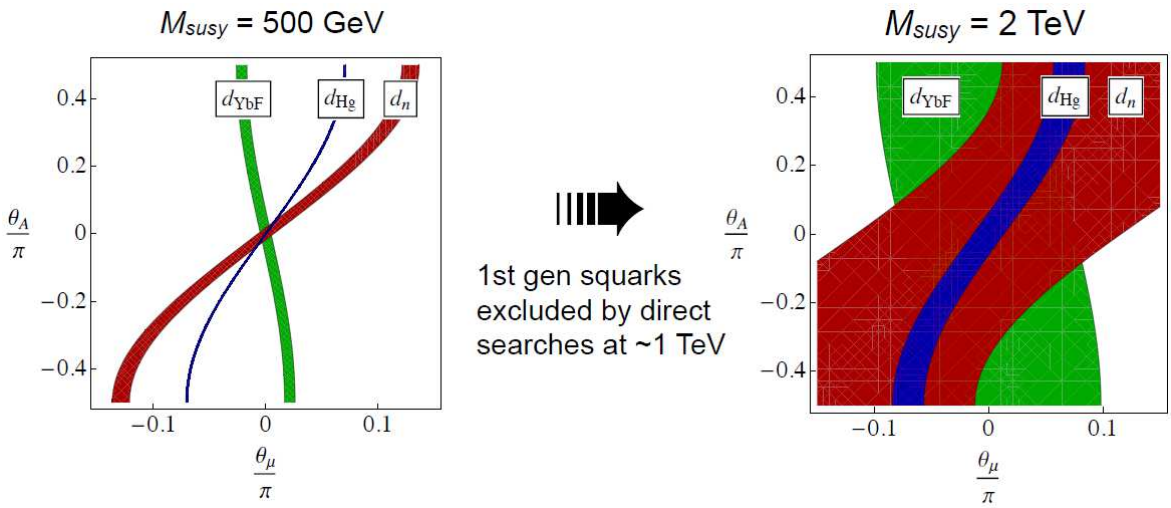

Figure 2.2: Illustration of the relaxation of the SUSY CP problem: constrains put by EDMs on SUSY CP violating phases. Picture taken from [15].

2.1.5 Other electric dipole moments

As shown in Fig. 2.2, other electric dipole moments can constrain models beyond the SM. Projects to measure directly the EDM of charged particles like protons, deuterons or muons on high precision rings are in development[48, 49]. There exist two types of atomic systems used for EDM measurements: diamagnetic atoms and paramagnetic atoms and molecules [17].

2.1.5.1 Paramagnetic atoms

In the case of paramagnetic atoms, there is a single electron in the external electronic shell. The contribution to the atomic EDM comes from the electron EDM by means of a relativistic effect linked to the electron movement around the atom [50]. Without this effect, the Schiff screening effect predicts that inside a neutral atom, electric charges arrange in such a way that the external electric fields cancel [51]. As a result, there would be no induced atomic EDM by the single electron EDM. Finally, the relation between the EDM of the paramagnetic atom d_{par} and the electron EDM d_e is given by [15]:

$$d_{\text{par}} \simeq 10 d_e \frac{Z^3 \alpha^2}{J\,(J+1/2)\,(J+1)^2} \tag{2.7}$$

where Z is the atomic number, α its polarisability and J its angular momentum. As the observable EDM depends on the cube of the atomic number, heavy paramagnetic atoms are used to measure d_e. As a result, the best current limit on the electron EDM coming from a paramagnetic atom comes from the ^{205}Tl EDM: $|d_e| < 1.6 \times 10^{-27}\, e$.cm [52].

This limit has been confirmed using YbF molecules [53] and has recently been improved using polar molecules of ThO down to $|d_e| < 8.7 \times 10^{-29}\ e$.cm [54]. This large increase of the sensitivity is mainly due to the higher electric field obtained in polar molecules than in atoms.

2.1.5.2 Diamagnetic atoms

Diamagnetic atoms are probes for nuclear EDMs. Indeed, the Schiff theorem applies for these atoms at first order but is violated at second order because of the finite size of nuclei. Unlike paramagnetic atoms EDMs, diamagnetic atoms EDMs are smaller than the sum of their constituents EDMs. As a result, the atom EDM comes from CP violating couplings between nucleons

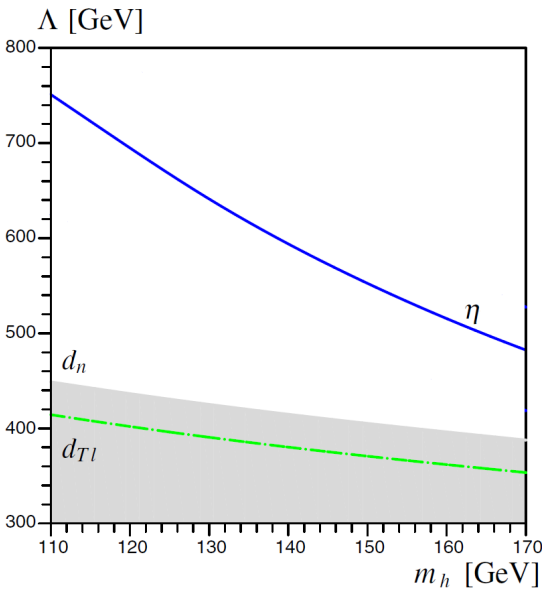

Figure 2.3: New physics mass exclusion areas in a minimal EWBG scenario due to EDMs limits in 2007. The blue line corresponds to the threshold mass scale required to produce the baryon asymmetry according to Sakharov criteria. Picture taken from [47].

and electrons and from couplings between nucleons. The present best limit on the ^{199}Hg EDM is $\left|d(^{199}Hg)\right| < 3.1 \times 10^{-29}$ e.cm [55], setting a limit on the proton EDM $|d_p| < 0.4 \times 10^{-23}$ e.cm.

2.2 The nEDM measurement

2.2.1 Principle

The principle of the nEDM measurement is visible through the interaction Hamiltonian of a neutron in static magnetic and electric fields:

$$H = -\vec{d_n}.\vec{E} - \vec{\mu_n}.\vec{B} \tag{2.8}$$

In the presence of a magnetic field and an electric field, the energy levels split as shown in Fig. 2.4.

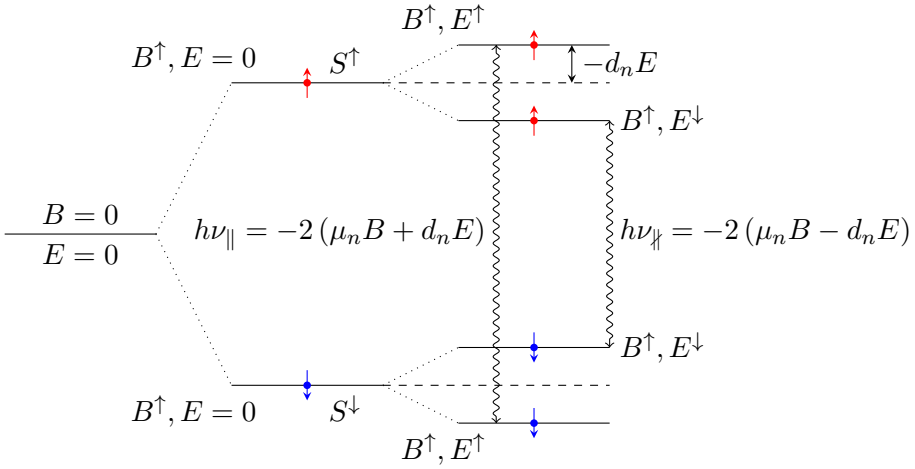

Figure 2.4: Scheme of the neutron energy levels splitting of a neutron in magnetic and electric fields. Subscripts $\parallel$ and $\nparallel$ correspond respectively to parallel and anti-parallel $\vec{B}$ and $\vec{E}$ fields configurations. It is assumed that d_n and μ_n have the same sign.

The nEDM is then measured via the difference of Larmor frequencies $\nu_\parallel$ and $\nu_\nparallel$ in parallel and anti-parallel static magnetic and electric fields through:

$$d_\mathrm{n} = \frac{-h(\nu_\parallel - \nu_\nparallel) - 2\mu_n(B_\parallel - B_\nparallel)}{2(E_\parallel + E_\nparallel)} \tag{2.9}$$

Because the magnetic interaction is dominant, the experimental strategy is always to apply a low magnetic field and a large electric field. In the case where the B field is unchanged in parallel and anti-parallel configuration and the electric field only changes its sign, the nEDM is given by:

$$d_n = \frac{-h(\nu_\parallel - \nu_\nparallel)}{4E} \tag{2.10}$$

The neutrons precession frequency is measured using the Ramsey's separated oscillating fields method. This method is explained in the following paragraph.

2.2.2 The experimental technique

The experimental technique used to determine the neutron Larmor frequency is the same for all storage experiments. Polarized ultra cold neutrons are stored in a precession chamber and the number of remaining spin up and spin down neutrons are counted after the Ramsey's separate oscillating fields procedure. This procedure is part of a cycle. It is repeated several times for a given magnetic and electric fields configuration. The Ramsey's method was used for nEDM beam measurements, but the oscillating fields were spatially separated instead of timely separated. This method is described thereafter and sketched out in Fig. 2.5.

2.2.2.1 Ramsey's separate oscillating fields method

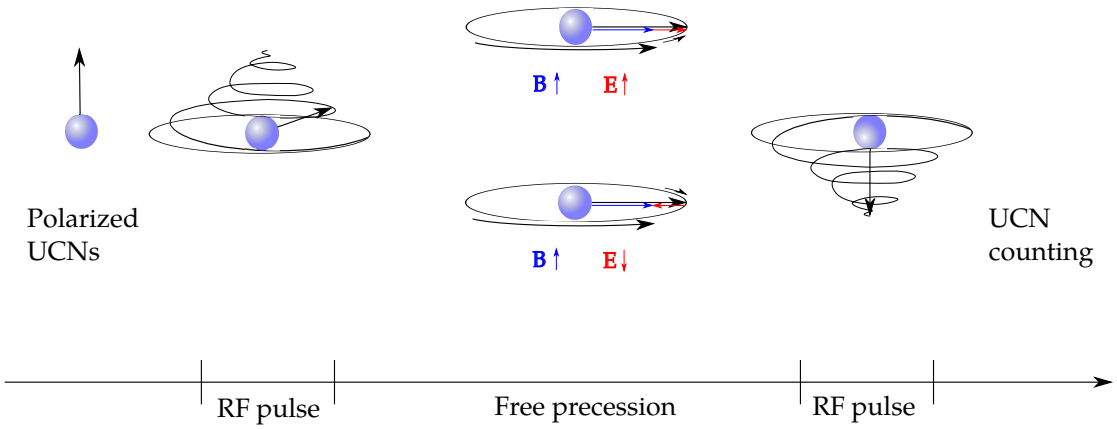

Figure 2.5: Principle of the Ramsey separated oscillating field method.

Polarized ultracold neutrons are stored in a precession chamber where parallel or antiparallel magnetic and electric fields are applied. The UCN spin is initially aligned along the main magnetic field B_0. During a short period τ_{RF}, a radiofrequency (RF) pulse with a frequency in principle equal to the neutron Larmor frequency $f_n = \frac{\gamma_n}{2\pi} B_0$ is applied. As a result, the neutron spin is flipped into the plane orthogonal to the static magnetic field and the applied RF pulse is called $\pi/2$ pulse. Neutrons are then free to precess during a time $T \gg \tau_{\mathrm{RF}}$. At the end of the precession time T, a second $\pi/2$ pulse is applied with the same frequency as the first one. A phase is accumulated during the free precession if $d_{\mathrm{n}} \neq 0$. This leads to a frequency shift. The actual Larmor frequency is determined by slighly detuning the RF pulse frequency and by counting the spin up and the spin down neutrons, in order to scan the so-called Ramsey pattern, shown in Fig. 2.6.

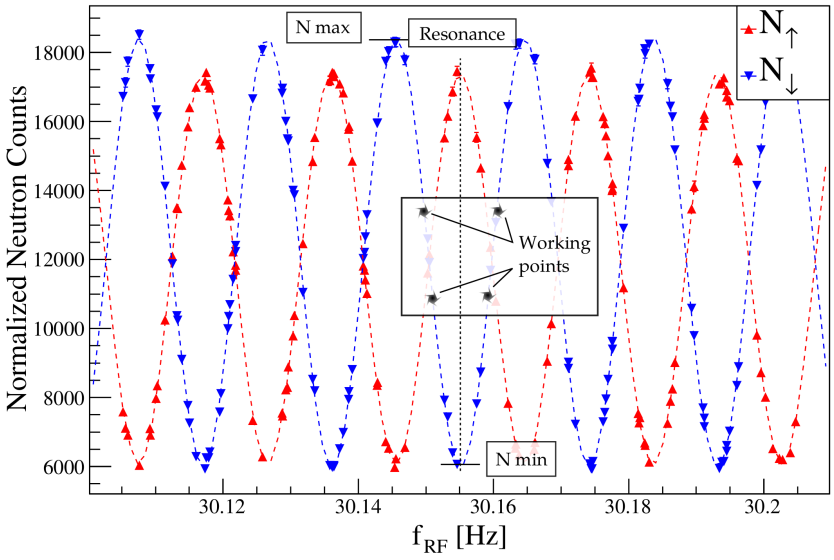

Figure 2.6: Ramsey pattern obtained in August 2012 after 50 s of precession in the oILL spectrometer at PSI. The most populated spin state at the beginning of each cycle is $N^{\downarrow}$.

In practice, only the Ramsey central fringe is scanned. Four working points, placed where the slope is the steepest, are used in order to increase the sensitivity of the Larmor frequency

measurement. For an initial spin up population, this central fringe is approximated by:

$$N^{\uparrow/\downarrow} = N_0^{\uparrow/\downarrow}\left(1 \mp \alpha^{\uparrow/\downarrow}\cos\left[\frac{(f_n - f_{RF})}{\Delta\nu}\pi\right]\right) \tag{2.11}$$

where $\Delta\nu = \frac{1}{2(T+4\tau/\pi)}$ is the half width of the central fringe, $N_0^{\uparrow/\downarrow}$ the number of detected neutrons for each spin state at half the resonnance with sign $-/+$ corresponding respectively to spin up/down UCNs. $\alpha^{\uparrow/\downarrow}$ is the visibility of the fringe defined as:

$$\alpha^{\uparrow/\downarrow} = \frac{N_{max}^{\uparrow/\downarrow} - N_{min}^{\uparrow/\downarrow}}{N_{max}^{\uparrow/\downarrow} + N_{min}^{\uparrow/\downarrow}} \tag{2.12}$$

Using a best fit of $N^{\uparrow}$ and $N^{\downarrow}$ with (2.11), the neutron Larmor frequency is determined for both parallel and antiparallel magnetic and electric fields.

2.2.2.2 Expected statistical sensitivity

From (2.11), it is possible to get the expression of the neutron Larmor frequency as a function of the number of detected neutrons:

$$f_n^{\uparrow/\downarrow} = f_{RF} + \frac{\Delta\nu}{\pi}\arccos\left(\frac{N^{\uparrow/\downarrow} - N_0^{\uparrow/\downarrow}}{\mp\alpha^{\uparrow/\downarrow}N_0^{\uparrow/\downarrow}}\right) \tag{2.13}$$

and the statistical error on the neutron precession frequency is determined through:

$$\begin{aligned}
\sigma_{f_n}^{\uparrow/\downarrow 2} &= \left(\frac{\partial f_n}{\partial N^{\uparrow/\downarrow}}\sigma_{N^{\uparrow/\downarrow}}\right)^2 + \left(\frac{\partial f_n}{\partial N_0^{\uparrow/\downarrow}}\sigma_{N_0^{\uparrow/\downarrow}}\right)^2 + \left(\frac{\partial f_n}{\partial \alpha^{\uparrow/\downarrow}}\sigma_{\alpha^{\uparrow/\downarrow}}\right)^2 \\
\sigma_{f_n}^{\uparrow/\downarrow 2} &= \left(\frac{\Delta\nu}{\pi\alpha^{\uparrow/\downarrow}N_0^{\uparrow/\downarrow}}\right)^2 \times \frac{1}{1 - \left(\frac{N_0^{\uparrow/\downarrow} - N^{\uparrow/\downarrow}}{N_0^{\uparrow/\downarrow}\alpha^{\uparrow/\downarrow}}\right)^2} \\
&\quad \times \left[N^{\uparrow/\downarrow} + \left(\sigma_{N_0^{\uparrow/\downarrow}}\frac{N^{\uparrow/\downarrow}}{N_0^{\uparrow/\downarrow}}\right)^2 + \left((N^{\uparrow/\downarrow} - N_0^{\uparrow/\downarrow})\frac{\sigma_{\alpha^{\uparrow/\downarrow}}}{\alpha^{\uparrow/\downarrow}}\right)^2\right]
\end{aligned} \tag{2.14}$$

The two last terms contribution (with $\sigma_{N_0^{\uparrow/\downarrow}}$ and $\sigma_{\alpha^{\uparrow/\downarrow}}$) corresponds to about 1% of the total error. In the present case, the four working points are around half of the resonnance, *i.e.* $N^{\uparrow/\downarrow} \simeq N_0^{\uparrow/\downarrow}$. Thus, the statistical uncertainty on the neutron Larmor frequency is approximated by:

$$\sigma_{f_n}^{\uparrow/\downarrow} \simeq \frac{\Delta\nu}{\pi\alpha^{\uparrow/\downarrow}\sqrt{N^{\uparrow/\downarrow}}} \tag{2.15}$$

Using (2.10), the statistical error on the nEDM becomes:

$$\sigma_{d_n} = \sqrt{\sigma_{f_n}^{\parallel\ 2} + \sigma_{f_n}^{\nparallel\ 2}}\frac{h}{4E} \tag{2.16}$$

$$\sigma_{d_n} \simeq \frac{\hbar}{2\alpha TE\sqrt{N_{\text{tot}}}} \tag{2.17}$$

The last formula gives the experimental key observables of the nEDM statistical sensitivity. The higher the applied electric field, the larger the nEDM sensivity. At the same time, increasing the precession time would allow neutrons to accumulate more phase during the free precession. The visibility of the central fringe exponentially decreases with the precession time. It depends on

precession chamber properties and on magnetic field conditions (UCN spin guiding fields and field homogeneity in the precession chamber). It also depends on the neutron spin analysis efficiency. The number of ultracold neutrons detected at the end of the precession also depends on precession chamber properties and roughly decreases exponentially with the precession time. Therefore, the setting of the precession time is closely linked to the central fringe visibility and the number of detected UCNs. This storage time was tuned to about 200 s in [56] for the nEDM experiment at PSI.

All the parameters have to be as high as possible in order to lower the statistical error σ_{d_n}. But there is some interplay between T, E and N_{tot}. During the nEDM history, the game has always been to increase these parameters, but also to lower the systematic errors.

2.2.3 nEDM measurement history

The evolution of the nEDM upper limit is shown in Fig. 2.7. Two main types of measurement are visible: beam and storage measurements.

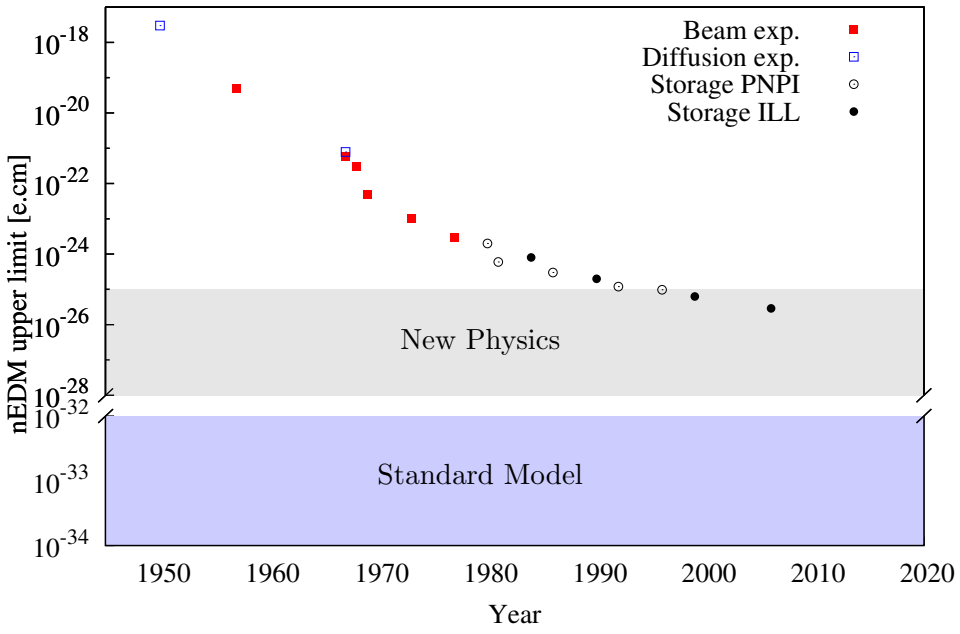

Figure 2.7: nEDM upper limit history.

2.2.3.1 Cold neutron beam based experiments

The first dedicated nEDM measurement was carried out by Smith, Purcell and Ramsey in 1957, setting the upper limit $|d_n| < 5 \times 10^{-20}\, e.\text{cm}$ [28]. The experiment used a 2000 m/s polarised neutron beam going through a homogeneous magnetic field in which the neutron spin precesses. During the experiment, an electric field was applied and the authors did not measure any correlation with the neutron precession frequency. These beam line experiments have continued during about 20 years, until the first ultra cold neutron sources were built in the 80's. nEDM measurements with these slower neutrons (v_n <5 m/s) are better for two main reasons. First, slow neutrons spend more time in the electric field area. Second, the so-called geometric-phase effect is reduced [8]. The consequence of this relativistic effect is that moving neutrons see a motional magnetic field $\vec{B}_v = \frac{\vec{E}\times\vec{v}_n}{c^2}$. As a result, the neutron precession frequency is shifted proportionally

to the electric field, like for a dipole electric moment. This effect can be cancelled up to a certain point, but was limited by the beam divergence in such beam line experiments, even with 150 m/s beams like in the last neutron beam EDM measurements [57].

2.2.3.2 Ultra cold neutron source based experiments

Following the first UCN observation in 1969 [58], nEDM measurements were mostly carried out with storage experiments. Systematics coming from the geometric-phase effect have been dramatically reduced thanks to low neutron speeds. The competition between two experiments – PNPI and RAL-Sussex-ILL – is visible after 1980. Both experiments use stored UCNs. The PNPI (Gatchina, Russia) experiment was made of two precession chambers, allowing the two Larmor frequencies in parallel and anti-parallel configurations to be measured simultaneously. The ILL (Grenoble, France) experiment was using a single precession chamber with a cohabiting magnetometer in order to monitor the magnetic field in both fields configurations. This latter gave the best upper experimental limit on the nEDM: $|d_n| < 2.9 \times 10^{-26}$ e.cm (90% CL) [1].

2.2.3.3 Current nEDM projects

Today, several collaborations aim at improving the nEDM upper limit by at least one order of magnitude. A map of these nEDM projects is shown in Fig. 2.8.

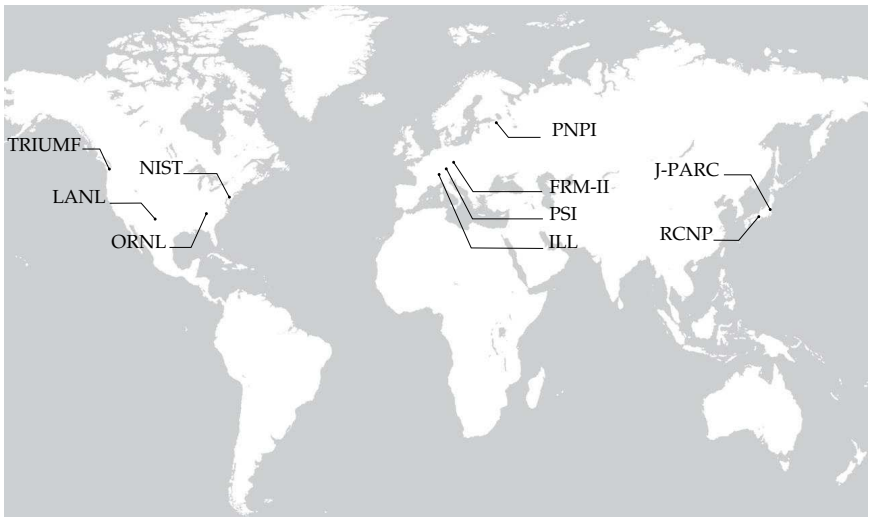

Figure 2.8: World wide nEDM competition.

Back to the cold neutron beam, at ILL, the nEDM is measured through an induced spin rotation during neutron reflection close to the Bragg condition on quartz. The nEDM upper limit coming from this experiment is in the 10^{-23} e.cm range [18] and can be further improved down to the current nEDM best sensitivity according to the authors. It takes advantage of the high electric fields inside a non-centrosymmetric crystal lattice ($\sim 10^8$ V/cm) and the high available cold neutron flux.

Other nEDM projects are UCN based experiments. Three of them plan to produce UCNs using superfluid ^{4}He. Two of them are cryogenic experiments. The experiment being developped at SNS (USA) should benefit from a superconducting screen. The expected sensitivity is in the range $10^{-28} - 10^{-27}$ e.cm. However, this experiment encounters technical challenges and is time consuming due to the cool-down and warm-up of the cryostat. The SNS collaboration first plans to build critical components of the apparatus (detector, HV, magnets and polarised ^{3}He system)

Experiment	Source	Cell	Measurement technique
ILL - CryoEDM	Superfluid ^{4}He	^{4}He	Cryo HV, Superconducting tech.
- UCN -			ν_L Ramsey tech., SQUIDS
SNS - EDM	Superfluid ^{4}He	^{4}He	Cryo HV, Superconducting tech., SQUIDS
- UCN -			ν_L: ^{3}He capture, ^{3}He co-magnetometer
RCNP - TRIUMF	Superfluid ^{4}He	Vacuum	Small volume, ^{129}Xe co-magnetomer
- UCN -			@RNCP and then @TRIUMF
ILL - PNPI	ILL turbine	Vacuum	ν_L: Ramsey tech.
- UCN -	PNPI:Solid D_2		$E = 0$ for magnetometer
PSI EDM	Solid D_2	Vacuum	ν_L: Ramsey tech., Hg co-magnetometer
- UCN -			^{132}Cs, ^{3}He external magnetometers
MUNICH - FRMII	Solid D_2	Vacuum	ν_L: Ramsey tech., Hg co-magnetometer
- UCN -			Cs external magnetometer
J-PARC - UCN	Solid D_2	Vacuum	Under development
LANL - UCN	Solid D_2	Vacuum	Under development
ILL-PNPI	Cold n. beam	Solid	Crystal diffraction
			Non-centrosymmetric crystal
J-PARC	Cold n. beam	Solid	Crystal diffraction
			Non-centrosymmetric crystal
NIST	Crystal	Solid	R & D

Table 2.2: Worldwide nEDM projects in competition. From [59]

and to test it at the NCSU[2] reactor over the next 4 years. Once this will be done, they could get approval to finish the construction of the cryogenic system, the neutron beam guide and the room temperature magnetic shield [26]. CryoEDM project at ILL [60], one of the most important nEDM projects, was recently stopped due to funding cutoff.

Room temperature experiments aim at measuring the nEDM at the $10^{-28} - 10^{-27}$ e.cm level. Among those, a project is being built at the Research Center of Nuclear Physics (RCNP) in Japan [23] and will be later moved to TRIUMF in Canada. This project, based on previous room-temperature measurements, plans to use a Xe buffer gas inside the precession volume in order to suppress the so-called systematic geometric phase effect.

A recent measurement performed at ILL with the PNPI spectrometer (a stack of two precession chambers placed in a common magnetic field) by Serebrov *et al.* reports an nEDM upper limit of $|d_n| < 5.5 \times 10^{-26}$ e.cm [20]. A later stage is planned at a new UCN source at PNPI.

At FRM-II, the Munich collaboration plans to use a four-layer stack of precession chambers (two with UCNs and a Hg co-magnetometer, two with only Hg). It also plans to use external Caesium magnetometers in order to have a better control on systematics. The progress with the apparatus is going fast (the magnetic shield is already installed). However, the UCN source has not started yet.

The other main room temperature project is the nEDM experiment at PSI, which aims at measuring the nEDM below the 10^{-27} e.cm level in two phases. The first phase uses the spectrometer which belonged to the RAL-Sussex-ILL collaboration. The spectrometer has been moved in 2009 to the new PSI UCN source and renamed oILL for old ILL spectrometer. The second phase is based on the development of a new spectrometer (n2EDM) involving two UCN storage chambers.

All these last experiments are based on the ultra cold neutrons use. Their properties are summarized in the next part.

[2]North Carolina State University

2.3 Ultra cold neutrons

The neutron electric dipole moment search is closely linked to the development of ultra cold neutron sources. Neutrons are called ultra cold when a particular energy regime is reached, below a few hundred neV. A short summary of different neutron regimes is given in this section, followed by a description of ultra cold neutron properties and different ways to produce them.

2.3.1 From the neutron to the ultra cold neutron

The neutron was discovered in 1932 by Chadwick [61]. Fast neutrons are mainly produced during fission or spallation reactions. Today, they are widely used to study materials, thanks to their property to deeply penetrate into matter because of their neutrality. They can be thermalized using collisions with light nuclei. Because neutrons show particular properties for different energy ranges, they are usually classified in different regimes (see Tab. 2.3), according to their kinetic energy, temperature or wavelength.

Regime	Energy	Wavelength [nm]	Temperature [K]
Fast	$> 500\,\mathrm{keV}$	$< 10^{-3}$	$> 6 \times 10^6$
Epithermal	$25\,\mathrm{meV} < \mathrm{E} < 500\,\mathrm{keV}$	$10^{-3} < \lambda < 0.18$	$300 < T < 6 \times 10^6$
Thermal	$25\,\mathrm{meV}$	0.18	300
Cold	$50\,\mu\mathrm{eV} < \mathrm{E} < 25\,\mathrm{meV}$	$0.18 < \lambda < 4$	$0.6 < T < 300$
Very cold	$300\,\mathrm{neV} < \mathrm{E} < 50\,\mu\mathrm{eV}$	$4 < \lambda < 52$	$0.0035 < T < 0.6$
Ultra cold	$< 300\,\mathrm{neV}$	>52	<0.0035

Table 2.3: Different neutron energy regimes and characteristic energy, wavelength, temperature ranges. The blue shaded rows correspond to optical neutrons.

The neutrons De Broglie wavelength λ_n is defined as follow:

$$\lambda_n = \frac{h}{\sqrt{2m_n E}} \tag{2.18}$$

where m_n is the neutron mass and E the neutron kinetic energy. When the neutron wavelength becomes larger than the distance between atoms of a material - neutrons are cooler - neutrons interact with a set of nuclei instead of a single nucleus. These neutrons are called optical neutrons ($E < 25\,\mathrm{meV}$, $\lambda > 0.2\,\mathrm{nm}$) and can be reflected by matter as observed by Fermi in 1947 [62]. Such reflexion happens if the incidence angle θ fulfils the following condition:

$$\sin\theta \leq \sqrt{\frac{V_F}{E}} \tag{2.19}$$

where V_F is the so-called Fermi potential or optical potential. It is one of the most important characteristic for UCNs and is defined as:

$$V_F = \frac{2\pi\hbar^2}{m_n} \sum_i N_i b_i \tag{2.20}$$

where N_i is the number of atoms per volume unit and b_i is the coherent scattering length of the nuclei constituting the material. A typical order of magnitude for the Fermi potential is a few hundred neV. Eq (2.19) shows an interesting property of neutrons: neutrons with lower energies than the Fermi potential are reflected whatever the incidence angle θ. In that case, one speaks about ultra cold neutrons (UCN). It is therefore possible to store them in material bottles. The existence of such very slow and storable neutrons was predicted by Zel'dovich in 1959 [63] and first experienced by Shapiro's group in 1969 [58].

2.3.2 Ultra cold neutron interactions

The UCNs particularity is that their kinetic energy is of the same order of magnitude as the energy associated to each fundamental interaction (except for the weak interaction).

2.3.2.1 Strong interaction

The strong interaction governs the UCNs interaction with matter, leading to their reflection or their absorption. A thorough study of UCNs interactions is given in [64]. Classically, UCNs with a lower energy than the Fermi potential are always reflected. Quantumly, the collision of a neutron with kinetic energy E with a material surface is described by the stationary Schrödinger equation:

$$\frac{-\hbar^2}{2m_n}\Delta\Psi + V\Psi = E\Psi \tag{2.21}$$

$$\begin{cases} V = 0 & x < 0 \\ V = V_F + iW & x > 0 \end{cases} \tag{2.22}$$

where V_F is the Fermi potential calculated in (2.20). This term is the volumic average of an effective potential taking into account a collection of nuclei at positions $\vec{r_i}$:

$$U(\vec{r}) = \frac{2\pi\hbar^2}{m_n}\sum_i b_i\delta(\vec{r} - \vec{r_i}) \tag{2.23}$$

This potential was introduced by Fermi [65] in order to describe a slow neutron diffusion ($< 1\,\text{eV}$) on a set of nuclear potentials ($\sim 40\,\text{MeV}$), without using the perturbation theory (because the interaction potential is much larger than UCN energies).

The imaginary part W reflects the possibility for UCNs to be absorbed or up-scattered during a reflection if the wave function penetrates the potential wall (in both cases, the neutron is lost). For UCNs, both the absorption and the up-scattering cross-sections are inversely proportional to the neutron velocity v_n [64]. W is calculated using absorption and up-scattering cross-sections σ_a and σ_{us}:

$$W = \frac{\hbar v_n}{2}\sum_i N_i\left(\sigma_a^i + \sigma_{us}^i\right) \tag{2.24}$$

Thus, in the low energy regime *i.e.* for UCNs, W is independent of the neutron velocity.

The neutron wave function behaviour is described by (see Fig. 2.9):

$$\Psi = \begin{cases} e^{ik_x x} + Re^{-ik_x x} & x < 0 \\ Te^{ik_t x} & x > 0 \end{cases} \tag{2.25}$$

with $k_x = \sqrt{\frac{2m_n}{\hbar^2}.E_\perp}$ and $k_t = \sqrt{\frac{2m_n}{\hbar^2}.(E_\perp - V_F)}$. Where $E_\perp$ is the orthogonal component of the energy, R and T are respectively the amplitudes of the reflected and transmitted waves. Thanks to the continuity conditions at $x = 0$, the amplitude of the reflected wave is given by:

$$R = \frac{\sqrt{E_\perp} - \sqrt{E_\perp - V}}{\sqrt{E_\perp} + \sqrt{E_\perp - V}} \tag{2.26}$$

In the majority of cases $W \ll V_F$, which leads to a reflection probability:

$$\begin{cases} R^2 = \left(\frac{1-\sqrt{1-V_F/E_\perp}}{1+\sqrt{1-V_F/E_\perp}}\right)^2 & E_\perp > V_F \\ |R|^2 = 1 - \frac{2W}{V_F}\sqrt{\frac{E_\perp}{V_F - E_\perp}} & E_\perp < V_F \end{cases} \tag{2.27}$$

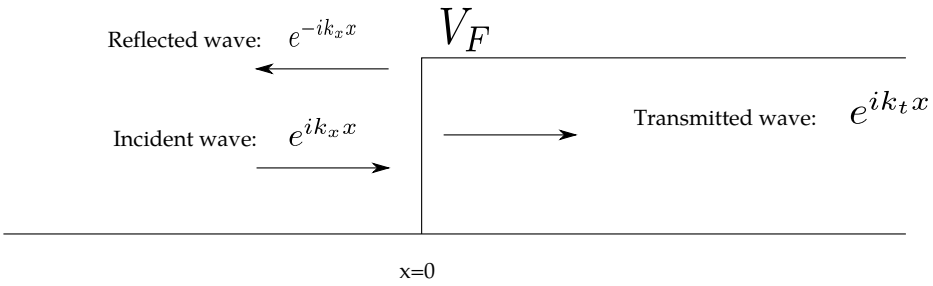

Figure 2.9: Scheme of the neutron interaction with a material surface.

Even with $E_\perp < V_F$, neutrons have a probability to be lost proportional to W, due to the evanescent transmitted wave function. The loss probability per bounce μ is defined as:

$$\mu(E_\perp) = 1 - |R|^2 = \eta\sqrt{\frac{E_\perp}{V_F - E_\perp}} \tag{2.28}$$

with $\eta = \frac{2W}{V_F}$ the loss factor. This loss factor is a characteristic of the material used and is at the $10^{-5} - 10^{-4}$ range.

Thus, when UCNs reach a material wall, they can be either reflected or transmitted through the wall according to Eq (2.27). But the reflection process can occur in two different ways. The neutron specular reflection is well suited in the case of a perfectly flat wall surface. But in the case where the surface exhibits some roughness, reflections can be either specular or diffuse. When a diffuse reflection occurs, the UCN reflection direction is given by Lambert's cosine law: the probability for a UCN to be reflected with an angle θ from the surface normal in the solid angle $d\Omega$ is given by $\cos\theta d\Omega$.

Thanks to the strong interaction of UCNs with a material wall, the UCN storage is possible. Moreover, thanks to the diffuse reflection process, a mechanical equilibrium can be reached, leading to the isotropy of the UCN speed distribution, as for a gas.

2.3.2.2 Magnetic interaction

UCN polarisation UCNs interact with magnetic fields by means of their magnetic moment $\mu_n = -9.6623647(23) \times 10^{-27}\,\mathrm{JT}^{-1}$ [66]. The resulting potential energy is:

$$V_{\mathrm{mag}} = -\vec{\mu_{\mathrm{n}}}.\vec{B} \tag{2.29}$$

For convenience, the magnetic moment can be expressed as $\mu_n \simeq 60.3\,\mathrm{neV/T}$. It means that UCNs crossing a 5 T magnetic field region experience a $\pm 300\,\mathrm{neV}$ potential if they have their spin parallel or anti-parallel to the field direction (the magnetic moment is anti-parallel to the spin). As a result, it is possible to use a sole magnetic field to polarise UCNs, as shown in Fig. 2.10.

Magnetic fields can also be used as magnetic shutters or fully magnetic traps. This method is used in order to avoid losses due to wall interactions [67, 68].

Polarisation handling Considering the spin as a classical angular momentum (even if a quantum approach is more appropriate for a spin as in [69]), the magnetic field exerts a torque on the UCN spin $\vec{S}$ and gives the following time dependence:

$$\frac{\mathrm{d}\vec{S}}{\mathrm{d}t} = \gamma_n \vec{S} \times \vec{B} \tag{2.30}$$

The Bloch equations (2.30) [70] describe the spin evolution in the presence of a magnetic field. The spin precesses around the magnetic field at the Larmor angular frequency:

$$\omega_{\mathrm{n}} = \gamma_{\mathrm{n}} B = \omega_L \tag{2.31}$$

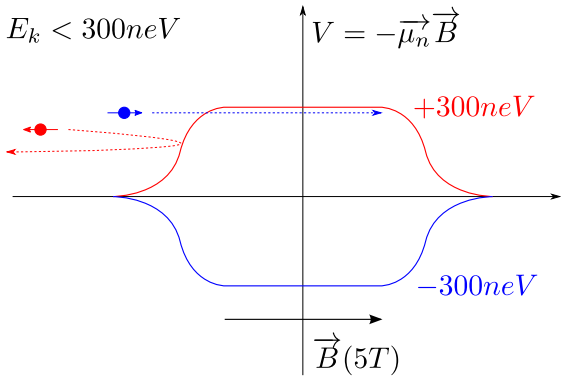

Figure 2.10: Scheme of the UCN polarisation process using a magnetic field barrier.

Like for Nuclear Magnetic Resonance (NMR) applications, longitudinal and transverse relaxation times T_1 and T_2 are added to (2.30) in order to take into account depolarisation. Assuming the main field direction along z, Eq (2.30) becomes for an ensemble of spins:

$$\begin{aligned} \frac{\mathrm{d}S_{x,y}}{\mathrm{d}t} &= \gamma_n \left(\vec{S} \times \vec{B}\right)_{x,y} - \frac{S_{x,y}}{T_2} \\ \frac{\mathrm{d}S_z}{\mathrm{d}t} &= \gamma_n \left(\vec{S} \times \vec{B}\right)_z - \frac{S_z - S_0}{T_1} \end{aligned} \tag{2.32}$$

where S_0 is the asymptotic value of S_z. In the PSI experiment, the longitudinal relaxation time T_1, related to wall depolarisation's is above the 1000 s level while the transverse relaxation time T_2, related to the homogeneity of the magnetic field is about 600 s with homogeneous field and weak gradient.

2.3.2.3 Gravity

As for all massive particles, UCNs are sensitive to gravity. Their gravitational potential energy of the same order as their kinetic energy and is given by:

$$E_p = m_n g z \tag{2.33}$$

where $m_n g \simeq 102.6\,\mathrm{neV/m}$. As a result, a 100 neV UCN can not rise above 1 m. This property can be used to vertically store them or to increase the UCN detector efficiency by letting them fall down to the detector (see 3.5.1). The effect of the gravitation on their trajectories is clearly visible as shown in Fig. 2.11.

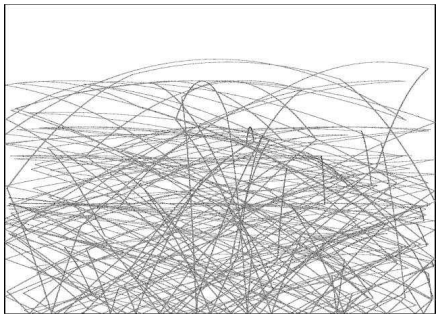

Figure 2.11: Parabolic UCN trajectories simulated using GEANT4-UCN, as an example of the gravity effect on ultra cold neutrons.

Because ultra cold neutrons have a very low energy, they can be used to characterize gravitational quantum states [71].

2.3.2.4 Weak interaction

The weak interaction is responsible of the neutron β decay as shown by the artistic Feynman diagram depicted in Fig. 2.12.

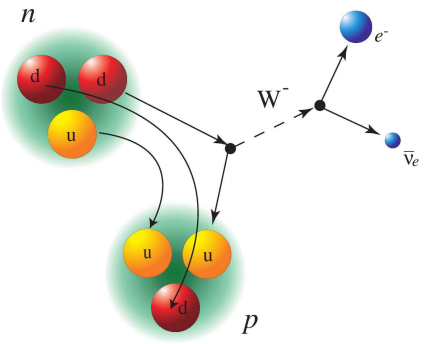

Figure 2.12: Feynman diagram of the neutron β decay.

The neutron lifetime $\tau_n = 880.0 \pm 0.9\,\mathrm{s}$ [72] is large enough to allow a long UCN storage. Thus, stored UCNs are used to determine τ_n which plays a role in the Big-Bang Nucleosynthesis and in the determination of the V_{ud} term, needed for the test of the CKM matrix unitarity [73]. UCNs are also used to perform angular correlation measurements in the neutron decay [74].

2.3.3 Ultra cold neutron production

Fast neutrons are produced either in reactors, through the fission process or with spallation process on heavy nuclei targets. They are then cooled down to the cold neutron regime in light nuclei volumes (heavy water, polyethylene moderators, deuterium...). Finally, cold neutrons are down scattered to the ultra cold regime by phonon excitation in superfluid He or in solid D_2 crystal. In order to suppress the reverse process, the moderator is cooled down to very low temperatures.

Another way to cool down neutrons to the ultra cold regime is to use the gravitational deceleration. This method is used at the ILL combined to the so called Steyerl turbine which lowers the neutron energy spectrum by about a factor 100 down to the 100 neV range using multiple neutron reflections on rotating nickel coated curved blades [75].

The UCN sources development is closely linked to the nEDM measurement projects. Indeed, the nEDM experiments need high density UCN sources in order to lower the statistical error. A summary of UCN sources projects with expected performances and characteristics is given in Tab. 2.4. The PSI UCN source working principle is described in the following chapter, in the context of the nEDM experiment at PSI.

Location	Neutron production	Moderator	Expected UCN density [cm^{-3}]	Status
ILL, PF2 (France)	Reactor	Liquid D_2+ Turbine	50	**Working**
PSI (Switzerland)	Spallation	Solid D_2	>500	**Working**
Triga (Germany)	Reactor	Solid D_2	10	Working
FRM-II (Germany)	Reactor	Solid D_2	10000	>2015
LANL (USA)	Spallation	Solid D_2	120	Working
RCNP (Japan)	Spallation	Superfluid He	15	Working
Triumf (Canada)	Spallation	Superfluid He	5800	>2015
PNPI (Russia)	Reactor	Superfluid He	10000	>2015
ILL, H172 (France)	Reactor	Superfluid He	>1000	>2014
SNS (USA)	Spallation	Superfluid He	150	Working

Table 2.4: Summary of UCN source projects with initial expected UCN densities.

Chapter 3

The nEDM experiment @ PSI

Contents

The nEDM experiment at PSI is supported by a collaboration of 12 European laboratories. The project is divided in three stages. First, the collaboration restarted operating the oILL spectrometer at ILL between 2005 and 2009. This spectrometer, operating at room temperature, holds the best nEDM limit [1]. During this time period, the spectrometer was restarted and refurbished. Then, it was moved to the new UCN source developed at the Paul Scherrer Institute in 2009 in order to take nEDM data and reach the 10^{-27} e.cm level. This goal has been recently reviewed to 10^{-26} e.cm, if source performances stay lower than former expectations. Finally, in the last phase of the experiment, a new spectrometer will be constructed. It has been designed to increase UCN statistics and to allow a better control on systematic effects.

Today, the nEDM experiment is installed in the West area at the PSI. Because the PSI houses a wide range of facilities in various topics, the nEDM experiment has also some rather close and large magnetic devices like the SULTAN [1] or EDIPO [2] magnets (see Fig. 3.1). They create magnetic fields up to 12 T at their centre. Once they are operating in a steady state, these magnets are not problematic anymore, thanks to the Surrounding Field Compensation (SFC) system (see 3.4.2.2). However, during the ramping up and down of the magnets, it is not possible to take nEDM data due to the magnetic field variations. This problem can not be circumvented because the nEDM apparatus has to be located close to the PSI UCN source, in order to get as many ultra cold neutrons as possible. This source, commissioned in 2011, is shortly described in the following section.

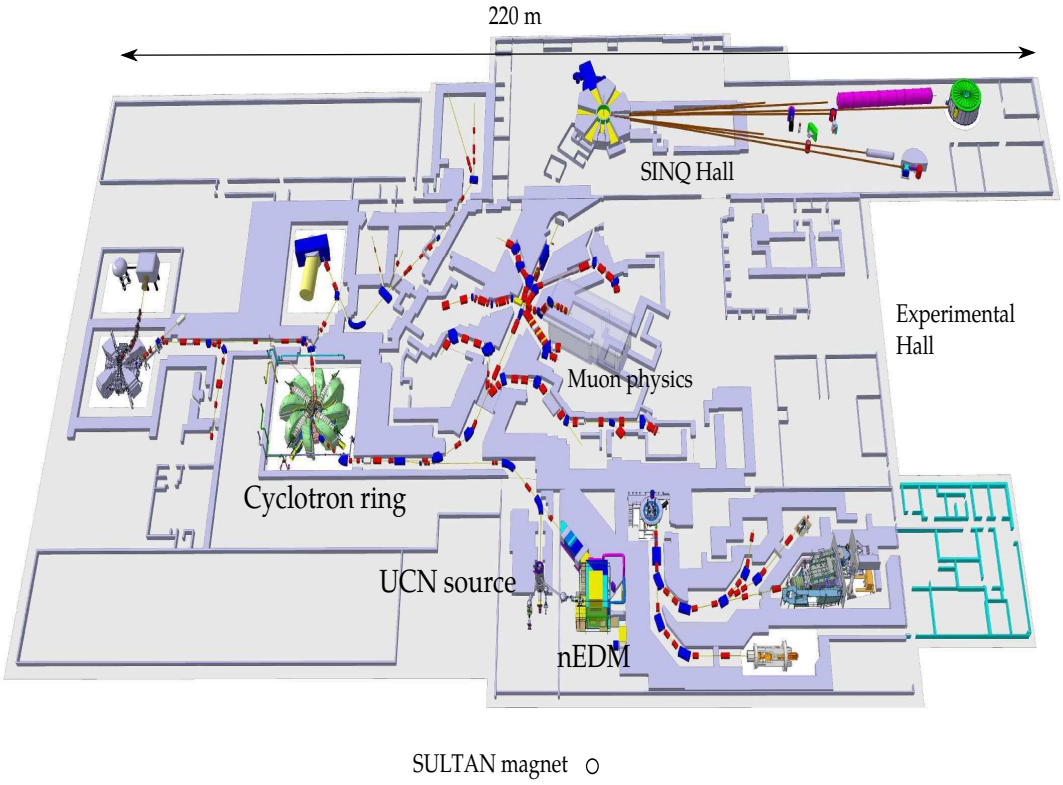

Figure 3.1: Facility site plan of the PSI West area where the nEDM experiment is located.

[1] SUpraLeiter Test ANlage: superconductor test facility.
[2] European Dipole project: used for instance in ITER conductors tests.

3.1 The PSI ultra cold neutron source

The PSI UCN source uses the fast proton beam delivered by the PSI cyclotron. In usual conditions, the source is operated with the full 590 MeV proton beam at 2.2 mA with a duty cycle around 1%. The proton beam is delivered during 3 or 4 s every 360 s or 480 s, according to users needs.

A scheme of the PSI UCN source is shown in Fig. 3.2 and a detailed description of the source can be found in [76]. During the proton pulse, fast neutrons are produced by spallation on a lead target. These neutrons are then thermalized in a volume of heavy water. Finally, cold and ultra cold neutrons are produced in a 30 ℓ solid deuterium (sD_2) crystal at 5 K. Such a technique to produce ultra cold neutrons was initially proposed by Golub and Pendlebury [77] and is called superthermal UCN production. It uses the phonons excitation in the crystal lattice which leaves incoming neutrons with almost no energy. The reverse process is suppressed by the low temperature of the converter. UCNs are then filled into a Diamond-Like Carbon (DLC) coated storage vessel before being distributed towards different UCN beam ports. The West-1 beam port, used to check the UCN source performances, provides about 25×10^6 detected UCNs for 4 s proton kicks. A measurement performed at this beam port using a 25 ℓ NiMo coated storage volume has shown a density above 30 UCNs/cm^3 after 3 s storage. The West-2 port is dedicated to UCN users for tests or experiments. The last port (South one), is connected to the nEDM experiment whose apparatus is described in the following section.

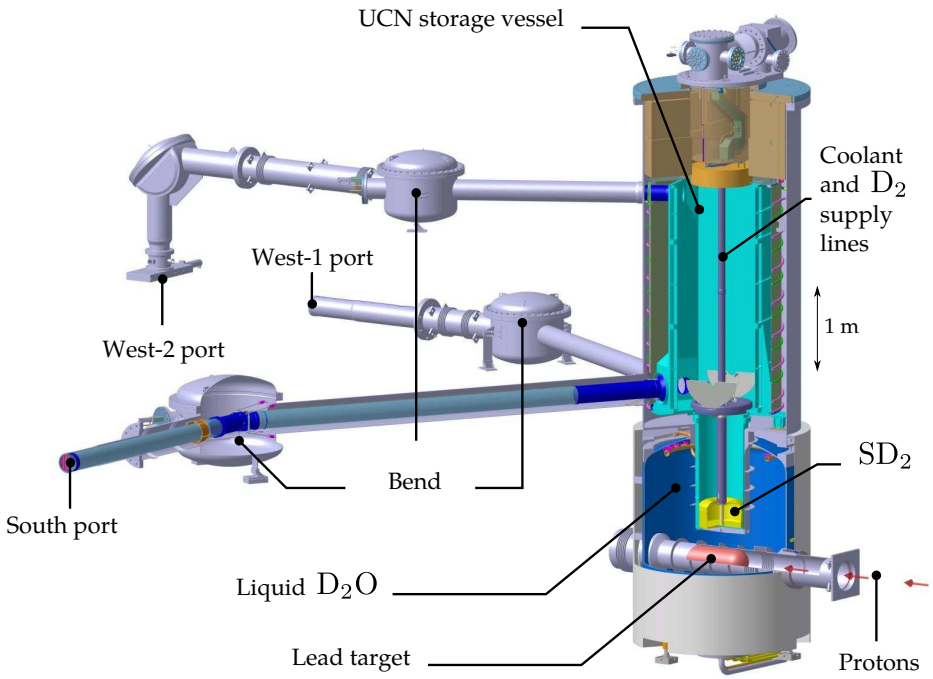

Figure 3.2: Sketch of the PSI ultra cold neutron source with its three available beam ports. The nEDM experiment is connected to the South beam port.

3.2 Experimental apparatus

For the current data taking, the former oILL spectrometer has been upgraded and moved to the Paul Scherrer Institute in 2009. The nEDM apparatus is shown in Fig. 3.3. The nEDM apparatus is enclosed in a wooden non-magnetic thermohouse with an air conditioning system in order to

stabilise the temperature at the 0.5-1 K level. The components of the nEDM apparatus and their role are described. For an exhaustive description of the experimental setup, see [56].

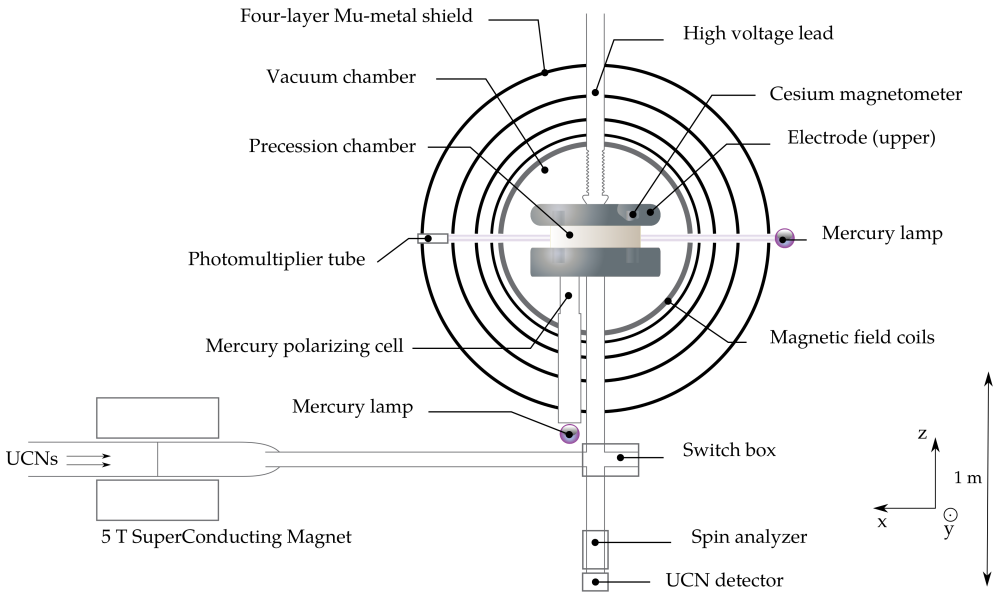

Figure 3.3: Sketch of the nEDM apparatus. The big surrounding field compensation coils (SFC) are not shown. On the bottom right corner of this figure, the nEDM reference frame axes used throughout this work is defined. It is centred on the Hg readout level at the centre of the precession chamber.

UCNs coming from the source first cross a super conducting magnet (SCM) which acts as a polariser. Then, they are guided towards the storage chamber via a switch box, used to provide neutrons in different parts of the experiment. After a precessing period, UCNs fall down to the spin analyser and are finally detected in the UCN detector.

3.3 UCN transport and polarisation

Downstream to the SCM, neutrons are transported towards the experiment within glass guides. Additional magnetic fields are used in order to keep the UCN polarisation along their way towards the precession chamber.

3.3.1 NiMo coated guides

In the experiment, glass guides of 73 mm inner diameter with a NiMo coating are used to transport UCNs. The same glass guides (with a larger diameter) are also used to bring neutrons from the UCN source to the SCM entrance. The NiMo coating is usually used in UCN transport because its Fermi potential is rather large (220 neV) and its weak depolarisation probability per bounce ($\sim 10^{-5}$) is appropriate to keep the UCN polarisation. These properties allow for a good UCN transmission.

3.3.2 Super Conducting Magnet

A super conducting magnet is located between the UCN tank and the nEDM apparatus. The SCM is used to polarise UCNs: when they are guided through the 5 T SCM, neutrons with less than

300 neV can be polarised. Indeed, neutrons with the wrong spin state are not able to cross the magnetic potential energy created by the SCM and are reflected back to the UCN tank. Because the UCN guides Fermi potential is around 220 neV, it is assumed that there are no UCNs with energies larger than 300 neV. Therefore, it is assumed that UCNs are fully polarised by crossing the SCM. The work reported in [7] states for a 100% UCN polarisation.

3.3.3 Guiding coils system

The visibility of the Ramsey central fringe α (see 2.2.2.1) is directly related to the UCN polarisation. Therefore, keeping a high polarisation is very important to get a competitive nEDM statistical sensitivity. In 2013, the initial UCN polarisation was measured to 75-80% (during neutron T_1 measurements). The role of the guiding coils system is to maintain the polarisation obtained thanks to the SCM along the way to the precession chamber. The guiding coils system is depicted in Fig. 3.4 [7].

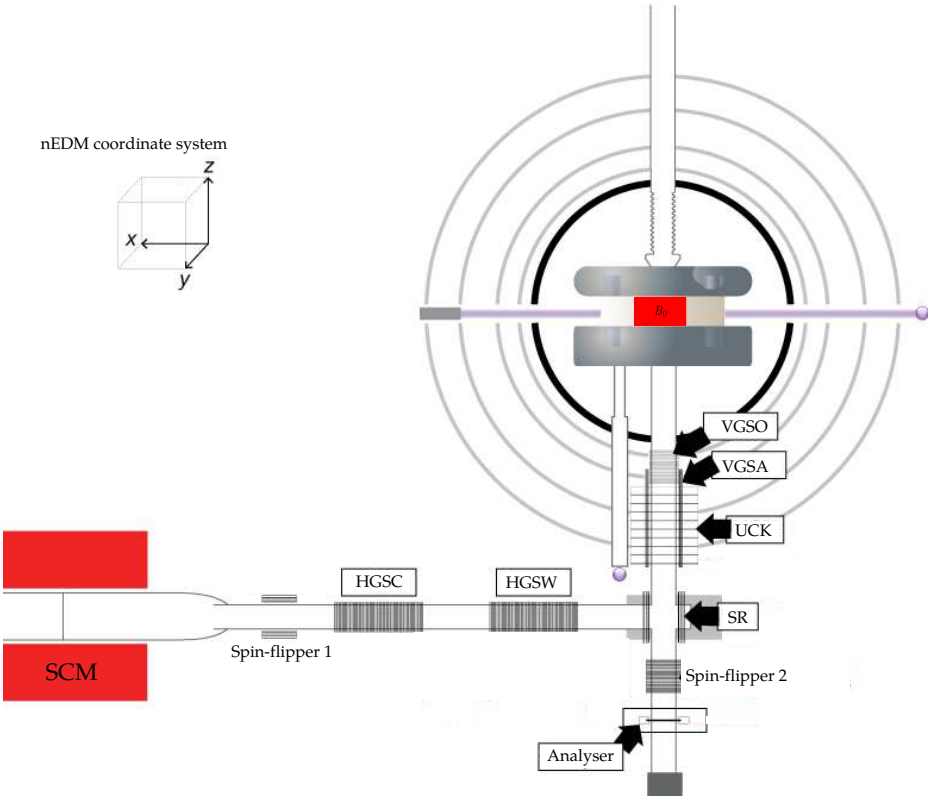

Figure 3.4: Scheme of the current nEDM apparatus guiding coils system. VGSA, VGSO, UCK... are the main guiding coils names.

The adiabaticity parameter k is used to quantify the UCN spin ability to follow the magnetic field created by guiding coils (see appendix A):

$$k = \frac{\gamma_n B^2}{|\mathrm{d}B/\mathrm{d}t|} \tag{3.1}$$

If the field change is much lower than the Larmor angular frequency ($k \gg 1$), then the neutron spin is able to adiabatically follow the magnetic field. On the contrary ($k < 1$) the UCN spin

is not able to stay aligned on the magnetic field and depolarisation occurs. $k \simeq 5 - 10$ is the transition between the two regimes. In the experiment, the UCNs polarisation is kept along their trajectories using smoothly varying holding fields produced by the guiding coils. In particular, a $\pi/2$ rotation has to be done between the horizontal initial field (stray field of the SCM) and the vertical field inside the precession chamber. The guiding coil system plays there a critical role for the transition between the two field directions, for both up and down field configurations inside the precession chamber. A study of the guiding coils system can be found in [7].

3.3.4 Switch box

The UCN switch box is used to deliver UCNs in different parts of the apparatus: from the UCN source to the precession chamber (filling), from the precession chamber to the UCN detector (emptying) and from the UCN source to the detector (monitoring). The whole switch is non-magnetic in order to avoid UCN depolarisations. As shown in Fig. 3.5, it is made of a disk on which tubes are mounted for the associated nEDM cycle phases: filling, monitoring and emptying positions. This disk is rotated by means of piezo motors.

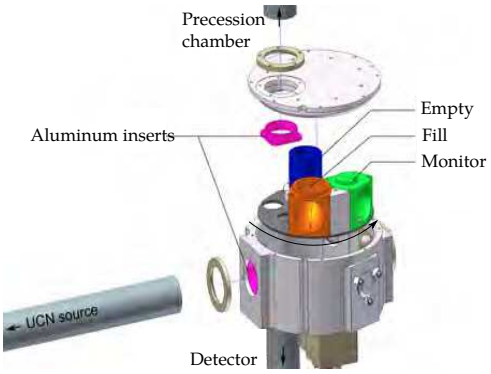

(a) Switch box scheme.

(b) Open view if the switch box.

Figure 3.5: Scheme and picture of the UCN switch box. Pictures taken in [56].

The curvature radius of the NiV coated filling and monitoring guides is 5 cm (V_F =220 neV). This quite low curvature radius could be the cause of a rather low transmission of these parts (about 67%) reported in [56], additionnally to the coating quality. However, due to mechanical constrains, it was not possible to increase this curvature radius. Storage times have also been measured and are in the 10 s range. Therefore, there is room to improve the UCN transmission at the switch level. It is planned to redo the coating inside the switch guiding parts.

3.3.5 UCN storage chamber

The precession chamber consists in two electrodes and one insulating ring, as shown in Fig. 3.6. The top electrode is connected to the High Voltage (HV) system while the bottom electrode is grounded. nEDM measurements are carried out in a 10^{-3} mbar ^{4}He atmosphere in order to apply high electric fields with a lower number of electric discharge, up to 11 kV/cm during the nEDM 2013 data taking. Because UCNs and Hg (see 3.4.3.1) have to be stored during a few hundred seconds, electrodes are made of aluminium coated with DLC which presents good UCN and Hg storage properties. In order to avoid electric discharges, polished aluminium corona rings are

used to suppress sharp edges. The former insulator ring used by the RAL-Sussex collaboration was made of quartz ($V_F = 90\,\text{neV}$). It has been replaced by a polystyrene one (PS), coated with Deuterated PS ($V_F = 160\,\text{neV}$). By this mean, the initial number of UCNs is increased by 80%, as shown during tests performed at ILL [78].

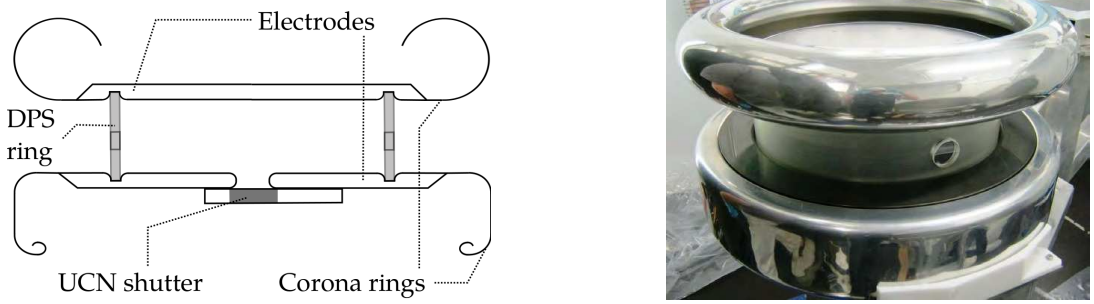

(a) Drawing of the precession chamber.

(b) Picture of the precession chamber.

Figure 3.6: Scheme and picture of the UCN precession chamber.

3.4 Magnetic field control

As shown in Eq (2.9), the magnetic field control is crucial for the nEDM measurement. All setup components contributing to the field control and monitoring are described in this section.

3.4.1 Magnetic field production

3.4.1.1 B_0 coil

The main magnetic field ($B_0 \simeq 1\,\mu\text{T}$) is produced along the vertical z axis of the experiment. It is created by a cosine-θ coil wound around the vacuum tank, as shown in Fig. 3.7. This coil must produce a field as homogeneous as possible in the precession chamber volume to lower related systematic errors. Unfortunately, about 40% of this field is due to the innermost shield magnetization (see 3.4.2.1). As a result, the field homogeneity depends on the shield degaussing, its openings as well as on its magnetic permeability homogeneity.

3.4.1.2 Hg and neutron radio-frequency coils

Radio-frequency (RF) pulses applied to induce the Hg and neutron $\pi/2$ spins flips are created by two set of coils (AS1 and AS2+TRF for respectively the neutron and the Hg pulses) located around the vacuum tank. The applied RF pulse for neutrons is linear. It has been shown that the use of a Hg linear pulse could tilt the UCN spin direction with respect to the B_0 direction and induce a shift of the Ramsey resonance [79]. Therefore, a circular Hg pulse is currently used. Both Hg and neutron pulses last 2 s.

3.4.1.3 Correcting coils

In order to compensate the asymmetries of the experimental setup (holes in the shield for the UCN and Hg guides, the HV feedthrough, permeability inhomogeneities of the shield...) 33 correcting coils have been added. They are used to give a relative homogeneity of $10^{-3} - 10^{-4}$ of the

magnetic field inside the chamber volume in order to suppress possible depolarisations during the precession. Some of them are also used to produce vertical gradients during systematic errors dedicated measurements and EDM runs (mostly TTC and BTC coils). Several correcting coils, as well as the main B_0 coil are shown in Fig. 3.7.

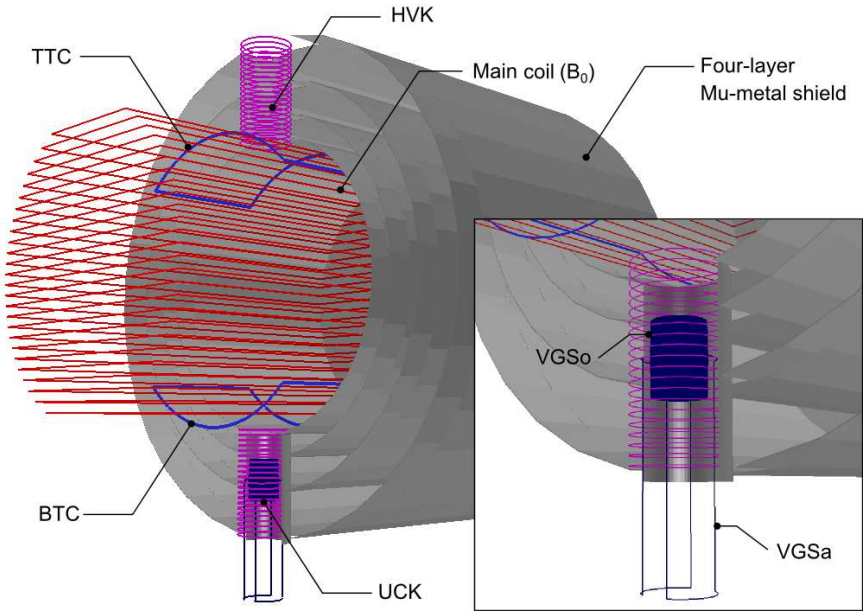

Figure 3.7: Sketch of the main correcting coils, the B_0 cosine-θ coil and the four-layer Mumetal shield (see 3.4.2.1). Picture from Maentouch simulations taken from [80].

3.4.2 Magnetic field stabilisation

3.4.2.1 Static magnetic shield

In order to get a low and homogeneous field area inside the precession chamber, a multilayer magnetic shield is used to reduce the external magnetic field contributions. It is made of 4 Mumetal (nickel iron alloy with high permeability) cylindrical layers. The innermost one has a diameter of 1.15 meters, leaving room for the concentric vacuum tank enclosing the precession chamber. The magnetic shield creates a path along the Mumetal layers which guides the field lines (and thus the magnetic flux) around the experiment. The shielding factors along the three different directions have been measured [81] for small static perturbations at the µT level and are summarized in Tab. 3.1.

Direction	x	y	z
Shielding Factor	13300 ± 600	1600 ± 20	8600 ± 300

Table 3.1: Shielding factors along the three main directions.

It has been shown that the shield needs to be idealised (degaussing procedure with B_0 ON) after large field changes in order to keep a low and stable field within the shield [81], otherwise it becomes sensitive to mechanical perturbations. Additionnal coils enclosing the shielding layers are used to perform its degaussing. An alternating current is applied and the shield hysteresis

curve is scanned. Along time, the signal amplitude is slowly reduced as well as the magnetization of the shield. Typical residual field after degaussing is below 2 nT.

3.4.2.2 Surrounding Field Compensation (SFC)

Three rectangular coils pairs of about 6 per 8 meters surround the nEDM apparatus, centered on the precession chamber. They have been conceived to try to compensate static external field sources like Earth's field or the iron shielding of the UCN source. The system uses a set of 10 three-axes fluxgates sensors serving as input for an active feedback loop, controlling the current (up to 10 A for x,y directions and 20 A for the z direction). This loop allows changes of the surrounding field to be attenuated. A detailed description of the SFC system is given in [80].

3.4.3 Magnetic field monitoring

Two kinds of scalar magnetometers are installed in the oILL spectrometer: the mercury co-magnetometer, measuring the average of the magnetic field modulus over the precession chamber, and an array of 16 external caesium magnetometers surrounding the storage chamber and used to monitor the field modulus vertical gradients.

3.4.3.1 Mercury cohabiting magnetometer

The use of a mercury co-magnetometer was initiated by the RAL-Sussex-ILL collaboration [82]. Since the neutron frequency is extracted from several cycles (see 2.2.2.1), any change of the magnetic field from one cycle to another would reduce the precision of the neutron frequency measurement. The co-magnetometer has been added in order to be able to compensate for such field fluctuations. The Hg system is shown in Fig. 3.8.

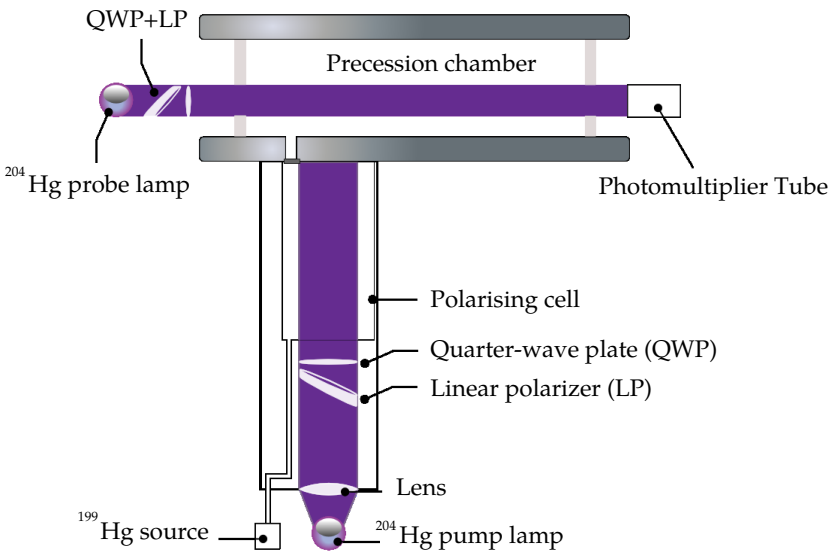

Figure 3.8: Scheme of the Hg co-magnetometer system. Picture taken from [80].

The Hg co-magnetometer gives the precession volume and time average of the magnetic field modulus for each cycle. The sampled volume is the precession chamber, in which polarised ^{199}Hg

atoms are introduced at the beginning of each cycle. The ^{199}Hg atoms are produced by heating mercury oxide and polarised by optical pumping with the UV light emitted by a ^{204}Hg discharge lamp. A second discharge lamp produces the read-out circularly polarised light beam crossing the precession chamber and read by a Photo Multiplier Tube (PMT). A $\pi/2$ pulse is applied as for neutrons at the beginning of the cycle to flip the Hg spins into the B_0 transverse plane and the Hg free induction decay (FID) of the precession signal is observed via the intensity modulation of the read-out light. The magnetic field value is then recovered by means of the signal frequency:

$$\omega_{Hg} = \gamma_{Hg}.B \tag{3.2}$$

Typical Hg frequencies are close to 7.85 Hz, corresponding to a magnetic field of about 1030 nT (it actually slightly depends on the B field direction). During 2013 EDM runs, the precision obtained with the Hg co-magnetometer was around 30 µHz, *i.e.* a precision of 400 fT on the magnetic field.

However, even if the use of the mercury co-magnetometer allows field fluctuations to be corrected for, systematic effects (Geometric Phase Effect and gravitationnal shift for instance) related to the use of the Hg itself and to gradients have to be taken into account (see Sec. 6.4). External caesium magnetometers are used to measure the magnetic field vertical gradient and are described below.

3.4.3.2 Caesium magnetometers array

The caesium scalar magnetometers have been developped by the FRAP group [83] (Fribourg, Switzerland). While the Hg co-magnetometer is based on a FID signal, CsM are used in a forced regime with a RF driving field. A picture of a CsM is shown in Fig. 3.9a.

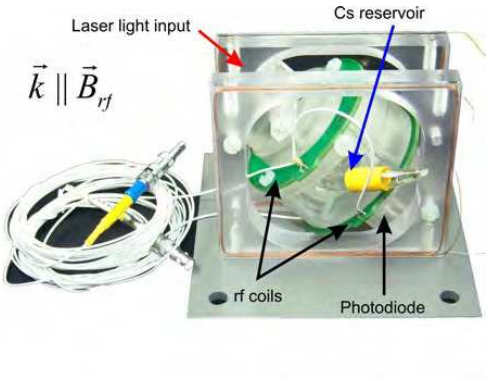

(a) Picture of an open CsM taken in [10].

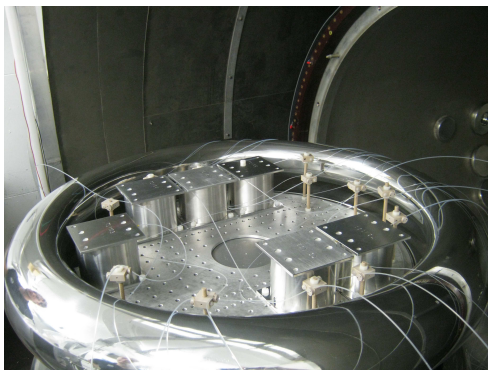

(b) HV CsM above the precession chamber.

Figure 3.9: Open view of a caesium magnetometer and positioning above the HV electrode.

Inside a bulb (not visible in Fig. 3.9a) located at the centre of the CsM, ^{133}Cs atoms polarised by optical pumping, start precessing around the magnetic field after applying an RF pulse by means of small RF coils. The circular polarised laser light used to polarise the atoms is also used as a readout light and is transported via optical fibers. The Cs spin precession creates a modulation of the transmitted light intensity which is detected by a photodiode. The phase difference between the applied RF field and the modulated signal is measured as a function of the exciting frequency. The resonance is found when the phase difference is equal to 90° and the applied RF frequency corresponds to the Larmor frequency of Cs atoms ω^L_{Cs} (about 3.6 kHz). The magnetic field magnitude is then recovered via $B = \omega^L_{Cs}/\gamma_{Cs}$. 16 CsM are located above and below

the precession chamber (see Fig. 3.9b), allowing the magnetic field at several positions around the chamber to be measured with a precision of about 200 pT (the precision on the caesium Larmor frequency is of about 0.7 Hz). Using these CsM layers, it is then possible to extract a mean vertical gradient of the field modulus over the chamber volume. Several methods are used to extract such a gradient. They are presented and tested in Chap. 7.

3.5 UCN spin analysis and detection

At the end of each cycle, the UCN shutter located at the bottom of the storage chamber is opened. Then, UCNs fall down to the detector crossing the spin analysing system. These two devices are described below.

3.5.1 Neutron detector

The NANOSC [3] neutron detector has been developped at LPC Caen [84]. It is based on ^{6}Li glass scintillators and made of 9 channels as shown in Fig. 3.10a. The number of channels has been chosen in order to avoid pile up and dead time due to high counting rates.

(a) NANOSC detector.

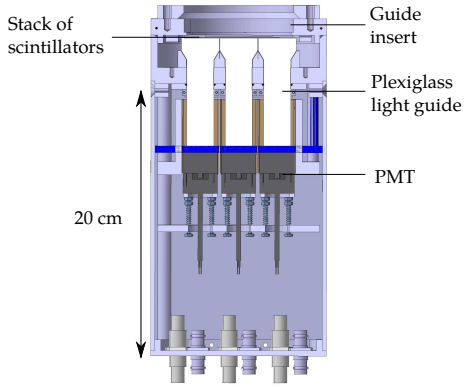

(b) Cut view.

Figure 3.10: Picture and cut view of the NANOSC detector.

As shown in Fig. 3.10b, UCNs first interact in a ^{6}Li based glass scintillators stack ($28\times28\,\mathrm{mm}^2$) [85]. The interaction leading to the UCN detection is the neutron capture in ^{6}Li:

$$^6\mathrm{Li} + \mathrm{n} \rightarrow \alpha + ^3\mathrm{T} + 4.78\mathrm{MeV} \tag{3.3}$$

The capture cross section is $\sigma_{\mathrm{abs}}^{\mathrm{th}} = 940$ barns for thermal neutrons, corresponding to a cross-section of about 4×10^5 barns for ultracold neutrons (assuming a $1/v_{\mathrm{n}}$ law for the capture cross-section). These glass scintillators stacks have been made in order to suppress edge events which corresponds to the loss of one of the two reaction products (mainly the triton) [13]. The stack principle is shown in Fig. 3.11a. UCNs first cross a ^{6}Li-depleted scintillator (GS20) before interacting in a ^{6}Li-enriched layer (GS30). With such an arrangement, the energy is fully deposited in the glass and the signal-to-noise separation is better, as shown in Fig. 3.11b. The first and second scintillator layers are respectively 55 µm and 110 µm thick in order to detect most of UCNs with a minimum of γ interactions to lower the background noise.

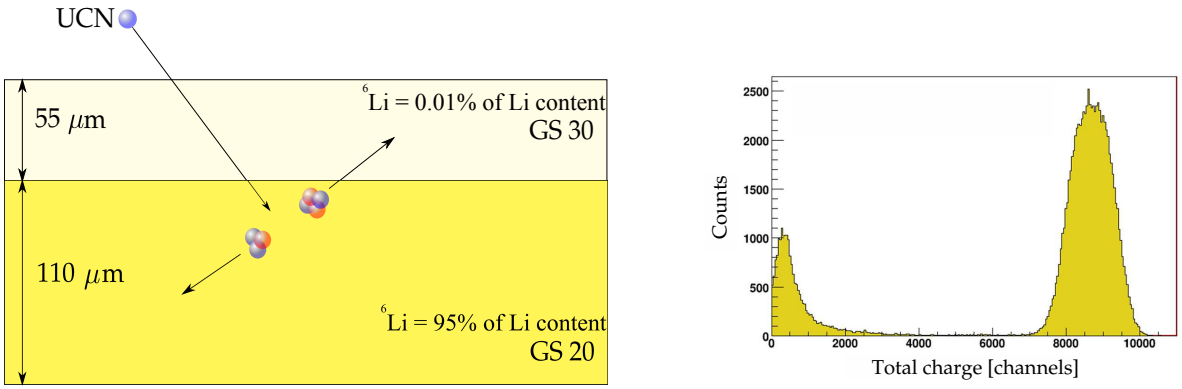

(a) Scintillator glass stack.

(b) QDC spectrum for one NANOSC channel.

Figure 3.11: Stack principle and obtained charge spectrum for one NANOSC channel.

The produced light by Ce^{3+} sites during a few 100 ns inside the scintillator is then guided towards a PMT through a PMMA[4] guide. In order to improve the light collection, the two scintillator layers are linked by molecular sticking.

The Fermi potential of the NANOSC's scintillators is 105 neV for the GS20 and 85 neV for the GS30. Since the detector is located 1.6 m below the storage chamber, UCNs have at least 160 neV energy at the detector entrance level. This ensures a minimal reflection probability at the interface between vacuum and the scintillators.

NANOSC PMTs are read out by the FASTER [5] acquisition system [86], based on FPGA and developed at LPC Caen for nuclear experiments. It is able to handle up to about 4×10^5 counts/s in continuous mode and up to a few 10^6 counts/s in pulse mode [87]. UCNs are discriminated from the background using different kinds of thresholds. First at the FASTER level: events have to pass a voltage threshold of 3 mV and last more than 12 ns at such a 3 mV level. This first step allows fast pulses such as electronic noise or Čerenkov events to be rejected. The remaining background is mainly made of γ rays which deposit less energy than neutrons within the scintillator stack. An offline threshold is applied on the charge distribution in order to discriminate neutron events from remaining background.

All events recorded by FASTER are time stamped. This allows the time distribution of UCNs during each cycle to be measureed. The interesting time periods for the neutron counting (described later in the following section) are the monitoring, spin up and spin down UCN detection. These three detection phases are shown in Fig. 3.14.

3.5.2 Spin analysing system

At the end of each Ramsey procedure, spin up and spin down UCNs are independently counted in order to extract the neutron frequency leading to the nEDM measurement. The two spin states measurement is performed by means of two devices: a spin analyser and an adiabatic spin-flipper shown in Fig. 3.12 and described hereafter.

[3]NANO SCintillator
[4]PolyMethyl Meta Acrylate
[5]Fast Acquisition System for nuclEar Research

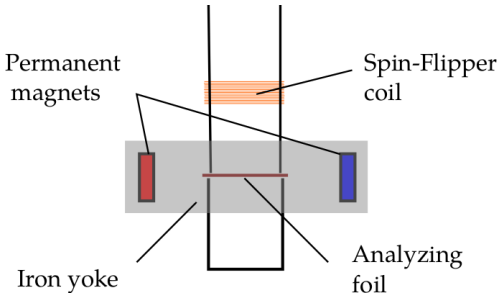

Figure 3.12: Scheme of the spin analysing system.

3.5.2.1 The spin analyser

The spin analyser is made of a magnetised thin iron layer with a thickness of 200–400 nm covering a 25 µm thick aluminium foil. The iron layer can be magnetised up to 2 T using a set of permanent magnets (1.32 T at surface) enclosed in an iron return yoke. Such a magnetisation system produces a 0.8 T magnetisation at the foil centre.

A sketch of the UCN interaction with the analyser is shown in Fig. 3.13. When UCNs reach the analyser, they undergo a potential step $V_{\text{foil}}^{\uparrow\downarrow} = V_F^{\text{Iron}} \pm \mu_n \text{B}$ which depends on the UCN spin state. The first contribution is the iron Fermi potential, $V_F^{\text{iron}} = 210\,\text{neV}$, the second arises out of the interaction of the UCN spin and the iron layer magnetisation $\overrightarrow{\mu_n}.\vec{\text{B}}$. This latter contribution amounts to about 120 neV for 2 T. Thus, the analysing foil lets only cross the UCN spin state anti-aligned on the magnetisation and the other one is reflected upwards the precession chamber. This kind of analyser presents the main advantage to be very compact with respect to a superconducting magnet but has the drawback to absorb a part of UCNs passing through the aluminium layer.

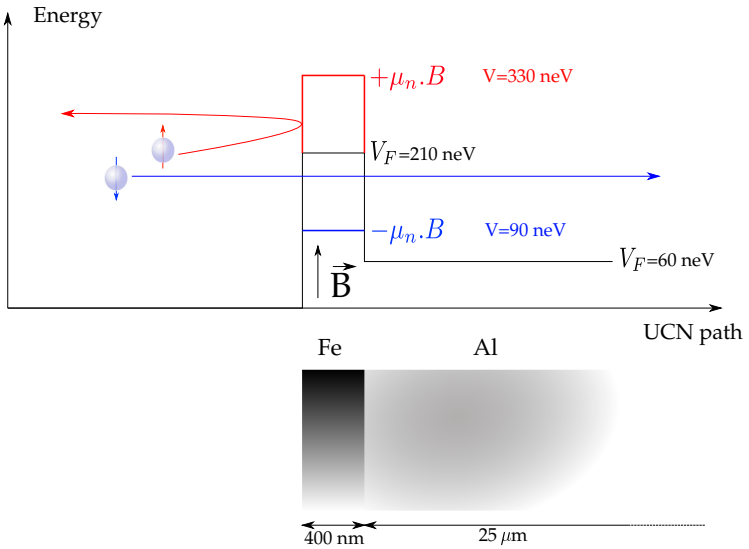

Figure 3.13: Sketch of the spin analyser principle.

3.5.2.2 The adiabatic spin-flipper

Because the analyser lets cross only one UCN spin component, it is necessary to flip the other UCN spin component to be able to detect both components. This is the role of the adiabatic spin-flipper (ASF). The ASF, located upstream of the analyser, is made of a solenoidal coil in which an

alternating current flows, creating an RF field. The ASF also uses the static field gradient coming from the analyser magnetisation system. The spin-flipper is called "adiabatic" because the UCN spin adiabatically follows the effective field which reverses its direction between the entrance and the exit of the ASF. The ASF principle and the way to calculate its spin-flipping efficiency by means of the adiabaticity parameter are given in Appendix B.

The amplitude of the linear RF field is in the 60-80 µT range. The value of the static stray field at the middle of the spin-flipper is of 700 µT, corresponding to an RF frequency between 20 and 25 kHz. The static field gradient is about 20 µT/cm. Finally, for $v_n = 5$ m/s, the adiabaticity coefficient is around 15, meaning that the spin-flip probability is close to 100%. This result has been confirmed by measurements [7].

3.5.2.3 The sequential spin analysis

In order to detect both spin states, the spin-flipper is alternatively switched ON and OFF following a particular sequence. This sequential detection is visible in Fig. 3.14. The ASF is OFF during the first 8 s and spin down neutrons are analysed. Then, the spin-flipper is switched ON for a 25 s period devoted to the spin up detection. Finally, it is switched OFF for 17 s and the spin down component is analysed again.

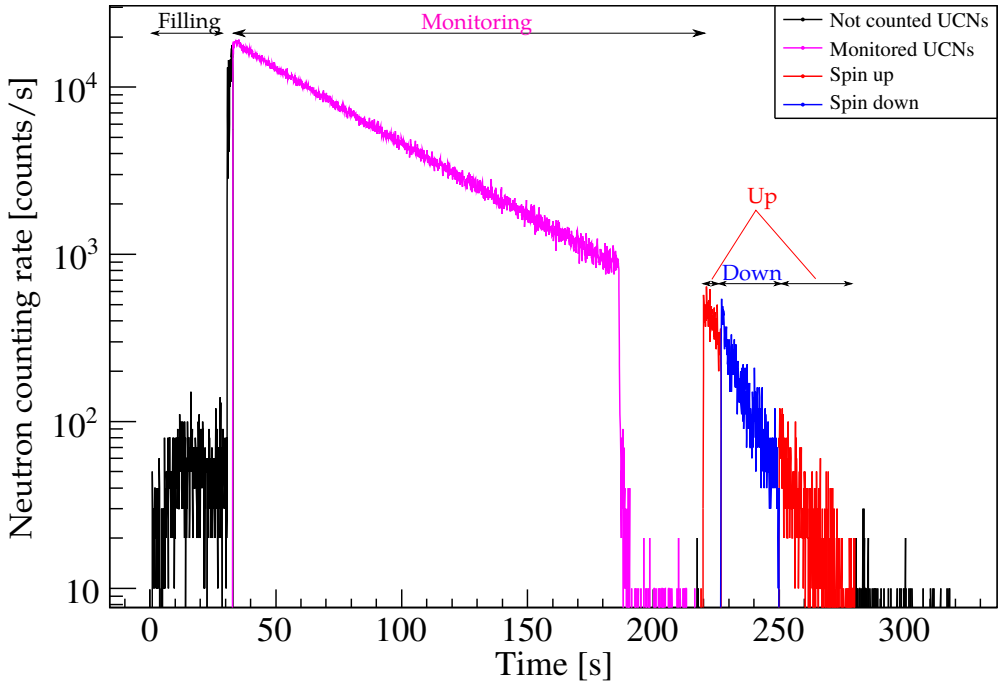

Figure 3.14: Neutron counting rate as a function of time for a full cycle.

The timing sequence of the spin analysis is set using unpolarized neutrons. The sequence is properly set when the measured asymmetry $\mathcal{A} = \frac{N^{\uparrow} - N^{\downarrow}}{N^{\uparrow} + N^{\downarrow}}$ is equal to 0. In that case, there are as many detected spin up UCNs as spin down UCNs. In spite of this sequence setting, this spin analysis presents some drawbacks, due to losses and depolarisations in the switch (see 3.3.4) and the rest of the apparatus.

The next chapter presents in details the drawbacks of the sequential analysis and the development of a more powerful system simultaneously detecting spin up and spin down UCNs.

Chapter 4

Simulations of spin analysing systems

Contents

4.1 Motivations for a new simultaneous spin analysis system

On the nEDM spectrometer, the current spin analysis system used was developed by the RAL-SUSSEX collaboration. It works in a sequential mode, *i.e.* UCN spin components are detected one after the other using a spin-flipper ON or OFF. The drawback of this method is that, when a spin component is analysed, the other one is stored above the analysing foil and UCNs can be lost or depolarised during this time period. Actually, the final number of detected UCNs has been estimated to be lower than 50% of the initial number of UCNs coming from the chamber at the end of the storage time period [10]. This is due to fast losses above the spin analysing foil (likely because of the presence of slits in the switch box). The decrease in the number of detected UCNs N_{UCN} lowers the nEDM sensitivity proportionnally to $\sqrt{N_{\mathrm{UCN}}}$. It means that recovering the other 50% would increase the nEDM sensitivity by a factor $\sqrt{2}$. In addition, since the spin states are treated differently, they are not subject to the same losses and depolarisations. Such an asymmetric treatment of the spin can induce spurious systematic effects in the nEDM measurement.

This last remark led to the idea of elaborating a spin analyser able to simultaneously analyse both UCN spin states. Such a technique had originally been pioneered in early EDM experiments at LNPI [11]. This can be done with one spin analyser for each spin component located in two identical arms. As a result, the storage time of each spin component above the analysing foil is reduced and UCN losses and depolarisations should be minimised. The development of such a Simultaneous Spin Analyser (SSA) is based on GEANT4-UCN simulations.

4.2 GEANT4-UCN simulations

This study is based on previous works [12, 13]. It simulates a realistic and achievable shape for each spin analyser, in order to select the best one. GEANT4 is particularly useful to test devices with complicated geometries. The GEANT4-UCN package, a dedicated version of GEANT4 adapted to UCN physics [88], has been used.

4.2.1 UCN physics

GEANT4 is usually used in high energy particle and nuclear physics and can handle many physical processes which describe particle interactions with matter and particle decays. In order to use it in the field of UCN physics, several additional processes have been included.

UCN interactions with walls are implemented in GEANT4-UCN simulations. They are described by means of probabilities for the total reflections (specular or diffuse) and for the bulk material processes (scattering and absorption). Interactions, as described in 2.3.2, are implemented in GEANT4-UCN. Diffuse reflections are governed by the diffuse reflection probability per bounce p_{diff}. The loss probability during a reflection is implemented via the loss factor η and is calculated according to Eq (2.28). During a reflection, depolarisation can occur with the probability β. If UCNs penetrate a material, they can be scattered or absorbed. This last process is included via exponential attenuation laws with absorption cross-sections proportional to $1/v_n$ – where v_n is the UCN velocity inside the material. The up-scattering process is neglected and the elastic scattering is treated by calculating the UCN mean free path using scattering cross-sections. Absorption and elastic scattering processes play an important role for losses inside analysing foils for instance.

4.2.2 Material properties

Interactions presented in previous sections (see 2.3.2 and 4.2.1) are related to the properties of materials constituting the apparatus. Materials used in simulations and their associated properties are presented hereafter and summarised in Tab. 4.1.

- The Fermi potential is in the 100-300 neV range. Its value comes from either measurements or calculations derived from the material chemical composition, according to Eq (2.20).
- Absorption and scattering cross-sections come from [89] for basic materials. For compound materials like DLC and DPS, they come from cross-sections of atomic elements constituting the material.
- The loss factor η is set to 10^{-4} (typical range measured in experiments) for all materials without experimental value.
- The depolarisation probability per bounce is set to $\beta = 10^{-5}$ for all materials without experimental value [13].

Syst. part	Material	V_F [neV]	η [$\times 10^{-4}$]	σ_s [b]	σ_a [b]	β [$\times 10^{-5}$]
Electrodes	DLC	260	4	12.6	4.9×10^{-3}	0.3
Ring	DPS	162	5	7.2	4.7×10^{-3}	0.3
Shutter	Ni	252	1.25	18.5	4.5	1
Foil	Fe	210	0.85	11.6	2.56	1
Foil support	Al	54	0.23	1.5	0.23	1
Analyser	NiMo	220	1	18.5	4.5	1
Analyser	Diamond	300	4	12.6	4.9×10^{-3}	0.3

Table 4.1: Material properties used in the simulations.

4.2.3 Spin handling

In the simulation, only two spin mechanisms are considered: depolarisations per bounce (governed by the β parameter, see 4.2.1) and adiabatic spin-flippers crossings. ASF are defined by a 4 cm wide area. When a neutron crosses the ASF area, a spin-flip occurs. The spin-flip probability is set to 100%.

This work does not track back the spin along UCN trajectories. This simplifies the spin handling during simulations and saves huge amounts of computing time. Thus, the spin is just represented by a flag which can be -1 or $+1$. When a spin-flip occurs, the flag is multiplied by -1.

The analysing foil is modelled by a 100 µm thick aluminium substrate and a 200 nm iron layer. When UCNs reach the iron volume, a potential of 120 neV (corresponding to a 2 T field) is added to or subtracted from the iron Fermi potential according to their spin state (see 3.5.2.1). For all geometries, the analysing foil is located 15 cm below the spin-flipper.

In the case of the sequential analysis, the spin-flipper is turned OFF/ON according to the experimental timing sequence shown in Tab. 4.2.

4.2.4 Initial conditions

For each simulation, $N_0 = 10^5$ UCNs are uniformly generated in the whole volume of the precession chamber. The UCN spin can be initialised according to the user choice, with a full spin up or spin

Timing sequence	[0,8 s]	[8,33 s]	[33,50 s]
Spin-flipper state	OFF	ON	OFF
Detected spin component	↓	↑	↓

Table 4.2: Counting sequence for the spin analysis.

down UCN population, or an unpolarised one. UCN speed components are gaussianly distributed, given a modulus distributed according to the Maxwell-Boltzmann spectrum shown in Fig. 4.1.

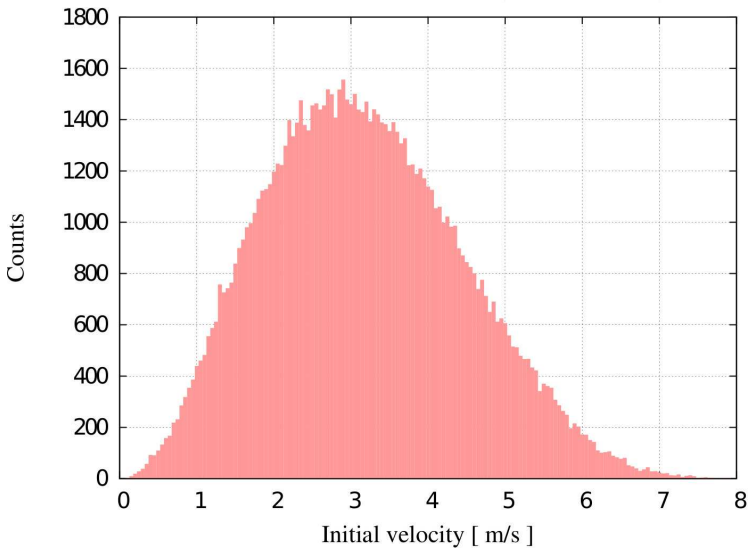

Figure 4.1: Initial UCN velocity spectrum.

4.3 Comparison criteria

Three spin analyser geometries have been simulated. The different shapes are shown in Fig. 4.2. For all geometries, the distance between the precession chamber and the spin analysing systems was set to 135 cm. This value is shorter than the real one by about 25 cm, because it was initially planned to simulate the spin analyser as close as possible to the switch box. It turned out that in the experiment there is not enough space beneath the switch box mainly due to the presence of its piezo-motors.

The first simulated geometry is the sequential system currently used in OILL. It gives the reference device to which the other analysing systems performances are compared to. Two main criteria are used. The first one is the UCN detection efficiency:

$$\varepsilon_{\text{det}} = \frac{N_{\text{det}}}{N_0} \tag{4.1}$$

where N_{det} is the number of detected neutrons (assuming 100% efficient UCN detectors).

The second criterion is the asymmetry:

$$\mathcal{A} = \left| \frac{N^{\uparrow} - N^{\downarrow}}{N^{\uparrow} + N^{\downarrow}} \right| \tag{4.2}$$

where $N^{\uparrow/\downarrow}$ is the number of spin up/down detected UCNs.

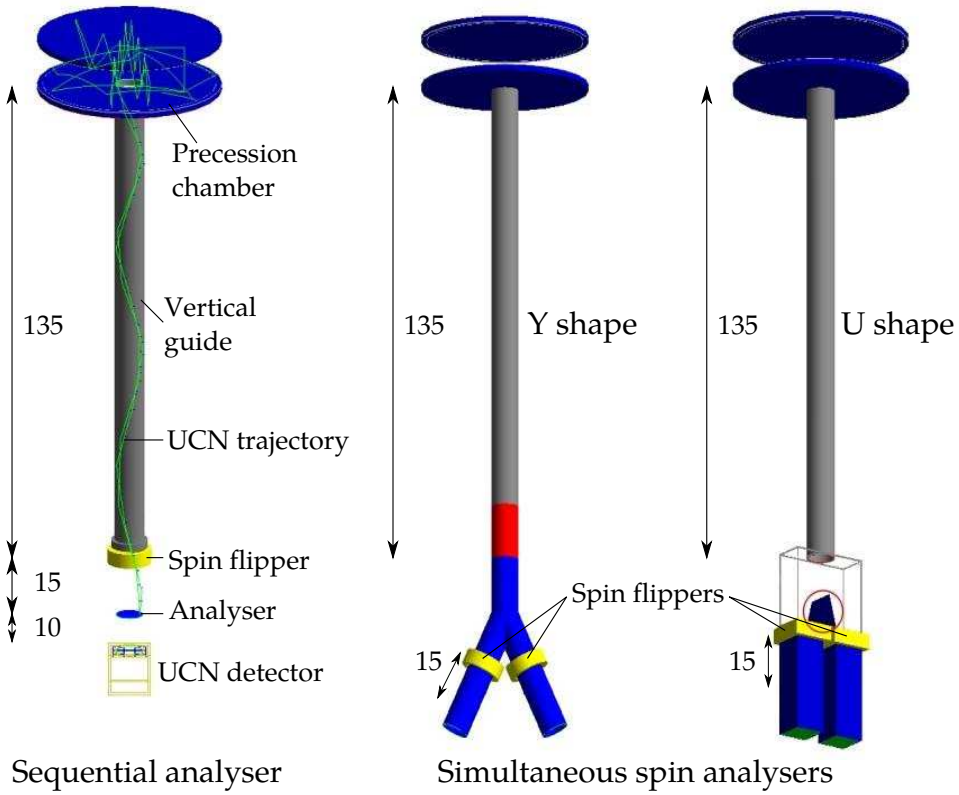

Figure 4.2: Analysing system geometries. The sequential system is at left. The two simultaneous spin analysers are shown at right: the YSSA and the USSA. Dimensions are in cm.

The asymmetry corresponds to the spin analysis efficiency of the studied system. For a fully polarised UCN population, this asymmetry is 100% in an ideal case (no depolarisation and a perfect spin analysis). For a non polarised UCN population, the asymmetry is 0.

In order to emphasise the counting sequence influences on the detection efficiency and the spin analysis, three simulations have been performed using different initial UCN populations: full spin up/down population, or randomised one.

4.4 The sequential analyser

4.4.1 UCN detection efficiency

4.4.1.1 Main results

The UCN detection efficiency has been calculated for the three different spin populations. Results are summarised in Tab. 4.3.

Spin population	↓	↑	↓/↑
Detection efficiency [%]	74.95(27)	73.55(27)	74.21(27)

Table 4.3: Detection efficiencies of the sequential system. ↓: 100% spin down UCNs. ↑: 100% spin up UCNs. ↓/↑: unpolarized UCNs.

There is a clear dependence on the initial spin population: more UCNs are detected (+1.4%) in the case of the spin down population, which is the spin state analysed during the first time period, than in the case of the spin up population. For an unpolarized UCN population, the detection

efficiency equals the average detection efficiency obtained for the two fully polarised populations and amounts to 74.2(3)%. This is the detection efficiency corresponding to nEDM data taking conditions, when the neutron pulse frequency is set such as there are about the same amounts of spin up and spin down UCNs. Because all the apparatus imperfections are not included in the simulation (slits in the switch box for instance), the obtained detection efficiencies are likely overestimated.

4.4.1.2 UCN losses

In order to explain the detection efficiency dependence on the initial spin population, the location and the timing of UCN losses have been studied. Summary of losses that occur during the whole sequence is shown in Tab. 4.4 and Tab. 4.5, respectively for spin down and spin up populations. These percentages are given by the ratio between the number of losses in a given volume and the number of generated UCNs in the simulation.

Time period Detected spin component	[0,8 s] (↓)	[8,33 s] (↑)	[33,50 s] (↓)	Total
Storage chamber	4.69(8)%	3.51(6)%	0.77(3)%	8.93(9)%
Vertical guide	0.56(2)%	2.47(5)%	0.47(2)%	3.48(6)%
Analysing foil	3.57(6)%	0.07(1)%	1.64(4)%	5.28(7)%
Total	8.81(9)%	6.06(8)%	2.86(5)%	17.69(13)%

Table 4.4: Losses percentages with an initial spin down population.

Time period [s] Detected spin component	[0,8 s] (↓)	[8,33 s] (↑)	[33,50 s] (↓)	Total
Storage chamber	6.32(8)%	3.58(6)%	0.25(2)%	10.14(10)%
Vertical guide	2.36(5)%	1.44(4)%	0.20(1)%	3.94(6)%
Analysing foil	0.033(6)%	5.15(7)%	0.11(1)%	5.29(7)%
Total	8.71(9)%	10.16(10)%	0.50(2)%	19.37(14)%

Table 4.5: Losses percentages with an initial spin up population.

For both cases, losses are larger inside the precession chamber. They amount to about 50% of the UCN losses (corresponding to a UCN fraction of 8.93/10.14% for spin down/up) and are mainly due to reflection losses. Even when the initial spin state is detected at first in the timing sequence, a UCN fraction of 4.69% is lost inside the precession chamber. This could mean that the initial energy spectrum used in the simulations is too hard. However, it is clear that the main detection efficiency difference comes from the fact that each spin component are not equally stored above the analysing foil. For the spin down population, 5.98% are lost in the vertical guide and the precession chamber during the storage above the analysing foil whereas 9.13% are lost in the case of an initial spin up population (mainly during the first 8 s). Finally, the losses difference amounts to 1.68% and partially explains the difference of detection efficiency between the two initial fully polarised UCN populations. It also shows that it is possible to detect more neutrons if the storage above the analysing foil is suppressed.

It is also important to note that about 5% of neutrons are still in the apparatus at the end of the counting sequence, *i.e.* after 50 s. With a faster emptying, it could be possible to recover such UCNs.

4.4.2 Spin analysing power

Asymmetries obtained for each UCN population are summarised in Tab. 4.6. The sequential analysis reduces the spin analysing power of the system by 1.23% (for the spin down population) and 3.83% (for the spin up population). As a result, the asymmetry is different by about 2.5% for the two fully polarised UCN populations. It means that the sequential system induces a non negligible bias for the spin analysis. Finally, for all initial polarisations, the asymmetry is not perfect and differs by about 3% from the ideal case.

Spin population	↓	↑	↓/↑
Asymmetry [%]	98.77(6)	96.17(10)	3.11(37)

Table 4.6: Asymmetries of the sequential system. ↓: 100% spin down UCNs. ↑: 100% spin up UCNs. ↓/↑: unpolarized UCNs.

4.4.3 Bias induced by the sequential analysis

In order to determine the mechanisms which give rise to the spin asymmetry bias, the time sequence has been analysed for each spin population.

4.4.3.1 Spin down UCN population

The number of detected UCNs as a function of the emptying time is shown in Fig. 4.3 for the spin down UCN population.

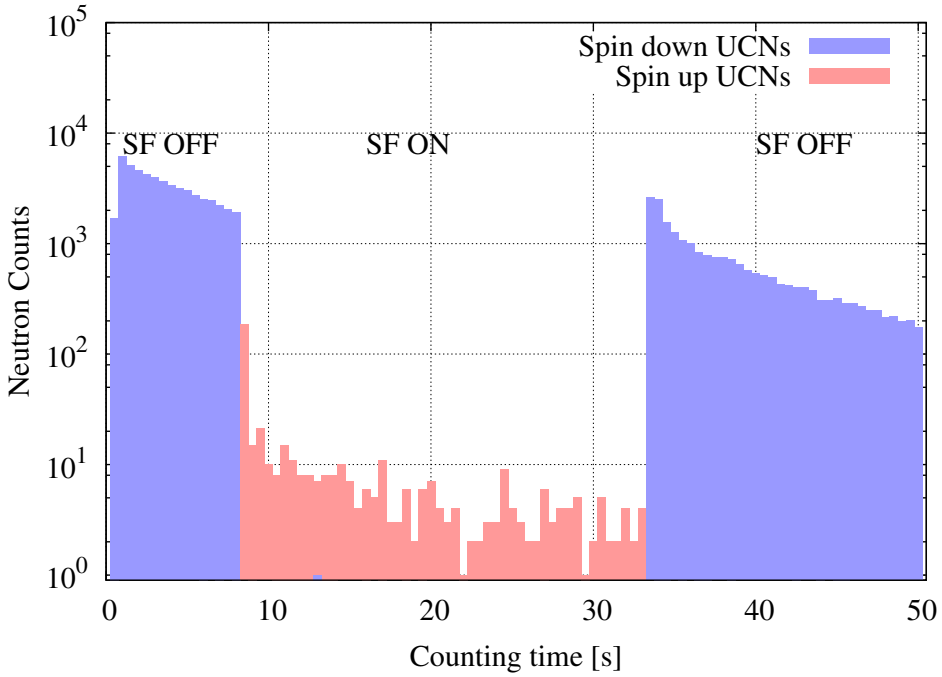

Figure 4.3: UCN counts as a function of the emptying time for a spin down population.

During the first time interval [0,8] s, the spin-flipper is OFF. Mainly spin down UCNs are detected. At 8 s, the spin-flipper is turned ON. In principle, no UCN should be detected during the second time interval [8,33] s. However, 0.6% of the UCNs are detected during this period, as shown in Tab. 4.7. They correspond to spin up UCNs. This is mainly due to two contributions.

First, 60% of these detected UCNs come from depolarisations induced by wall reflections. The remaining 40% are detected during the first 0.1 s just after the switching of the spin-flipper. Actually, these are spin down UCNs which already crossed the spin-flipper during the first time period and are detected during the second time period because of the flight path (25 cm) between the spin-flipper and the UCN detector. As a result, 0.6% of UCNs are detected with the wrong spin state due to wall depolarisations and to the spatial separation between the analyser and the spin-flipper.

Time period	[0,8 s]	[8,33 s]	[33,50 s]
Spin down	70.15(40)%	0.01(1)%	29.23(22)%
Spin up	0.0%	0.61(3)%	0.0%

Table 4.7: Fraction of spin up/down UCNs detected for a given time period, for an initial spin down UCN population. The ratio is calculated with respect to the total number of detected UCNs.

4.4.3.2 Spin up UCN population

The number of detected UCNs as a function of the emptying time is shown in Fig. 4.4 for a spin up UCN population. Proportions of detected UCNs for each counting period are shown in Tab. 4.8.

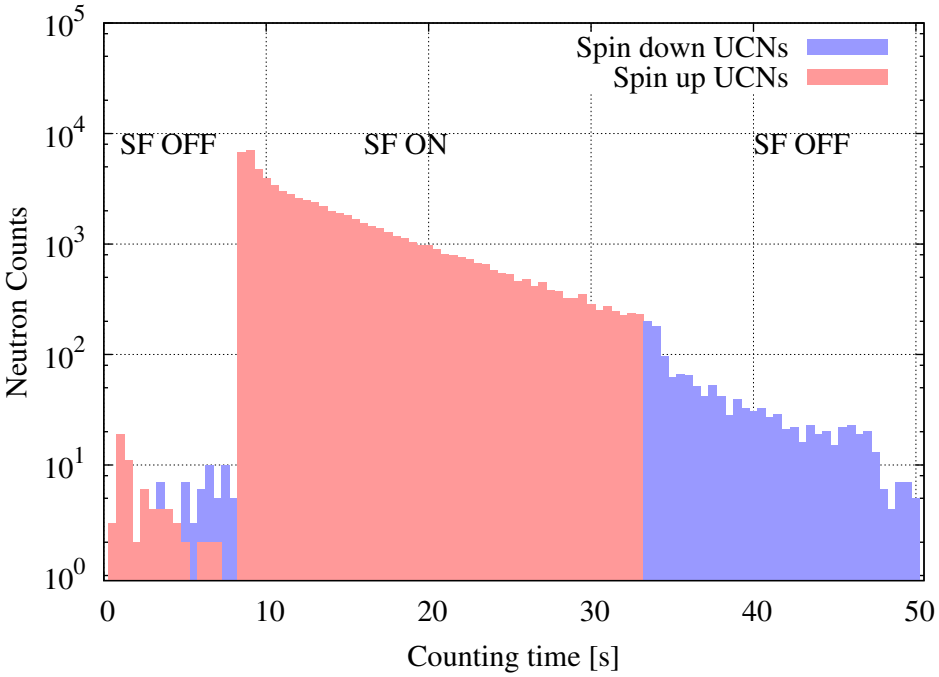

Figure 4.4: UCN counts as a function of the emptying time for an spin up population.

In the first time interval [0,8] s, one should detect no neutron. However, 0.09% of the UCNs are detected. Those UCNs have an energy above the energy range that can be analysed by the analyser. Therefore, they can cross it whatever their spin state. Another fraction of UCNs (0.09%), detected during the first time interval is due to wall depolarisations. But the most interesting effect is visible during the last part of the sequence: 1.82% of UCNs are detected while no UCN should be detected. This important contribution decreases the asymmetry from 99.5% down to 96%. About 0.4% comes from wall depolarisations. Almost 1.3% comes from neutrons which are located between the analysing foil and the spin-flipper when this one is turned ON at

the end of the first time period. At that time, UCNs can not cross the foil and undergo a spin-flip when they go back across the spin-flipper area to the precession chamber. They are stored above the analysing foil during the second time period [8,33] s and are finally detected during the last one [33,50] s. A rather small contribution (about 4%) to this fraction comes from the flight path between the spin-flipper and the detector (see previous section for more details). As a result, 1.8% of UCNs are detected with the wrong spin state in the sequential analysis for an initial spin up population.

Time period	[0,8 s]	[8,33 s]	[33,50 s]
Spin down	0.09(1)%	0.0%	1.82(5)%
Spin up	0.09(1)%	98.00(51)%	0.0%

Table 4.8: Fraction of spin up/down UCNs detected for a given time period, for an initial spin up UCN population. The ratio is calculated with respect to the total number of detected UCNs.

4.4.4 Conclusions

It has been shown that the sequential analysis introduces a bias on the spin analysis by means of two main mechanisms related to the change of the spin-flipper state. The mechanism is different for each initial UCN polarisation. As a result, both of them are involved when the UCN population is not polarised. As expected, the number of detected UCNs also depends on the initial spin population, because of losses during the storage above the analysing foil. A possible way to avoid such problems is to use a simultaneous spin analysis in which the spin-flipper state is the same during the whole emptying time. Two different geometric configurations are studied in the next sections.

4.5 Y-shape Simultaneous Spin Analyser study

The Y-shape Simultaneous Spin Analyser (YSSA) is made of two cylindrical arms with an angle between them as shown in Fig. 4.5. In the arm A, the spin-flipper is ON. Therefore, spin up UCNs are detected. In the arm B, the spin-flipper is OFF. As a result, spin down UCNs are detected.

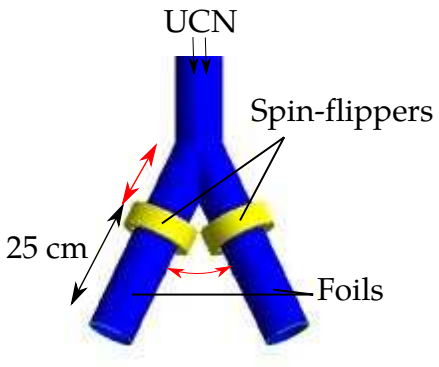

Figure 4.5: YSSA geometry. Tunable dimensions are in red: the angle between the two arms with the corresponding upper arm length.

The angle θ between the two arms has been varied from 20 to 60 ° in order to find the best geometry. The arm length is set according to this angle such that the two spin-flippers can be

placed side by side and as close as possible to the arms crossing. This length depends on θ and is in the range 317 mm – 568 mm corresponding to an angle range from 60 down to 20 °.

Similarly to the sequential system, the UCN detection efficiency and the asymmetry are studied. These observables are invetigated as a function of the angle θ and of the diffuse probability (which plays an important role for UCN losses).

4.5.1 UCN detection efficiency

4.5.1.1 Main results

The detection efficiency as a function of the angle θ between the two arms is shown in Fig. 4.6. Same results have been obtained for both fully polarised UCN populations. The simulations have been performed for several diffuse reflection probabilities in the analysing system (*i.e.* below the vertical guide). In the rest of the apparatus (vertical guide and storage chamber), the diffuse probability is set to 1%.

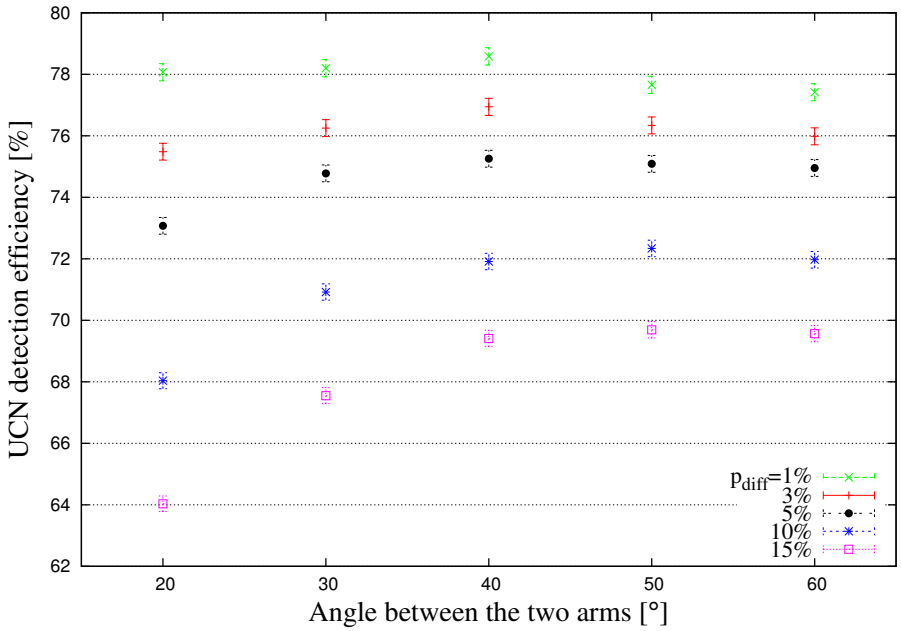

Figure 4.6: YSSA UCN detection efficiency as a function of the θ angle between the two analysing arms. The simulation has been preformed for several diffuse probabilities p_{diff} in the two arms.

The best angle between the two arms is 40°, whatever the diffuse probability. Indeed, the detection efficiency increases from 20 to 40° and then slightly decreases until 60°.

A strong dependence on the diffuse probability is visible: for a given angle θ, the larger the diffuse probability, the weaker the UCN detection efficiency. The best UCN detection efficiency, obtained for $p_{\text{diff}} = 1\%$ is 78.9(3)%. It is better than the UCN detection efficiency obtained with the sequential system. For a diffuse probability of 1%, the UCN detection efficiency is nearly independent of the angle between YSSA's arms while for $p_{\text{diff}} = 15\%$, the UCN losses are important at low angle θ.

4.5.1.2 UCN losses

In order to explain the UCN detection efficiency dependence on the diffuse probability, UCN loss locations have been studied and summarised in Tab. 4.9.

p_{diff}	Chamber	Guide	Arms	Foils	Remain after 50 s	Decay
1%	7.04%	0.55%	3.75%	5.55%	2.58%	1.14%
10%	6.85%	0.72%	10.34%	5.40%	2.64%	1.18%

Table 4.9: UCN losses in the apparatus with the YSSA geometry.

The most important contribution comes from UCN losses in the analysing arms. They are shown as a function of the angle between arms for different diffuse probabilities in Fig. 4.7.

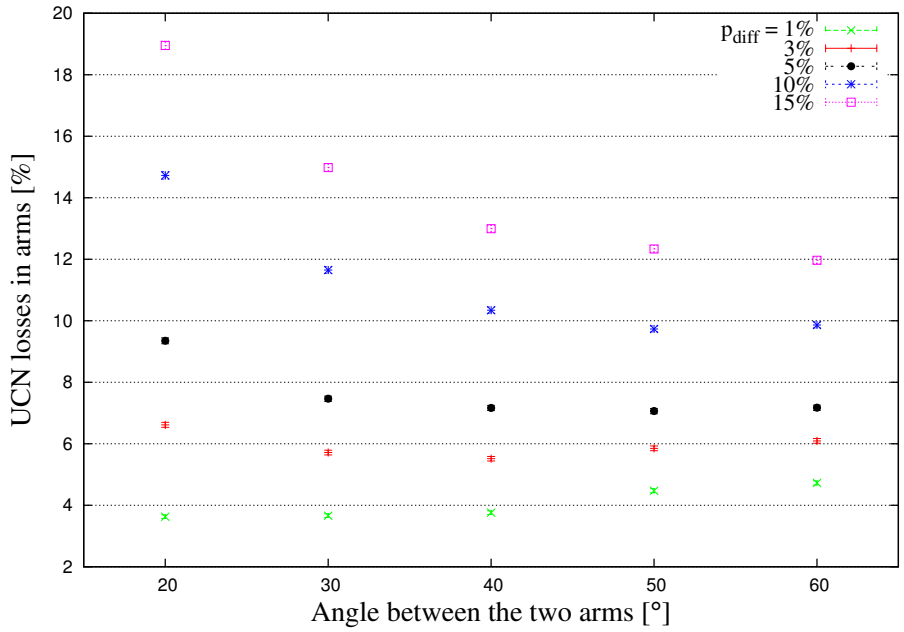

Figure 4.7: Losses in YSSA as a function of the angle between arms. It has been simulated for several diffuse probabilities p_{diff} in the analysing arms.

For a diffuse probability higher than 3%, losses in arms increase for small angles between arms. This is explained by the larger arms length when the angle between arms is smaller. Therefore, the probability for UCNs to undergo a diffuse reflection is higher when the arm length is larger. On the other hand, at large angles between arms correspond low incidence angles. Thus, direct losses are increased at the first reflection onto the two arms.

For a given angle, the larger the diffuse probability, the larger losses in arms. Indeed, when a diffuse reflection occurs, the reflected UCN momentum is not along the guide axis anymore. Thus, after a diffuse reflection, chances for UCNs to have an energy component normal to the wall higher than with specular reflections is increased. Therefore, the probability to have an energy higher than the Fermi potential is larger.

For diffuse probabilities smaller than 3%, there are many less diffuse reflections than specular ones and arm losses also occur at the first UCN reflection into analysing arms. For low diffuse probabilities, the diffuse and direct loss processes are in competition. For 1% and 3% of diffuse probability, direct losses are slightly more important than losses due to diffuse reflections and a small minimum shows up at 40°, corresponding to the small maximum observed in the UCN detection efficiency.

4.5.2 Spin analysing power

The asymmetry as a function of the angle between the two arms is shown in Fig. 4.8 for a fully polarised UCN population. Same results have been obtained for the two fully polarised populations. The asymmetry is close to 100%. It is slightly increased by about 0.7% from 20 to 60°. The main reason is the arm length which depends on this angle. Thus, the analysing foil height for θ =20° is about 29 cm lower than for θ =60°. Therefore, with the gravitational boost, UCNs have more energy at the foil level, about 30 neV, which increases the probability for fast UCNs to go across the foil whatever their spin state. The asymmetry does not depend on the diffuse probability.

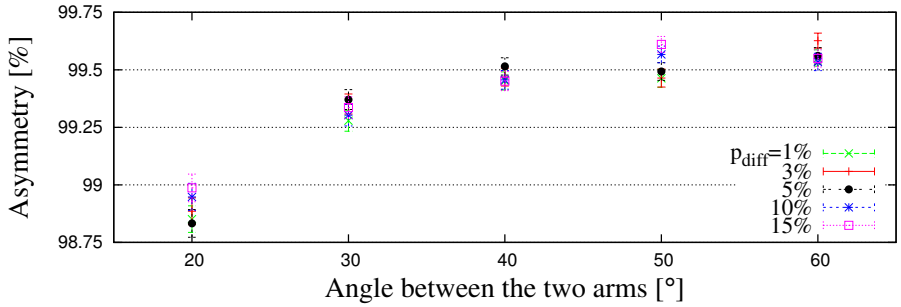

Figure 4.8: YSSA asymmetry as a function of the angle between the two arms. It has been simulated for several diffuse probabilities p_{diff}.

4.5.3 Conclusions

The most appropriate angle between the two arms is the θ = 40° because the UCN detection efficiency is maximal and the spin asymmetry is almost as good as the maximum reached for a θ = 60° angle. This 99.5(3)% spin asymmetry for fully polarised UCNs is better than the one reached with the sequential system (98.8% at best) and does not depend on the initial polarisation. For an unpolarised UCN population, the asymmetry amounts to 0.2(4)% and is also better than the one obtained with the sequential system (3.1%).

4.6 Study of the U-shape Simultaneous Spin Analyser

The last studied shape is the U-shape Simultaneous Spin Analyser (USSA) shown in Fig. 4.9.

There are two main differences between the USSA and the YSSA: an intermediate volume at the USSA entrance and arms with flat walls in the USSA. The role of this intermediate volume is to keep UCNs close to the detectors instead of letting them going back upwards to the precession chamber. Several parameters have been tuned in the simulation in order to find the most efficient geometry: the θ_W angle of the piece located between the two arms (called central wedge), the height of the upper volume and the ϕ angle of the USSA roof. The goal of the central wedge is to guide as much UCNs as possible in the detectors during the "first shot". Then, the roof is used to guide UCNs from one arm to the other if they are reflected by the analysing foil.

4.6.1 UCN detection efficiency

4.6.1.1 Main results

The UCN detection efficiency as a function of the central wedge angle θ_{w} is shown in Fig. 4.10. This simulation has been performed for different roof angles ϕ ranging from 20 to 60° with a

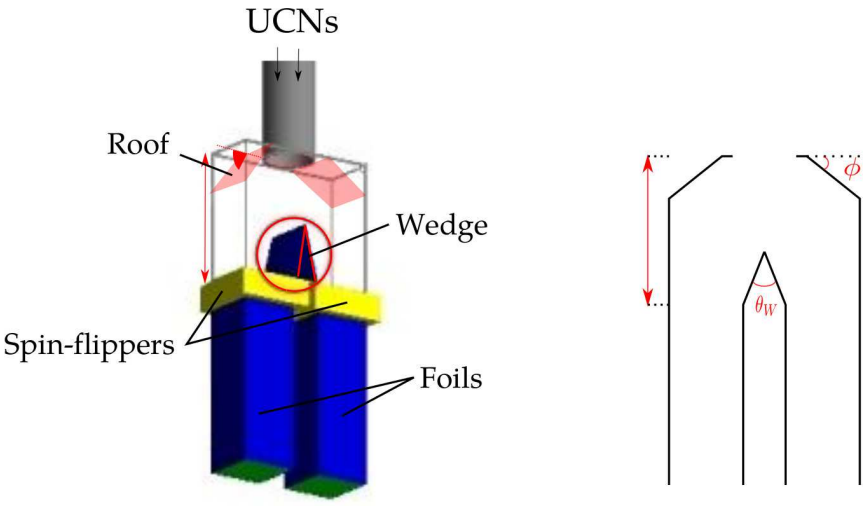

Figure 4.9: USSA geometry. Tunable dimensions are in red: roof angle ϕ, wedge angle θ_W and height of the upper box.

diffuse probability of 1%. The initial UCN population is fully polarised. Results do not depend on the UCN polarisation.

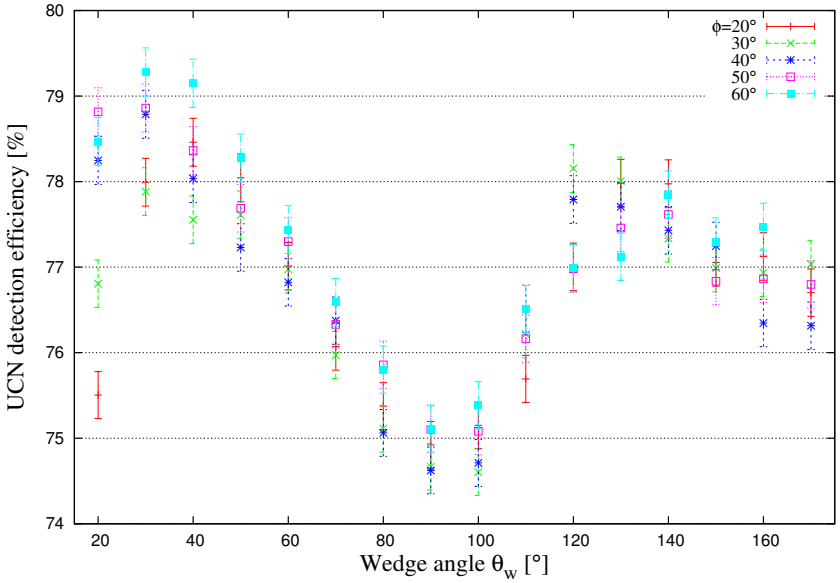

Figure 4.10: USSA detection efficiency as a function of the θ_w wedge angle for different values of the roof angle ϕ. No influence of the roof angle on the USSA detection effiency is observed. The best wedge angles are around 30 and 130°.

For a given roof angle ϕ, the UCN detection efficiency is minimum for wedge angles close to 90° and it decreases when the central wedge becomes flatter (θ_W >140°). The UCN detection efficiency does not strongly vary with the roof angle except for $\theta_w < 30°$. For those θ_w angles, the lower the roof angle, the lower the UCN detection efficiency. As a result, it is better to use roof angles above 30°.

The upper box height has been varied from 15 cm to 30 cm. No large influence has been found on the UCN detection efficiency within the 0.5% level.

The best USSA detection efficiency amounts to about 79%. This is the of the same order of

magntiude as obtained with the YSSA, and better than with the sequential system. It has been obtained for a wedge angle of 30° and for roof angles larger than 40°. In that case, about 85% of UCNs entering into the USSA are finally detected. The USSA detection efficiency is the same whatever the initial polarisation.

4.6.1.2 UCN losses

The minimum in the detection efficiency observed for angles close to 90° is mainly due to losses on the arms walls. At the USSA entrance, the UCN momentum is mainly vertical and directed downwards. When the angle between the wedge surface and the vertical is 45° (corresponding to θ_w =90°), UCNs are reflected towards a direction which is perpendicular to the USSA external wall. As a result, the UCNs number with an energy higher than the wall Fermi potential increases as well as the UCN losses, as shown in Fig. 4.11.

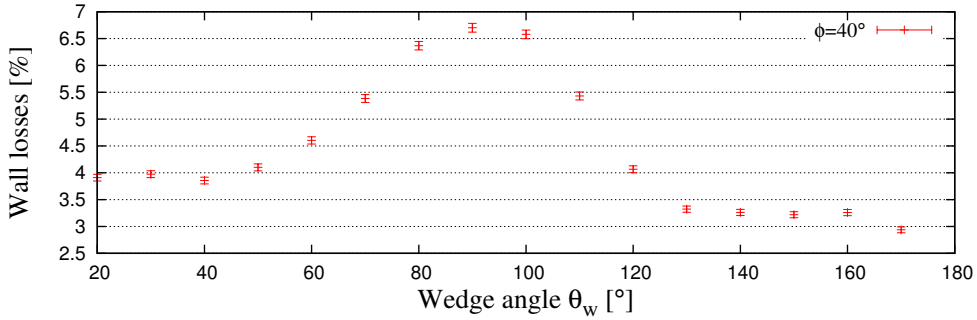

Figure 4.11: Wall losses as a function of the wedge angle θ_w.

For large θ_w, the central wedge is close to be a flat surface and fast UCNs hitting perpendicularly the wedge can be lost. This is shown in Fig. 4.12, presenting the central wedge losses as a function of θ_w.

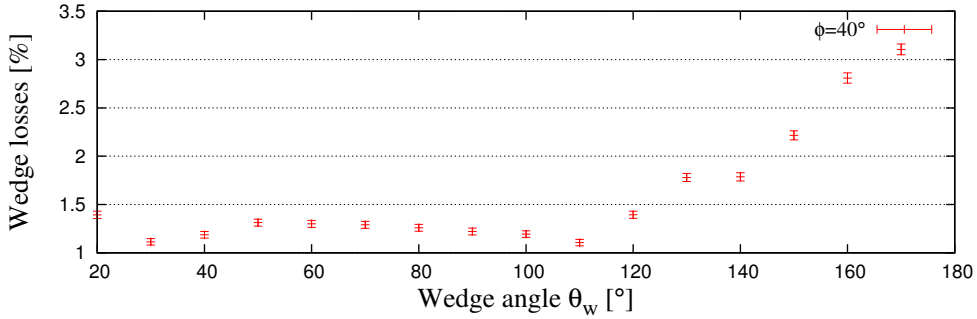

Figure 4.12: Central wedge losses as a function of the wedge angle θ_w for ϕ =40°.

The UCN losses locations in the USSA simulation are summarised in Tab. 4.10 for a θ_w wedge angle of 30° and a roof angle of 40°. About 2% more UCNs which were remaining at the end of the emptying time with the YSSA are detected with the USSA. At the same time, there are slightly less UCNs lost in the chamber in the case of the USSA with respect to the YSSA. Among the 14.6% UCN lost in the USSA, 5.75% are due to absorptions in the analysing foils.

In order to increase the USSA detection efficiency, it is possible to use a new coating on its walls. But since such coatings are very expensive, it is better to select which USSA walls are of interest. For such a purpose, the losses locations and proportions are summarised in Tab. 4.11.

Location	Chamber	Guide	USSA	Remain after 50 s	Decay
Losses	6.6%	0.8%	14.6%	0.5%	1.1%

Table 4.10: UCN losses in given apparatus parts for θ_w =30° and ϕ =40°.

Location	Roof	Upper box	Wedge	Arms
Proportion	17.3%	25.4%	18.1%	39.2%

Table 4.11: Proportion of USSA losses in each USSA's part.

UCN losses on USSA in the upper box and the two arms amounts to 64.6% of the UCN losses. As a result, it would be interesting to first improve the coating on the USSA vertical walls, going from the roof down to the detectors.

4.6.1.3 Diffusivity influence

The study of the diffuse reflection probability influence on the USSA detection efficiency has been performed using the best geometry found previously, *i.e.* $\theta_W = 30°$ and $\phi = 40°$. Several coatings have been used in order to search for a possible improvement using a higher Fermi potential on the USSA walls, as shown in Fig. 4.13.

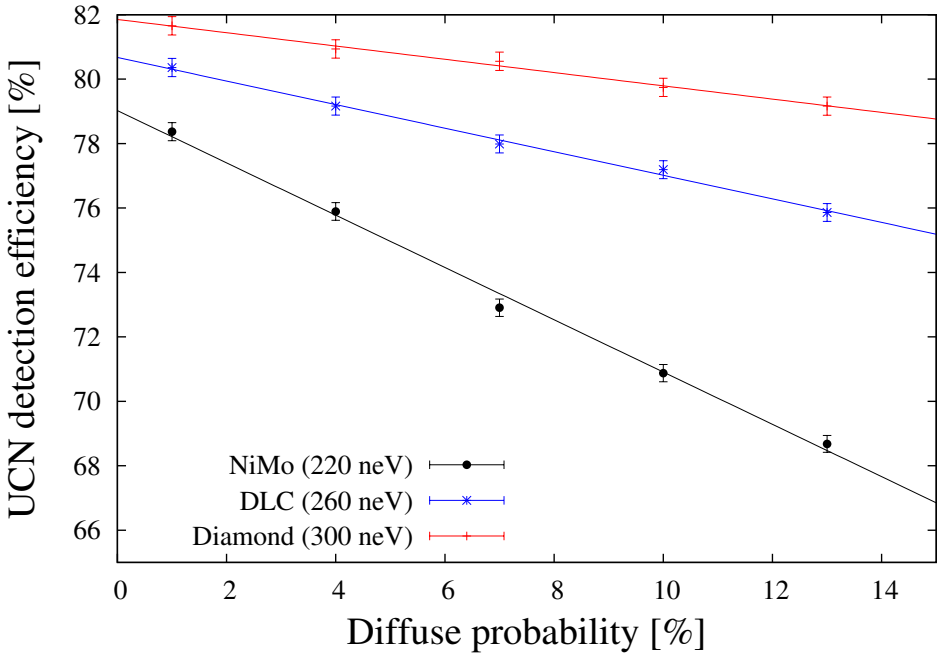

Figure 4.13: UCN detection efficiency as a function of the diffuse probability in the USSA for three wall coatings: NiMo, DLC and Diamond.

The dependence of the detection efficiency $\varepsilon_{\text{coating}}$ on the diffuse probability p_{diff} has been linearly fitted for each coating and is summarised as:

$$\varepsilon_{\text{NiMo}} = 79.0\% - 0.82\% p_{\text{diff}}$$
$$\varepsilon_{\text{DLC}} = 80.7\% - 0.37\% p_{\text{diff}}$$
$$\varepsilon_{\text{Diamond}} = 81.9\% - 0.21\% p_{\text{diff}}$$

Increasing the diffuse probability produces more UCN losses because more UCNs have a larger transverse energy to the USSA walls. The improvement brought by a larger Fermi potential is clearly visible: the UCN detection efficiency is larger whatever the p_{diff} value and the slope is smaller when the diffuse probability gets larger. Thus, the influence of the wall surface roughness is lowered when a material with a high Fermi potential is used.

It has to be noticed that the distance between the precession chamber and the USSA has been underestimated by about 25 cm in GEANT4-UCN simulations with respect to real conditions, because of non expected mechanical considerations in the present simulations. As a result, the influence of the Fermi potential on the USSA transmission has been likely underestimated (see Sec. 4.3). As a result, using diamond instead of NiMo would lead to a detected UCN gain of at least 3 to 6% for reasonnable p_{diff} values between 1% and 5%.

4.6.2 Detected UCNs after reflection in the wrong arm

When UCNs come into the USSA, they can be either detected at the first shot or be reflected in the wrong arm before being detected. The goal of this part is to determine how many UCNs are recovered after being reflected in the wrong arm. This study has been performed with $p_{\text{diff}} = 1\%$, $\theta_W = 30°$ and $\phi = 40°$.

First shot detected UCNs: The number of reflections per UCN on the analysing foil is shown in the left panel of Fig. 4.14. Zero reflection means that UCNs directly fall down into the arm analysing their spin state ("first shot" UCNs). 50.5% of the total number of detected UCNs is detected without any reflection in the other arm. Among them, about 70% directly go across the analysing foil. This means that the remaining 30% are reflected at least once in the right arm.

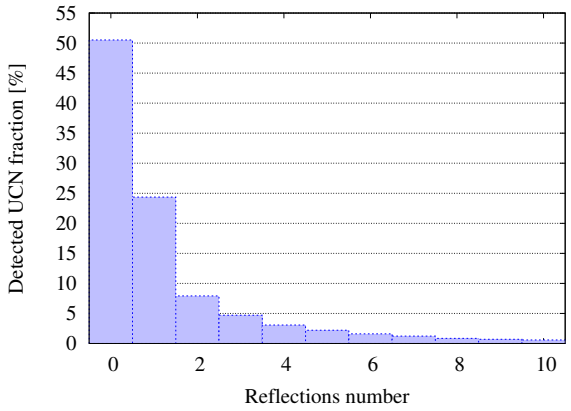

(a) Reflections number per UCN on the foil located in the wrong analysing arm.

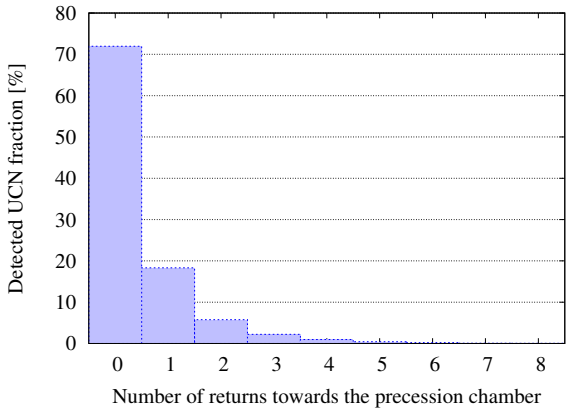

(b) Number of returns towards the precession chamber.

Figure 4.14

Second chance detected UCNs: Detected UCNs coming from the other arm ("second chance" UCNs) amount to 49.5% of the total detected UCNs. It represents 84.5% of UCNs entering in the wrong arm, meaning that 15.5% of the UCNs entering the wrong arm are lost. About 50% of not lost UCNs are directly reflected from the wrong to the right arm while the others are reflected several times on analysing foils. Among them, UCNs which go back upwards to the precession chamber amount to slightly less than 30%, as shown in the right panel of Fig. 4.14. A perfect

system would reflect 100% of UCNs with the wrong spin state towards the other arm, instead of about 60%. It means that there might be some room of improvement. However, a study of the USSA roof angle influence on the recovered UCN fraction showed no real improvement.

It has to be noticed that there is no slit included in the simulations neither in the USSA nor in the upper part of the apparatus. Thus, the reflections upwards to the precession chamber are not ideally simulated and UCN losses within the vertical guide are underestimated. As a result, the fraction of second chance detected UCNs of 84.5% is likely overestimated. A simulation improvement would be to model the slits (below the 100 µm level) of the switch box and the USSA slits at the 10 – 50 µm level.

4.6.3 Spin analysing power

The spin asymmetry is neither sensitive to θ_W nor to ϕ. An asymmetry decrease of 0.2% has been observed between an upper box length of 15 cm and 30 cm for polarised UCNs. This is due to the gravitational boost. The spin asymmetry for a fully polarised UCN population amounts to 99.3(4)% and is better than with the sequential analysis (97.5%). The same observation is done with an unpolarised initial UCN population with an asymmetry of 0.4(4)% instead of 3.1(4)% from the sequential analysis.

4.7 Analysing systems comparison

UCN detection efficiencies and asymmetries obtained for the three analysing systems have been summarized in Tab. 4.12 for both fully polarised and unpolarised UCNs. Both simultaneous spin analysers show better performances than the sequential analyser. Keeping in mind that slits are not included in simulations and that the analysers location is 25 cm too high, the 5% improvement on the UCN detection efficiency does not lead to a significant increase of the EDM statistical sensitivity (about 2.5%). It shows that it is rather difficult to increase UCN statistics by means of the spin analysing system. But at least, the symmetric treatment of both spin states shows that the asymmetry is almost as good as in the ideal case.

	Sequential	Y shape	U shape	Ideal case
${\varepsilon_{\text{det}}}^{(1)}$	74.2(3)%	78.9(3)%	78.5(3)%	100%
$\mathcal{A}^{(1)}$	3.1(4)%	0.2(4)%	0.1(4)%	0%
${\varepsilon_{\text{det}}}^{(2)}$	74.2(3)%	78.8(3)%	78.8(3)%	100%
$\mathcal{A}^{(2)}$	96.9(1)%	99.5(3)%	99.3(4)%	100%

Table 4.12: Detection efficiency and asymmetry for $^{(1)/(2)}$ initial unpolarised/polarised UCN population. The simultaneous analysers give asymmetries close to the ideal case and about the same detection efficiencies, larger than the sequential system.

4.8 Conclusions

It has been shown that the sequential analysis induces a bias on the asymmetry which depends on the initial UCN polarization. The simultaneous spin analysis removes the error due to the spin-flipper state change. The UCN detection efficiency is increased using simultaneous spin analysers by about 5% compared to the sequential system and spin analysis performances are close to the ideal spin treatment. It has to be noticed that these simulations have been performed using a perfect upper part of the apparatus, *i.e.* that there is no slit above the spin analysers. Thus, losses

during the storage above the analysing foil are not fully taken into account in those simulations. Therefore, it is expected to get even better UCN detection efficiencies with simultaneous spin analysers compared to the sequential analysis.

The USSA and the YSSA have shown similar UCN detection efficiencies and spin analysing powers. However, the USSA has modular and flat walls. This allows one to easily exchange parts. In addition, diamond can only be coated on flat surfaces and could be used to further improve the USSA. It is an advantage only if one takes care of having no slit in the USSA. The USSA's squared arms also allow to nearly cover the whole surface of the NANOSC detectors compared to the cylindrical surface of YSSA's arms. Because of those mechanical considerations which allow for a long term improvement of the simultaneous spin analyser, the USSA has been chosen to be built and tested. This is the topic of the following section.

Chapter 5

Experimental tests of the U-shape Simultaneous Spin Analyser

Contents

5.1 USSA design

The USSA mechanical design is shown in Fig. 5.1a. Its walls are made of float glass held by an aluminium exo-skeleton on which the analysing foils are also fixed. The whole apparatus is surrounded by an aluminium vacuum chamber. The magnetisation system (iron yoke along with its set of permanent magnets) is mounted around the analysing foils and outside the whole setup. The USSA's parts dedicated to the UCN transport and detection as well as to the UCN spin handling are described below.

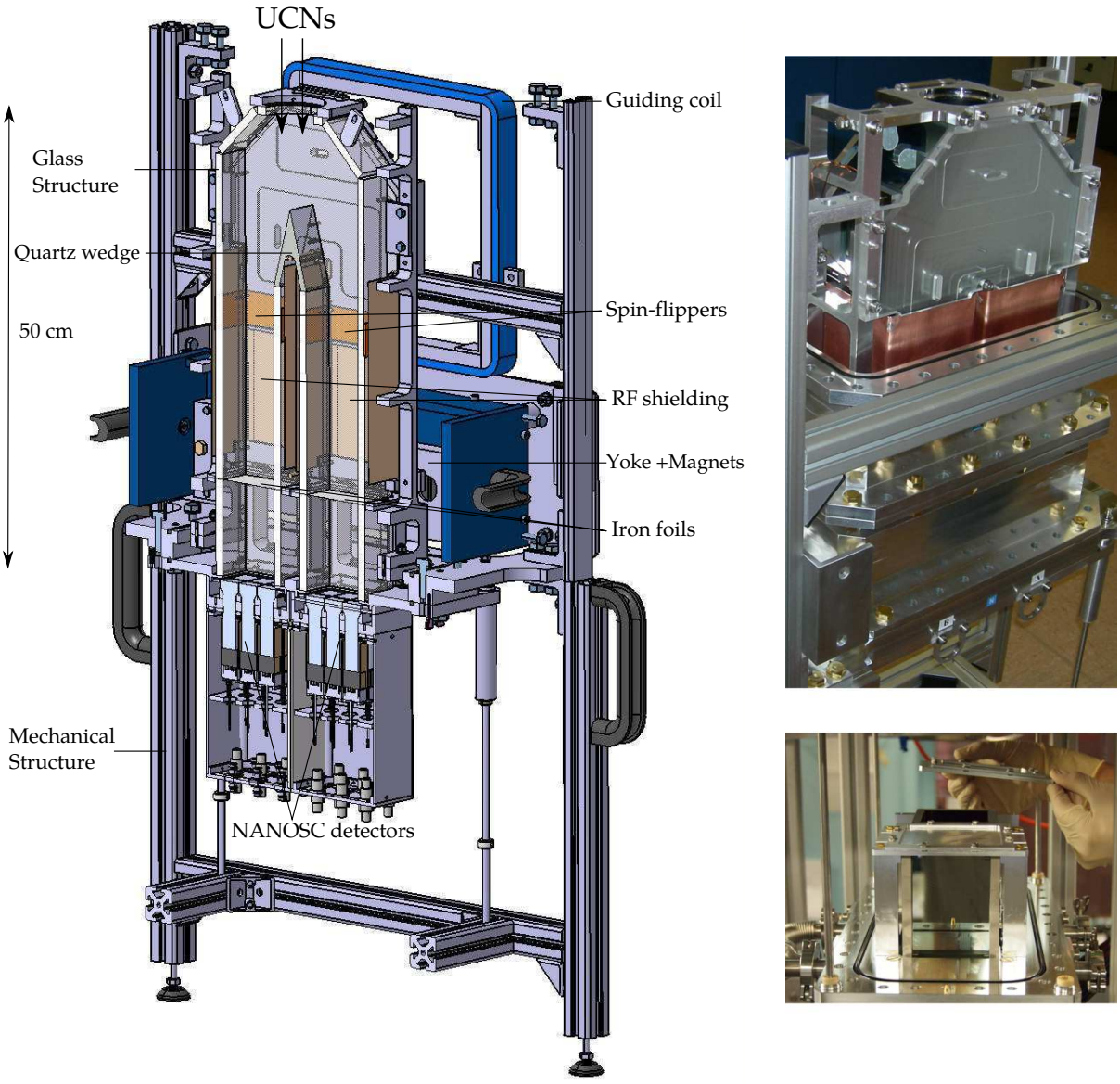

(a) (b)

Figure 5.1: Left panel: Cut view of USSA mechanical drawing. Upper right panel: open view of the USSA with visible RF shielding and vacuum chamber. Lower right panel: installation of USSA analysing foils.

5.1.1 UCN transport and detection

When UCNs enter into the USSA, they are guided towards the NANOSC detectors by a structure made of float glass plates coated with NiMo.

5.1.1.1 NiMo coated glass plates

GEANT4-UCN simulations have shown that the strong effect of the diffusivity on the USSA detection efficiency is lowered when materials with a high Fermi potential are used. In this context, the possibility to change the glass plates of the USSA is helpful if one wants to modify the wall properties. Thus, either the coating (different Fermi potential) or the substrate (different wall roughness) can be potentially improved.

The float glass used for all USSA's pieces but the central wedge has a roughness of a few nm, which suppresses diffuse reflections. Because plates are tightened up by an external aluminium structure, their flatness has to be as good as possible in order to avoid slits where UCNs could leak. The largest slits found are located at the top of the USSA between the roof and the vertical walls. They are of about 100 µm along a few centimetres. In the rest of the apparatus, slits are below the 50 µm range. The glass structure is split in two parts, on each side of the analysing foils. The gap between the two parts has been set to 200 µm in order to avoid any potential foil break during the USSA assembly.

For the moment, this glass structure is covered by a thin layer of sputtered NiMo (85% Ni 15% Mo weight ratio) of about 300-500 nm. The sputtering has been performed at the PSI facility. A diamond coating process on a quartz substrate or ^{58}NiMo on glass are under investigations in order to increase the Fermi potential inside the USSA.

5.1.1.2 NiMo coated central wedge

The central wedge is located just below the USSA entrance. Because of its 30° opening angle and the need to machine its bottom to let room for the RF shielding (see 5.1.2.3), the central wedge is made of quartz which is a material hard enough to keep a sharp ridge. In addition, quartz properties are fairly close to the float glass ones for the UCN guiding (roughness of about 10 nm). It has also been coated with NiMo over a few hundred nanometres, in the PSI sputtering facility at PSI [1].

5.1.1.3 NANOSC detectors

In addition to the first existing NANOSC already part of the nEDM apparatus (NANOSC-A), a second UCN detector (NANOSC-B) identical to the first one has been built. The UCN detection efficiency is similar at the 2-3% level. The FASTER acquisition has been upgraded: a µTCA rack is now used with 10 available channels for each NANOSC detector (*i.e.* 2 spares). In order to have a good neutron-background discrimination, only the last part of the PMT signal is integrated, between 9 and 200 ns. A typical charge spectrum for each channel of NANOSC B is shown in Fig. 5.2. The peak on channel 12 shows up a shoulder which might be due to a bad optical contact between the pipe guide and the photomultiplier or to the PMT itself. However, this is not a problem to discriminate neutron and background thanks to the set QDC threholds. The whole channel (PMT, light pipe and scintillators) has been exchanged for 2014.

[1] Thanks to B. Lauss.

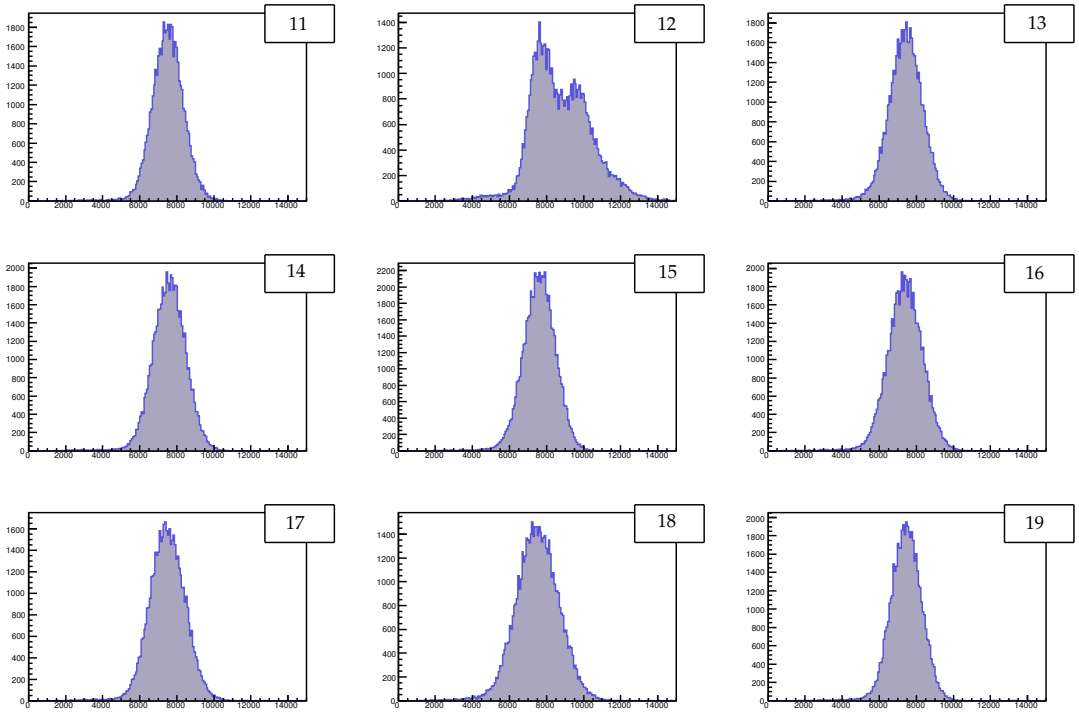

Figure 5.2: Charge distribution measured with NANOSC B at PSI in August 2013 over one cycle (threshold: 3 mV, validation gate: 12 ns). The y axis is the number of count for a given QDC value (arbitrary unit). The shoulder on the UCN peak of channel 12 might be due to a bad optical contact between the pipe guide and the photomultiplier or to the PMT. The whole channel (PMT, light pipe and scintillators) has been exchanged for 2014.

5.1.2 Spin handling

Each USSA's arm is made of a spin-flipper, an analysing foil and a radiofrequency (RF) shielding. A return yoke with a set of 40 permanent magnets is used to magnetise analysing foils. Its fringe field is also used to create the ASF field gradient. Finally, additionnal guiding coils are used to keep the UCN polarization. These different parts are described thereafter.

5.1.2.1 Guiding coils

In order to keep the UCN polarization along their path inside the USSA, guiding coils have been added (see Fig. 5.1a). They produce an additionnal guiding field transverse to the arm axis (a few 100 µT) in order to compensate a potential zero crossing due to the return yoke. The typical current flowing in these coils is in the range of a few hundred mA.

5.1.2.2 Adiabatic spin-flippers

USSA adiabatic spin-flippers are based on the same principle as usual solenoidal spin-flippers [90]: an alternating current flows into the coil which produces an RF magnetic field at frequencies in the 10–40 kHz range. The only difference is that the USSA coils have a square shape of 10 cm side to fit around USSA's arms along 4.4 cm.

Characteristics of the SF coil field The produced RF field is described by the following function:

$$B_z(z,t) = B_z(z).\cos(2\pi\nu_{\mathrm{RF}}t) \tag{5.1}$$

where ν_{RF} is the frequency of the sinusoidal signal with an amplitude $B_z(z)$. The amplitude of the magnetic field $B_z(j)$ along the arm axis at the level of the turn j in a coil of N square turns with a current I is obtained by Biot & Savart integration:

$$B_z(j) = \frac{\mu_0 I}{\pi}\left[\frac{2\sqrt{2}}{a} + a^2\sum_{n=1}^{N/2-j}\frac{1}{(a^2/4+n^2d^2)\,(a^2/2+n^2d^2)^{1/2}} + \frac{a^2}{2}\sum_{n=N/2-j}^{N/2+j}\frac{1}{(a^2/4+n^2d^2)\,(a^2/2+n^2d^2)^{1/2}}\right] \tag{5.2}$$

where $a = 10\,\mathrm{cm}$ is the side length of the coil and $d = 1.1\,\mathrm{mm}$ is the diameter of the used wire. The shape of the obtained magnetic field for a 1 A current and for a 4.4 cm long spin-flipper is compared with a Maentouch [2] simulation [91] in Fig. 5.3. Measurements performed with a Magneto-Impedance (MI) sensor have confirmed these estimations of the SF field amplitude along its axis.

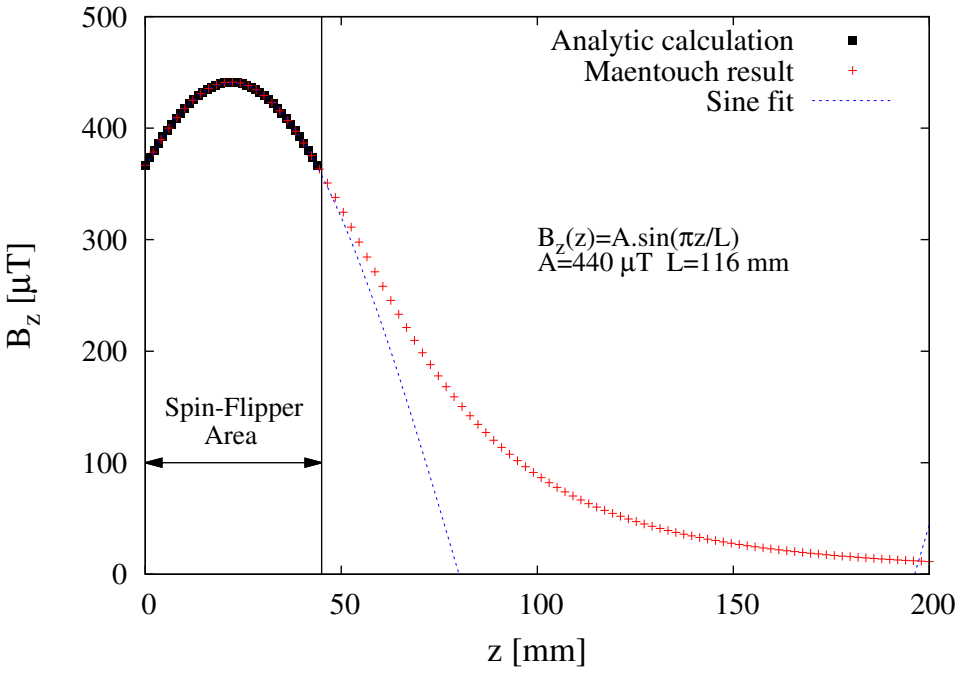

Figure 5.3: B_z produced with 1 A along the spin-flipper axis. The point at 0 mm is the beginning of the spin-flipper area.

A cross view of B_z inside the plane at the spin-flipper centre is shown in Fig. 5.4. The arm boundaries are between -40 and 40 mm. It shows that the lowest field amplitude is located at the

[2] "MAENTOUCH(to be pronounced [mentoosh]) means "magnetic stone" in Breton, the Celtic language spoken in Brittany, a French colony for the time being..." dixit G.Q. Maentouch is a home made software based on Boundary Element Method (BEM) and allows magnetostatic field due to coils to be calculated, background fields function of spatial coordinates and permanent magnets in the presence or not of ferromagnetic materials [91].

centre of the SF. Thus, reference measurements are done at the centre of the spin-flipper in order to determine the ability of the device to perform the spin-flip.

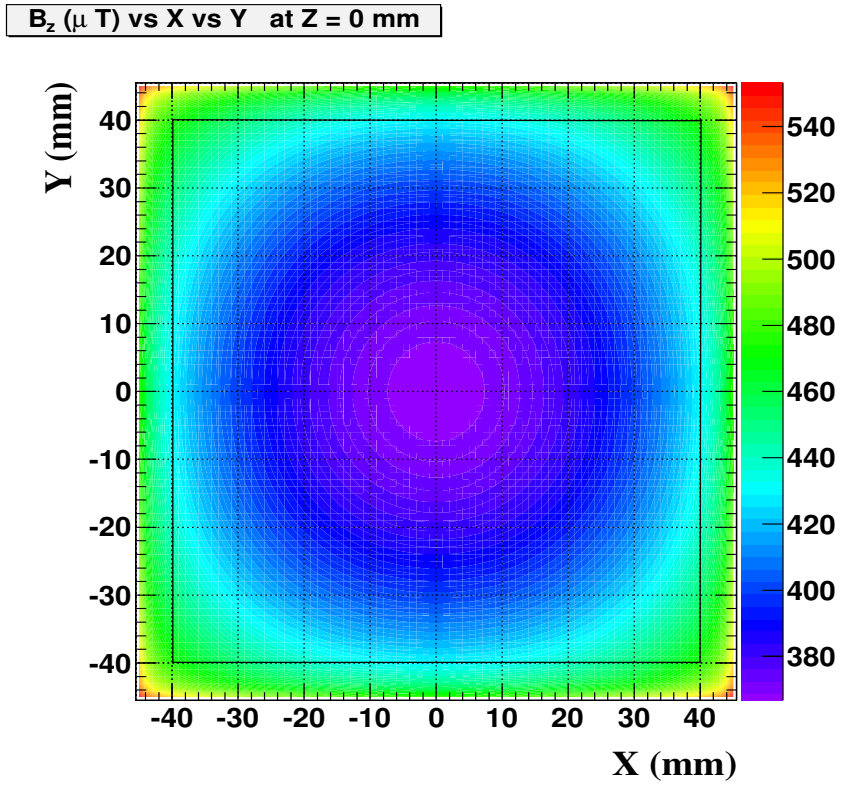

Figure 5.4: Cross view of the RF magnetic field amplitude produced by 1 A at the centre of the spin-flipper from Maentouch [91]. Limits of the UCN guide are shown by the full black line.

The effective RF amplitude is obtained for an input signal at 6 V_{pp} and 30 kHz and is of about 230/2 µT (the amplitude of the effective field contributing to the adiabatic spin-flip is half of the linear oscillating field [92]) at the centre of the spin-flipper. This amplitude is large enough to perform the adiabatic spin-flip, as presented in Fig. 5.7, showing the spin-flip probability obtained as a function of the RF field amplitude by means of Eq (B.12) and the adiabaticity coefficient given by Eq (B.10), according to the sine-cosine model [90].

Applicability of the sine-cosine model to USSA's spin-flippers As shown in Appendix B, particular field conditions, described by Eq (B.11), have to be fulfilled to perform the UCN adiabatic spin-flip following the sine-cosine model. One of those conditions is that the field shape of the RF field can be described by a sine. The analytic data set shown in Fig. 5.3 can be fitted using a sine function and therefore the field shape of USSA's spin-flippers fulfills the first condition to apply the sine-cosine model. It will be shown later in 5.1.2.5 that the static field shape fulfills the second condition to apply this model.

5.1.2.3 RF shielding

As described in the previous chapter, the principle of the simultaneous spin analysis is to detect both spin states at the same time using one spin-flipper ON and the other OFF. It means that

any RF magnetic field cross-talk between arms has to be removed.

From the existing literature about radio-frequency shielding (see [93]), one has to play with the skin effect to remove the RF field coming from the active spin-flipper in the other arm. The fraction of RF signal going through the material of thickness e around the RF field signal source is $e^{-e/\delta}$ where δ is the skin depth associated to the shielding material. The skin depth is expressed as a function of the RF field frequency ν, the magnetic permeability μ and the electric conductivity σ of the material:

$$\delta = \frac{1}{\sqrt{\pi \nu \mu \sigma}} \tag{5.3}$$

The main constraint in the USSA is that the opening of RF shielding around the UCN guiding arms. Indeed, usual RF shielding surround the whole RF source or shielded antena. Copper has been chosen because it is non magnetic and its electrical conductivity is high ($\sigma = 5.96 \times 10^7$ S/m at 20°C). The corresponding skin depth is much smaller than most materials: at 20-30 kHz, the frequency range corresponding to the static field inside the spin-flipper, 0.8 mm of copper is sufficient (in theory) to attenuate 99% of the RF field. Therefore, a 1 mm copper layer has been placed around each USSA's arm.

Experimental tests of the RF shielding For these tests, the spin-flip probability p_{SF} within the non-active arm is estimated through the adiabaticity parameter k (see Appendix B) calculated from the RF magnetic field amplitude in the non-active arm B_{eff}:

$$\begin{cases} k = \frac{\gamma_n B_{\mathrm{eff}}^2}{v_n^{\min} \partial H_0 / \partial z} \\ p_{\mathrm{SF}} = 1 - \frac{\sin^2\left(\frac{\pi}{2}\sqrt{1+k^2}\right)}{1+k^2} \end{cases} \tag{5.4}$$

From yoke measurements, $\frac{\partial H_0}{\partial z}$ is set to 0.15 mT/cm (see 5.1.2.5). Because of the gravitational boost below the nEDM spectrometer, the UCN energy at the spin-flipper level is at least 180 neV. This is why the minimum speed $v_{\mathrm{n}}^{\min}$ is set to 5 m/s in order to be conservative.

The RF magnetic field measurements have been performed using an MI sensor from the Inphynix company. RF shielding measurements have been performed on different planes along the arm axis as shown in Fig. 5.5.

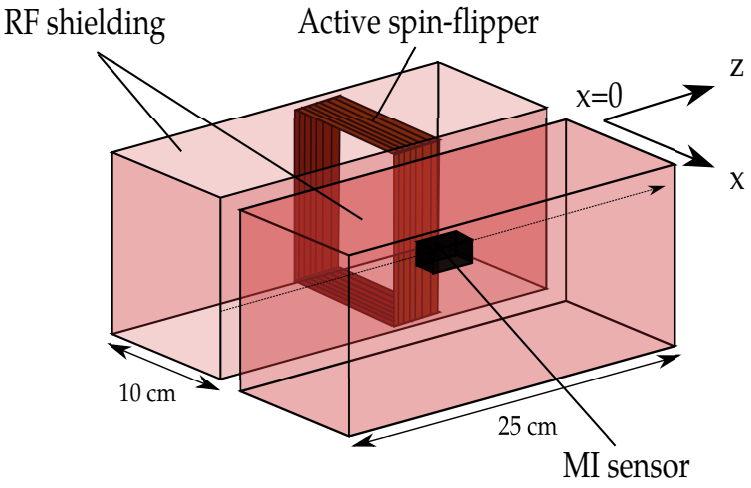

Figure 5.5: RF shielding tests setup. The plane x=0 corresponds to the internal wall of the non-active arm.

Measurements in the non-active arm have been performed with a 30 kHz signal producing an effective magnetic field amplitude at the centre of the active spin-flipper of 115 µT . Without shielding, the maximal amplitude of the magnetic field in the non-active arm is about 7.5 µT close to the internal wall as shown in Fig. 5.5 and Fig. 5.6.

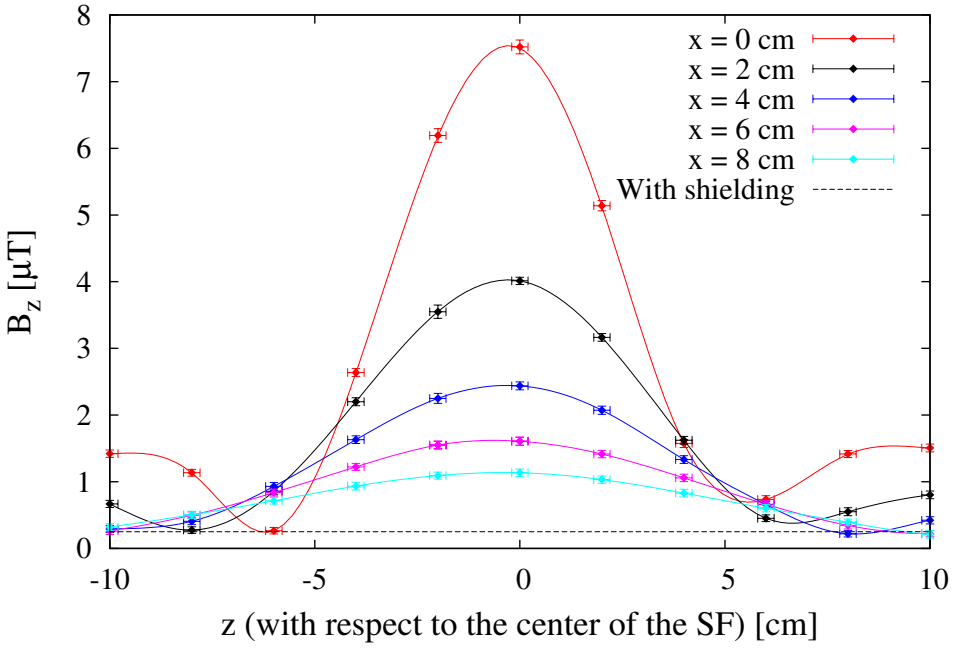

Figure 5.6: B_z amplitude along z in different x planes in the non-active spin-flipper without shielding for diamond points. Lines are just used to guide eyes. The black dash line corresponds to the highest measured amplitude with the RF shielding.

According to Eq (5.4), such a field amplitude leads to a spin-flip probability of about 1.9%, which is obviously not satisfaying. Using the copper RF shielding, the maximal RF amplitude has been decreased to less than 0.3 µT . The corresponding spin-flip probability is below the ppm level as shown in Fig. 5.7.

In order to get such an RF magnetic field attenuation, the RF shielding end has been extended by 5 cm above the spin-flipper. That is why the arm length has been increased by 5 cm with respect to GEANT4-UCN simulations and the quartz wedge is machined to let room for the RF shielding. With such a shielding, the field amplitude inside the active arm is slightly decreased down to 105 µT, which is enough to perform the spin-flip.

5.1.2.4 Analysing foils

The USSA analysing foils are made of a 25 µm aluminium substraste coated by a 400 nm iron layer. These foils have been made at the PSI sputtering facility because the magnetic field required (about 40 mT) to reach the saturation is lower than other foils made in Caen or Mainz [94]. At saturation, the theoretical magnetisation of the iron layer is about 2 T. This corresponds to an additional potential of ±120 neV according to the neutron spin state. The two analysers are made

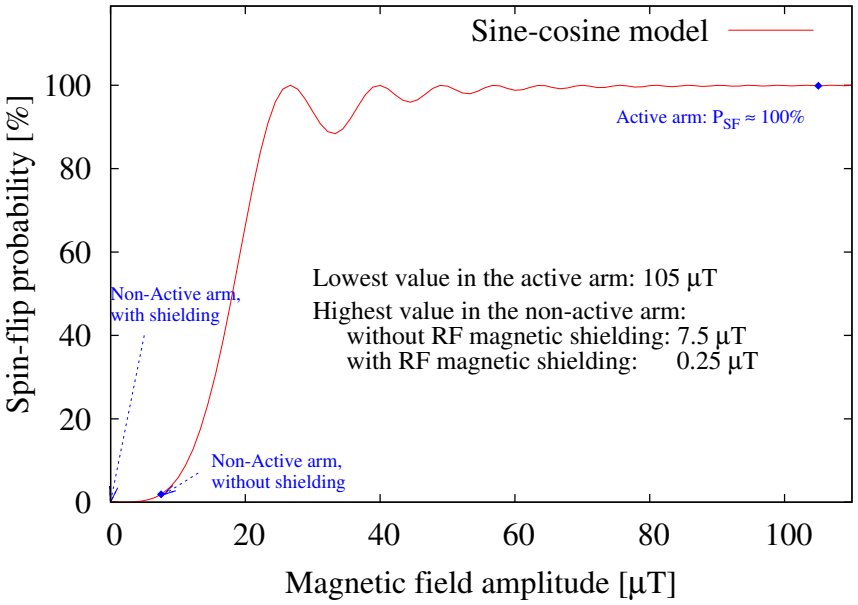

Figure 5.7: Spin-flip probability as a function of the RF amplitude, calculated by means of Eq (5.4).

with the same foil in order to keep USSA arms as identical as possible. These foils are placed between the two glass parts in the 200 µm wide gap and are magnetised by a set of permanent magnets.

5.1.2.5 Magnetisation system

A set of 40 neodym permanent magnets is used to magnetize the analysing iron foils. It is enclosed in an iron yoke as shown in Fig. 5.8.

Figure 5.8: Iron yoke with the set of 40 permanent magnets.

The field at the iron foils level is in the range of 80–120 mT . According to [94], it is high enough to saturate the iron foil layer. The fringe field from the yoke is used in the spin-flipper area to perform the adiabatic spin-flip. A Maentouch simulation of the yoke has been benchmarked with a map of the return yoke performed thanks to a mapping device at GANIL [95] and with a 3D magnetic field probe [96]. The magnetic field evolution as a function of the position along one arm axis coming from a Maentouch simulation combining the yoke and the USSA guiding coils [97] is shown in Fig. 5.9 with the corresponding gradient evolution in Fig. 5.10.

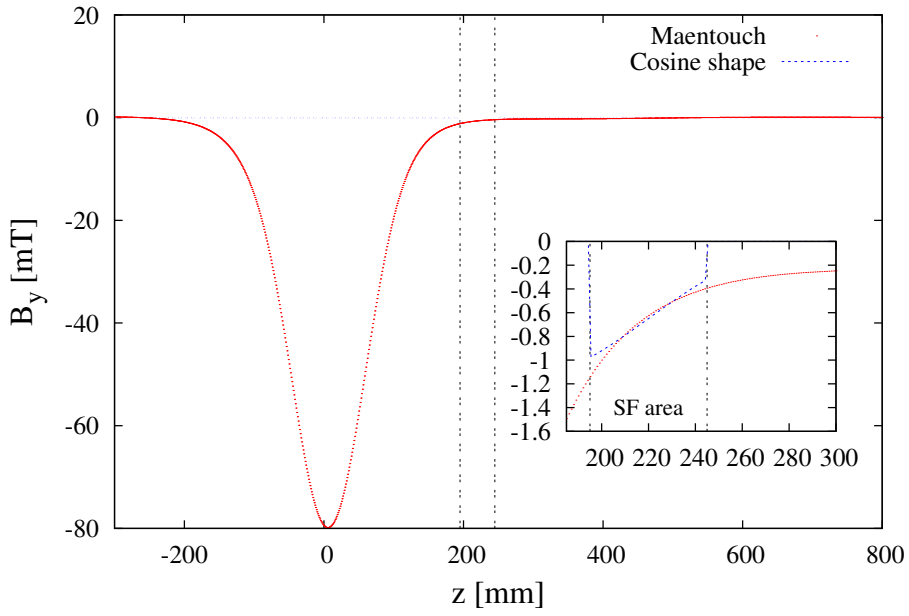

Figure 5.9: Maentouch simulation of B_y component as a function of the position along the vertical axis.

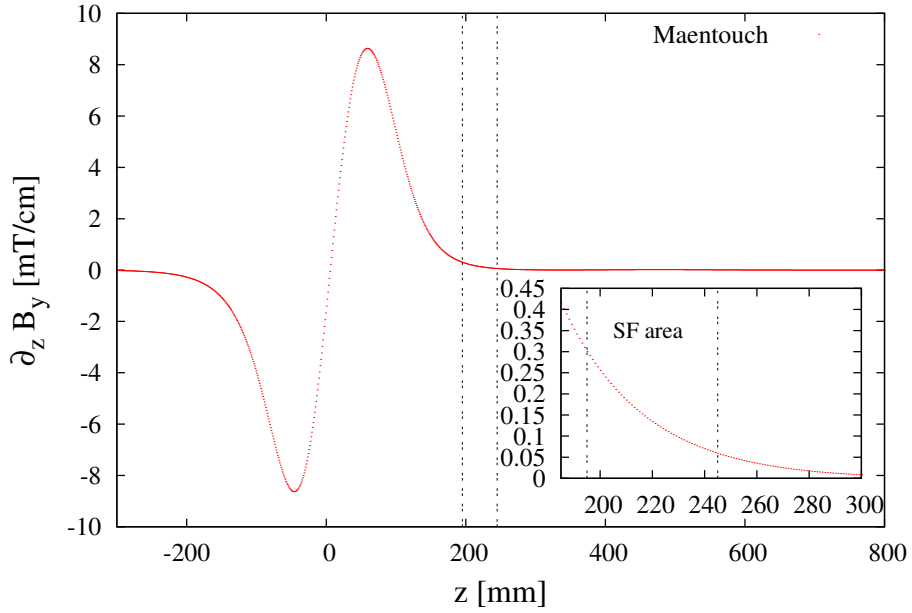

Figure 5.10: Maentouch simulation of B_y vertical gradient as a function of the position along the vertical axis.

At the level of the spin-flipper centre, the gradient amounts to 0.15 mT/cm and the transverse field is in the range 0.05 – 0.8 mT. The gradient value has been used to calculate a spin-flip probability close to 100% in the ASF (see 5.1.2.3). In the spin-flipper area, it is also visible that the field has approximately a cosine shape. This is the second field condition given by Eq (B.11) to apply the sine-cosine model which is used to predict the spin-flip probability.

Besides, another important piece of information is the field value at the level of NANOSC PMTs (Hamamatsu R11187). Even if those PMTs have a low sensitivity to high fields (Mumetal shield around PMTs), a large magnetic field in the electron multiplication area would degrade or even damage the PMTs. The field coming from the iron yoke is 0.7 mT at 20 cm downstream. This is low enough to allow a good working of NANOSC photomultipliers compared to the constructor limit of 2 mT.

5.1.3 Conclusions

The design and the assembly of each USSA's part have been done in order to optimize the UCN transmission and to handle the UCN spin as well as possible. Particularly, a lot of care has been taken on the magnetic fields shape in order to get efficient spin-flippers and a spin holding field. In the next section, performances tests of USSA's subdevices are presented. These tests have been carried out on the West-2 beam line at PSI.

5.2 USSA test on the West-2 beam line

After two weeks of preliminary tests at ILL[3], performances of each USSA's subsystem (spin-flippers, analysing foils, guiding parts...) have been measured on the West-2 beam line at PSI in order to demonstrate that the new spin analyser was ready to be installed below the nEDM spectrometer.

5.2.1 Experimental setup

The experimental setup is shown in Fig. 5.11. UCNs come from the top, follow the bend and fall down into the USSA. A stainless steel T-shaped guide was used between the bend and the USSA in order to suppress the high energy component from the UCN energy spectrum. A magnetised iron foil was used as a polariser right after the T-shaped guide. In order to carry out spin-flipper efficiencies and analysing power measurements, a spin-flipper (#1) was placed below the polariser. At the end of the line, a removable PMMA tube with a length of 27 cm was used in order to perform measurements at two different heights. Thus, the distance D between the polariser and USSA's foils can be set either to 74 cm or to 101 cm.

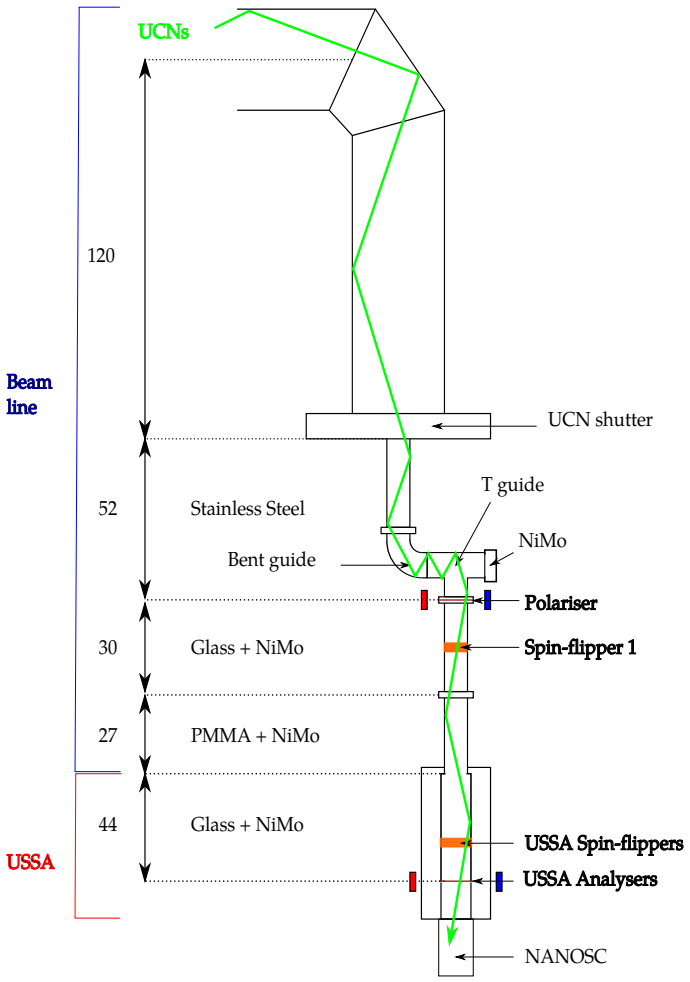

Figure 5.11: West-2 beam line setup.

[3]Thanks to P. Geltenbort and Th. Brenner for the beam time and their warm welcome.

5.2.2 Preliminary measurements

5.2.2.1 Background

During each proton kick, fast neutrons are produced and are detected by the USSA's detectors. Even though data recorded during the kick are not taken into account, the time shape of the kick is not perfectly square as shown in Fig. 5.12. This time spectrum has been recorded with the UCN shutter closed such as only fast neutrons coming from the source are detected. A small amount of fast events is still produced 0.1 s after its end. In order to remove this contribution, a set of 10 to 20 cycles with the UCN shutter closed is performed for each setup configuration. The average number of fast events which occur right after the kick (normalised by the number of detected UCNs on the West-1 beam line in a Cascade-U detector[4]) is then subtracted to the detected UCN number for the runs of interest.

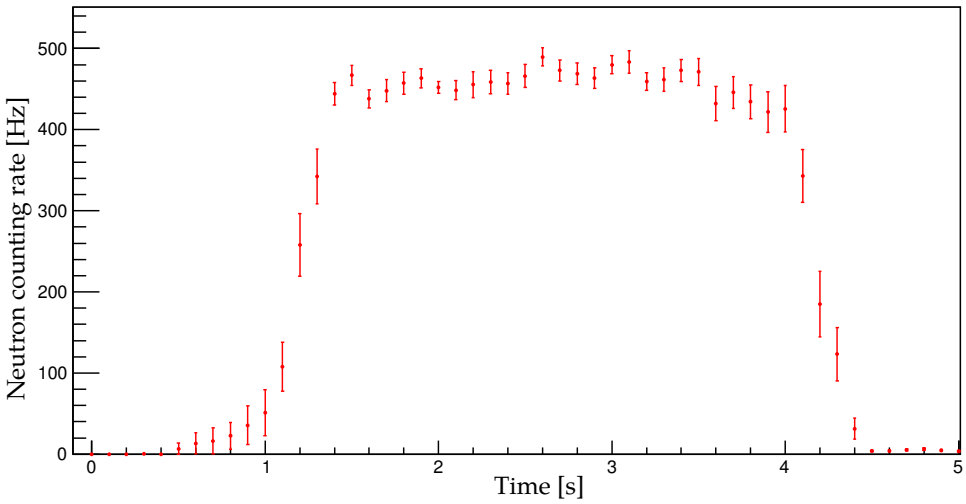

Figure 5.12: Detected events in NANOSC-A during the 3 s proton kick.

5.2.2.2 Rough characterisation of the UCN energy spectrum

The lowest UCN energy ($\simeq 250$ neV at USSA's foils level) is calculated from the height difference between the bottom of the West-2 beam line horizontal part and the USSA entrance. In order to have an estimation of the fast UCN amount entering into the USSA, the polariser has been replaced by a 100 µm aluminium foil with a NiMo coating and the USSA by a single NANOSC detector. Measurements have been performed with and without the NiMo coated foil. Thus, the UCN fraction with a larger energy than the NiMo Fermi potential is given by:

$$\varepsilon_{220} = \frac{N_{\mathrm{w}}}{N_{\mathrm{w/o}}\left(1 - \mathrm{p}_{\mathrm{abs}}^{\mathrm{Al}}\right)} \tag{5.5}$$

where N_{w} and $N_{\mathrm{w/o}}$ are respectively the detected UCN numbers with and without the NiMo coated foil and $\mathrm{p}_{\mathrm{abs}}^{\mathrm{Al}}$ is the absorbed UCN fraction in the aluminium foil ($\sim 30\%$ [98]). The fast UCNs fraction has been estimated to about 10%. It means that when the distance between the NiMo coated foil and USSA's foils is about 1 m (lowest USSA height), the UCN fraction with

[4] Detector based on the neutron capture in a ^{10}B layer and the GEM technology.

an energy larger than 330 neV at the USSA's foil height is 10%. The maximum reachable USSA analysing power in such a configuration is therefore about 80% (without considering the fact that UCNs do not come perpendicularly onto analysing foils).

5.2.2.3 Initial polarisation

In order to measure the initial polarisation produced by the polariser, the setup shown in Fig. 5.13 has been used. The beam line is the same until the end of the first glass tube. Thus, the polarisation measurement is carried out with the same polariser and spin-flipper locations as for the USSA measurements. Two magnetised iron foils (P1 and P2) and one spin-flipper (#2) were added at the end of the beam line before a single NANOSC detector.

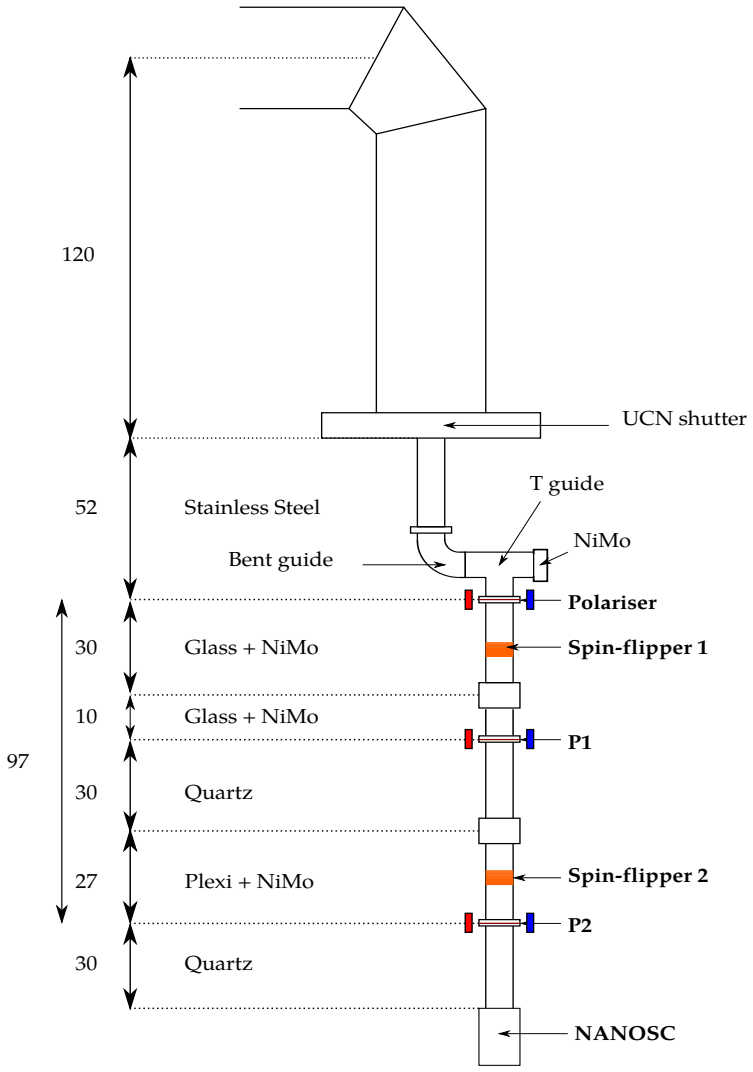

Figure 5.13: Initial polarisation measurement setup.

For the polarisation determination, one foil among the three is removed. Three measurements are required, corresponding to the three polarising/analysing power products $P_i \times P_j$ given by [99]:

$$P_i \times P_j = \frac{N_{00} - N_{01}}{f_1 N_{00} - N_{10}} = \frac{N_{00} - N_{10}}{f_2 N_{00} - N_{01}} \tag{5.6}$$

where $P_{i/j}$ is the polarising/analysing power of foils i/j, $f_{1/2}$ is the spin-flipper efficiency of spin-flipper 1/2. N_{12} indices are the SF1 and SF2 states: 0 for SF OFF and 1 for SF ON. The SF efficiencies f_1 and f_2 are obtained using only the polariser and the last foil. The results are:

$$f_1 = \frac{N_{11} - N_{01}}{N_{00} - N_{10}} = 96.1 \pm 4.6\% \tag{5.7}$$

$$f_2 = \frac{N_{11} - N_{10}}{N_{00} - N_{01}} = 99.3 \pm 4.8\% \tag{5.8}$$

The three measured polarising/analysing power products are:

$$P \times P_1 = 41.0 \pm 1.5\% \quad P \times P_2 = 46.2 \pm 1.9\% \quad P_1 \times P_2 = 38.0 \pm 1.3\%$$

The initial polarisation P is deduced from those measurements:

$$P = \sqrt{\frac{P \times P_1 . P \times P_2}{P_1 \times P_2}} = 70.6 \pm 3.2\% \tag{5.9}$$

5.2.3 Tests with unpolarised UCNs

5.2.3.1 Arm detection asymmetry

The USSA has to symmetrically detect spin up and spin down UCNs. In order to check such a behaviour, the USSA detection asymmetry between arms A and B, $(N_A - N_B)/(N_A + N_B)$ has been measured. For such a purpose, the polariser and USSA's analysing foils are removed. The neutron counting rates for arms A and B and asymmetry are shown in Fig. 5.14. The average asymmetry between arms A and B is $0.43 \pm 0.07\%$. It combines different arm transmissions and the two NANOSCs different detection efficiencies. The conclusion is that the arms detection is nearly symmetrical.

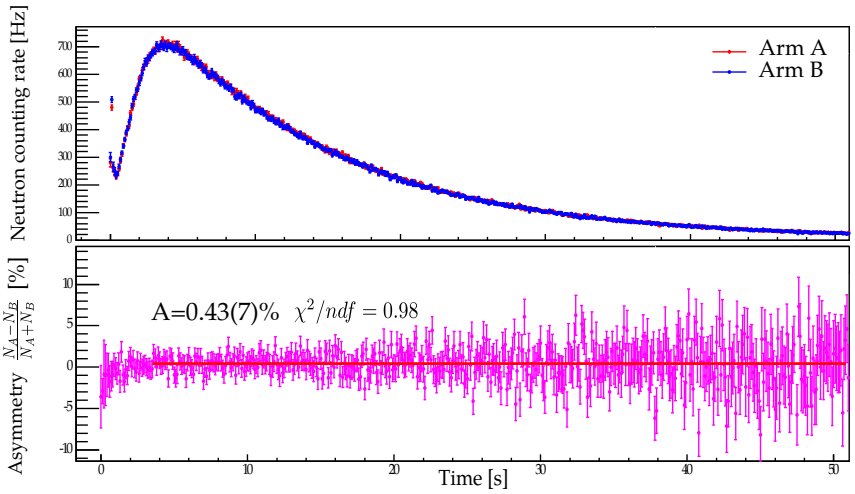

Figure 5.14: Detection asymmetry and neutron counting rates as a function of the detection time.

Another measurement was carried out with the two USSA's analysers in order to know whether the analysing foils have the same UCN transmission. There is no polariser in the apparatus and all spin-flippers are turned OFF. The average asymmetry is $\mathcal{A} = 0.40 \pm 0.11\%$ ($\tilde{\chi}^2 = 0.96$). This asymmetry is consistent with the previous detection asymmetry. It means that USSA's foils do not introduce any additional asymmetry.

5.2.3.2 USSA transmission

Transmission measurements were performed using a single NANOSC detector and then the USSA at the same location on the beam line. The transmission is defined as the ratio between the number of detected neutrons with the USSA and a single NANOSC detector. These numbers were normalised with the number of detected neutrons simultaneously measured on the West-1 beam line by a Cascade-U detector. The worst transmission, $T = 80.8 \pm 0.6\%$ was obtained for the lowest position ($D = 105$ cm), hence for the largest distance between the polariser and USSA foils. For the shortest distance ($D = 75$ cm), a transmission of $83.2 \pm 0.7\%$ was measured. This is an indication that one needs a higher Fermi potential in the USSA in order to increase its UCN transmission.

5.2.3.3 Fraction of detected UCNs after reflection in the other arm

In order to measure the probability for a UCN to be reflected on an analysing foil and then to be detected in the other arm, the two configurations of the Fig. 5.15 were used.

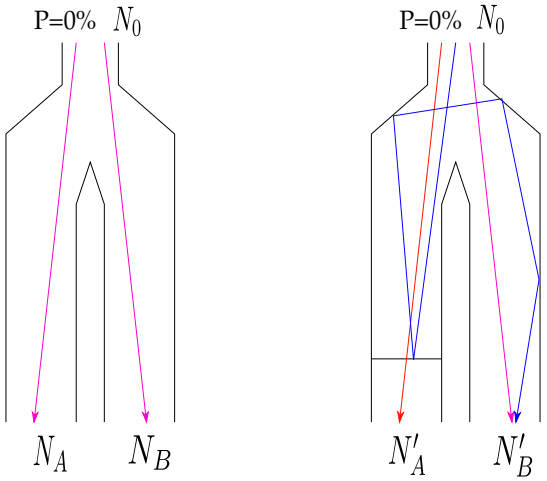

Figure 5.15: USSA configurations used to determine the reflection probability from the wrong spin detection arm to the good one on the West-2 beam line. In one case there is no foil. In the other case, a single analysing foil is added.

For both configurations, N_0 unpolarised UCNs fall down into the USSA. The difference between the two configurations is the presence of a single analysing foil in one of the two USSA arms. During the measurement with no foil, the number of detected UCNs is the same in both arms:

$$N_A \simeq N_B = \frac{N_0}{2} \tag{5.10}$$

In the second case, roughly $N_0/4$ UCNs are going through the analysing foil in arm A. The UCN fraction absorbed inside the analyser is ε_{abs} and the probability for a UCN to be reflected on the analyser to the other arm is p_{ref}. Assuming negligible losses per reflection on the analysers, numbers of detected UCNs in arms A and B are:

$$\begin{cases} N'_A = \frac{N_0}{4}(1 - \varepsilon_{\text{abs}}) \\ N'_B = \frac{N_0}{2} + \frac{N_0}{4} p_{\text{ref}} \end{cases} \tag{5.11}$$

Using Eq (5.10) and Eq (5.11) the reflection probability p_{ref} and the UCN absorption fraction ε_{abs} are finally determined as:

$$\begin{cases} p_{\text{ref}} = \frac{2N'_B}{N_B} - 2 = 33.6 \pm 3.1\% \\ \varepsilon_{\text{abs}} = 1 - \frac{2N'_A}{N_A} = 2.7 \pm 1.3\% \end{cases} \tag{5.12}$$

The UCN fraction absorbed inside the analysing foil, $2.7 \pm 1.3\%$, is of the same order of magnitude as the calculated UCN attenuation in a 25 µm aluminium foil. The probability for a neutron to be reflected from one arm to the other amounts to $33.6 \pm 3.1\%$. It is much lower than the calculated value from GEANT4-UCN simulations of 84% (see 4.6.2). This can be partly explained by the fact that UCNs reflected upstream go back into the UCN tank and can hardly come back to the USSA. In addition, UCN simulations were made with a perfect coating and glass structure, without slits which overestimate the number of UCNs able to go to the other arm.

5.2.4 Tests with polarised neutrons

5.2.4.1 Spin-flippers efficiencies

Spin-flippers efficiencies measurements were carried out with the polariser using a single foil located in the arm where the spin-flipper is characterised. This has been done in order to avoid multiple passages between the two arms. In such a case, since the number of passages is not known, it is not possible to use the transmission matrices formalism defined in [99]. Spin-flippers efficiencies have been measured using Eq (5.8): $f_A = 97.0 \pm 1.2\%$ and $f_B = 97.1 \pm 0.9\%$. These efficiencies do not change with the height of the USSA with respect to the horizontal beam line. It means that USSA's spin-flippers can handle quite fast UCNs without efficiency loss. However, USSA's spin-flippers are not fully efficient. Two explanations are possible. The first one would be the existence of a non-adiabatic area in the spin-flippers. The other one could be multiple passages through the active SF and multiple reflections on the USSA analyzer. In that case, the effect would be to depolarise UCNs and thus allow their passage through the analysing foil. As a result, it would lower the effective spin-flipper efficiency.

5.2.4.2 RF cross-talk measurements

Possible RF cross-talk between the two arms was studied. For these tests, a single foil was used in the non-active arm (SF OFF). The number of detected UCNs in the non-active arm is measured when the spin-flipper of the active arm is turned ON or OFF. No change has been observed. The relative deviation $\frac{N_{\text{OFF}} - N_{\text{ON}}}{N_{\text{OFF}}}$ is equal to $0.15 \pm 0.62\%$. The conclusion is that there is no cross-talk between USSA's arms.

5.2.4.3 Analysing power of the USSA's foils

Measurements of the spin analysing power of the USSA's foils have been carried out using two different methods. First, the measurements devoted to the spin-flippers efficiencies determination have been used to find the analysing power of the active arm foil. Second, both foils stayed in the USSA and the effective spin analysing power of the USSA have been measured.

With a single analysing foil: Analysing power measurements performed with a single foil in the USSA are summarised in Tab. 5.1. For the shortest distance, the analysing powers of both foils are the same, which shows that the analysing foil spin treatment is similarly performed in each arm. The analysing power difference (about 15%) between the two height setup configurations can be explained using the NiMo foil transmission results (see 5.2.2.2). Indeed, with the lowest

Polariser→USSA foils	$D = 74\,\text{cm}$	$D = 101\,\text{cm}$
P_A [%]	91.0 ± 3.4	77.4 ± 1.7
P_B [%]	89.7 ± 2.7	Not measured

Table 5.1: Single foil analysing powers measurements.

USSA height setup ($D = 101\,\text{cm}$), the fast UCN fraction is larger. As a result, the UCN fraction that USSA's foils are not able to analyse is larger and the USSA spin analysing power is lowered.

With two analysing foils: The USSA analysing power measurements are shown in Tab. 5.2.

Polariser→USSA foils	$D = 74\,\text{cm}$	$D = 101\,\text{cm}$
P_{USSA} [%]	83.5 ± 2.5	77.3 ± 2.8

Table 5.2: USSA analysing power measurements.

For $D = 74\,\text{cm}$, the analysing power is different by about 6% from a single foil to two foils. This is not the case for the setup with $D = 101\,\text{cm}$. This is not expected since the spin analysing power should be lower with the two USSA foils. Indeed, because of bounces from one arm to the other on analysing foils and crossings of the SF, one expects to observe more depolarisations with the two foils in the USSA.

5.2.5 Conclusions

Similar efficiencies of 97% were measured for both spin-flippers A and B. The deviation due to a possible cross-talk between the two arms was measured at $0.15 \pm 0.62\%$ and cross-talk is thus excluded below the percent level. The analysing powers of USSA foils have been measured to $91.0 \pm 3.4\%$ and $89.7 \pm 2.7\%$. It shows that USSA foils analyse the spin symmetrically. In addition, the arm detection asymmetry has been estimated to $0.43 \pm 0.07\%$ in transmission and $0.40 \pm 0.11\%$ with the two analysers in the USSA. It confirms the symmetry between the two arms.

The USSA analysing power was measured to be about 80%. It is lower than with a single analysing foil by about 6%. A possible explanation would be the multiple bounces onto the analysing foils and passages through the active spin-flipper which could lead to UCN depolarisations. The USSA transmission was measured to 80% for the highest energy conditions. It could be further improved by replacing the current NiMo coating by diamond or ^{58}NiMo coatings which are known to have larger Fermi potentials (> 280 neV).

Measurements performed with the USSA on the West-2 beam line showed that all USSA's subsystems work properly and that the USSA symmetrically treat the two UCN spin states. As a result, the USSA was installed below the nEDM experiment to be tested as described in the next section. Below the nEDM spectrometer, USSA performances are expected to be better than below the West-2 beam line because of a softer UCN energy spectrum.

5.3 USSA test below the oILL spectrometer

In order to measure the possible nEDM statistical sensitivity improvement with respect to the sequential system, the USSA was integrated in the nEDM apparatus. A drawing of the setup is shown in Fig. 5.16. The distance between the precession chamber centre and the USSA analysing foils is about 2.1 m. It means that the UCN energy is gravitationally boosted by 210 neV at the foil location. The USSA hangs on an aluminium plate below the switch box and is also maintained by an external aluminium profile structure fixed in the concrete floor below the thermohouse. One pair of additional guiding coils have been added between the switch and the USSA in order to maintain the UCN polarisation.

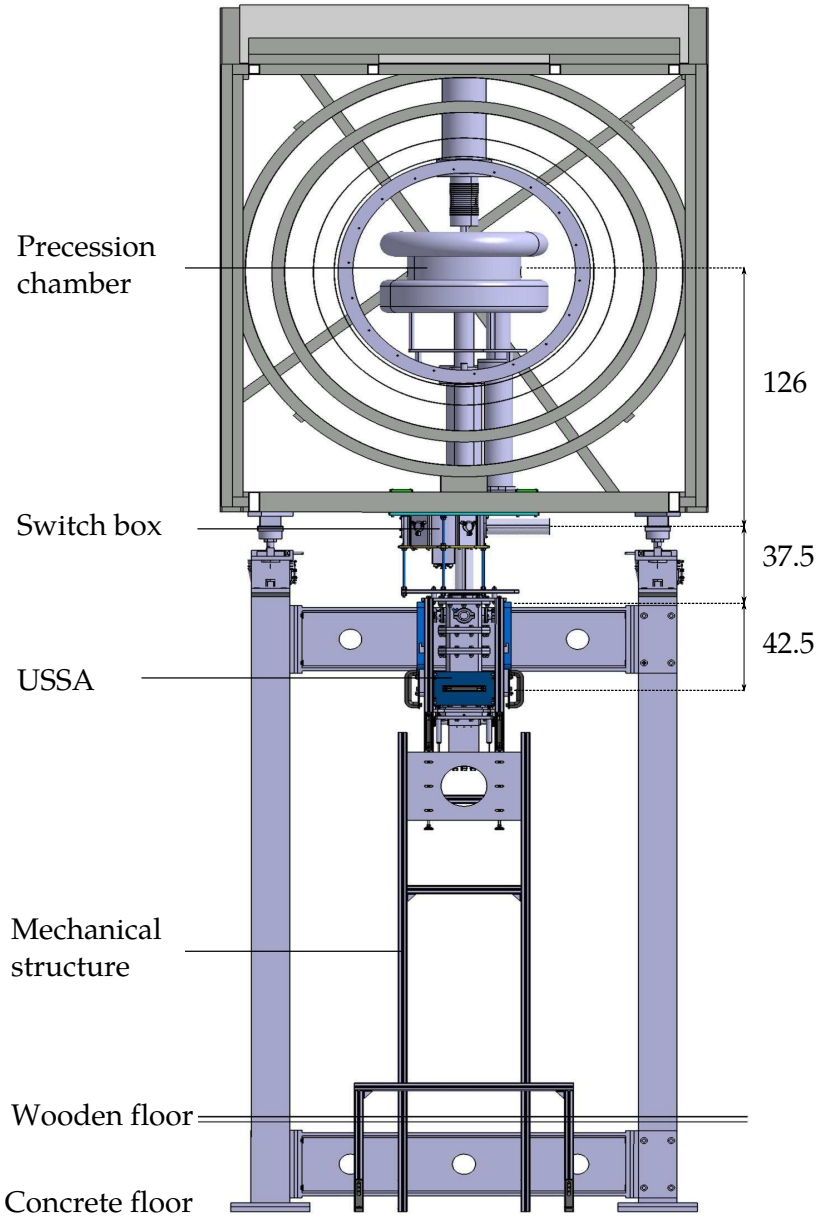

Figure 5.16: USSA integration drawing in the nEDM apparatus. Dimensions are in cm.

The UCNs detected in the Cascade-U detector on the West-1 beam line were used for the monitoring. It allowed one to take care of UCN source fluctuations in order to compare measurements performed with the USSA and the sequential system. An important difference between the two systems is the analysing foils height: they are 40 cm lower in the USSA. Three types of runs have been performed: direct mode, T_1 measurement and EDM run. The guiding field configuration did not change for the sake of the comparison.

5.3.1 Direct mode measurements

In direct mode, polarised UCNs coming from the horizontal guide are directly going into the USSA. With such a configuration, the USSA asymmetry was found to be $77.35 \pm 0.16\%$. The analysing power of the sequential system was estimated with the upstream spin-flipper during 2013, a few months before the USSA installation. The measured asymmetry was $83.83 \pm 0.35\%$ *i.e.* larger than with the USSA. The lower USSA spin analysis efficiency can be partly explained (at the 2% level) by a fast UCN component visible in the arm B in Fig. 5.17 at the beginning of the counting rate distribution between 3 and 6 s. These fast UCNs are able to cross the USSA's analysers whatever their polarisation and thus decrease the asymmetry. Once they are detected, the USSA asymmetry saturates at 79%. Additional possible explanations for the lower USSA analysing power with respect to the sequential system could be a bad guiding field along the UCN path or a lower foil ability to analyse the UCN spin, either due to the foil itself or to the foil height difference in the two setups. The last possible explanation is that depolarisations occuring in the USSA (because of multiple foil reflections) could decrease the effective analysing power of the system (see 5.2.4.3).

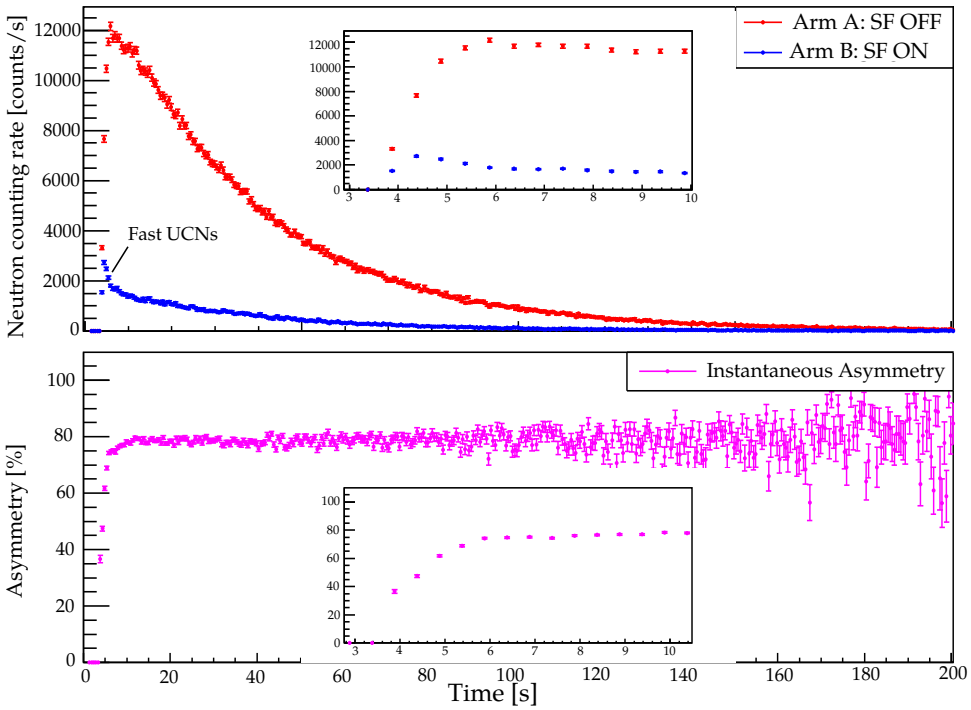

Figure 5.17: UCN counting rates (arms A and B) and asymmetry as a function of the emptying time in direct mode.

5.3.2 T_1 measurements comparison

T_1 measurements are performed in order to estimate the longitudinal relaxation time T_1. In this case, it is used to study the influence of the UCN storage on the spin analysing power of the USSA and to compare USSA performances with respect to the sequential sytem. In this kind of run, the precession chamber is filled by UCNs during 30 s, then UCNs are stored during a time T and finally counted during 50 s. The asymmetry as a function of the storage time is shown in Fig. 5.18 for both the USSA and the sequential system.

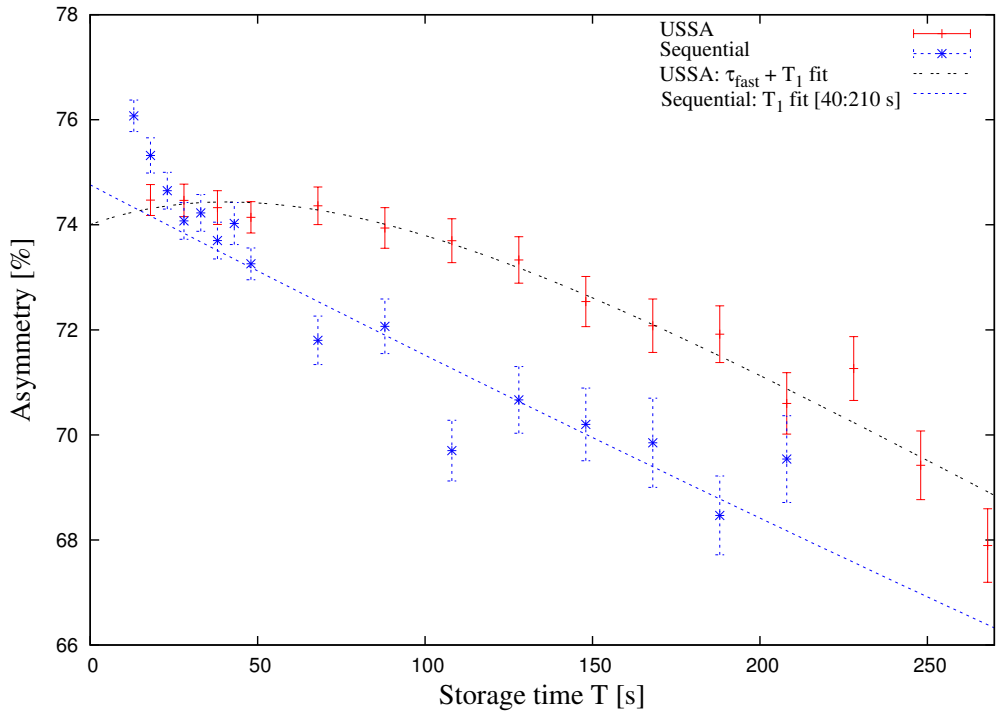

Figure 5.18: Asymmetry as a function of storage time for the USSA (red cross) and the sequential system (blue star) during T1 measurement. The black dashed line corresponds to the USSA data fit using Eq (5.19). The blue dash line corresponds to the usual T_1 fit applied to the sequential analyser data between 40 and 210 s.

With the USSA, a maximum is visible around $T = 50$ s and then the T_1 exponential decrease is observed for larger storage times. This maximum is thought to arise from a fast UCN component. An attempt to model the phenomenon has been carried out hereafter.

The UCN spin populations as a function of the storage time are described by:

$$\begin{cases} \frac{dN_\uparrow}{dT} = \frac{1}{\tau_{\text{flip}}}\left(N_\downarrow - N_\uparrow\right) - \frac{N_\uparrow}{\tau_{\text{loss}}} = \frac{1}{2T_1}\left(N_\downarrow - N_\uparrow\right) - \frac{N_\uparrow}{\tau_{\text{loss}}} \\ \frac{dN_\downarrow}{dT} = \frac{1}{\tau_{\text{flip}}}\left(N_\uparrow - N_\downarrow\right) - \frac{N_\downarrow}{\tau_{\text{loss}}} = \frac{1}{2T_1}\left(N_\uparrow - N_\downarrow\right) - \frac{N_\downarrow}{\tau_{\text{loss}}} \end{cases} \tag{5.13}$$

where $N_{\uparrow/\downarrow}$ are respectively the number of spin up/down UCNs stored in the precession chamber at a given time T, T_1 is the longitudinal relaxation time and τ_{loss} the time constant associated to wall losses and the beta decay.

Solving (5.13) for a neutron population with an initial polarisation P_0 gives:

$$\begin{cases} N_\uparrow(T) = \frac{N_0}{2}\mathrm{e}^{-T/\tau_{\text{loss}}}\left[1 + P_0\mathrm{e}^{-T/T_1}\right] \\ N_\downarrow(T) = \frac{N_0}{2}\mathrm{e}^{-T/\tau_{\text{loss}}}\left[1 - P_0\mathrm{e}^{-T/T_1}\right] \end{cases} \tag{5.14}$$

where N_0 is the initial number of UCNs inside the precession chamber.

In order to take into account the energy loss dependence, the number of stored UCNs can be described with two time constants:

$$N(T) = N_0^{\text{slow}} \mathrm{e}^{-T/\tau_{\text{slow}}} + N_0^{\text{fast}} \mathrm{e}^{-T/\tau_{\text{fast}}} \tag{5.15}$$

τ_{slow} is assigned to UCNs with low energies compared to the wall Fermi potential and τ_{fast} is assigned to UCNs with higher energies. The number of detected UCNs as a function of the storage time is shown in Fig. 5.19. One gets: $\tau_{\text{slow}} = 210 \pm 15\,\text{s}$ and $\tau_{\text{fast}} = 59.0 \pm 8.7\,\text{s}$. Using such an energy partition, the UCN population can be split as followed:

$$\begin{cases} N_\uparrow(T) = \frac{N_0}{2}\left[1 + P_0 \mathrm{e}^{-T/T_1}\right]\left[(1-\mathrm{p}_{\text{fast}})\mathrm{e}^{-T/\tau_{\text{slow}}} + \mathrm{p}_{\text{fast}}\mathrm{e}^{-T/\tau_{\text{fast}}}\right] \\ N_\downarrow(T) = \frac{N_0}{2}\left[1 - P_0 \mathrm{e}^{-T/T_1}\right]\left[(1-\mathrm{p}_{\text{fast}})\mathrm{e}^{-T/\tau_{\text{slow}}} + \mathrm{p}_{\text{fast}}\mathrm{e}^{-T/\tau_{\text{fast}}}\right] \end{cases} \tag{5.16}$$

where p_{fast} is the initial proportion of fast UCNs.

The UCN population called "fast" has an energy comparable or larger than the Fermi potential of the DPS in the chamber, around 160 neV. This energy is close to the limit that analysing foils can handle (330 neV in theory *i.e.* about 130 neV in the precession chamber). Because the fastest UCNs are too energetic to be analysed by USSA's foils, the number of fast UCNs detected in each arm is the same:

$$N_A^{\text{fast}}(T) = N_B^{\text{fast}}(T) = \frac{N_{\text{tot}}^{\text{fast}}(T)}{2} = \frac{N_0}{2}\mathrm{p}_{\text{fast}}\mathrm{e}^{-T/\tau_{\text{fast}}} \tag{5.17}$$

Thus, the USSA asymmetry is described by:

$$\mathcal{A}(T) = \frac{N_A - N_B}{N_A + N_B} = \frac{N_\uparrow^{\text{slow}}(T) - N_\downarrow^{\text{slow}}(T)}{N_\uparrow^{\text{slow}}(T) + N_\downarrow^{\text{slow}}(T) + N_{\text{tot}}^{\text{fast}}(T)} \tag{5.18}$$

$$= \frac{P_0 \mathrm{e}^{-T/T_1}}{1 + \frac{\mathrm{p}_{\text{fast}}}{1-\mathrm{p}_{\text{fast}}}\mathrm{e}^{-T(1/\tau_{\text{fast}} - 1/\tau_{\text{slow}})}} \tag{5.19}$$

Using τ_{fast} and τ_{slow} extracted from (5.15) as inputs, the fit of the USSA data with the function (5.19) gives the following parameters ($\tilde{\chi}^2 = 0.63$):

$$P_0 = 79.4(9)\% \quad T_1 = 1930(90)\,\text{s} \quad \mathrm{p}_{\text{fast}} = 6.8 \pm 1.3\%$$

The P_0 and T_1 values are of the same order of magnitude as previous measurements performed over the year 2013 (*e.g.* $P_0 = 72.2 \pm 5.5\%$, $T_1 = 2090 \pm 210\,\text{s}$). The proportion of fast UCNs not analysed by iron foils is consistent with MCUCN simulations results [100] which gives an initial UCN fraction with energies higher than 130 neV in the precession chamber (*i.e.* corresponding to 330 neV at USSA foils level) of a few percents. It has to be precised that the "slow" and "fast" components do not correspond here to well defined parts of the UCN spectrum. Therefore, quantitative results of this model have nonetheless to be taken with care. Finally, the asymmetry decrease due to the fast component is found to be negligible for storage times above 150 s, *i.e.* for typical EDM storage times. In that case, the low USSA height has therefore no influence on the USSA spin analysing power.

With the sequential system, a larger asymmetry is observed for $T < 50\,\text{s}$. It is likely due to the fast UCN component which go through the analyser, whatever the UCN spin state. As the sequence starts with the most populated spin state for this set of measurements, this spin state population is overestimated and thus the corresponding asymmetry.

The most interesting measurements for the comparison between the USSA and the sequential system are above 150 s *i.e.* for typical storage times in the nEDM experiment. The polarisation and the number of detected UCN are summarised in Tab. 5.3 for a storage time $T = 180\,\text{s}$. During the USSA measurements, there was no monitoring recorded on West-1. The monitored UCN count has been therefore extrapolated from measurements surrounding this measurement within a day.

	$\mathcal{A}$ [%]	N_{tot}	$N_{\text{West-1}}$
USSA	71.9(3)	4160(30)	$2.07(5)\times10^6$ (extrapolated)
Sequential	68.5(8)	3020(45)	$1.700(13)\times10^6$
Ratio	1.050(13)	1.131(33)	

Table 5.3: Asymmetry $\mathcal{A}$ and total number of detected UCNs N_{tot} for the USSA and the sequential analyser with a storage time of 180 s. $N_{\text{West-1}}$ is the monitored UCN counts on the West-1 beam line. The ratio of the total number of detected UCNs is calculated with the number of detected UCNs normalised with $N_{\text{West-1}}$.

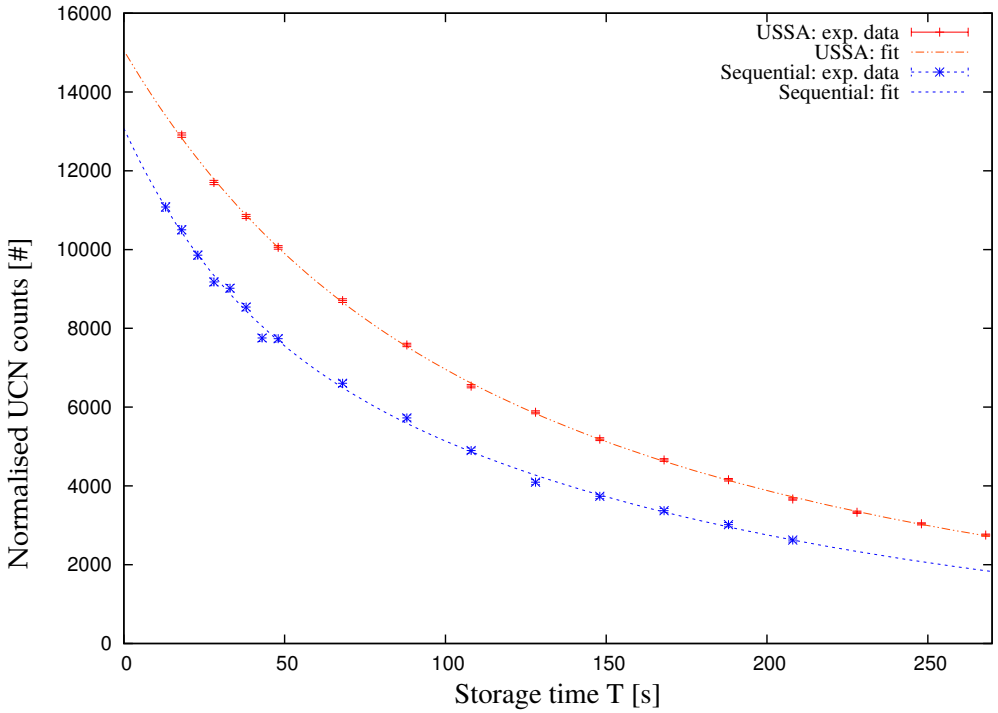

Figure 5.19: Number of detected UCNs as a function of the storage time inside the precession chamber. Dash lines correspond to USSA and sequential system data fits using (5.15).

As visible in Fig. 5.18, the UCN polarisation measured with the USSA is larger than the one with the sequential analyser by about 5% for $T = 180$ s. Besides, the number of detected UCNs is also larger using the USSA by 13%, as shown in Fig. 5.19. The statistical improvement coming from the USSA with respect to the sequential system is estimated through the variable $\mathcal{A}\sqrt{N}$ and amounts for $11.6 \pm 3.7\%$.

5.3.3 Detected UCNs fraction after reflection in the other arm

In order to measure the probability for UCN to be reflected from one arm and then detected in the other arm, the configurations of the Fig. 5.20 have been used.

For both configurations, N_0 unpolarised UCNs fall down on the USSA after 50 s of storage time. The only difference between the two configurations is the presence of a single analysing foil located

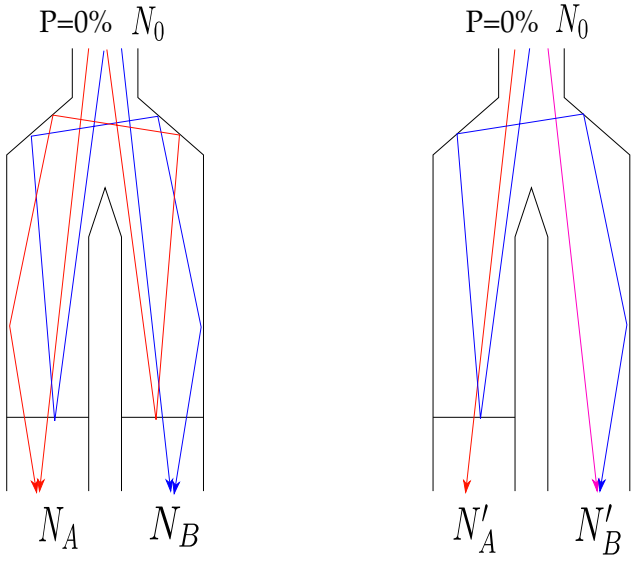

Figure 5.20: USSA configurations used to determine the reflection probability from the wrong spin detection arm to the right one. In one case, the two analysing foils are installed. In the other case, one foil is removed.

in one of the two USSA arms. With two foils, the number of detected neutrons is the same in both arms:

$$N_A = N_B = \frac{N_0}{4}\left(1 - \varepsilon_{\text{abs}}\right)\left(1 + \text{p}_{\text{ref}}\right) \tag{5.20}$$

where ε_{abs} and p_{ref} have been already defined in 5.2.3.3.

With a single foil, less UCNs are detected in the arm A because they are not reflected from the arm B. Thus, numbers of detected UCNs in arms A and B in that case are:

$$\begin{cases} N'_A = \frac{N_0}{4}\left(1 - \varepsilon_{\text{abs}}\right) \\ N'_B = \frac{N_0}{2}\left(1 + \frac{\text{p}_{\text{ref}}}{2}\right) \end{cases} \tag{5.21}$$

Using Eq (5.20) and (5.21) the reflection probability p_{ref} and the UCN absorption fraction ε_{abs} are finally determined:

$$\begin{cases} \text{p}_{\text{ref}} = \frac{N_A}{N'_A} - 1 = 52.8 \pm 2.8\% \\ \varepsilon_{\text{abs}} = 1 - \frac{N'_A}{N'_B}\left(2 + \text{p}_{\text{ref}}\right) = 5.8 \pm 1.5\% \end{cases} \tag{5.22}$$

The UCN fraction absorbed in the aluminium foil substrate is twice larger than the one measured on the West-2 beam line (2.7±1.3%). It might be due to the UCN energy spectrum difference between the two setups. Indeed, UCNs are more energetic on the West-2 beam line. As the absorption cross section varies proportionally to $1/v_{\text{n}}$, the proportion of absorbed UCNs in the aluminium is larger.

The second point is that the fraction of reflected UCNs from one arm to the other (52%) is larger on the EDM line than on West-2 (about 34%). This may be explained by the fact that a part of reflected UCNs on West-2 can be lost afterwards, as the West-2 beam line is open towards the UCN tank. On the contrary, during the emptying below the nEDM spectrometer, UCNs can be stored between the chamber and the USSA. Thus, UCNs can go upwards to the chamber and fall back into the USSA where they may be detected.

5.3.4 EDM run type comparison

The last comparison between the USSA and the sequential system has been performed for usual nEDM runs. The Ramsey central fringe fitting using normalised $N^{\uparrow}$ and $N^{\downarrow}$ is shown in Fig. 5.21. The normalisation is performed with the number of UCNs recorded in the monitoring position. The average number of UCN counts is almost symmetric and both visibilities $\alpha^{\uparrow}$ and $\alpha^{\downarrow}$ are consistent. This shows that both spin states are symmetrically treated in the USSA.

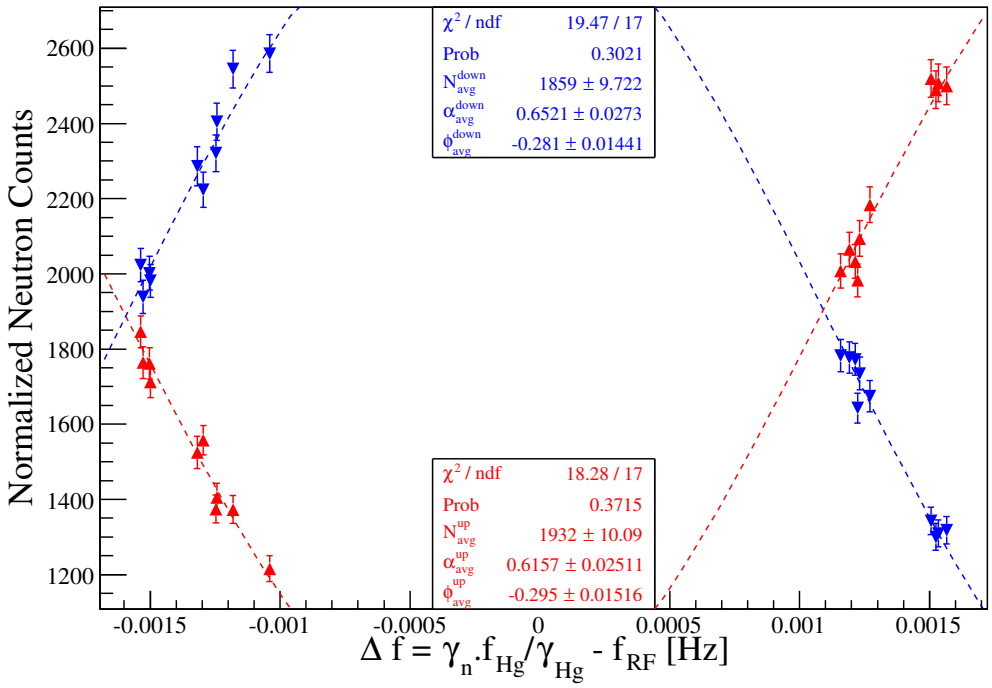

Figure 5.21: First Ramsey pattern taken with the USSA (in B_0 up configuration).

	α [%]	N_{tot}	$N_{\text{West-1}}$
USSA	63.4(18)	3791(14)	1.878(5) $\times 10^6$
Sequential	59.7(22)	2692(15)	1.651(16) $\times 10^6$
Ratio	1.062(49)	1.239(10)	

Table 5.4: Visibility α and total number of detected UCNs measured with the USSA and the sequential analyser for EDM runs. $N_{\text{West-1}}$ is the number of detected UCNs on the West-1 beam line. The UCN ratio is calculated with the number of detected UCNs normalised with $N_{\text{West-1}}$.

The comparison between the USSA and the sequential system is summarised in Tab. 5.4. With the USSA, both the visibility and the number of detected UCNs are larger than with the sequential system. This is consistent with results coming from T_1 measurements. However, the statistical error on the visibility is large, because of the rather low number of cycles (20). The improvement of the EDM sensitivity is estimated through the variable $\alpha\sqrt{N}$ and amounts for $18.2 \pm 6.1\%$. The largest contribution on this improvement is coming from the larger number of detected UCNs.

5.3.5 Conclusions

In direct mode, the USSA analysing power is smaller than the analysing power of the sequential system by about 6.5%. This may be explained by the lower height of USSA analysing foils with respect to the sequential system analysing foils (25 cm lower). However, in case UCNs are stored, the USSA spin analysis efficiency is not decreased for storage times larger than 150 s, due to the UCN spectrum softening in the precession chamber. For measurements carried out with such storage times and UCN energy conditions, the USSA asymmetry is larger than the sequential one by 2-3%.

From nEDM runs, the visibility and the UCN counts are respectively increased by $6.2 \pm 4.9\%$ and by $23.9 \pm 1.0\%$ with the USSA. This leads to an improvement of the nEDM statistical sensitivity of $18.2 \pm 6.1\%$ with respect to the sequential analysis. In addition, the spin treatment is almost symmetric. During preliminary measurements performed at ILL, the NANOSC detection efficiencies have been measured to be different by $1.1 \pm 0.4\%$ and the arms transmissions by $0.5 \pm 1.5\%$. On the West-2 beam line, the asymmetry for unpolarised UCNs has been measured to 0.4% in transmission (without analysing foils). When USSA foils are added, no change is measured. In addition, their analysing powers are of the order of 90% and are equal. Spin-flippers efficiencies have also been measured and are equal (97%), without influencing the non-active arm. Since the USSA has shown better performances than the sequential system, with a spin treatment almost symmetric, it is now part of the nEDM apparatus.

Finally, the USSA design with GEANT4-UCN and its building have succeeded in the production of a new simultaneous spin analyser, able to symmetrically treat the two spin components and also to increase the UCN statistics.

In order to further improve the UCN statistics, the NiMo coating ($V_F = 220$ neV) could be replaced by diamond or ^{58}NiMo coatings which have a theoretical Fermi potential around 300 neV. The Fermi potential of a diamond coating over a quartz substrate has been measured by means of cold neutron reflectometry on the NARZISS [5] instrument at PSI to be about 305 neV and loss per bounce measurements are planned to be studied on the West-1 beam line. But the first USSA upgrade will be performed with ^{58}NiMo. The coating will be performed either at PSI on the sputtering device or at LPC with the evaporator. Tests are planned for Autumn 2014 or in 2015.

[5] Test instrument for neutron optical devices.

Chapter 6

nEDM data analysis

Contents

In the nEDM collaboration, two groups independently analyse the nEDM data: the French group (LPC, LPSC and CSNSM) and the PSI group. This chapter presents the analysis performed by the French team with the 2013 PSI data. The basics of the neutron Electric Dipole Moment measurement has been already described in 2.2.1. A previous analysis, performed by the PSI team on 2012 data is presented in [56].

The 2013 data set was collected in August. Even if only 13 runs have been recorded, some of them are particularly long (three days for the longest one) and the key parameters for a low nEDM sensitivity were rather good. The precession time was set to 180 s with an applied electric field of 10 kV/cm in average. With such a storage time, the final visibility was close to 60% and the number of mean detected UCNs per cycle was 6650. Using Eq (2.17), the expected nEDM sensitivity per cycle should be close to 4×10^{-24} e.cm. In total, about 2900 cycles have been recorded during this month, leading to an expected integrated sensitivity of about 8×10^{-26} e.cm for the 2013 data set.

The first part explains how the neutron frequency is recovered with either neutron counts or with the asymmetry. Furthermore, a study of the raw data selection before the main analysis is performed. Then, the effect of different methods to estimate the Hg precession frequency is studied. Then, a study of the neutron frequency extraction procedure is presented, using either experimental data or simulated one. Finally, results of the 2013 nEDM data campaign will be presented, summarising the systematic errors budget and the current nEDM sensitivity of the experiment.

6.1 The neutron frequency extraction

The neutron Larmor frequency is measured via the Ramsey separated oscillating fields method. The principle of the extraction – as it was performed in the previous stage of the nEDM experiment [101] – is described in section Sec. 2.2 and in the following section. An alternative method is described in section 6.1.3.

6.1.1 Cycle definition

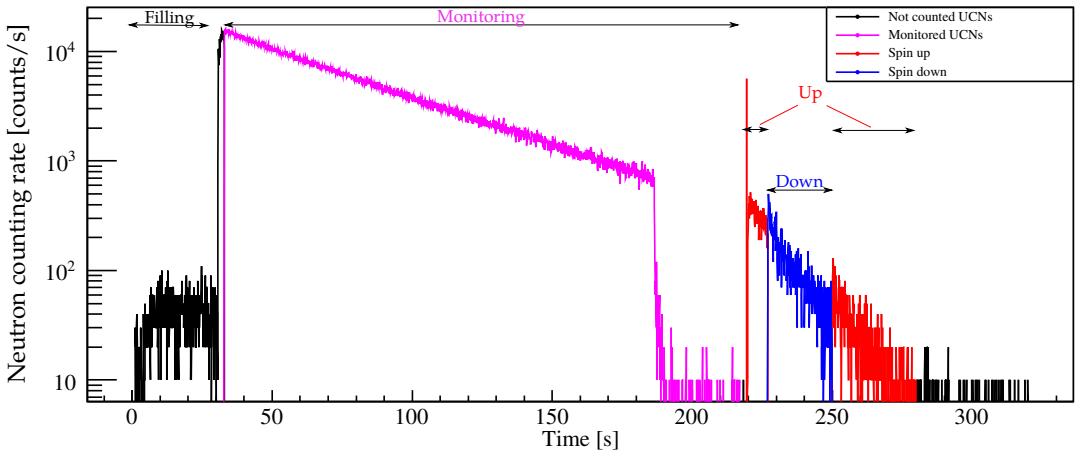

Figure 6.1: Neutron counting rate as a function of the detection time. Colours indicate different periods of detection given by the main acquisition: monitor (mauve), spin up (red) and spin down neutrons (blue). The peak visible before the first spin up detection period ($t \simeq 220$ s) does not correspond to physical events.

A measurement of the neutron Larmor frequency is performed every cycle. A cycle lasts 6 min and defines the following sequence, as illustrated in Fig. 6.1.

First, the precession chamber is filled for about 30 s. Then, the switch moves to the monitoring position and the remaining UCNs located in guides and the UCN tank are directly going to the UCN detector. This number of neutron counts is used to normalise the number of detected UCNs at the end of each cycle. In the mean time, UCNs are stored during 180 s and the Ramsey method is applied. Finally, the UCN shutter is open and UCNs directly fall downwards to the detector. During this period, UCNs are sequentially detected.

During a typical run, about 100 - 200 cycles are collected, with regular electric field polarity changes, according to the following pattern: -0++0–0+... with 12 cycles for both positive and negative polarities and only 6 cycles without electric field.

6.1.2 Principle

During nEDM measurements, one works around the resonance where the Ramsey curve can be approximated by a cosine curve. It has been shown that the relative error on the neutron frequency f_n done using this approximation is negligible [102]. Thus, the approximated number of counted neutrons $N^\uparrow$ and $N^\downarrow$ can be written as:

$$N^{\uparrow\downarrow} \simeq N_a^{\uparrow\downarrow}\left[1 \mp \alpha_a^{\uparrow\downarrow}\cos\left(\pi\frac{\Delta f}{\Delta\nu} - \phi_a^{\uparrow\downarrow}\right)\right] \tag{6.1}$$

where $\Delta\nu = \frac{1}{2(T+4\tau_\mathrm{RF}/\pi)}$ is the width of the Ramsey central fringe, T the precession time and τ_RF the neutron RF pulses duration. The neutron frequency extraction procedure uses the Hg co-magnetometer frequency f_Hg in order to compensate for the magnetic field variations along the run. This normalisation is performed via the variable $\Delta f = f_0 - f_{RF} = \frac{\gamma_\mathrm{n}}{\gamma_\mathrm{Hg}} f_\mathrm{Hg} - f_\mathrm{RF}$ with f_RF the applied neutron RF pulse frequency. The fit is performed with four working points surrounding the resonance, as shown in Fig. 6.2. The RF frequency of those working points is calculated via the previous cycle Hg frequency:

$$f_\mathrm{RF}^i = \frac{\gamma_\mathrm{n}}{\gamma_\mathrm{Hg}} f_\mathrm{Hg}^{i-1} \pm \frac{\Delta\nu}{2}\,(1 \pm 0.1) \tag{6.2}$$

where superscript ^{i} refers to the cycle number.

Using Eq (6.1), the number of spin up and spin down neutrons is fitted as a function of Δf for several cycles from the same run (for a given electric field polarity). The following parameters: $N_a^{\uparrow\downarrow}$, $\alpha_a^{\uparrow\downarrow}$ and $\phi_a^{\uparrow\downarrow}$ are extracted (where subscript $_a$ stands for average), where $\phi_a = \pi\frac{\langle f_0 - f_n\rangle}{\Delta\nu}$ and $N_a^{\uparrow\downarrow}$ is the average UCN number at fringe half width for spin up and spin down neutrons. $\alpha_a^{\uparrow\downarrow}$ is the average visibility for each spin state over the whole data used for the fit.

The neutron Larmor frequency is derived from Eq (6.1) and is given by:

$$f_\mathrm{n} = f_\mathrm{RF} + \frac{\Delta\nu}{\pi}\arccos\left(\frac{N^{\uparrow\downarrow} - N_a^{\uparrow\downarrow}}{\mp\alpha_a^{\uparrow\downarrow} N_a^{\uparrow\downarrow}}\right) \tag{6.3}$$

Two neutron Larmor frequencies are extracted using the number of spin up UCNs and the number of spin down UCNs. It is also possible to get the average value of f_n directly from the phase $\phi_a^{\uparrow\downarrow}$ but

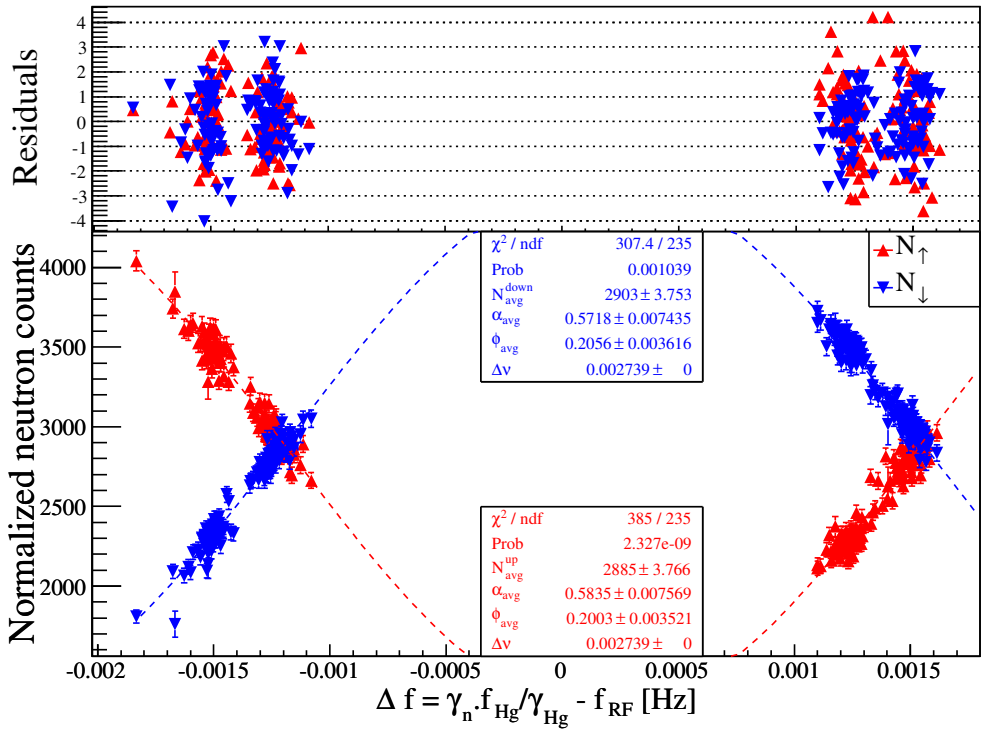

Figure 6.2: Illustration of the neutron Larmor frequency fit.

the determination of the neutron resonance frequency for each cycle allows some useful analysis cross-checks.

In order to avoid non statistical fluctuations due to the UCN source, the monitor count N_{mon} (currently done during the storage time) is used to normalise spin up and spin down neutron counts:

$$N^{\uparrow/\downarrow}_{\text{norm}} = N^{\uparrow/\downarrow} \frac{\langle N_{\text{mon}} \rangle}{N_{\text{mon}}} \tag{6.4}$$

6.1.3 Alternative method

A new technique to extract the UCNs Larmor frequency is to fit the asymmetry $\mathcal{A} = \frac{N^{\uparrow} - N^{\downarrow}}{N^{\uparrow} + N^{\downarrow}}$ instead of the number of UCN counts $N^{\uparrow}$ and $N^{\downarrow}$. The asymmetry is by definition normalised and therefore does not require any normalisation from the monitoring.

For a perfectly symmetric UCN counting, the asymmetry expression is:

$$\mathcal{A} = \alpha_a \cos\left(\pi \frac{\Delta f}{\Delta \nu} - \phi_a\right) \tag{6.5}$$

However, if the mean number of detected UCNs and/or the visibility are different for the two spin components, two additional terms A_a and δ appear. This difference can come from a bad setting of the counting sequence with the sequential analysis. If the USSA is used (see Chap 5), then this difference can directly arise from different detection efficiencies of the two NANOSC detectors. An other contribution to δ can come from different visibilities for each spin state. Such a difference can be induced by different UCN depolarisations due to the storage of one spin component above the analyser during the sequential analysis.

If one writes:

$$\begin{cases} N_a^{\uparrow} = N_a + D & \alpha_a^{\uparrow} = \alpha_a + d \\ N_a^{\downarrow} = N_a - D & \alpha_a^{\downarrow} = \alpha_a - d \end{cases} \quad \text{with } D \ll N_a \text{ and } d \ll \alpha_a \tag{6.6}$$

then, at first order in D and d, one gets:

$$\mathcal{A} \simeq \frac{D}{N_a} - \alpha_a \cos\phi - \left(\frac{\alpha_a^2 D}{N_a} + d\alpha_a\right)\cos^2\phi \tag{6.7}$$

$$\mathcal{A} \simeq A_a - \alpha_a \cos\phi + \delta\cos^2\phi \qquad \text{with } \phi = \pi\frac{\Delta f}{\Delta\nu} - \phi_a = \pi\frac{f_{\mathrm{RF}} - f_{\mathrm{n}}}{\Delta\nu} \tag{6.8}$$

As the working points are set such as $f_{\mathrm{RF}} \simeq f_{\mathrm{n}} \pm \frac{\Delta\nu}{2}$, $\phi \simeq \pm\frac{\pi}{2}$. Hence, the derivative of the term $\delta\cos^2\phi \simeq -\delta \sin\frac{\pi}{2}\cos\frac{\pi}{2}$ is close to 0 and this term does not vary significantly with respect to the term $\alpha_a\cos\phi$. As a result, the δ term is expected to play a minor role in the neutron frequency fit if deviations D and d are not too large. In a first step, this term can be neglected during the fitting procedure. It will be shown later that it does not lead to a significant error on the estimated neutron Larmor frequency (see 6.7.7).

Using the same procedure as described in 6.1.2, $\mathcal{A}_a$, α_a, δ and ϕ_a are recovered by fitting the asymmetry curve. An example of the asymmetry fitting is shown in Fig. 6.3 on a full run (for the positive electric field polarity). Here, fitted terms A_a and δ using the asymmetry are consistent with expectations.

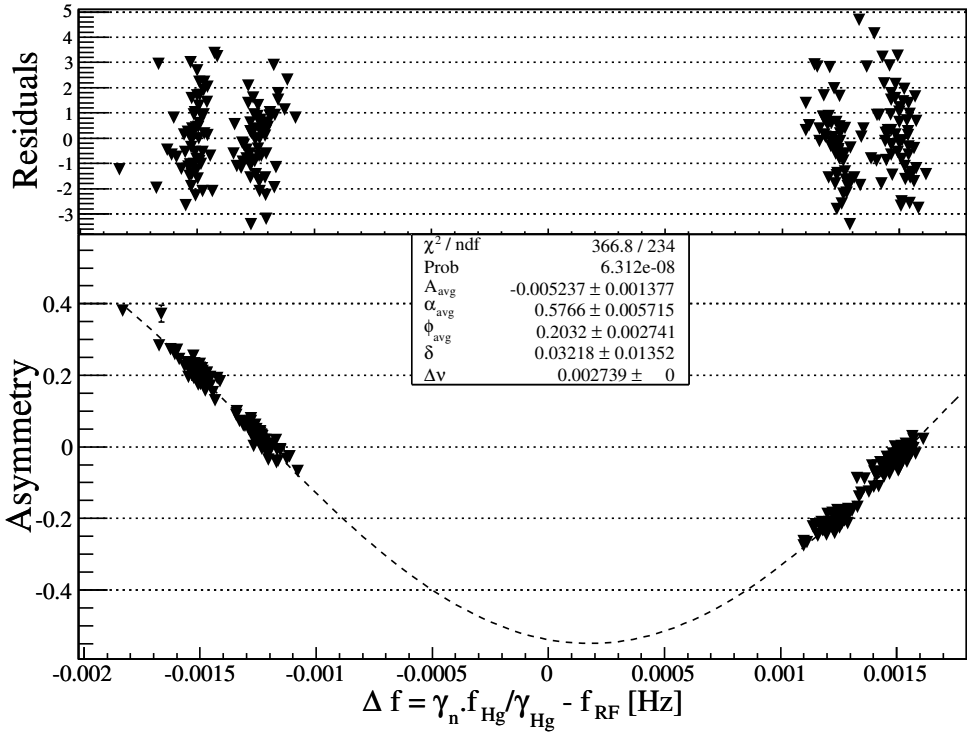

Figure 6.3: Asymmetry fitting procedure used to extract the neutron Larmor frequency. In order to compensate for magnetic field variations, the $\pi/2$ pulse frequency is normalised by the mercury frequency.

In the case of the asymmetry fitting (without the δ term), the neutron frequency is then given by:

$$\begin{cases} f_{\mathrm{n}} = f_{\mathrm{RF}} + \frac{\Delta\nu}{\pi} \arccos\left(\frac{\mathcal{A}_a - \mathcal{A}}{\alpha_a}\right) \\ \sigma_{f_{\mathrm{n}}} = f_{\mathrm{RF}} + \frac{\Delta\nu}{\pi(\mathcal{A}_a - \mathcal{A})^2} \sqrt{\sigma^2_{\mathcal{A}_a} + \sigma^2_{\mathcal{A}} + \sigma^2_{\alpha_a} \frac{(\mathcal{A}_a - \mathcal{A})^2}{\alpha_a^2}} \end{cases} \tag{6.9}$$

It will be shown in Sec. 6.7 that with perfect simulated data, both the UCN counts fit and the asymmetry give the same results. However, with real data, the asymmetry is more robust than the UCN counts fit, as shown in section 6.2.2.

6.2 Raw data selection

After data collection, the data set is pre-processed in order to keep the relevant runs or cycles used to extract the nEDM. The number of detected spin up and spin down UCNs and the Hg measured frequency are essential for the neutron frequency extraction and need to be re-estimated offline. At the same time, the data pre-processing allows one to put some "flags" in order to have milestones during the data analysis. For instance, these flags can be used for possible cuts on the data.

6.2.1 Offline analysis of the detected UCN number

As said in 3.5.1, recorded FASTER events are time stamped. Fig. 6.1 shows the number of detected UCNs as a function of the time during a cycle. Four periods can be seen: the filling, the monitoring, the spin up and spin down counting.

The UCN time spectrum in Fig. 6.1 shows an abnormal peak at the beginning of the precession chamber emptying. Such spikes have been observed for about 1% of the total number of cycles in the 2012 and 2013 nEDM data. They systematically occur 0.5 s after the UCN shutter opening and correspond to 100 to 500 events detected during 100 µs, contributing to 5-20% of the spin up neutron counts. The time structure of the QDC distribution shows a first event that occur during 50 ns on the 9 NANOSC channels, followed by an exponential decay of the QDC after 10 to 15 µs [103]. The charge of such spike events is located just above the threshold used to discriminate neutrons and background. The spikes are detected through their high counting rate and their timing location and the corresponding cycles are rejected. However, it should be possible to take them into account by subtracting the fake neutron events. Further investigations are ongoing to find out the source of such events. It has to be noted that the highest spikes (in intensity) are correlated to the negative electric field polarity and to the UCN shutter opening.

6.2.2 Other cuts

Further data selections (cuts) have been applied before extracting the neutron Larmor frequency. The cut listing is described hereafter.

Cycles for which the guiding system (valves, switch) did not work properly or the UCN source failed usually correspond to cycles with a low amount of UCNs. As a result, cycles with less than 100 detected neutrons are disregarded. It is important to note that from times to times, the switch box did not properly work and was not in its nominal position. As a result, neutrons counts are still above 100 and pass the cut. These cycles are not excluded yet and therefore, can contribute to decrease the fit quality.

Cycles with sudden magnetic field variations have also been rejected. An arbitrary threshold of 6.6 pT (jump of 50 µHz on f_{Hg}) between the current cycle and the previous one is defined for such

a purpose. Indeed, a sudden variation of the field during a cycle can not be properly compensated by the mercury co-magnetometer.

6.2.3 Cuts effects on the χ^2 of the Ramsey central fringe fit

The effect of the cuts in the neutron frequency measurement is investigated through the reduced χ^2 resulting from the central Ramsey fringe fit (with function (6.8)), noted $\tilde{\chi}^2$. Results are shown in Fig. 6.4 for 2013 EDM runs. In that case, the Hg frequency estimated with the signal-to-noise threshold method (threshold of 50) has been used to extract the neutron frequency (see Sec. 6.3). Furthermore, the full data set for each electric field polarity has been fitted using the asymmetry (and not using normalised neutron counts).

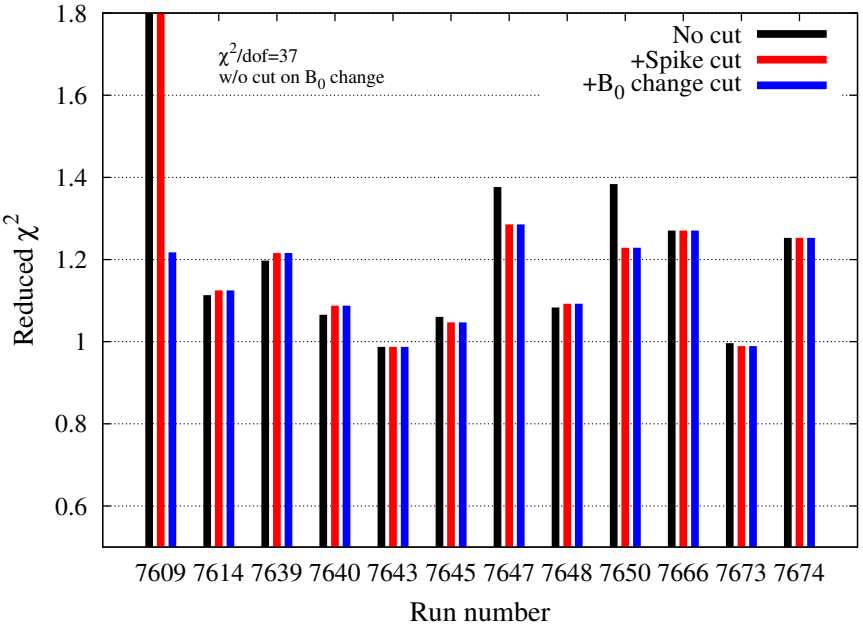

Figure 6.4: Reduced χ^2 of the neutron Larmor frequency fit averaged over all electric field polarities for different applied cuts.

For most of the runs, the cut effect on $\tilde{\chi}^2$ is negligible. However, for particular runs (7609, 7647, 7650), the effect is very important, lowering $\tilde{\chi}^2$ towards 1. The effect of each cut on the $\tilde{\chi}^2$ is summarised in Tab. 6.1 for each electric field polarity. Results are averaged over 2013 runs (even if the number of degrees of freedom is not the same).

The main improvement on the $\tilde{\chi}^2$ comes from the cut on sudden magnetic field changes, observed in a single run (7609). The cut on the neutron spikes visible in FASTER data is observed for the negative electric field polarity for few runs (runs 7647 and 7650). This behaviour is expected as spikes containing the largest amount of neutron like events mainly occur for the negative electric field polarity. It has to be noticed that both cuts on huge spikes and on sudden magnetic field changes are correlated to the negative electric field polarity, perhaps indicating a problem linked to sparks.

Field polarity	$E < 0$	$E = 0$	$E > 0$
Applied cut	$\langle\tilde{\chi}^2\rangle$ - Rem. cyc.	$\langle\tilde{\chi}^2\rangle$ - Rem. cyc.	$\langle\tilde{\chi}^2\rangle$ - Rem. Cyc.
None	4.22 - 0	1.12 - 0	1.19 - 0
Low counts	4.22 - 0	1.11 - 2	1.19 - 13
Spike	4.18 - 17	1.11 - 2	1.19 - 23
Spike+B_0 change	1.16 - 26	1.11 - 2	1.19 - 23

Table 6.1: Summary of Ramsey fringe fit $\tilde{\chi}^2$ obtained for different cuts and electric field polarities. The number of removed cycles (Rem. cyc.) associated to the applied cuts is also shown.

The reduced χ^2 of the neutron frequency fit using all cuts (1.8% of removed cycles) is in average $\tilde{\chi}^2 \simeq 1.15$, which is not consistent with the expected value of 1. No cut has been set neither on leakage currents (which should help in case of sparks), nor on the UCN switch mismatching positions. As a result, a possible contribution can arise from there.

Finally, the $\tilde{\chi}^2$ of the neutron frequency fit obtained with normalised neutron counts was about twice as large as using the asymmetry, suggesting a problem of normalisation. As a result, it has been chosen to only use the asymmetry for the analysis.

6.3 Hg frequency extraction

The study of the Hg frequency extraction procedure is carried out at LPSC [104] in the French analysis team and also in the Cracow group. The Hg frequency is used to compensate for magnetic field fluctuations along cycles. The Hg precession frequency, averaging the magnetic field in the precession chamber, is measured using the so-called two windows method, first introduced by the RAL-Sussex-ILL collaboration [82]. After applying a $\pi/2$ pulse to flip the Hg atoms spin in the transverse plane (orthogonal to the main B_0 field), the phase of the free induction signal is extracted at the beginning and the end of the precession time, as shown in Fig. 6.5. The Hg frequency is then calculated from the phase difference between the beginning and the end of the cycle and the number of zero crossings [105].

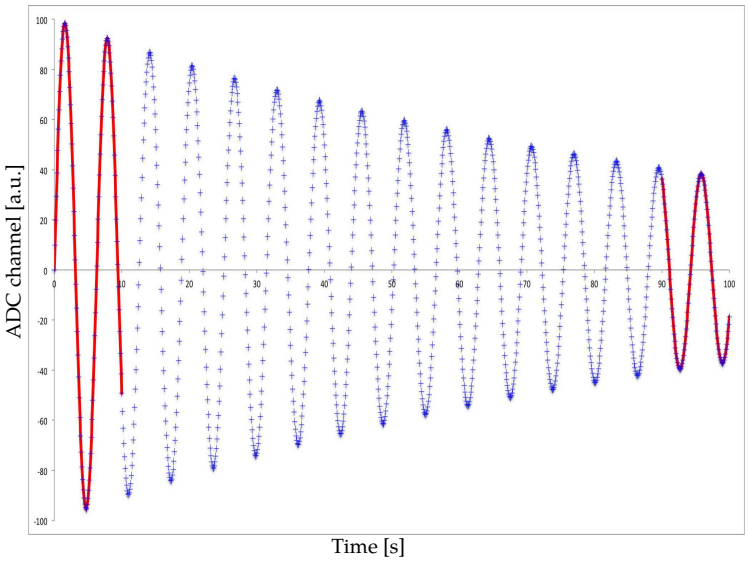

Figure 6.5: Illustration of the two windows method used by the RAL-Sussex-ILL collaboration to extract the Hg Larmor precession frequency.

The typical statistical precision of the Hg co-magnetometer on the magnetic field measurement was about 300 to 400 fT during the 2013 nEDM data taking. This is due to the low Hg transverse depolarisation time ($T_2 \sim 45$ s). With T_2 above 90-100 s (good Hg running conditions), the magnetic field precision is rather around 50-100 fT.

The data analysis presented in this section is based on an estimation of the mercury frequency using a revisited two windows method [1]. Indeed, because of the low T_2 time, the signal-to-noise ratio of the last window (using the usual method) is too low to accurately measure the Hg frequency. A solution to avoid this problem is to average the Hg frequency only during a period with a signal-to-noise ratio above a given threshold. Of course, the method suffers of a major drawback: the B field is not monitored during the entire cycle. Nevertheless, the Hg frequency extracted from the newly developed method allows magnetic field variations to be properly normalised, as illustrated by the neutron frequency normalisation using the Hg co-magnetometer shown in Fig. 6.6.

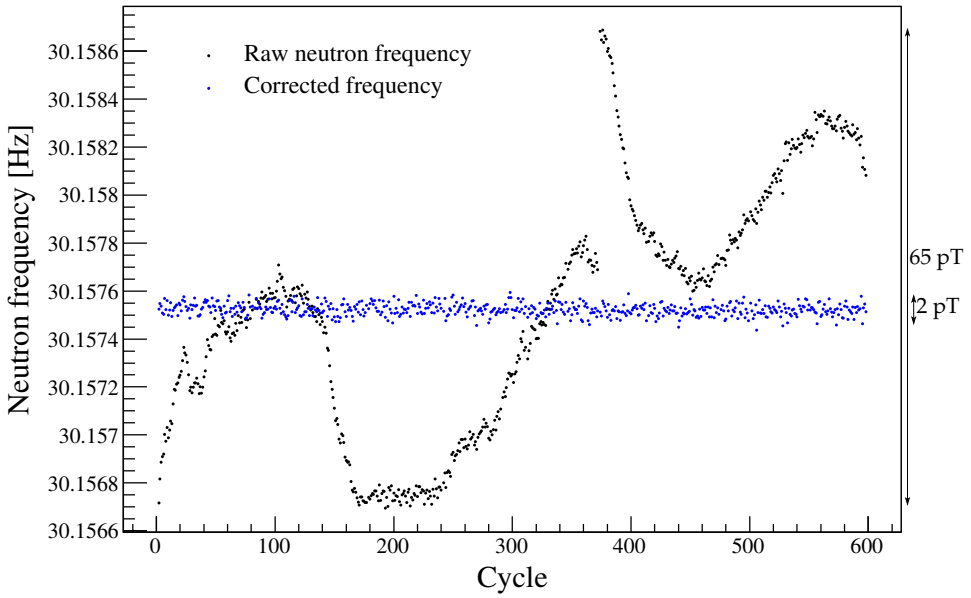

Figure 6.6: Illustration of the correction of magnetic field drifts using the Hg normalisation on the neutron resonant frequency over a 60 h long run. Error bars, of the order of 22 µHz ($\sim$ 800 fT) for this data set, are omitted for clarity.

Another method is also under development. It consists in fitting the full signal along the neutron precession. The fitting function is [107]:

$$A(t) = A_0 e^{-t/T_2} \sin\left(\frac{f_{\mathrm{Hg}}}{2\pi} t + \phi\right) \tag{6.10}$$

The two methods have been compared to the former two windows method through the neutron fit procedure in the section 6.3.1 .

[1] A similar method was already used and cited in [106].

6.3.1 Effect of the Hg frequency estimator on the neutron frequency fit

In this part, the quality of the Ramsey central fringe fit is studied as a function of the method used to extract the Hg frequency. The precision on the Hg frequency has been multiplied by the factor 6 which takes into account the use of the Hg signal bandpass filters [108]. Again, the $\tilde{\chi}^2$ parameter is used to qualify the appropriateness of the fit. In Fig. 6.7, it is shown for all runs, including the cuts defined in Sec. 6.2.

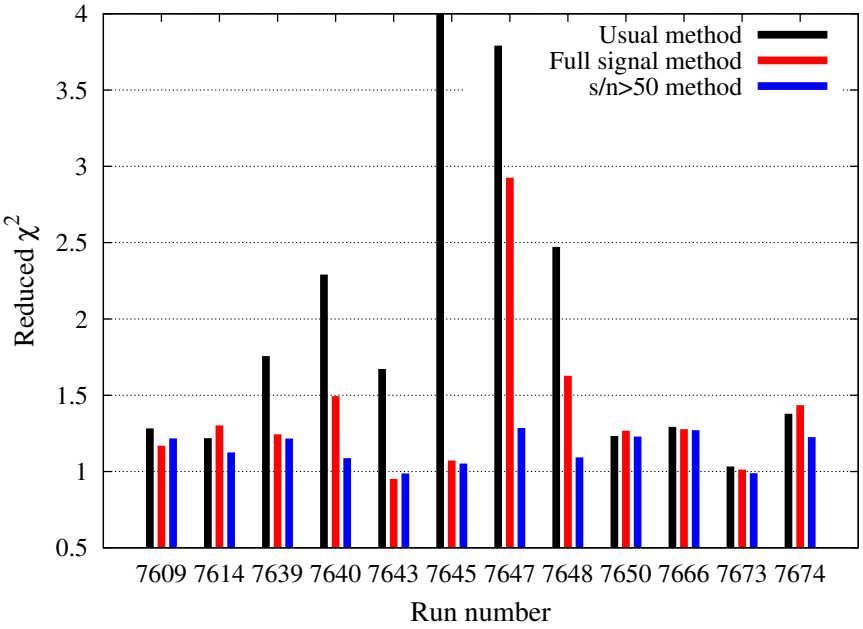

Figure 6.7: Reduced χ^2 of the neutron Larmor frequency fit averaged over all electric field polarities using different Hg frequencies (according to the method used to extract the Hg frequency). Here, the usual method is the method used by the RAL-Sussex-ILL collaboration to extract the Hg frequency. The $\tilde{\chi}^2$ for the run 7645 with the usual method of about 10 is not shown in this figure.

The new Hg frequencies determination techniques (*s/n* method and full signal fitting (*FSF*) method) clearly improve the neutron frequency fit quality for about half of the 2013 runs. The *s/n* method works better than the *FSF* one. Tab. 6.2 summarises the mean values of the neutron frequency fit reduced χ^2 obtained for each electric field polarity.

Method to extract f_{Hg}	$\langle\tilde{\chi}^2\rangle_{E<0}$	$\langle\tilde{\chi}^2\rangle_{E=0}$	$\langle\tilde{\chi}^2\rangle_{E>0}$
Usual two windows	2.02	1.45	3.94
Signal-to-noise>50 (*s/n*)	1.16	1.11	1.19
Full signal fit (*FSF*)	1.50	1.18	1.52

Table 6.2: Mean reduced χ^2 of the Ramsey central fringe fit obtained for the three Hg frequency extracting methods and electric field polarities.

The Hg transverse relaxation time is decreased after each electric field polarity reversal, the signal-to-noise ratio of the Hg signal tail is lower. This results in a lower accuracy and precision

of the Hg frequency with the RAL-Sussex method (right after each polarity reversal). As a result, the magnetic field normalisation performed for the neutron Larmor frequency fit is worse. This is visible in Tab. 6.2, where the $\tilde{\chi}^2$ is less improved when $E = 0$ than in other cases.

For about 60% of runs, the *FSF* method and the *s/n* method give similar results. For the remaining 40%, the $\tilde{\chi}^2$ from *FSF* are in between the RAL-Sussex method and the *s/n* method. A possible interpretation is that the *FSF* method is not able to properly extract the Hg frequency when large magnetic field drifts arise along cycles.

As far as is concerned the precision, it should also be noticed that the precision on the Hg frequency obtained with the *FSF* method is about 3 µHz larger than the *s/n* one.

Finally, the most suited method to extract the Hg frequency in 2013 nEDM runs is the *s/n* method. The *FSF* method needs more investigation and the RAL-SUssex method is not well suited to the Hg running conditions of the 2013 nEDM data. As a result, the *s/n* method is used for the nEDM analysis presented later in this work.

The reduced χ^2 problem is still not solved. But a hint to explain this point comes from the study of the vertical gradient evolution as a function of time along EDM runs. This is the subject of the next section.

6.4 Effect of gradient variations on the neutron Larmor frequency fit

In the experiment, the main B_0 field is vertical. It is as uniform as possible but a vertical gradient remains over the chamber volume. Such a gradient plays an important role in the nEDM analysis through the ratio R of the neutron to mercury precession frequencies and false EDM induced by the geometric phase effect of the Hg.

The centre of mass of UCNs is slightly lower than the precession chamber centre by a distance Δh. This is not the case for the thermal Hg atoms. As a result, UCNs and mercury do not average the same magnetic field and their frequencies write (not taking into account the transverse component):

$$\begin{cases} f_{\mathrm{n}} = \frac{\gamma_{\mathrm{n}}}{2\pi}\left[B_0 \pm \langle \partial_z B_z \rangle \left(\frac{H_{\mathrm{Ch}}}{2} - \Delta h\right)\right] \\ f_{\mathrm{Hg}} = \frac{\gamma_{\mathrm{Hg}}}{2\pi}\left[B_0 \pm \langle \partial_z B_z \rangle \frac{H_{\mathrm{Ch}}}{2}\right] \end{cases} \tag{6.11}$$

where B_0 is the constant magnetic field at the bottom of the precession chamber and H_{Ch} is the height of the precession chamber. Here, it is assumed that the z dependence of the magnetic field is due to a vertical gradient: $\vec{B} = \vec{B_0} + \langle \partial_z B_z \rangle \vec{z}$. The $\pm$ sign depends on the gradient direction with respect to the magnetic field: it is positive for the B_0 up direction and negative for the down direction.

It results in a shift $\Delta f_{\partial_z B_z}$ between the neutron Larmor frequency f_{n} and the Hg frequency normalised by the ratio of gyromagnetic ratios $f_{\mathrm{Hg}}.\gamma_{\mathrm{n}}/\gamma_{\mathrm{Hg}}$. It amounts to:

$$\Delta f_{\partial_z B_z} = f_{\mathrm{n}} - \frac{\gamma_n}{\gamma_{Hg}} f_{\mathrm{Hg}} \simeq \mp \frac{\gamma_{\mathrm{n}}}{2\pi} \left(\Delta h \, \langle \partial_z B_z \rangle\right) \tag{6.12}$$

Δh has been estimated using the ratio $R = \frac{f_{\mathrm{n}}}{f_{\mathrm{Hg}}}$ during measurements without electric field. The R dependence on $\langle \partial_z B_z \rangle$ is:

$$R = \frac{f_{\mathrm{n}}}{f_{\mathrm{Hg}}} \simeq \frac{\gamma_{\mathrm{n}}}{\gamma_{\mathrm{Hg}}} \left[1 \mp \frac{\langle \partial_z B_z \rangle \, \Delta h}{B_0}\right] \tag{6.13}$$

The - and + signs corresponds respectively to B_0 up and B_0 down configurations. The vertical magnetic field gradient can be varied using two coils in anti-Helmholtz configuration (TTC and

BTC). This gradient is monitored using caesium magnetometers and Δh is estimated through the slope of the R versus gradient curves (so-called "R-curves"). In 2012, Δh has been measured at $\Delta h = 2.35 \pm 0.05\,\mathrm{mm}$ [109].

The dependence of the Ramsey fringe visibility on the gradient has also been measured. The best fit function found in [110] is:

$$\alpha = \alpha_0 \mathrm{e}^{-a|\langle \partial_z B_z \rangle|} \tag{6.14}$$

where α_0 is the visibility with no gradient and a the visibility decay parameter, estimated to be about $3.5 \times 10^{-3}\,(\mathrm{pT/cm})^{-1}$.

For such measurements, caesium magnetometers are essential to determine the vertical gradient. The method used to extract the gradient over the chamber volume - the harmonic Taylor fit - is studied in the Chap. 7. The caesium data is averaged over a cycle, excluding the first and the last 2 s at the beginning and the end of the precession because of the neutron $\pi/2$ pulse. The precision on the gradient amounts to about 1 pT/cm. An example of the extracted gradient as a function of time during a 2013 nEDM run is shown in Fig. 6.8. In this particular run, a general periodic trend is observed. It corresponds to a 2 pT/cm daily variation. Similar variations have been observed during other nEDM runs.

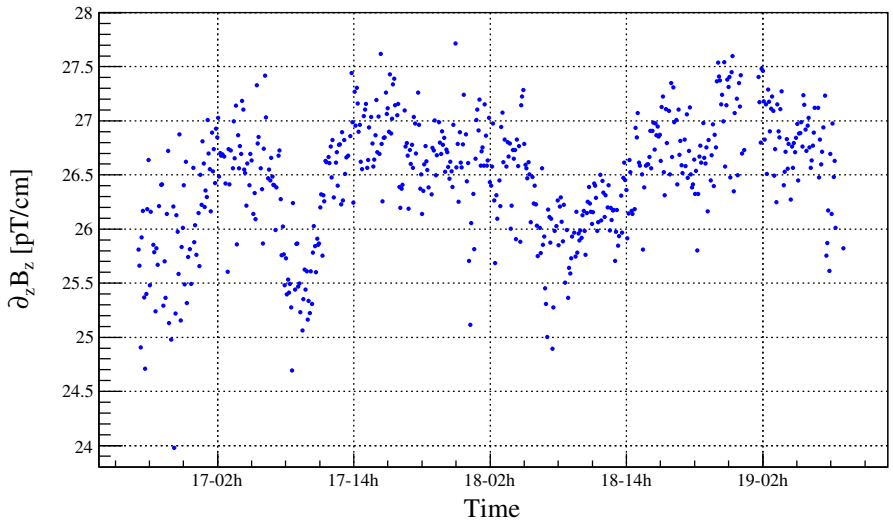

Figure 6.8: Average gradient over the precession volume as a function of time during a 60 h nEDM run (run 7650). It is determined using a set of 12 scalar magnetometers. For clarity, statistical error bars, at the pT/cm level, have been omitted.

Because of this magnetic field gradient variation, the visibility varies as well as the neutron Larmor frequency with respect to the mercury one. Since these two parameters change from one cycle to the other, the neutron fit is impacted by such gradient variations. This may explain the large measured reduced χ^2. The influence of gradient variations on the neutron Larmor frequency fit is investigated using a toy model in 6.7.6.1.

It has recently been shown that this gradient variations are correlated to 0.5° temperature daily variations of the experimental environment [111]. Thus, gradient variations could be avoided with a better thermal insulation and stabilisation of the thermohouse.

6.5 Study of the neutron Larmor frequency precision

Even if the neutron frequency fit is not perfect ($\tilde{\chi}^2 > 1.1$), the neutron frequency extraction method has been further checked, studying the neutron Larmor frequency statistical error given by the analysis. This study is done using a single run (n° 7650) which lasts 60 hours, representing the typical mean statistical precision obtained during the 2013 data taking. The study is based on the comparison between the spread of the quantity $f_\mathrm{n} - \frac{\gamma_\mathrm{n}}{\gamma_\mathrm{Hg}} f_\mathrm{Hg}$, which does not depend on the magnetic field (the gradient influence will be studied in 6.7.6.1), and its expected statistical spread.

First, the neutron Larmor frequency fit is performed with all cycles (with a reduced χ^2 of 1.23) and then the neutron frequency is calculated for each cycle using Eq (6.9). The $f_\mathrm{n} - \frac{\gamma_\mathrm{n}}{\gamma_\mathrm{Hg}} f_\mathrm{Hg}$ distribution is shown in Fig. 6.9.

The distribution RMS is equal to the standard deviation of the gaussian fit performed on the distribution (within errors). The statistical error of $f_\mathrm{n} - \frac{\gamma_\mathrm{n}}{\gamma_\mathrm{Hg}} f_\mathrm{Hg}$ is equal to 25.3 µHz.

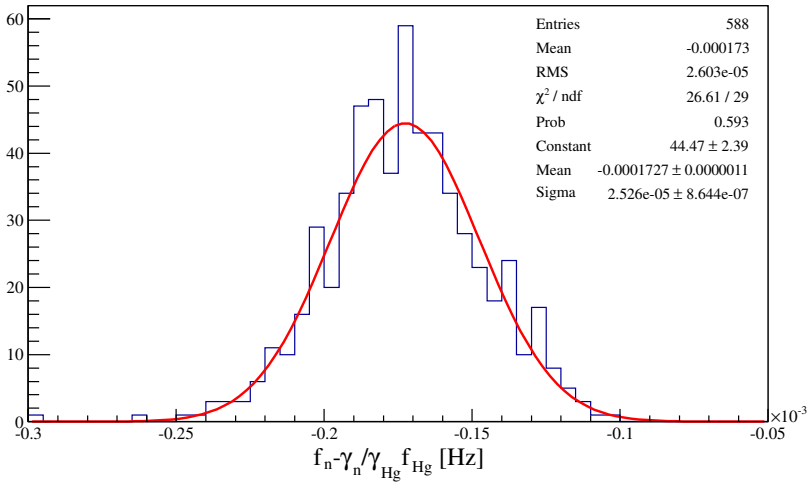

Figure 6.9: $f_\mathrm{n} - \frac{\gamma_\mathrm{n}}{\gamma_\mathrm{Hg}} f_\mathrm{Hg}$ distribution obtained in the run 7650. It is not centred on 0 because of the gravitational shift due to a magnetic field gradient (measured to about 27 pT/cm with CsM).

The expected neutron Larmor frequency precision per cycle is given by (see Eq (2.14)):

$$\sigma_{f_\mathrm{n}} \simeq \frac{1}{2T\alpha_a\sqrt{N_a^\mathrm{tot}}} \tag{6.15}$$

with a precession time $T = 180\,\mathrm{s}$, a visibility $\alpha_a = 59.2\%$ and a mean total number of detected UCNs $N_a^\mathrm{tot} = 5850$. The resulting precision on the neutron frequency is σ_{f_n} =19.3 µHz. The average precision of the mercury frequency $\langle \sigma_{f_{Hg}} \rangle \simeq 3.36\,\mu\mathrm{Hz}$ has to be propagated in order to get the total uncertainty on $f_\mathrm{n} - \frac{\gamma_\mathrm{n}}{\gamma_\mathrm{Hg}} f_\mathrm{Hg}$.

The total expected uncertainty (given by Eq (2.15)) on $f_\mathrm{n} - \frac{\gamma_\mathrm{n}}{\gamma_\mathrm{Hg}} f_\mathrm{Hg}$ amounts to 22.6 µHz. It has to be compared to the spread $25.3 \pm 0.9\,\mu\mathrm{Hz}$ of the distribution. The apparent disagreement between the two values can be solved considering that the neutron Larmor frequency fit is not perfect. Indeed, the re-scaling of the neutron frequency error by the square root of the reduced χ^2 brings the expected uncertainty on $f_\mathrm{n} - \frac{\gamma_\mathrm{n}}{\gamma_\mathrm{Hg}} f_\mathrm{Hg}$ up to 25.0 µHz, consistent with the spread of the distribution. As a result, the neutron frequency precision given by the analysis is validated.

Nevertheless, the poor precision of the Hg frequency is problematic. It contributes to about 15% of the $f_{\mathrm{n}} - \frac{\gamma_{\mathrm{n}}}{\gamma_{\mathrm{Hg}}} f_{\mathrm{Hg}}$ uncertainty while in good running conditions, it should contribute only for a few percent.

This error is also propagated to the nEDM precision. It is thus very important to identify all the possible errors leading to a bad neutron frequency fit.

6.6 R auto-correlation

The procedure used to determine the neutron frequency (Sec. 6.1) combines a set of cycles (in order to measure $\mathcal{A}$, α_a and ϕ_a) from which the neutron frequency is calculated for each cycle (Eq (6.9)). As a result, the measured neutron frequencies may be correlated. The study of the neutron frequency auto-correlation has been performed using the ratio $R = \frac{f_{\mathrm{n}}}{f_{\mathrm{Hg}}}$, chosen in order to cancel possible magnetic field variations (at first order). The R auto-correlation function $\mathcal{C}(\Delta i)$ is defined by:

$$\mathcal{C}(\Delta i) = \frac{\langle (R_j - \langle R \rangle)\,(R_{j+\Delta i} - \langle R \rangle) \rangle_j}{\sigma_R^2} \tag{6.16}$$

where $\mathcal{C}(\Delta i)$ is the auto-correlation between the cycle j and the cycle $(\Delta i + j)$. An auto-correlation close to 1/-1 implies a perfect correlation/anti-correlation between points while an auto-correlation close to 0 means that the points are not correlated. Fig. 6.10 shows the R auto-correlation averaged over all runs of the 2013 data set. This study shows that the neutron fitting method gives non correlated neutron frequencies. The R auto-correlation is calculated for each run and each polarity and then averaged for all the 2013 runs.

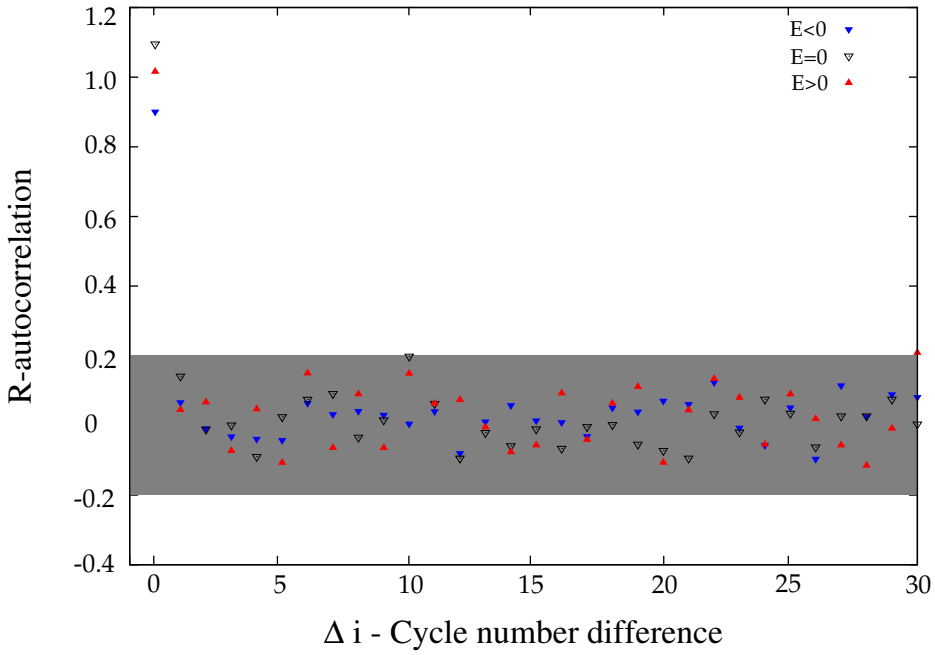

Figure 6.10: R auto-correlation averaged over all 2013 runs. The shaded region has been calculated with the toy model presented in the next section. It contains 95% of non-correlated events.

6.7 Study of the neutron Larmor frequency extraction with simulated data

In order to test the neutron Larmor frequency fitting procedure, simulated data have been produced and the analysis software has been applied. The goal is to deconvolute possible contributions of several effects on the fit in order to find out why large $\tilde{\chi}^2$ are observed in the experimental data. Additionally, this toy data can be used as a first level analysis tool to compare the results given by the two analysis teams of the nEDM collaboration. The next section explains how the simulated data are produced. Then, a study of the neutron frequency extraction routine is presented.

6.7.1 Data production

The data production method is rather simple: the number of UCNs is calculated for a given applied RF frequency f_{RF} for the $\pi/2$ pulse and neutron frequency f_{n} with:

$$N^{\uparrow\downarrow} = N_a^{\uparrow\downarrow}\left[1 \mp \alpha_a^{\uparrow\downarrow}\cos\left(\pi\frac{f_{\mathrm{RF}} - f_{\mathrm{n}}}{\Delta\nu}\right)\right] \tag{6.17}$$

The electric field direction is changed according to the same pattern as the experimental one: 12 cycles with $E > 0$, 6 cycles with $E = 0$ and 12 cycles with $E < 0$ like: +0–0++0–0++0– ... The duration of the electric field ramping is not included. For the following studies, 10^4 cycles per run are generated. Several running conditions have been investigated.

The fit of a typical toy data set is shown in Fig. 6.11.

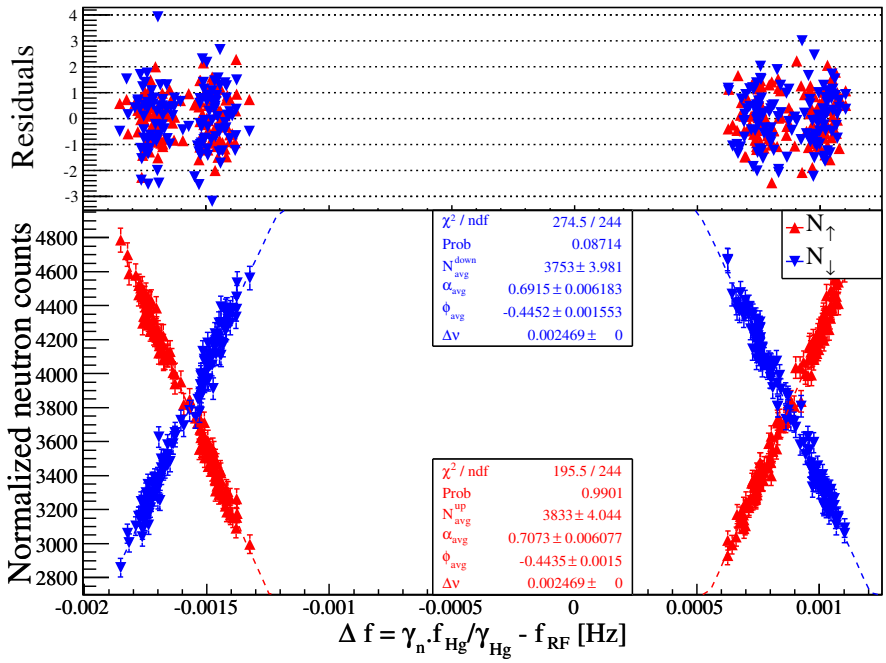

Figure 6.11: Example of data produced using the toy model, for asymmetric UCN counting conditions (2% asymmetry for both the number of spin up and down UCNs and the Ramsey fringe visibility). A varying gradient of 2 pT/cm has been added to the 20 pT/cm static magnetic field gradient.

6.7.2 Ideal conditions

The basic running conditions in the toy model follow. The mercury frequency does not change from cycle to cycle, *i.e.* the magnetic field does not vary along the run. The Hg T_2 time is not simulated and the Hg frequency statistical error is fixed to 1 µHz. Two values are computed from the mercury frequency: the $\pi/2$ pulse RF frequency f_{RF} and the neutron frequency:

$$\begin{cases} f_{\mathrm{n}}^{i} = \frac{\gamma_{\mathrm{n}}}{\gamma_{\mathrm{Hg}}} f_{\mathrm{Hg}}^{i} \\ f_{\mathrm{RF}}^{i} = \frac{\gamma_{\mathrm{n}}}{\gamma_{\mathrm{Hg}}} f_{\mathrm{Hg}}^{i-1} \pm \frac{\Delta\nu}{2}\,(1 \pm 0.1) \end{cases} \tag{6.18}$$

The visibility of the fringe α_a, the average number of detected neutrons N_a, the number of monitored UCNs... are constant. Statistical fluctuations of the number of detected/monitored UCNs and the Hg frequency are used.

For such ideal conditions, the reduced χ^2 of the neutron frequency fit is 1. The $f_{\mathrm{n}} - \frac{\gamma_{\mathrm{n}}}{\gamma_{\mathrm{Hg}}} f_{\mathrm{Hg}}$ precision of precision (standard deviation of its distribution) of 13.0 ± 0.2 µHz is in agreement with the expected value given by Eq (2.15) of 13.2 µHz. Finally, the accuracy of the neutron frequency extraction is -0.15 ± 0.13 µHz. It is obtained via the mean difference between the simulated neutron frequencies and the extracted one.

6.7.3 B field fluctuations

In order to reproduce typical magnetic field fluctuations, magnetic field variations from cycle to cycle have been extracted over a three days run via the Hg frequency (run n° 7650). The distribution of such variations is roughly gaussian, centred on 0 with a standard deviation of 13.5 µHz. In the toy data, the Hg frequency is thus randomly varied according to a gaussian distribution using these experimental parameters. Typical magnetic field changes are shown in Fig. 6.12 The simulated magnetic field fluctuation is then applied to the neutron frequency.

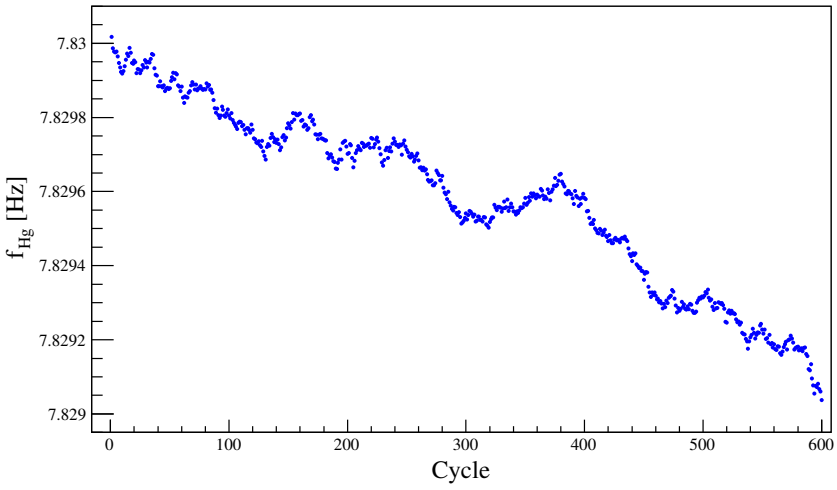

Figure 6.12: Hg frequency generated along cycles in simulated data.

With B field fluctuations, the reduced χ^2 of the neutron frequency fit is 1. The $f_{\mathrm{n}} - \frac{\gamma_{\mathrm{n}}}{\gamma_{\mathrm{Hg}}} f_{\mathrm{Hg}}$ precision of 13.0 ± 0.2 µHz is in agreement with the expected value of 13.2 µHz. Finally, the accuracy of the neutron frequency extraction is 0.10 ± 0.13 µHz. It means that the normalisation using the Hg frequency is properly performed in the analysis software.

6.7.4 UCN source production decay

The UCN source production decays along time. It has been included in the toy model by means of a decay time constant of 2.89×10^6 s, fitted from the experimental data. Then, non-statistical fluctuations of the source are also implemented. They amount to approximately 10^4 counts for a number of monitored UCNs which is of the order of 8×10^5 UCN counts. These fluctuations are then propagated to the number of detected neutrons.

For such conditions, the reduced χ^2 of the neutron frequency fit is 1. The $f_\mathrm{n} - \frac{\gamma_\mathrm{n}}{\gamma_\mathrm{Hg}} f_\mathrm{Hg}$ precision of 15.5 ± 0.2 µHz is in agreement with the expected value of 15.3 µHz. Finally, the accuracy of the neutron frequency extraction is 0.13 ± 0.15 µHz. The same results are obtained with both the asymmetry and the neutron counts fit. It means that the normalisation of the neutron counts with the monitor properly works and does not affect the fit quality.

6.7.5 Static magnetic field gradient

As seen in Sec. 6.4, a static magnetic field gradient shifts the neutron Larmor frequency with respect to the mercury one. As a result, the working points location, calculated from the mercury frequency (as in the data acquisition), are slightly shifted on the Ramsey fringe, with respect to the resonance frequency. This shift is set using:

$$\Delta f_{\partial_z B_z} = \mp \frac{\gamma_\mathrm{n}}{2\pi} \left(\Delta h \left\langle \partial_z B_z \right\rangle \right) \tag{6.19}$$

where the - and + signs hold for the B_0 up and B_0 down configurations.

In addition, the fringe visibility is modified by the gradient, according to [110]:

$$\alpha = \alpha_0 \mathrm{e}^{-a|\langle \partial_z B_z \rangle|} \tag{6.20}$$

The a parameter is derived from a fit of the 2012 R-curve data giving: $a \simeq 3.4 \times 10^{-4} \left(\mathrm{pT/cm}\right)^{-1}$.

The static magnetic field gradient used for this study is 10 pT/cm. For such conditions, the reduced χ^2 of the neutron frequency fit is 1. The $f_\mathrm{n} - \frac{\gamma_\mathrm{n}}{\gamma_\mathrm{Hg}} f_\mathrm{Hg}$ precision of 15.6 ± 0.2 µHz is in agreement with the expected value of 15.3 µHz. Finally, the accuracy of the neutron frequency extraction is 0.13 ± 0.15 µHz.

6.7.6 Daily variation of the magnetic field gradient

Daily variations of the gradient of a few pT/cm peak-to-peak have been observed during 2013 data (see Sec. 6.4). This variation has been implemented in the toy model by means of an additional time dependent gradient $\delta \left\langle \partial_z B_z \right\rangle (t)$:

$$\delta \left\langle \partial_z B_z \right\rangle (t) = \frac{g_0}{2} \cos\left(\frac{2\pi t}{24 \times 3600} \right) \tag{6.21}$$

Here, a simple *ad-hoc* cosine function has been taken to model the observed daily gradient variations but it could be further sophisticated. For $g_0 = 3$ pT/cm, the maximum variation of the shift $\Delta f_{\partial_z B_z}$ is 20 µHz. As well as for a static gradient, the visibility varies with the field gradient. For a 3 pT/cm variation and a non-zero static gradient, the visibility change is about 1%. The two effects are shown in Fig. 6.13 for g_0 =10 pT/cm. Such a large variation has been used in order to clearly show the resulting effect on the Ramsey fringe.

In order to meet the experimental conditions, a 2 pT/cm variation of the magnetic field gradient has been set in addition to a 20 pT/cm static gradient. For such conditions, the accuracy of the

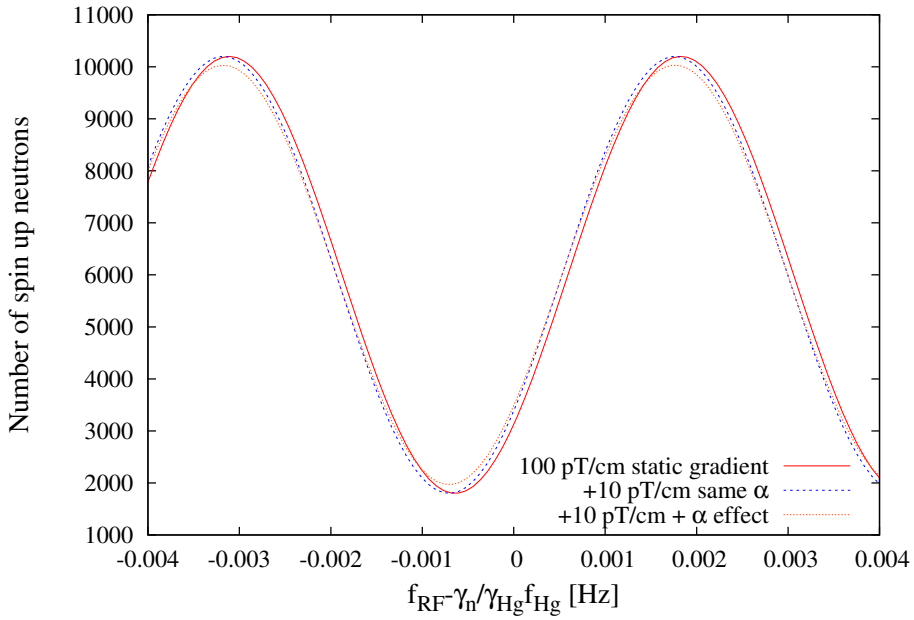

Figure 6.13: Illustration of a 10 pT/cm vertical gradient variation effect on the neutron frequency resonance and the Ramsey pattern visibility. A static magnetic field gradient of 100 pT/cm is also used. The central fringe is globally shifted towards negative values due to this static magnetic field gradient.

neutron frequency extraction is 0.15 ± 0.15 µHz. However, the reduced χ^2 of the neutron frequency fit is 1.12. The $f_n - \frac{\gamma_n}{\gamma_{Hg}} f_{Hg}$ precision of 16.3 ± 0.2 µHz is 6.5% larger than the expected value of 15.3 µHz. This behaviour looks like the effect observed in experimental data. This effect is further investigated in the next section.

6.7.6.1 Effect of a daily gradient variation on the $\tilde{\chi}^2$

In order to assess the effect of a gradient variation along a run on the $\tilde{\chi}^2$ neutron frequency fit, toy data have been produced with different input gradient variations g_0, with a static gradient of 20 pT/cm. 600 cycles have been generated for each sample. Results are summarized in Fig. 6.14.

As expected, the larger the gradient variation, the larger the $\tilde{\chi}^2$. For gradient variations of 2 pT/cm (as observed in experimental data), the reduced χ^2 of about 1.15 is consistent with the average $\tilde{\chi}^2$ obtained with the 2013 nEDM runs (see Sec. 6.2 and Sec. 6.3). It does not prove that the gradient variation is the only source of problems for the neutron frequency fit, but it can explain the measured $\tilde{\chi}^2$.

A possible way to avoid the effect of a slow gradient variation could be to perform the fit on sub-samples of each run. As a result,the gradient variation is low and the Ramsey fringe visibility as well as the neutron resonance frequency with respect to the mercury do not change significantly. This has been tested with the toy model. The pattern used for the electric field polarity changes is: $-0+0-0+$... with 24 cycles for positive or negative polarity and 12 cycles without electric field.

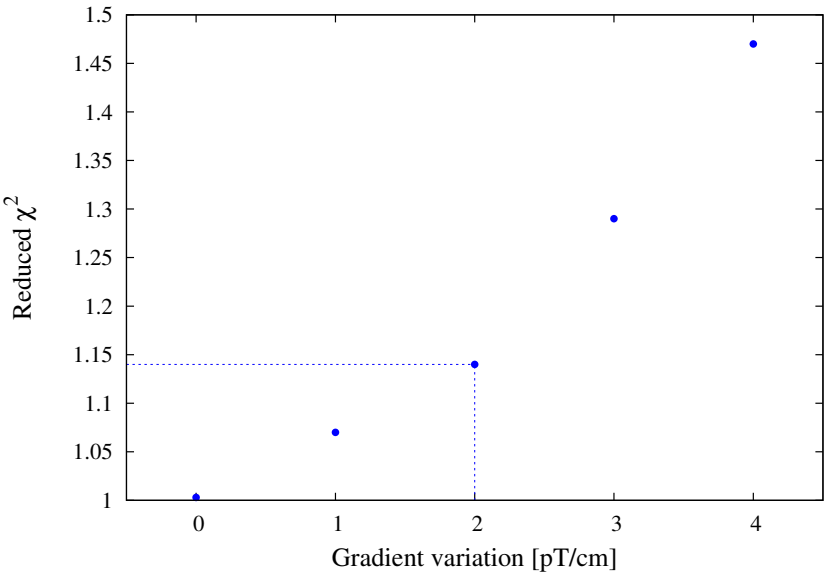

Figure 6.14: Effect of a cosine daily variation of the magnetic field gradient on the neutron Larmor frequency fit quality. The point corresponding to the 2 pT/cm gradient variation observed in experimental data is emphasized.

The averaged resulting χ^2 obtained for different number of cycles used to perform the fit and for different gradient variations is shown in Fig. 6.15. The number of cycles is a multiple of 24. A large step is visible when going from 24 cycles to 48 cycles. It means that using smaller samples may help to remove gradient effects on the fit quality.

6.7.7 Relevance of the δ term use

In this part, the relevance of the δ term used in the asymmetry fit function (Eq (6.8)) is studied.

In this study, previous conditions have been included to generate the data. Reasonable running conditions are used: $\langle \partial_z B_z \rangle = 20\,\mathrm{pT/cm}$, $g_0 = 2\,\mathrm{pT/cm}$. In order to determine the influence of the δ term on the fit quality, a 2% asymmetry is added between spin up and spin down detection, both on the number of counts and on the visibility. This is visible in Fig. 6.11.

Whatever the use or not of the δ term, obtained results are the same: the accuracy on the extracted neutron frequency is of the order of 0.15 µHz. Same results have been obtained using the normalised neutron counts fitting procedure.

Since no improvement has been observed with the δ term, it has been chosen to perform the fit without it.

6.7.8 Conclusions on the neutron frequency extraction

Both the experimental study of the neutron Larmor frequency and the use of the toy model have shown that the analysis code can reliably extract neutron frequencies, even if some checks are still not present in the current experimental analysis (*e.g.* the leakage current or the right switch positioning). The major improvement of the fit quality comes from the development of a new method for the Hg frequency extraction. This new technique is adapted to low Hg tranverse relaxation times. It gives improved results, even without taking into account the entire signal.

It has also been shown that the 2 pT/cm gradient variation observed in experimental data could explain the $\tilde{\chi}^2$ of the neutron frequency fit.

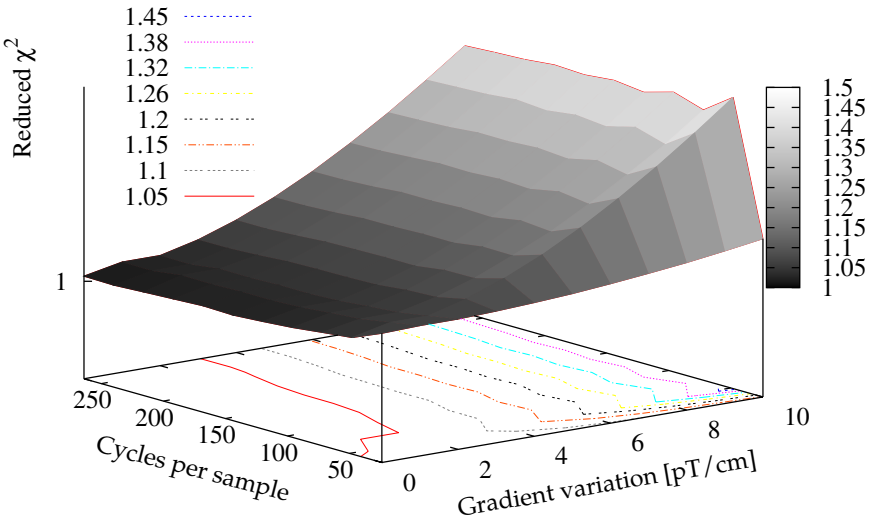

Figure 6.15: Map of the reduced χ^2 as a function of the number of cycles used to perform the fit and the amplitude of the daily gradient variation. Toy data have been produced using a 50 pT/cm static gradient.

6.8 nEDM measurement with 2013 data

This 2013 data analysis is based on the work presented in [1, 112]. The neutron Larmor frequency is extracted using the procedure described in Sec. 6.1, with the asymmetry fit (section 6.1.3). First, a short overview of nEDM systematic effects is given. Then, the nEDM $d_{\mathrm{n}}^{\mathrm{meas}}$ is extracted.

6.8.1 Systematic errors

Using Eq (2.8), the ratio R of the neutron to mercury Larmor frequencies is:

$$R = \frac{f_{\mathrm{n}}}{f_{\mathrm{Hg}}} = \frac{|(\mu_{\mathrm{n}} B_{\mathrm{n}} \pm d_{\mathrm{n}} E)|}{|(\mu_{\mathrm{Hg}} B_{\mathrm{Hg}} \pm d_{\mathrm{Hg}} E)|} \tag{6.22}$$

where the + sign corresponds to parallel magnetic and electric fields and the - sign to antiparallel fields. Here, B_{n} and B_{Hg} correspond to the magnetic fields respectively seen by the neutrons and the mercury atoms. Assuming that $B_{\mathrm{n}} = B_{\mathrm{Hg}}$ and considering EDMs to first order, one gets:

$$R = \frac{\mu_{\mathrm{n}} B_{\mathrm{n}}}{\mu_{\mathrm{Hg}} B_{\mathrm{Hg}}} \frac{\left(1 \pm \frac{d_{\mathrm{n}} E}{\mu_{\mathrm{n}} B_{\mathrm{n}}}\right)}{\left(1 \pm \frac{d_{\mathrm{Hg}} E}{\mu_{\mathrm{Hg}} B_{\mathrm{Hg}}}\right)} \tag{6.23}$$

$$R \simeq \frac{\gamma_{\mathrm{n}}}{\gamma_{\mathrm{Hg}}} \pm \frac{2E}{h f_{\mathrm{Hg}}} \left(d_{\mathrm{n}} - \frac{\gamma_{\mathrm{n}}}{\gamma_{\mathrm{Hg}}} d_{\mathrm{Hg}}\right) \tag{6.24}$$

where h is the Planck constant.

Then the nEDM is recovered by means of a linear fit of R versus the electric field E. The raw d_{n} extracted from Eq (6.24) is given by:

$$d_{\mathrm{n}}^{\mathrm{meas}} = d_{\mathrm{n}} - \frac{\gamma_{\mathrm{n}}}{\gamma_{\mathrm{Hg}}} d_{\mathrm{Hg}}^{\mathrm{meas}} \tag{6.25}$$

The measured Hg EDM (which can contain false contributions) propagates to the neutron EDM itself due to the frequency normalisation.

In addition, any magnetic field change $\Delta B = B_{\parallel} - B_{\nparallel}$, correlated to electric field directions and intensity, results in a false EDM signal (see Eq (2.9)):

$$d_{\mathrm{n}}^{\mathrm{meas}} = d_{\mathrm{n}} + \frac{\hbar \gamma_{\mathrm{n}}}{4E} \Delta B \tag{6.26}$$

Any shift of the neutron and/or the Hg precession frequency linear in the electric field results in a direct systematic effect (see Tab. 6.3) while indirect systematic effects are due to the technique used to suppress the geometric phase effect (see 6.8.1.1).

The global systematic effects budget is summarised in Tab. 6.3. The overall systematic error is of the order of $4 \times 10^{-27} e$.cm, far below the current statistical precision. A short description of the largest systematic effects (uncompensated B-drift, geometric phase effect and quadrupole difference) follows.

Effect	Status [$\times 10^{-27}$ e.cm]
Direct effects	
Uncompensated B-Drifts	-0.7 ± 1.1
Leakage current	0.00 ± 0.05
$v \times E$ UCN	0 ± 0.1
Electric forces	0 ± 0
Hg EDM	0.02 ± 0.06
Hg direct light shift	0 ± 0.008
Indirect effects	
Hg Light Shift	0 ± 0.05
Quadrupole difference	1.3 ± 2.4
Dipoles	
At surface	0 ± 0.4
Other dipoles	0 ± 3
Total	0.2 ± 4.0

Table 6.3: Systematic effects status [110].

6.8.1.1 Geometric Phase Effect (GPE)

The major systematic error comes from the so-called geometric phase effect. For the nEDM experiments, such a relativistic effect appears for particles (Hg or neutrons) moving in the precession chamber where a vertical electric field is applied and inhomogeneous transverse magnetic fields are present. This effect is described in details in [113, 114]. The particles movement in the electric field creates a "motional" magnetic field:

$$B_{\perp}^{v} = \frac{E \times v}{c^2} = \frac{E.v_{xy}}{c^2} \tag{6.27}$$

An additional transverse field arise from the vertical magnetic field gradient through the Maxwell's equation $\nabla B = 0$ (assuming a magnetic field with a cylindrical symmetry)

$$B_{\perp}^{\partial_z B_z} = -\frac{\langle \partial_z B_z \rangle \, r}{2} \tag{6.28}$$

A $\Delta\omega$ shift of the particles precession frequency (with respect to $\omega_0 = \gamma B_0$) is produced. It is called the Ramsey-Bloch-Siegert shift [115, 116]:

$$\Delta\omega \simeq \frac{(\gamma B_\perp)^2}{2\,(\omega_0 - B_\perp/\gamma)} \tag{6.29}$$

with:

$$B_\perp^2 = \left(B_\perp^{\langle\partial_z B_z\rangle} + B_\perp^v\right)^2 \tag{6.30}$$

$$= (B_\perp^{\langle\partial_z B_z\rangle})^2 + (B_\perp^v)^2 + \frac{\langle\partial_z B_z\rangle\, v_{xy} r E}{c^2} \tag{6.31}$$

where v_{xy} is the particle speed component perpendicular to the electric field, the only speed contributing in the product $\vec{v} \times \vec{E}$. Through Eq (6.29) and (6.31), it is visible that the frequency shift $\Delta\omega$ has a term linearly proportionnal to E. Because UCNs move slower (adiabatic regime) than the Hg atoms (non-adiabatic regime), the effect is about 10 to 15 times larger for the mercury than for neutrons [113] and is transmitted to the false neutron EDM by [114]:

$$d^{\text{false}}_{\text{Hg}\to\text{n}} = \frac{\hbar|\gamma_{\text{Hg}}\gamma_{\text{n}}|\,\langle\partial_z B_z\rangle\, D^2}{32c^2} \tag{6.32}$$

where D is the diameter of the nEDM precession chamber. This effect, estimated in [117], induces a false neutron EDM of:

$$d^{\text{false}}_{\text{Hg}\to\text{n}} \simeq \frac{3.8\times10^{-27}\times\langle\partial_z B_z\rangle\ e.\text{cm}}{1\,\text{pT/cm}} \tag{6.33}$$

Fortunately, as the false EDM scales linearly with the gradient and also depends on the magnetic field direction, it is possible to cancel its contribution using the so-called crossing point analysis, introduced by the RAL-Sussex-ILL collaboration [1]. This method is described and used in 6.8.4.

However, Eq (6.32) only holds for a uniform cylindrical gradient. In the presence of a localised magnetic field inhomogeneity, for instance a magnetic dipole located close to the precession chamber, the general expression is given by [114]:

$$d^{\text{false}}_{\text{Hg}\to\text{n}} = \frac{\hbar|\gamma_{\text{Hg}}\gamma_{\text{n}}|}{2c^2}\,\langle xB_x + yB_y\rangle \tag{6.34}$$

Such inhomogeneties have been measured during the mapping of the bottom electrode at the PTB[2]. The induced false EDM has been estimated to $0 \pm 3\times10^{-27}$ e.cm [118], corresponding to the "Other dipoles" value in Tab. 6.3.

6.8.1.2 Quadrupole difference

This systematic effect comes from the fact that neutrons and mercury average differently the magnetic field inside the precession chamber and the use of the crossing point technique. Indeed, because the neutron Larmor frequency is larger than the UCN wall collision rate (because of the low UCN speed), UCNs average the modulus of the magnetic field $\left\langle|\vec{B}|\right\rangle$. They are able to follow the magnetic field variation (adiabatic regime). On the contrary, the Hg co-magnetometer, fastly moving through the precession chamber, probes the modulus of the averaged magnetic field $\left|\langle\vec{B}\rangle\right|$. They are not able to follow the magnetic field variation (non adiabatic regime). This difference propagates to the EDM through the ratio R:

$$R = \frac{f_{\text{n}}}{f_{\text{Hg}}} = \frac{\left\langle|\vec{B}|\right\rangle}{\left|\langle\vec{B}\rangle\right|} \simeq \frac{\left\langle\sqrt{B_x^2 + B_y^2 + B_z^2}\right\rangle}{B_z} \simeq 1 + \frac{\langle B_T^2\rangle}{2B_z^2} \tag{6.35}$$

[2] Physikalisch-Technischen Bundesanstalt (Berlin)

where $\langle B_T^2 \rangle$ is the average of the squared transverse field and $B_z \simeq B_0$ the modulus of the field. If $\langle B_T^2 \rangle$ is different for $B_0^{\uparrow}$ and $B_0^{\downarrow}$ configurations, the false EDM resulting from the crossing point analysis is:

$$d_{\mathrm{n}}^{\mathrm{false}} = \frac{\hbar \gamma_n \gamma_{Hg} D^2}{128 c^2 B_0 \Delta h} \left(\langle B_T^2 \rangle^{\downarrow} - \langle B_T^2 \rangle^{\uparrow} \right) \tag{6.36}$$

$$\simeq \frac{4.55 \times 10^{-27} \times \left(\langle B_T^2 \rangle^{\downarrow} - \langle B_T^2 \rangle^{\uparrow} \right) e.\mathrm{cm}}{1\,\mathrm{nT}^2} \tag{6.37}$$

The magnetic field mapping of the precession chamber during winter shut-down is used to estimate the squared transverse field difference $\left(\langle B_T^2 \rangle^{\downarrow} - \langle B_T^2 \rangle^{\uparrow} \right)$. The 2010 measurement for the nEDM magnetic field configuration gave:

$$\left(\langle B_T^2 \rangle^{\downarrow} - \langle B_T^2 \rangle^{\uparrow} \right) = 0.3 \pm 0.5 \mathrm{nT}^2 \tag{6.38}$$

The resulting false EDM is thus:

$$d_{\mathrm{n}}^{\mathrm{false}} = (1.3 \pm 2.4) \times 10^{-27}\ e.\mathrm{cm} \tag{6.39}$$

Using vectorial magnetometers, this quantity could be monitored along EDM runs and used to correct online this important systematic effect (see Tab. 6.3). A preliminary study of such a monitoring using vector caesium magnetometers is presented in Chap 7.

6.8.1.3 Uncompensated B-Drifts

When a current (induced by HV charging or discharges) flows in a direction correlated to the electric field direction, it creates a small magnetic field which may magnetise the innermost magnetic shield layer. This magnetisation induces a dipole like field, correlated to the electric field direction. The corresponding gradient change is differently seen by neutrons and Hg because of their different centres of mass. The gradient difference $\Delta \langle \partial_z B_z \rangle$ between the two electric field polarities gives a B field difference $\Delta \langle \partial_z B_z \rangle \Delta h$, not compensated by the Hg co-magnetometer. Such an effect has been estimated during dedicated measurements in 2012, giving the induced false EDM [3]:

$$d_{\mathrm{n}}^{\mathrm{false}} = (-0.7 \pm 1.1) \times 10^{-27}\ e.\mathrm{cm} \tag{6.40}$$

It has to be noticed that measurements have not been carried out as in nEDM measurements, but during a shorter time with a constant electric field. As a result, the number of electric discharges is likely different in this measurement compared to EDM data taking conditions.

6.8.2 Raw nEDM extraction

Back to Eq (6.24), the nEDM recovery can be performed through the slope of a linear fit of R versus the applied High Voltage (HV), such as $R = R_0 + s.HV$. The slope s is equal to:

$$s = \frac{2 \left(d_{\mathrm{n}} - \frac{\gamma_{\mathrm{n}}}{\gamma_{\mathrm{Hg}}} d_{\mathrm{Hg}} \right)}{d_{\mathrm{Elec}} h f_{\mathrm{Hg}}} \tag{6.41}$$

where $d_{\mathrm{Elec}} = 12\,\mathrm{cm}$ is the distance between the two electrodes. An example of such a fit is shown in Fig. 6.16.

[3] A recent re-analysis of data from 2010 to 2013 data estimates the false EDM coming from the uncompensated B-drift to $(-0.05 \pm 0.43) \times 10^{-27}$ $e.\mathrm{cm}$.

The current limit on the mercury EDM $d_{\mathrm{Hg}} = (0.49 \pm 1.29 \pm 0.79) \times 10^{-29}$ e.cm [55] induces a negligible systematic effect on the neutron EDM:

$$d^{\mathrm{false}}_{\mathrm{Hg}\to\mathrm{n}} = (1.9 \pm 5.0 \pm 3.1) \times 10^{-29}\ e.\mathrm{cm}$$

The ratio R is calculated using the neutron precession frequency extracted for each cycle and the corresponding Hg frequency estimated by the s/n method (see 6.3.1). The error on the Hg frequency takes into account the factor 6 coming from the use of the Hg signal bandpass filters [108].

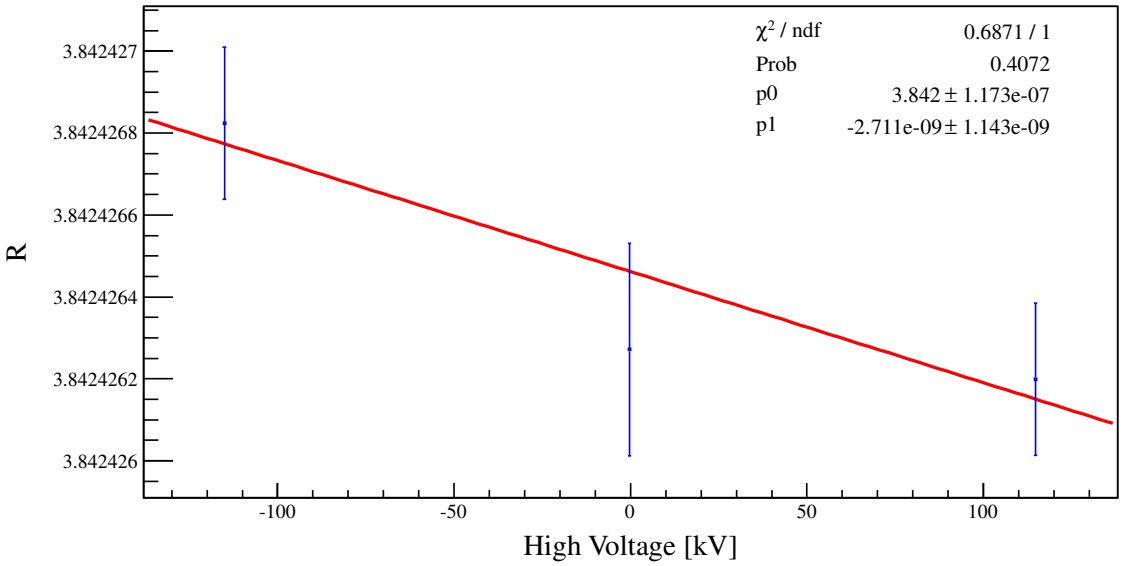

Figure 6.16: nEDM extraction via the fit of R versus High Voltage.

For more than half of 2013 EDM runs (7 runs over 12), the reduced χ^2 of the fit is above 4.5. Such χ^2 can not be statistically explained. The reasons for which the relation $R = f(E)$ is not fully linear is not understood yet. Electric discharges are possible candidates to explain such non linearity. The study of the leakage current between the shutter opening and closing has to be performed in order to find possible sparks which could influence the magnetic field during the precession. Nevertheless, the data analysis has been continued in order to determine the statistical precision reached with the 2013 data.

A summary of 2013 EDM runs used in this analysis as well as their running conditions are presented in the appendix C. The expected nEDM statistical error calculated from Eq (2.17) does not agree with the measured precision. However, if the bad χ^2 of the neutron Larmor frequency fit and the Hg frequency error (which propagates to the ratio R) are taken into account, the measured d_{n} precision becomes consistent with expectations for 5 runs over 13. The remaining 8 runs have a measured precision 11% larger than the expected one in average. Study is ongoing.

Summing all the runs, the total expected d_{n} sensitivity is 0.80×10^{-25} e.cm (by rescaling with the Hg frequency statistical error and the neutron Larmor frequency fit reduced χ^2 as previously). The total measured nEDM sensitivity has been extracted as follows. The measured nEDM have been plotted as a function of $R_a - 1$ (see Eq (6.49)) for B_0 up and B_0 down configurations and have been fitted by a constant, as shown in Fig. 6.17.

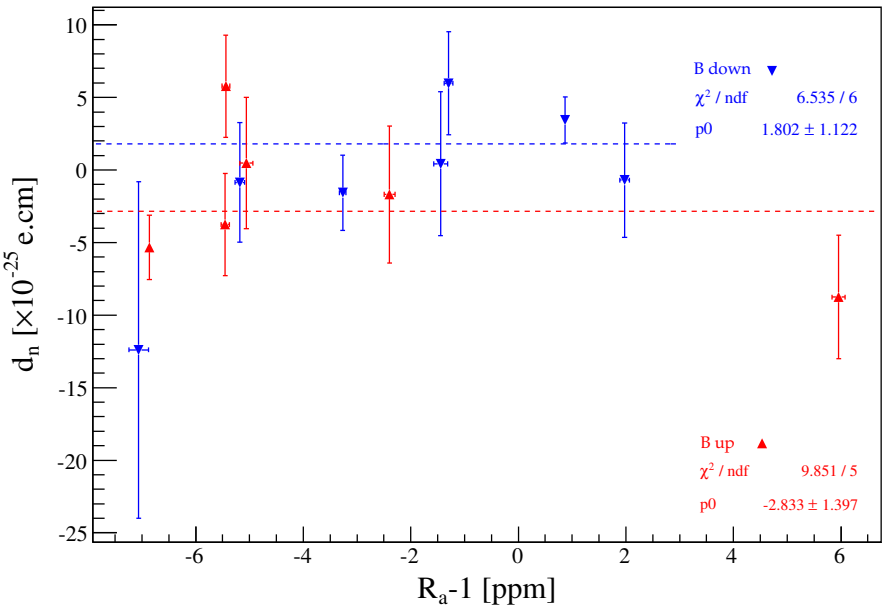

Figure 6.17: Constant fits of the B_0 up and the B_0 down nEDM data. B_0 up correspond to the up red triangles and B_0 down to the down blue triangles.

Combining the results for each magnetic field direction, one gets:

$$d_{\mathrm{n}}^{\uparrow} = (-2.8 \pm 1.4) \times 10^{-25} e.\mathrm{cm} \quad \tilde{\chi}^2 = 1.97 \tag{6.42}$$

$$d_{\mathrm{n}}^{\downarrow} = (+1.8 \pm 0.9) \times 10^{-25} e.\mathrm{cm} \quad \tilde{\chi}^2 = 1.08 \tag{6.43}$$

it results in the nEDM measurement of 2013 data without the GPE correction:

$$d_n = (-0.50 \pm 0.83) \times 10^{-25} e.\mathrm{cm} \tag{6.44}$$

The measured statistical sensitivity is about 4% larger than the expected one. But this measurement does not account for the geometric phase effect. The GPE correction is done later using the so-called crossing-point analysis.

6.8.3 Correction of the Earth's rotation frequency shift

Because the neutron spin precession is observed in the Earth frame and not in a fixed frame, the Earth rotation adds up or subtracts from the Larmor precession frequency, according to the B_0 direction. Its contribution to the ratio R amounts to [119]:

$$\delta_R^{\mathrm{Earth}} = \pm \frac{\gamma_{\mathrm{n}}}{\gamma_{\mathrm{Hg}}} \frac{\Omega_T \sin\lambda}{B_0} \left(\frac{1}{|\gamma_{\mathrm{Hg}}|} + \frac{1}{|\gamma_{\mathrm{n}}|} \right) \tag{6.45}$$

where $\Omega_T = 11.6\,\mu\mathrm{Hz}$ is the sideral angular rotation frequency of the Earth and $\lambda = 47.517°$ is the PSI latitude. The + and - signs respectively hold for the B_0 up and B_0 down configurations. The effect on R is thus:

$$R = \frac{\gamma_{\mathrm{n}}}{\gamma_{\mathrm{Hg}}} + \delta_R^{\mathrm{Earth}} = \frac{\gamma_{\mathrm{n}}}{\gamma_{\mathrm{Hg}}} \pm 5.3\mathrm{ppm} \tag{6.46}$$

This effect has been taken into account to perform the crossing point analysis, presented in the next part.

6.8.4 Suppression of the geometric phase effect

The false EDM coming from the geometric phase of the Hg depends on the vertical magnetic field gradient as well as the R ratio. This common property is used for the crossing point analysis. One writes:

$$R \simeq \frac{\gamma_{\mathrm{n}}}{\gamma_{\mathrm{Hg}}}\left(1 \mp \frac{\Delta h \,\langle \partial_z B_z \rangle}{B_0}\right) \tag{6.47}$$

Where the - and + signs correspond respectively to B_0 up and B_0 down configurations. The vertical gradient can be expressed as a function of R

$$\langle \partial_z B_z \rangle = \mp \left(R\frac{\gamma_{\mathrm{Hg}}}{\gamma_{\mathrm{n}}} - 1\right)\frac{B_0}{\Delta h} \tag{6.48}$$

$$= \mp \left(R_a - 1\right)\frac{B_0}{\Delta h} \text{ with } R_a = R\frac{\gamma_{\mathrm{Hg}}}{\gamma_{\mathrm{n}}} \tag{6.49}$$

As a result, Eq (6.32) gives:

$$d^{\mathrm{false}}_{\mathrm{Hg}\to\mathrm{n}} = \mp \frac{h|\gamma_{\mathrm{n}}| f_{\mathrm{Hg}} D^2}{32c^2\Delta h}\left(R_a - 1\right) \tag{6.50}$$

Thus, there is a linear dependence between the false EDM $d^{\mathrm{false}}_{\mathrm{Hg}\to\mathrm{n}}$ and $R_a - 1$.The curve corresponding to the B_0 up configurations and the curve associated to the B_0 down configurations have opposite slopes. They cross at the point where $R_a - 1 = 0$. For such a point, the false EDM induced by the GPE is null. This is the so-called crossing point technique pioneered by the RAL-Sussex-ILL collaboration [1].

Using the value $\Delta h = 0.235 \pm 0.005\,\mathrm{cm}$ extracted during the 2012 R-curve measurements [109], the expected slope s_{GP} of Eq (6.50) can be calculated:

$$s_{GP} = \mp\left(6.67 \pm 0.14\right) \times 10^{-20}\, e.\mathrm{cm/ppm} \tag{6.51}$$

The error bar of the slope comes from the uncertainty of Δh.

The crossing point analysis has been performed over the 2013 nEDM runs as shown in Fig. 6.18.

For both field directions, the slope is consistent with the expected one:

$$s^{\uparrow}_{GP} = -\left(3.7 \pm 3.6\right) \times 10^{-20}\, e.\mathrm{cm/ppm} \quad \tilde{\chi}^2 = 2.20 \tag{6.52}$$

$$s^{\downarrow}_{GP} = +\left(7.8 \pm 5.0\right) \times 10^{-20}\, e.\mathrm{cm/ppm} \quad \tilde{\chi}^2 = 0.82 \tag{6.53}$$

Two runs belonging to the B_0 up configuration are off the expected curve ($R_a - 1 \simeq -5\,\mathrm{ppm}$ and $R_a - 1 \simeq -7\,\mathrm{ppm}$), particularly one at more than 3σ. This is likely related to the problem observed in 6.8.2, since these two runs belong to the data set with a non-statistical behaviour for the fit which determines $d^{\mathrm{meas}}_{\mathrm{n}}$. Investigations are still ongoing.

As a result, the precision of the slopes is poor and the coordinates of the crossing point are not precise: $R_a - 1 = -5.9 \pm 3.8\,\mathrm{ppm}$ and $d_{\mathrm{n}} = (-2.3 \pm 3.4) \times 10^{-25}\ e.\mathrm{cm}$.

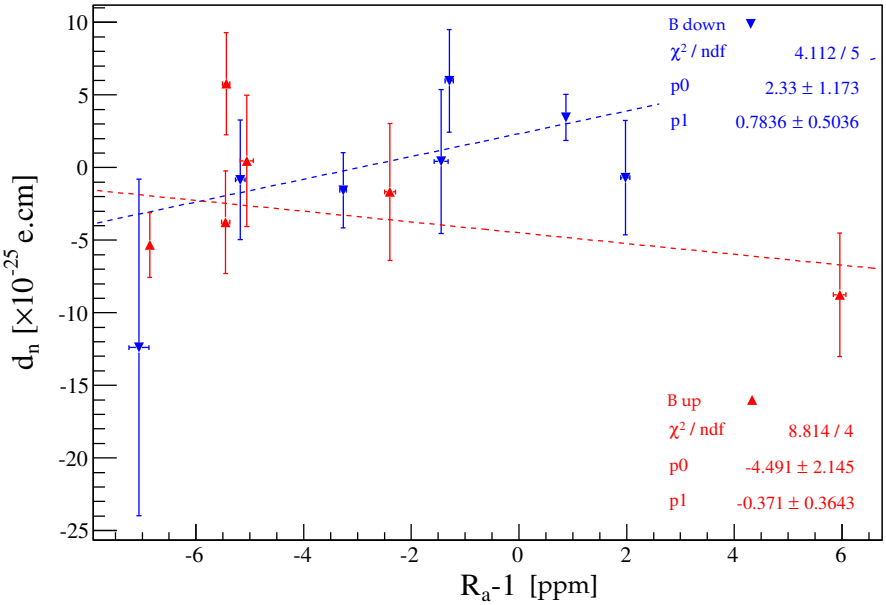

Figure 6.18: Crossing point analysis of 2013 nEDM data. The B_0 up configurations correspond to the up red triangles and the B_0 down configurations to the down blue triangles.

6.9 Conclusion

From both the experimental analysis and the toy model results, the reliability of the neutron Larmor frequency extraction has been studied.

Using simulated data, the accuracy of the fit has been estimated to be about 0.15 µHz. The statistical precision is in agreement with the expected one for both simulated and experimental data.

With simulated data, the reduced χ^2 is equal to 1 using usual running conditions. For experimental data, the average reduced χ^2 of the neutron Larmor frequency fit is larger ($\tilde{\chi}^2 \simeq 1.15$). A possible explanation supported by simulations has been pointed out. A small and slow magnetic field gradient variation (with a daily period for instance) deteriorates the fit quality. In the toy model, a daily sinusoidal variation of the vertical magnetic field gradient with a 2 pT/cm amplitude produces a $\tilde{\chi}^2 \simeq 1.14$, consistent with observations. A possible way to suppress this effect is to use smaller data samples, for both the neutron Larmor frequency fit and the nEDM extraction. However, it has recently been shown that this magnetic field gradient is correlated to temperature changes [111]. Therefore, a better thermal insulation and stabilisation of the thermohouse would be more efficient.

During the last stage of the nEDM analysis, it has been shown that the Hg frequency precision is critical and may significantly degrade the nEDM precision. The collaboration is actively working to find out the source of the low Hg transverse relaxation time, which is the cause of the low Hg frequency precision. A new method has been developped, the *s/n* Hg frequency fitting method. It is more suited to the bad Hg running conditions than the usual two windows method. However, a problem with this new technique is not excluded, since it does not average the magnetic field during the full neutron precession.

Finally, the last part of the 2013 nEDM analysis pointed out a problem for the d_n recovery via the linear fit of R versus E. For more than 50% of EDM runs, the reduced χ^2 of this fit lies above 4.5, meaning that an additionnal non-expected effect correlated to the electric field

is present in the data. Further investigations are required. In spite of this important problem, the 2013 data was analysed. The outcoming result is a preliminary estimation of the nEDM: $d_{\mathrm{n}} = (-2.3 \pm 3.4) \times 10^{-25}$ e.cm.

Vertical magnetic field gradient variations may degrade the neutron Larmor frequency fit. They have been measured with the scalar caesium magnetometers array. The next chapter is dedicated to the test and the improvement of methods used to extract magnetic field observables from caesium data, relevant for the control of systematic effects.

Chapter 7

Study of magnetic observables estimators

Contents

As seen previously, the Hg co-magnetometer and ultra cold neutrons do not average the same magnetic field during the free precession time. Combined to a non-zero vertical gradient, this gives rise to several systematic effects (gravitational shift, geometric phase effect). In order to determine these systematics, an array of optically pumped scalar caesium magnetometers (CsM) is used to measure the vertical gradient inside the precession chamber (see 3.4.3.2). The vertical gradient has also been used in the 2012 R-curve measurements to determine the centre of mass difference Δh and to estimate the ratio γ_n/γ_{Hg}.

In this section, the different ways to estimate the vertical gradient through the CsM data are studied. A prospective study for the n2EDM phase is also presented, testing the efficiency of 3D CsM to extract information about the transverse fields, involved in the so-called quadrupole difference systematic effect.

7.1 Harmonic polynomials series expansion

In order to parametrise the magnetic field inside the precession chamber, a new set of Cartesian harmonics has been developed [120]. This set of harmonic polynomials can be used to expand the magnetic scalar potential Ψ, solution of the Laplace's equation in a magnetisation and current-free region:

$$\nabla^2\Psi(\vec{r}) = 0 \tag{7.1}$$

such as:

$$\Psi(\vec{r}) = \sum_{n=0}^{\infty} \mathcal{H}_n \mathcal{Q}_n(\vec{r}) \tag{7.2}$$

The magnetic induction $\vec{B} = -\nabla\Psi$ is then given by:

$$\vec{B}(\vec{r}) = \begin{pmatrix} B_x(\vec{r}) \\ B_y(\vec{r}) \\ B_z(\vec{r}) \end{pmatrix} = \sum_{n=1}^{\infty} \mathcal{H}_n \begin{pmatrix} P_{x_n}(\vec{r}) \\ P_{y_n}(\vec{r}) \\ P_{z_n}(\vec{r}) \end{pmatrix} \tag{7.3}$$

where $P_{i_n}(\vec{r}) = -\partial_i \mathcal{Q}_n(\vec{r}) \quad i = x, y, z$. The harmonic polynomials $\vec{P}_{i_n}(\vec{r})$ are listed in Tab. 7.1 up to the order 15.

Once the spectrum $\{\mathcal{H}_n\}$ is known, *i.e.* once the $\mathcal{H}_n$ coefficients are known up to a given order, it is then possible to perform the harmonic synthesis of the magnetic field (Eq (7.3)) and to determine the field everywhere in a mapped volume $\mathcal{V}_{Ch}$.

In the case of the nEDM experiment, the harmonic spectra of the main coils have been extracted by fitting fluxgate 3D magnetic field maps, performed with a mapper designed and built at LPC Caen during winter 2013 [121, 122]. The mapped volume is a bit larger than the precession chamber and includes the caesium magnetometers arrays as shown in Fig. 7.1. This has been obtained using 5 z planes ($\{-160, -80, 0, 80, 160\}$ mm), 2 cm radius steps up to 35 cm with 10° azimutal steps. The best reduced χ^2 has been found for an expansion of the field up to the fourth degree, equivalent to the harmonic order 35.

One has now the ability to produce a magnetic field at every position in the mapped volume and for instance test methods for extracting the averaged vertical gradient over the precession chamber volume. The presentation of this toy model is the topic of the following section.

$\mathcal{H}_n$	$P_{x_n}(\vec{r})$	$P_{y_n}(\vec{r})$	$P_{z_n}(\vec{r})$
$\mathcal{H}_1$	1	0	0
$\mathcal{H}_2$	0	1	0
$\mathcal{H}_3$	0	0	1
$\mathcal{H}_4$	x	0	$-z$
$\mathcal{H}_5$	y	x	0
$\mathcal{H}_6$	0	y	$-z$
$\mathcal{H}_7$	z	0	x
$\mathcal{H}_8$	0	z	y
$\mathcal{H}_9$	$x^2 - z^2$	0	$-2xz$
$\mathcal{H}_{10}$	$2xy$	$x^2 - z^2$	$-2yz$
$\mathcal{H}_{11}$	$y^2 - z^2$	$2xy$	$-2xz$
$\mathcal{H}_{12}$	0	$y^2 - z^2$	$-2yz$
$\mathcal{H}_{13}$	$2xz$	0	$x^2 - z^2$
$\mathcal{H}_{14}$	yz	xz	xy
$\mathcal{H}_{15}$	0	$2yz$	$y^2 - z^2$
$\vdots$	$\vdots$	$\vdots$	$\vdots$

Table 7.1: Harmonic polynomials series expansion for the three components of the magnetic field up to order 15. Higher order polynomials are tabulated in [120].

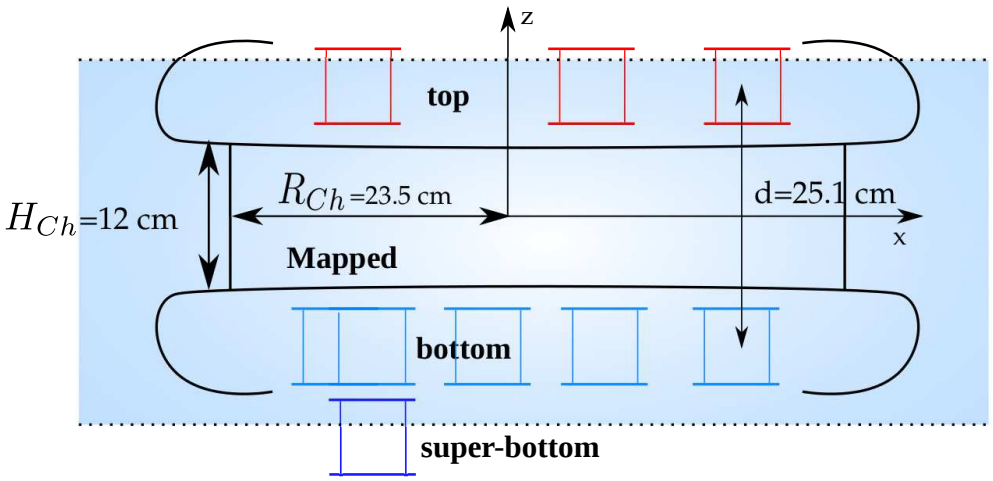

Figure 7.1: The blue rectangle corresponds to the mapped volume $\mathcal{V}_{Ch}$ during the 2013 mapping campaign.

7.2 Toy model principle

As said previously, from the 3D fluxgate maps, one extracts the harmonic spectrum of different coils used for the magnetic field homogenisation or for the spin guiding along tubes in the apparatus. From these harmonic spectra, the modulus of the magnetic field at caesium magnetometers positions is produced for a given coil currents configuration. Then, the vertical gradient created for this field configuration is estimated using the different existing methods (see Sec. 7.3).

Because the total harmonic spectrum is given as an input, the averaged vertical gradient over the chamber volume coming from the map is calculated:

$$\langle \partial_z B_z \rangle_{\mathcal{V}_{Ch}}^{\text{input}} = \frac{1}{V_{Ch}} \int\limits_{\mathcal{V}_{Ch}} \partial_z B_z dV \tag{7.4}$$

$$\begin{aligned} \langle \partial_z B_z \rangle_{\mathcal{V}_{Ch}}^{\text{input}} = &- (\mathcal{H}_4 + \mathcal{H}_6) - \left(z_2^2 - z_1^2\right) \frac{(\mathcal{H}_{13} + \mathcal{H}_{15})}{H_{Ch}} \\ &+ (\mathcal{H}_{16} + \mathcal{H}_{18} + \mathcal{H}_{20}) \left[\frac{\left(z_2^3 - z_1^3\right)}{H_{Ch}} - \frac{3R_{Ch}^2}{4} \right] \\ &+ (\mathcal{H}_{31} + \mathcal{H}_{33} + \mathcal{H}_{35}) \left[\frac{\left(z_2^4 - z_1^4\right)}{H_{Ch}} - \frac{3}{2} \frac{\left(z_2^2 - z_1^2\right) R_{Ch}^2}{H_{Ch}} \right] \end{aligned} \tag{7.5}$$

where $z_2 = 80\,\text{mm}$ and $z_1 = -40\,\text{mm}$ are respectively the top and bottom electrodes locations, $H_{Ch} = 120\,\text{mm}$ is the height of the precession chamber and $R_{Ch} = 235\,\text{mm}$ its radius.

Finally, the gradient estimated by each method $\langle \partial_z B_z \rangle^{\text{meth}}$ is compared to the input average gradient through the difference $\Delta \langle \partial_z B_z \rangle = \langle \partial_z B_z \rangle^{\text{input}} - \langle \partial_z B_z \rangle^{\text{meth}}$ in order to find the best estimation, giving at the same time the accuracy of each method for a given field configuration.

7.3 Methods used to determine the vertical gradient

Three methods have been used to extract the average vertical gradient $\langle \partial_z B_z \rangle$. Two of them are based on the difference of magnetic field modulus between two z planes. The other one uses a parametrisation of the field like the one presented previously in Sec. 7.1.

7.3.1 Top-Bottom averaging

The top-bottom averaging method consists in averaging the field seen by the top layer of caesium magnetometers and by the bottom one and then in extracting the gradient by subtracting the two values:

$$\langle \partial_z B_z \rangle^{\text{tb}} = \frac{\langle B \rangle_{\text{top}} - \langle B \rangle_{\text{bottom}}}{d} \tag{7.6}$$

with $d = 251$ mm the vertical distance between the 2 CsM layers (see Fig. 7.1).

This method is simple and does not take into account magnetometers location in each layer. Another method, which cares about Cs magnetometers positions is briefly described thereafter.

7.3.2 Pairs

The pairs method is basically the same method as the previous one except that only magnetometers having the same x and y position and occupying two different z layers can be coupled together in order to extract the vertical gradient.

$$\langle \partial_z B_z \rangle^{\text{Pairs}} = \left\langle \frac{B_{\text{top}} - B_{\text{bottom}}}{d} \right\rangle_{\text{Pairs}} \tag{7.7}$$

Once again, the position of magnetometers is not fully taken into account. Besides, the full available information is not used: magnetometers which are not paired are useless for this analysis.

7.3.3 Harmonic Taylor fit of B_z

Another method has been initially used by G. Pignol [123] to extract the vertical gradient during R-curve measurements in September 2012. This method uses the fact that during nEDM data taking, the magnetic field is mostly vertical in the usual coordinates frame (along the electric field direction). Using the assumption that transverse components of the field are very small compared to the vertical component, $||\vec{B}|| \simeq B_z$. This means that the modulus seen by caesium magnetometers can be considered to be approximately the vertical component of the field.

Starting from that point, it is possible to parametrise the measured field by a Taylor fit series expansion:

$$||\vec{B}|| \simeq B_z = B_{0z} + g_x x + g_y y + g_z z + g_{xx}(x^2 - z^2) + g_{yy}(y^2 - z^2) + g_{xy}xy + g_{xz}xz + g_{yz}yz \quad (7.8)$$

This expansion uses the same spatial dependence as the harmonic polynomials series expansion presented in Sec. 7.1. The correspondence between coefficients in Eq (7.8) and those shown in Tab. 7.1 is presented in Tab. 7.2.

B_{0z}	g_x	g_y	g_z	g_{xx}	g_{yy}	g_{xy}	g_{xz}	g_{yz}
$\mathcal{H}_3$	$\mathcal{H}_7$	$\mathcal{H}_8$	$-\mathcal{H}_4 - \mathcal{H}_6$	$\mathcal{H}_{13}$	$\mathcal{H}_{15}$	$\mathcal{H}_{14}$	$-2(\mathcal{H}_9 + \mathcal{H}_{11})$	$-2(\mathcal{H}_{10} + \mathcal{H}_{12})$

Table 7.2: Correspondence between harmonics coefficients and Taylor coefficients up to order 15 (polynomials of degree 2).

The position of each magnetometer being known, one can then fit the field seen by CsM using Eq (7.8). Indeed, one has at most 16 operating magnetometers, which is enough degrees of freedom to extract the 9 parameters of the harmonic Taylor series (7.8). Using some of those fitted parameters, it is then possible to get back to the vertical gradient:

$$\langle \partial_z B_z \rangle^{fit}_{\mathcal{V}_{Ch}} = g_z - \left(z_2^2 - z_1^2\right) \frac{(g_{xx} + g_{yy})}{H_{Ch}} \quad (7.9)$$

Error bars on the estimated gradient coming from the Taylor fit are obtained by means of the Jackknife estimator [124].

7.4 R-curve gradients reproducibility with 2013 maps

The goal of the toy model is to extract the error done during the vertical gradient estimation. Before applying this tool, it has to be shown that the reconstructed magnetic field from 2013 maps reproduces well the vertical gradient measured in real data. For such a purpose, a comparison has been performed between toy data and experimental 2012 R-curve data.

The different R-curve coils configurations have been reconstructed (with several B_0 maps). Then, the estimated Taylor fit gradient from the map $\langle \partial_z B_z \rangle^{\text{map}}$ is compared with the gradient estimated from R-curve data $\langle \partial_z B_z \rangle^{\text{exp}}$. Fig. 7.2 shows the difference between the two estimated gradients as a function of the R-curve run number.

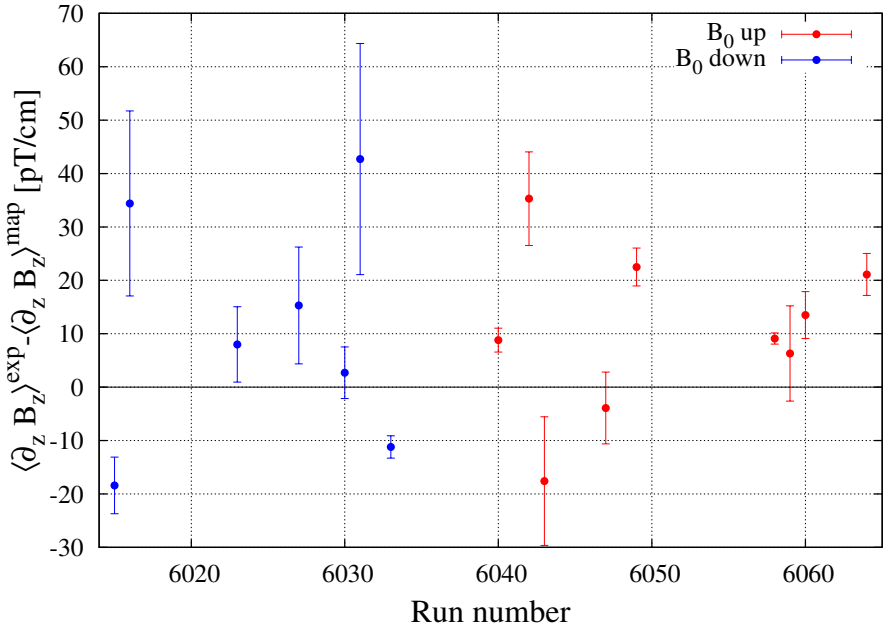

Figure 7.2: Difference between the estimated gradients from R-curve data and the reconstructed map as a function of the R-curve run number.

The mean difference between the extracted gradients, estimated through its RMS value, amounts to 9.9 pT/cm for B_0 up and to 16.8 pT/cm for B_0 down.

The largest gaps are observed for runs with larger currents in TTC and BTC (coils creating the vertical gradient), *i.e.* for larger vertical gradients ($\sim$150 pT/cm). It could mean that there is a problem with the reproduction of the field created by TTC or BTC. This is supported by the fact that residuals coming from the fit of the input BTC 2013 map have an unusual spread of about 3 nT on B_z, indicating a bad fit result [125]. This procedure has to be tried again with the new 2014 fluxgates maps in order to make sure that there is no problem with the map of this coil.

The conclusion of this check is that the online and offline gradient estimations give results consistent at the 15 pT/cm level. The difference can be partly explained by a gradient reproducibility of 6 pT/cm for both B_0 up and and down maps. Another reason could be that, on one hand, the fit is performed on perfect CsM data (reconstructed maps) and on the other hand, it is performed on real CsM data, in experimental conditions (CsM offsets due to cross-talk...). Finally, the reconstruction of the field using the 2013 maps is good enough to test the different gradient estimations.

7.5 Comparison of the three methods

7.5.1 Comparison in R-curve configurations

For this comparison, only two layers of CsM are used (as used for the 2012 R-curve and nEDM data taking) even if two super-bottom CsM are available. The difference between the vertical gradient from each method and the reconstructed map (used as input for the toy model) is shown in Fig. 7.3 for different gradients / currents in TTC and BTC, and for B_0 up field configuration.

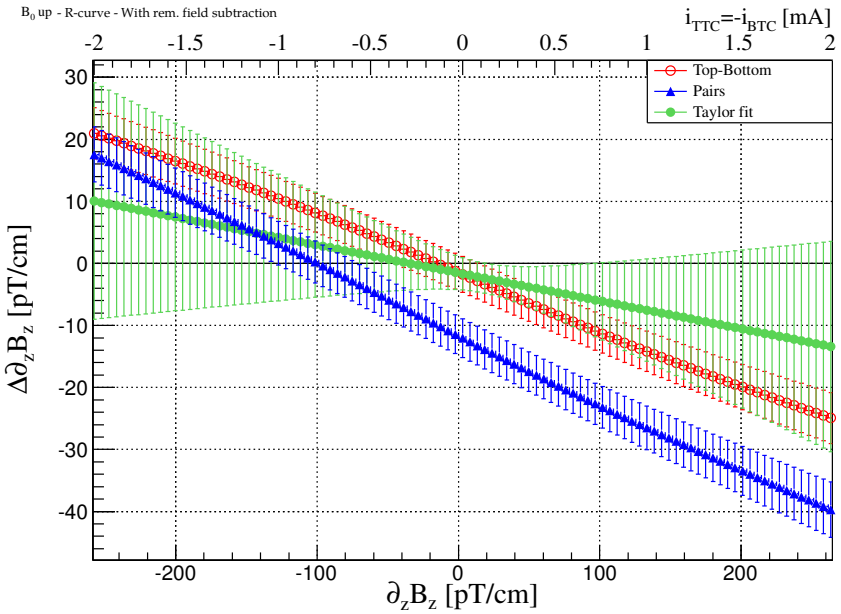

Figure 7.3: Difference between the estimated gradients and the reconstructed map gradient as a function of the input vertical gradient.

The difference between the input gradient and the estimated one can be expressed as a function of the input gradient:

$$\Delta \langle \partial_z B_z \rangle = a \langle \partial_z B_z \rangle^{\text{input}} + b \tag{7.10}$$

Fitted parameters values for each method are summarised in Tab. 7.3 for $B_0^{\uparrow}$ and $B_0^{\downarrow}$.

Method	$B_0^{\uparrow}$		$B_0^{\downarrow}$	
	a [%]	b [pT/cm]	a [%]	b [pT/cm]
Top-Bottom	-9.16(24)	-1.58(33)	-9.10(36)	-0.19(52)
Pairs	-11.22(26)	-1.14(36)	-11.15(38)	7.05(56)
R-curve Taylor fit	-4.50(76)	-1.56(56)	-4.45(84)	-1.5(10)

Table 7.3: Fitted parameters obtained from Eq (7.10) for each method.

The harmonic Taylor fit is the most accurate method, with the smaller slope. The gap between the input and the fitted values is lower than 7 pT/cm for currents used for the R-curve analysis, *i.e.* for currents in TTC-BTC between -1 and 1 mA. Besides, the non accuracy of the Taylor fit is consistent with 0 within error bars (see Fig. 7.3), which validates the Jackknife tool to estimate the statistical error on the gradient.

The map reconstruction has been done for all 2012 R-curve configurations in order to get an estimation of the gradient uncertainty coming from the harmonic Taylor fit in the framework of the γ_n/γ_{Hg} measurement. Results are shown in Fig. 7.4. The RMS values for B_0 up and B_0 down configurations are respectively 3.7 pT/cm and 4.7 pT/cm. For the other methods, the difference is larger, particularly for the pairs method. Thus, even if the precision of the averaging methods is better than the harmonic Taylor fit, their accuracy is lower.

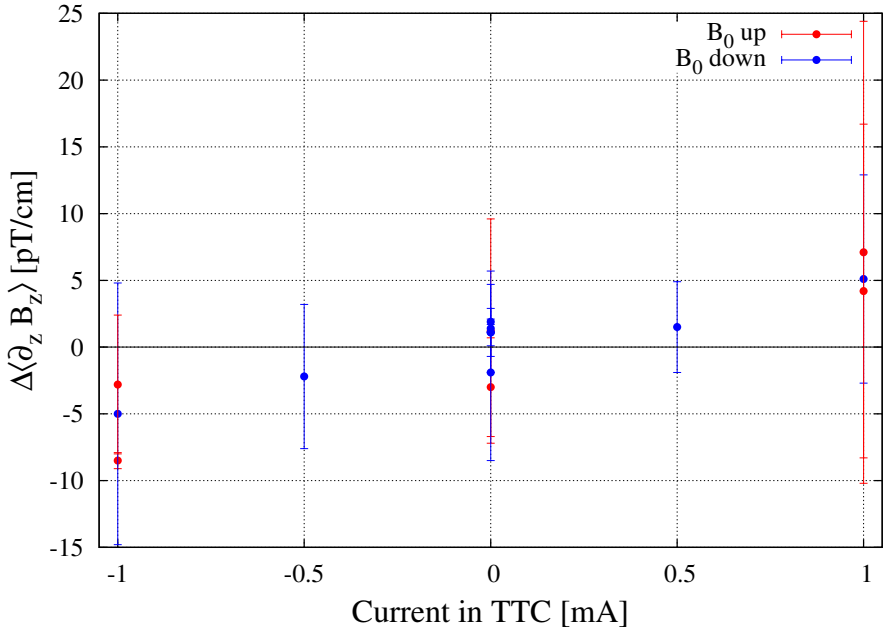

Figure 7.4: Difference between the input gradient and the estimated gradient for all 2012 R-curve current configurations, using the harmonic Taylor fit.

It has to be noticed that the super-bottom CsM ($z = -175\,\mathrm{mm}$) use decreases the accuracy of the Taylor fit by a factor 2, down to the same level as averaging methods. This is thought to be due to a larger fit sensitivity to high order field harmonics because of the large super-bottom CsM z position. It brings the idea to study the effect of the CsM positioning around the precession chamber on fit results. This study could help to improve the harmonic Taylor fit method and could be important in order to choose the CsM positions for further data taking with oILL and n2EDM.

7.5.2 Transverse field components effect on the gradient estimate

Because the harmonic Taylor fit is based on the assumption that $||\vec{B}|| \simeq B_z$, the effect of a large transverse field component on the gradient extraction has been studied. The H1B coil brings a main contribution along B_y. The difference of average gradients $\Delta \langle \partial_z B_z \rangle$ as a function of the B_y component created by the H1B coil up to order 15 is shown in Fig. 7.5. The field has only been produced until harmonic 15 in order to make sure that all B_z terms can be fitted during the harmonic Taylor fit.

The usual largest transverse fields one expects during nEDM data taking are at the 10 nT level. The studied range is larger in order to see limits of each method in terms of accuracy. The harmonic Taylor fit gives again the best results, below the 0.5 pT/cm level error, followed by the averaging methods which are at worst 5 pT/cm accurate for rather large transverse fields of 10 nT (the -11 pT/cm offset for the pairs method is obviously not due to the transverse field itself). The conclusion of this study is that low order transverse fields are not a problem for the harmonic Taylor fitting method, but could be problematic for the top-bottom averaging method.

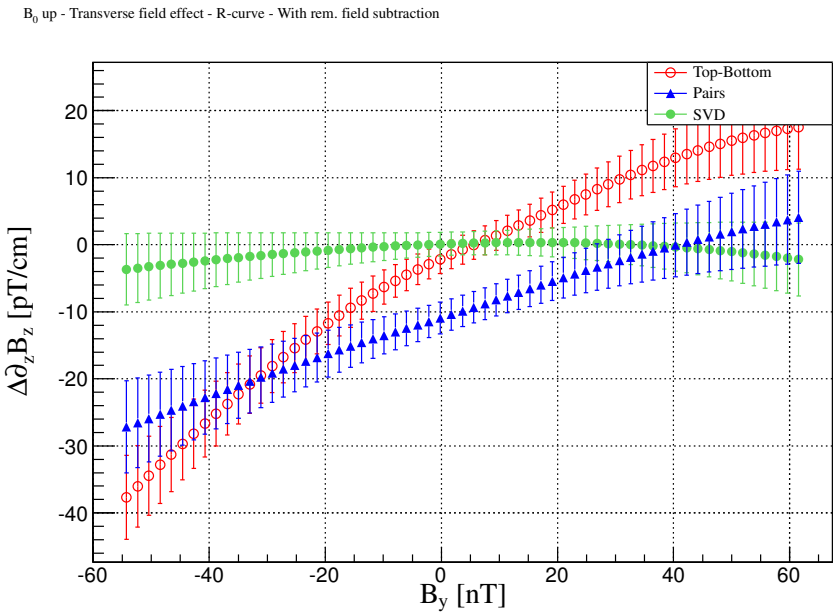

Figure 7.5: Difference between the estimated gradients and the reconstructed map gradient as a function of the B_y field component strength. The field is only reconstructed using the B_0 coil (up direction) and the H1B coil.

7.5.3 Harmonic Taylor fitting method improvement

It has been shown in the previous section that the transverse field effect on the gradient estimate by means of the harmonic Taylor fit is lower than the 0.5 pT/cm level for usual transverse fields. The remain of the harmonic fit non-accuracy is mainly due to the field contribution of harmonics higher than 15. Indeed, higher harmonics are not fitted because of the limited number of CsM (12 here). This effect is visible in Fig. 7.6 where is shown the difference of average gradients $\Delta \langle \partial_z B_z \rangle$ as a function of the last harmonic used to produce the magnetic field. To further emphasise the effect, a B_0 up R-curve configuration with 1/-1 mA currents in TTC/BTC coils is used as an example.

The first observation is that the Taylor fit is accurate up to the order 15, the last fitted harmonics. Then, for harmonics 16, 20 and 31, a clear step in the error is visible. This is explainable looking at the terms difference between (7.5) and (7.9). In the Taylor fit, 3 harmonic coefficients for 3$^{\text{rd}}$ ($\mathcal{H}_{16}$,$\mathcal{H}_{18}$,$\mathcal{H}_{20}$) and 4$^{\text{th}}$ ($\mathcal{H}_{31}$,$\mathcal{H}_{33}$,$\mathcal{H}_{36}$) degrees polynomials, contributing to the mean gradient, are not taken into account. The consequence of that is first to decrease the fit accuracy, but also to decrease its precision, for instance as visible starting from harmonics 20 with error bars increased from 2 pT/cm to more than 5 pT/cm. Therefore, a possible improvement for next steps of the nEDM experiment in the vertical gradient control could be to use more CsM located on different z layers in order to be able to fit those 6 additional harmonics which have a non negligible contribution to the average vertical gradient.

To test this possibility, it was first assumed that all CsM located around the precession chamber work but the super-bottom, *i.e.* 14 magnetometers in total. The additional fitted parameters are ($\mathcal{H}_{16}$,$\mathcal{H}_{18}$,$\mathcal{H}_{20}$) and $\mathcal{H}_{31}$, increasing the number of fit parameters up to 13. This time, the difference between the reconstructed map gradient and the fitted gradient does not exceed 3.6 pT/cm ($\langle \partial_z B_z \rangle^{\text{input}} \sim 120$ pT/cm). In average, this difference has been decreased from 4.7 and 3.7 pT/cm

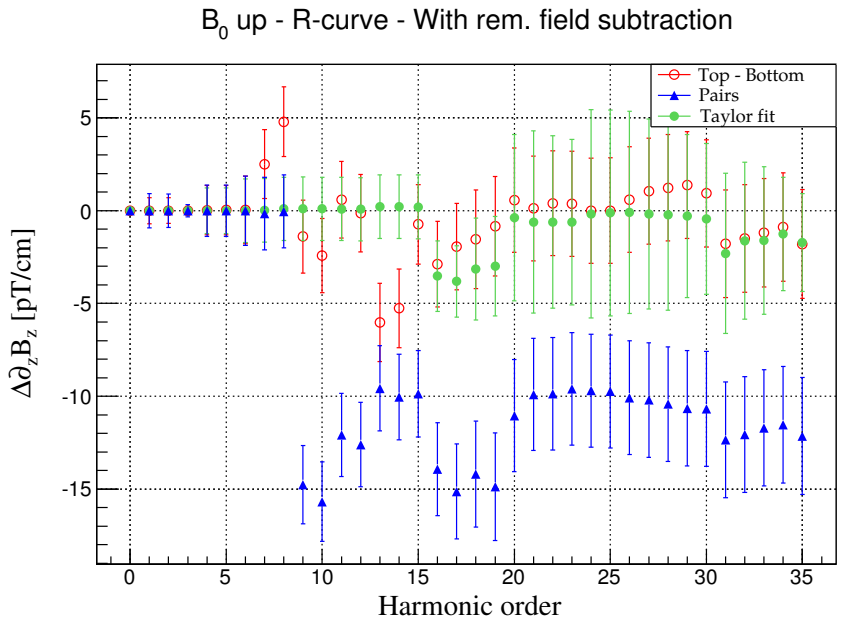

Figure 7.6: Difference between the estimated gradients and the reconstructed map gradient as a function of the last harmonics used to produce $\vec{B}$.

for respectively B_0 down and B_0 up configurations down to 1.9 and 1.3 pT/cm using the fit with additional harmonics. It shows that the harmonic Taylor fit can be improved by carefully selecting the harmonics to be fitted.

7.6 Test of a 3D harmonic fit

The vertical gradient is not the only magnetic field observable which induces a false EDM. The squared transverse field to the main field direction $\langle B_\perp^2 \rangle$ is also the source of a systematic error during the so-called crossing point analysis (see 6.8.1.2). The false EDM arising from $\langle B_\perp^2 \rangle$ is given by:

$$d_{\text{false}} = \frac{\hbar \gamma_n \gamma_{Hg} D^2}{128 c^2 B_0 \Delta h} \left(\langle B_\perp^2 \rangle^\downarrow - \langle B_\perp^2 \rangle^\uparrow \right) \tag{7.11}$$

For the moment, scalar CsM which are used can not provide enough information to recover this transverse component by means of the harmonic Taylor fit. The related systematic error is currently estimated through the magnetic field maps which are measured each winter shut-down. Current estimates of $\langle B_\perp^2 \rangle$ give values at the 1-2 nT^2 level with precisions of about 0.5 nT^2.

A possible way to get online the systematic effect in the near future could be to use 3D caesium vector magnetometers [126] and perform a full 3D harmonic fit on the field created from a reconstructed map [127]. The aim of such a method is to determine $\langle B_\perp^2 \rangle$ as accurately as possible in order to correct precisely the corresponding systematic effect and keep a good determination of the vertical gradient.

The goal of the following study is to use the same toy model as previously and replace scalar CsM by 3D vector CsM in order to get an idea of the reachable accuracy on $\langle B_\perp^2 \rangle$ using 3D magnetometers. This time, the fit is performed using the R-curve CsM configuration with two additional CsM on the top plate in order to have 16 CsM values (to be able to fit 15 parameters). The fit is performed now on the three field components and not only on the field modulus ($||\vec{B}|| \simeq B_z$). From the 15 fitted first harmonics, the average field over the precession chamber volume $\langle \vec{B} \rangle$

is recovered by Monte-Carlo. Then, the average transverse field is recovered by averaging:

$$B_\perp(\vec{r})^2 = B(\vec{r})^2 - \left(\frac{\vec{B}(\vec{r}).\langle\vec{B}\rangle}{||\langle\vec{B}\rangle||} \right)^2 \tag{7.12}$$

Then, the average value of $B_\perp(\vec{r})^2$ over the chamber volume obtained with the harmonic fit is compared to the value obtained from the reconstructed map itself $\langle B_\perp^2 \rangle^{\text{map}}$. In average, the reachable accuracy given by the fit is about 0.2 nT^2.

At the same time, the average gradient over the chamber volume is recovered through the 15 first harmonics. Again, because ($\mathcal{H}_{16}$,$\mathcal{H}_{18}$,$\mathcal{H}_{20}$,$\mathcal{H}_{31}$) are not fitted, the accuracy of the fit is limited, here to about 20 pT/cm.

7.6.1 Improvement of the 3D harmonic fit

In order to reach a better accuracy on $\langle B_\perp^2 \rangle$, it is possible to use the same method as for the vertical gradient, *i.e.* by identifying the harmonics at larger orders contributing to the observable of interest. An example of such contributions is shown in Fig. 7.7 for a B_0 up configuration with 1/-1 mA currents in TTC/BTC (which showed the largest $\langle B_\perp^2 \rangle$ difference of about 0.5 nT^2).

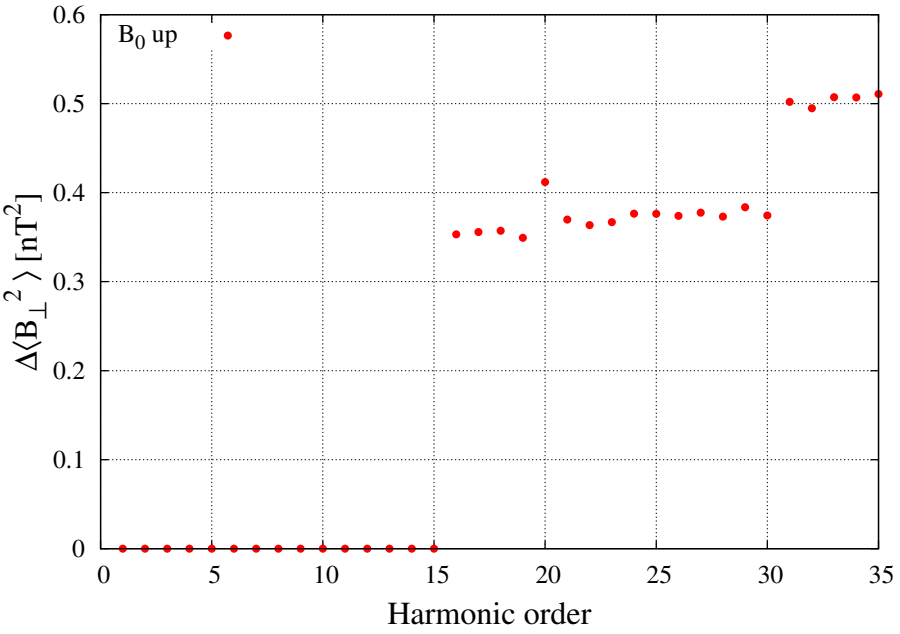

Figure 7.7: Difference between the estimated $\langle B_\perp^2 \rangle$ from the 3D harmonic Taylor fit and from the reconstructed map as a function of the last harmonics used to produce $\vec{B}$.

From this study, harmonics $\mathcal{H}_{16}$, $\mathcal{H}_{20}$ and $\mathcal{H}_{31}$ show a rather large influence on the $\langle B_\perp^2 \rangle$ determination with the 3D harmonic fit for B_0 up configurations ($\mathcal{H}_{18}$ is also important for B_0 down configurations). As a result, it shows that these harmonics, already important for the gradient estimation, have to be fitted in order to estimate the transverse field properly. In order to fit these additional parameters, one needs more 3D magnetometers around the precession chamber.

Four virtual additional CsM have been placed around the precession chamber at cardinal positions, at $z = 0$, and at $r = 300$ mm. With these magnetometers, one ends up with a total

of 20 vector magnetometers used to fit 19 parameters. The difference of $\langle B_\perp^2 \rangle$ between the 3D harmonic fit and the reconstructed map is shown in Fig. 7.8 for each field configuration used during R-curve measurements.

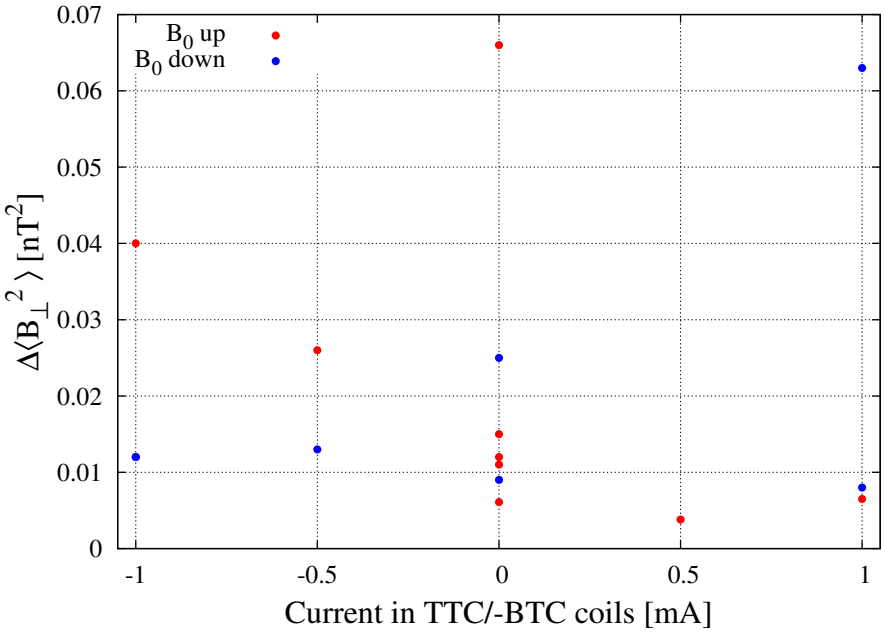

Figure 7.8: Difference between the estimated $\langle B_\perp^2 \rangle$ from the 3D harmonic Taylor fit and from the reconstructed map as a function of the current in TTC/BTC.

The result of this study is that it is possible to reach a rather accurate measurement of $\langle B_\perp^2 \rangle$ – most of the time below the $0.03\,\mathrm{nT}^2$ level – using the 3D harmonic fit, assuming a large amount of working 3D magnetometers. At the same time, the obtained accuracy on the average gradient is improved down to 2.0 and 1.2 pT/cm in average, for respectively B_0 up and B_0 down configurations, with a statistical precision of 4 pT/cm, *i.e.* at the same level as from the "scalar" Taylor fit. It shows that it is necessary to determine first which harmonics mainly contribute to $\langle B_\perp^2 \rangle$ for each field configuration before performing the harmonic Taylor fit. Once this step is done, determinations of both the squared transverse field and the average gradient are accurate enough to properly estimate systematics in R-curves and nEDM measurements. The location of the CsM could also be optimised for the field configurations used in these measurements.

7.7 Conclusions

This toy model has shown that vertical gradients measured during the 2012 R-curve campaign are reproduced using a reconstruction of the field from 2013 maps at a better level than 15 pT/cm in average. From this toy model, the harmonic Taylor fit has been shown to be the best method to get an online estimation of the vertical gradient in the precession chamber, at the 4 pT/cm accuracy level. At the same time, this accuracy is consistent with the gradient errors estimated by means of the Jackknife tool after the fitting process. The accuracy of the harmonic Taylor fit can be further improved to the 2 pT/cm level by selecting additional harmonics at higher orders and using the full set of available caesium magnetometers. A possible way to fit additional harmonics without using too many CsM could be to remove low order harmonics which does not contribute

to the gradient estimation and to find a clever place for each magnetometer around the precession chamber (for instance using genetic algorithms).

The toy model has also been used to prospect an online determination of $\langle B_\perp^2 \rangle$ using vector caesium magnetometers which could be used for the n2EDM phase. It showed that using at least 20 vector CsM and fitting the appropriate harmonics, it is possible to determine $\langle B_\perp^2 \rangle$ down to the $0.05\,\mathrm{nT}^2$ level, with the same accuracy and precision on the average gradient as using scalar magnetometers. It gives a perspective towards an estimation of the false EDM due to the quadrupole difference during the nEDM data taking down to the 10^{-28} e.cm level.

Chapter 8

Conclusion and perspectives

The work presented in this thesis is three fold: the design, the building and the test of a new simultaneous analyser, the analysis of the 2013 nEDM data and the study of estimators of the vertical magnetic field gradient and the squared transverse magnetic field.

The USSA, a new simultaneous spin analyser for ultra cold neutrons, has been tested. It has been designed using Geant4-UCN simulations and built at LPC Caen. One of its initial goals was to symmetrically treat the two UCN spin states. With the characterisation of USSA subsystems on the West-2 beam line at PSI, it has been shown that this goal is fulfilled. The USSA was then installed below the nEDM spectrometer in order to test its performances with nEDM data taking conditions. This test was also successful: the number of detected UCNs is increased by $23.9 \pm 1.0\%$ and the Ramsey central fringe visibility by $6.2 \pm 4.9\%$ with respect to the sequential analyser. These improvements lead to an nEDM statistical sensitivity gain of $18.2 \pm 6.1\%$. Since the USSA tests below the apparatus lasted only one week, this conclusion has to be confirmed with the 2014 nEDM data. Nevertheless, the USSA is now part of the nEDM apparatus.

This sensitivity gain can be further increased using a coating with a higher Fermi potential, as suggested by Geant4-UCN results which predict an increase of the number of detected UCNs of a few percents using a diamond coating. This estimate is likely underestimated since in the simulation the USSA is 25 cm too high with respect to the real location in the nEDM apparatus. Furthermore, it has been shown that 50 to 60% of the UCNs coming from the chamber are detected with the USSA. A fraction of them could therefore be recovered using a higher Fermi potential. It is planned to coat the USSA walls with ^{58}NiMo. R&D efforts to perform such a coating will also benefit other guiding parts of the apparatus. Another coating option is the diamond but the coating technique is still under development. However, diamond coating samples have already been produced. The measured Fermi potential is about 305 neV. Tests of its storage properties are planned (the loss per bounce parameter η and the depolarisation probability β). Such a coating could also be used in the precession chamber and would therefore allow a wider UCN energy range to be stored.

During August 2013, nEDM data have been collected. The key parameters for a high nEDM sensitivity were rather good: $T = 180\,\mathrm{s}$, $N_a = 6660$, $\alpha_a = 59.6\%$ and $E = 10\,\mathrm{kV/cm}$. A part of this thesis is dedicated to this data set analysis. Such analysis is important since it allows one to check the data quality during the experiment.

The neutron Larmor frequency estimation has been investigated. An alternative technique - based on the asymmetry - has been tested using experimental and simulated data. A better robustness of the asymmetry fit has been observed with respect to the normalised neutron counts fit. If the switch is not properly positionned for the monitoring, the neutron counts normalisation does not work while the asymmetry does. Therefore, it suggests that there could be a problem of switch mispositionnings which are not accounted for in the analysis yet, ending by normalisation problems. Further detailed investigations are therefore strongly required.

The study of the neutron Larmor frequency fit has been performed with several methods to estimate the Hg frequency. It has been shown that the choice of the method is indeed crucial to obtain a reliable fit quality. The RAL-Sussex-ILL method has been revisited. A new technique

developed at LPSC appears to be more suited since it takes into account the low performances of the Hg co-magnetometer. The rather low transverse relaxation time of the mercury ($T_2 \sim 45\,\mathrm{s}$) led to a poor Hg statistical error ($\sigma_{f_{\mathrm{Hg}}} \simeq 3\,\mu\mathrm{Hz}$), which significantly contributes (15%) to the R ratio. This contribution propagates then to the nEDM uncertainty. Therefore, the collaboration is actively working on increasing the Hg T_2 time. In case the depolarisation time T_2 would remain low, efforts in the Hg frequency analysis have to be pursued at LPSC, as it is currently the most important contribution to the Larmor frequency fit quality.

In order to further check the analysis, a toy model has been set-up and simulated data have been produced. A potential explanation for the poor neutron Larmor frequency fit quality has been found. A small and slow magnetic field gradient variation is enough to deteriorate the fit quality. Magnetic field gradient variations observed in experimental data have been simulated. The resulting reduced χ^2 of the neutron Larmor frequency fit is in good agreement with experimental observations ($\tilde{\chi}^2 \simeq 1.15$). Because temperature variations are a possible cause for the variations of the magnetic field gradient variation [111], a better thermal insulation and stabilisation of the thermohouse could possibly solve this problem.

The next step was to perform the nEDM data analysis. Even if the measured statistical precision is in agreement with expectations, the analysis pointed out a problem linked to the electric field: the fit providing the nEDM value ($R = f(HV)$) produced a $\tilde{\chi}^2$ larger than 4.5 for more than 50% of the runs. This problem - perhaps related to HV discharges - has to be confirmed and solved for the next nEDM data taking.

With a simple averaging without correction of the geometric phase effect (GPE), the measured nEDM is $d_{\mathrm{n}} = (-0.50 \pm 0.83) \times 10^{-25}\,e.\mathrm{cm}$, *i.e.* corresponding to a sensitivity of about $4 \times 10^{-24}\,e.\mathrm{cm}$ per cycle. Thus, it shows that in spite of problems mentioned above, the nEDM collaboration is able to reach the $2 \times 10^{-26}\,e.\mathrm{cm}$ sensitivity over 3 years, if the oILL spectrometer reliably runs for 4 months every year.

For the last step of the analysis, the crossing point technique, the GPE correction is not fully satisfactory since two runs are off the expected curve for the B_0 up configuration ($\tilde{\chi}^2 \simeq 2.2$). However, the technique properly worked for the B_0 down configuration ($\tilde{\chi}^2 \simeq 0.8$). The final result is $d_{\mathrm{n}} = (-2.3 \pm 3.4) \times 10^{-25}\,e.\mathrm{cm}$.

In the last part of this work, estimators of the magnetic field vertical gradient using scalar caesium data have been studied using a "toy model". This study, relying on realistic field simulations from measured magnetic field maps, has shown that the best method to estimate the magnetic field gradient is the so-called harmonic Taylor fitting method, reliable up to a few pT/cm. A possible improvement has been proposed, by selecting the most contributing harmonics in the fitting function. Such a technique would allow the magnetic field gradient accuracy to be improved by more than a factor 2, down to the 1-2 pT/cm level. This study was initially carried out in the framework of the neutron to Hg magnetic moments ratio measurement $\gamma_{\mathrm{n}}/\gamma_{\mathrm{Hg}}$ in order to estimate the reliability of the harmonic Taylor fit used to extract the magnetic field gradient. The uncertainty on the ratio has been reduced down to 1 ppm, using the 2012 R-curve data [14].

In the n2EDM phase, vector caesium magnetometers localised around the precession chamber should be able to measure the magnetic field at the pT precision level. They are currently under development at PSI. A prototype has been installed on the mapper built at LPC and used during the 2014 winter magnetic field mapping. The toy model has also been used to prospect the online recovery of the squared transverse magnetic field using such vector magnetometers. The technique used to estimate the squared transverse field is the harmonic fit in three dimensions. Combined to the selection of the most important harmonics, it allows the average gradient over the precession volume to be measured close to the pT/cm level and the squared transverse field with a very good accuracy of a few $0.01\,\mathrm{nT}^2$. With such an accuracy on the squared transverse field, the quadrupole

effect could be corrected with an error improved by a factor 10 with respect to the current value, down to the 10^{-28} e.cm level. Thus, it gives a perspective towards the control of one of the main nEDM systematics during the n2EDM phase.

The goal of the second phase of the nEDM project is twofold. First, the collaboration aims at improving the UCN statistics and second at achieving a magnetic field as homogeneous as possible in the precession volume. The nEDM measurement will be carried out in a double storage chamber in order to simultaneously measure the neutron Larmor frequencies in parallel and anti-parallel magnetic and electric fields configurations. The number of detected UCNs will be doubled with respect to a single precession chamber. Higher electric fields will be applied thanks to a new geometry of the electrodes. The control of the magnetic field will be achieved by means of a new multilayer magnetic shield with a shielding factor of about $5 \times 10^4 - 1 \times 10^5$, to lower the field gradient below 1 pT/cm. In addition, the n2EDM B_0 coil is being designed in such a way that it would not induce a magnetisation of the shield [110], providing a better magnetic field homogeneity. The precession volume will be monitored by a laser based Hg co-magnetometer. In addition to the external vector caesium magnetometers, two "layers" of ^{3}He magnetometers above and below the UCN storage volume will be used as gradiometers to control gradient related systematics. Thanks to these improvements on the statistical precision and the systematic errors control, it is planned to improve the limit on the neutron EDM down to 4×10^{-27} e.cm in about 10 years with current performances of the UCN source. If the UCN source reaches its nominal performances, the 10^{-28} e.cm range will be explored, allowing decisive tests of new physics scenarios.

Appendices

Appendix A

Adiabaticity parameter for the guiding coils system

The goal of this short part is to show how the UCN spin ability to follow guinding fields produced by the guiding coils system can be quantified. For such a purpose, let us go back to Eq (2.30), giving the classical description of the UCN spin dynamics in the laboratory frame $\mathcal{R}_{\text{lab}}$, in a static magnetic field:

$$\left(\frac{\mathrm{d}\vec{S}}{\mathrm{d}t}\right)_{\mathcal{R}_{\text{lab}}} = \gamma_n \vec{S} \times \vec{B}$$

Along the UCN path, the magnetic field becomes time dependent as neutrons move. Locally, any change of the magnetic field can be expressed as a rotation. In the neutron rest frame rotating $\mathcal{R}_{neutron}$ with the angular frequency $\vec{\Omega}$, Bloch equations become:

$$\begin{aligned}\left(\frac{\mathrm{d}\vec{S}}{\mathrm{d}t}\right)_{\mathcal{R}_{neutron}} &= \gamma_n \vec{S} \times \left(\vec{B} - \frac{\vec{\Omega}}{\gamma_n}\right) \\ &= \vec{S} \times \left(\vec{\omega_L} - \vec{\Omega}\right)\end{aligned} \tag{A.1}$$

Eq (A.1) explicitly shows the contribution from the Larmor angular frequency ω_L and from the field rotation rate $\Omega = \left|\frac{\mathrm{d}B/\mathrm{d}t}{B}\right|$. These frequencies are compared through the adiabaticity coefficient k defined by:

$$k = \frac{\omega_L}{\Omega} \tag{A.2}$$

$$= \frac{\gamma_n B^2}{|\mathrm{d}B/\mathrm{d}t|} \tag{A.3}$$

If the field change is much lower than the Larmor angular frequency ($k \gg 1$), then the neutron spin is able to adiabatically follow the magnetic field. On the contrary ($k < 1$) the UCN spin is not able to stay aligned on the magnetic field and depolarisation occurs. $k \simeq 5 - 10$ is the transition between the two regimes. In the experiment, the UCNs polarisation is kept along their trajectories using smoothly varying holding fields produced by the guiding coils.

Appendix B

Adiabaticity parameter equation in the adiabatic spin-flipper case

The spin-flipper is called "adiabatic" because the UCN spin adiabatically follows the effective field in this device. This effective field is the sum of two orthogonal fields. The first one is the static field $\overrightarrow{H_0} = H_0(z)\vec{u}_x$ coming from the magnetic field used to magnetize the analyser, decreasing along the spin-flipper area. The other one is the RF field created by the spin-flipper itself, rotating in the plane perpendicular to $\overrightarrow{H_0}$.

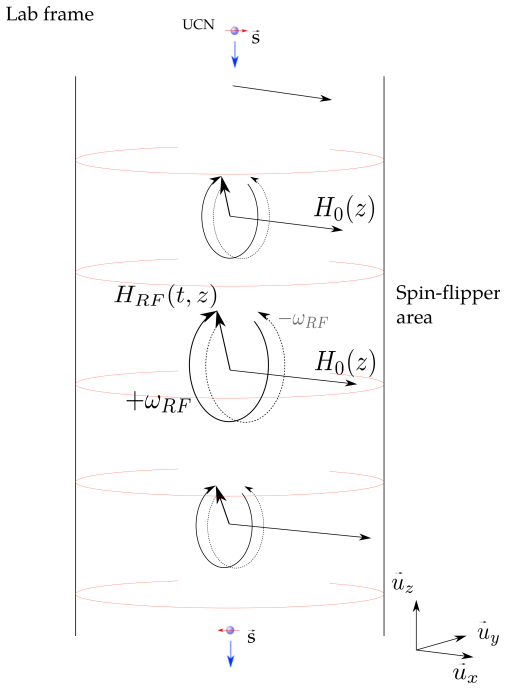

Figure B.1: Scheme of the magnetic fields used to perform the neutron spin-flip, in the laboratory frame.

In this part, the spin is treated as classical magnetic moment in external fields. The goal is to find the equation of the adiabaticity parameter in the case of a particular magnetic fields configuration. A scheme of the UCN motion is shown in Fig. B.1. The UCN spin is initially aligned along the static field $\vec{H}_0(z)$. The RF frequency ω_{RF} of the spin-flipper with a length L is set such as a resonance between the static and the RF fields occurs in the middle-plane of the spin-flipper:

$$H_0(L/2) - \frac{\omega_{\mathrm{RF}}}{\gamma_{\mathrm{n}}} = 0 \tag{B.1}$$

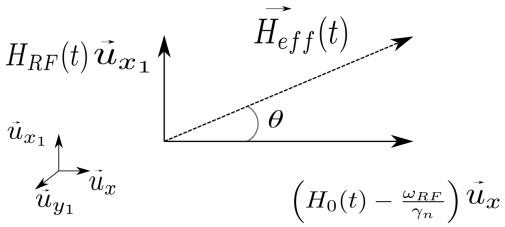

Figure B.2: Magnetic fields scheme in the neutron rest frame rotating at the frequency ω_{RF} around the $\vec{H}_0$ axis.

In the neutron rest frame rotating at the frequency ω_{RF} around the $\vec{H}_0$ axis (see Fig. B.2), one has:

$$\vec{H}_{\mathrm{eff}} = \left(H_0(t) - \frac{\omega_{\mathrm{RF}}}{\gamma_{\mathrm{n}}}\right)\vec{u}_x + H_{\mathrm{RF}}(t)\,\vec{u}_{x1} \tag{B.2}$$

The UCN spin undergoes a torque due to this field:

$$\frac{\mathrm{d}\vec{S}}{\mathrm{d}t} = \gamma_{\mathrm{n}}\vec{S} \times \overrightarrow{H_{\mathrm{eff}}} \tag{B.3}$$

It can be re-written in the coordinate frame along the effective field as:

$$\frac{\mathrm{d}\vec{S}}{\mathrm{d}t} = \gamma_{\mathrm{n}}\vec{S} \times \left(\vec{H}_{\mathrm{eff}} + \frac{\vec{\Omega}}{\gamma_{\mathrm{n}}}\right) \tag{B.4}$$

where $\Omega = \frac{\mathrm{d}\theta}{\mathrm{d}t}$, with θ the rotation angle between the component along $\vec{z}$ and the effective field $\vec{H}_{\mathrm{eff}}$. The adiabatic spin-flip can occur only if the adiabaticity coefficient $k = \frac{\gamma_{\mathrm{n}} H_{\mathrm{eff}}}{\Omega} \gg 1$. In order to determine k, one first needs to determine the value of Ω as a function of the used fields. In that case, one has:

$$\begin{cases} \vec{H}_{\mathrm{eff}}(t) = H_{\mathrm{eff}}(t)\sin\theta\,\vec{u}_{x1} + H_{\mathrm{eff}}(t)\cos\theta\,\vec{u}_x \\ \vec{H}_{\mathrm{eff}}(t) = H_{\mathrm{RF}}(t)\,\vec{u}_{x1} + \left(H_0(t) - \frac{\omega_{\mathrm{RF}}}{\gamma_{\mathrm{n}}}\right)\vec{u}_x \end{cases} \tag{B.5}$$

Identifying the terms along $\vec{u}_{x1}$ and $\vec{u}_x$ in the system of equations (B.5) gives:

$$\begin{cases} H_{\mathrm{RF}}(t) = H_{\mathrm{eff}}(t)\sin\theta \\ H_{\mathrm{eff}}(t)\cos\theta = H_0(t) - \frac{\omega_{\mathrm{RF}}}{\gamma_{\mathrm{n}}} \end{cases} \tag{B.6}$$

Through the first equation of (B.6), one makes appear Ω:

$$\Omega = \frac{\mathrm{d}\theta}{\mathrm{d}t} = \left(\frac{\partial H_{\mathrm{RF}}}{\partial t} - \frac{\partial H_{\mathrm{eff}}}{\partial t}\sin\theta\right) \cdot \frac{1}{H_{\mathrm{eff}}\cos\theta} \tag{B.7}$$

$$= \frac{\partial H_{\mathrm{RF}}}{\partial t}\frac{\cos\theta}{H_{\mathrm{eff}}} - \frac{\partial H_0}{\partial t}\frac{\sin\theta}{H_{\mathrm{eff}}} \tag{B.8}$$

At the resonance (middle of the spin flipper), the spin has to be flipped by $\theta = \pi/2$ to be fully flipped at the exit of the spin-flipping area. Therefore, the contribution coming from the H_{RF} time derivative cancels and $H_{\mathrm{eff}} = H_{\mathrm{RF}}$. For the vertical UCN speed v_{n}, Ω reads:

$$|\Omega| = \left| v_{\mathrm{n}} \frac{\frac{\mathrm{d}H_0}{\mathrm{d}z}}{H_{\mathrm{RF}}} \right| \tag{B.9}$$

Finally, the adiabaticity coefficient is:

$$k = \frac{\gamma_n H_{\mathrm{RF}}^2}{v_{\mathrm{n}}\frac{\mathrm{d}H_0}{\mathrm{d}z}} \tag{B.10}$$

In the case of the adiabatic spin-flipper use, the oscillating and static fields can be described as:

$$\begin{cases} H_{\mathrm{RF}}(z) = H_{\mathrm{RF}_0} \sin \frac{\pi z}{L} \\ H_0(z) = B + A \cos \frac{\pi z}{L} \end{cases} \tag{B.11}$$

This particular field configuration allows the adiabatic spin-flip probability to be calculated according to the sine-cosine model [69, 90]:

$$p = 1 - \frac{\sin^2\left(\frac{\pi}{2}\sqrt{1+k^2}\right)}{1+k^2} \tag{B.12}$$

This spin-flip probability is shown in Fig. B.3 as a function of the adiabaticity coefficient. It shows that starting from a given adiabaticity parameter, the spin-flip probability is about 100%. As a result, with appropriate field conditions, neutrons undergo a spin-flip in the UCN energy range.

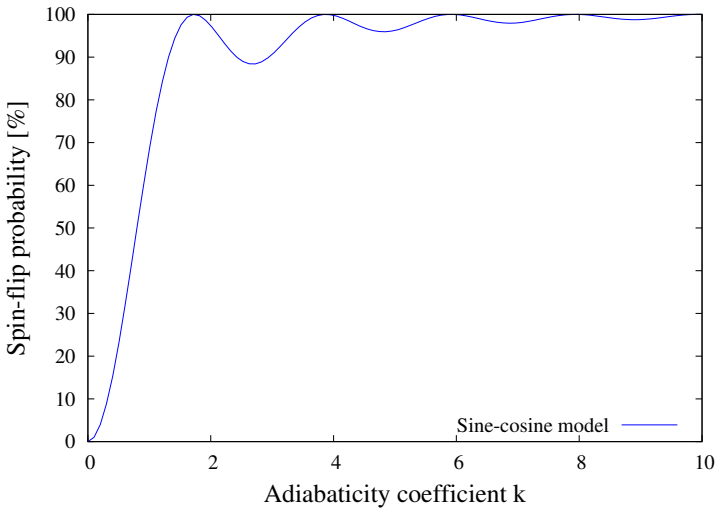

Figure B.3: Spin-flip probability given by the sine-cosine model.

Experimentally, the spin-flipper produces a linear polarized field with an amplitude H_{RF_i}, along the guide axis around which the ASF is wound. As a result, the efficient part of the RF signal contributing to the resonance is lower than the full signal amplitude. Indeed, it is possible to consider the linear oscillating field as the superposition of two fields rotating in opposite directions (see Fig. B.4 [92]). One field rotates at the angular speed $+\omega_{\mathrm{RF}}$ at resonance and the other one at $-\omega_{\mathrm{RF}}$ out of resonance. Finally, the effective amplitude of the signal is $H_{\mathrm{RF}_0} = H_{\mathrm{RF}_i}/2$.

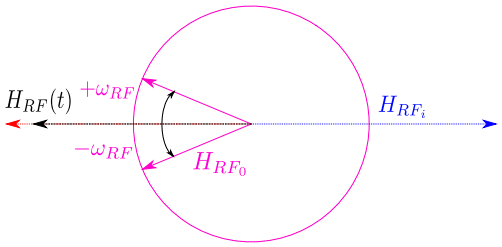

Figure B.4: Oscillating linear field polarisation decomposition into two circular contributions.

Appendix C

2013 nEDM runs summary

The 2013 EDM running parameters are summarised in this appendix, by means of Tab. C.1.

Run	Cycles	N_a	α_a [%]	HV [kV]
7454	62	5465	62.6 ± 1.9	80
7609	120	4400	61.7 ± 1.8	132
7614	110	4600	61.7 ± 1.4	132
7639	550	8100	59.4 ± 0.5	132
7640	84	7700	56.9 ± 1.3	132
7643	200	7300	58.5 ± 0.9	115
7645	228	6300	62.0 ± 1.0	115
7647	126	6550	63.6 ± 1.3	115
7648	231	6700	60.4 ± 1.0	115
7650	600	5850	59.2 ± 0.6	115
7666	117	7250	58.6 ± 1.0	115
7673	276	6800	57.6 ± 0.7	120
7674	163	6600	56.6 ± 0.9	120

Table C.1: Summary of 2013 EDM running parameters. The precession time was 180 s during these runs.

Run	$\tilde{\chi}^2_{\mathcal{A}}$	σ_{f_n} [µHz]	σ_{f_Hg} [µHz]	R	$\sigma^{\mathrm{exp}}_{d_\mathrm{n}}$ [$\times 10^{-25}$ e.cm]	$d^{\mathrm{meas}}_{\mathrm{n}}$ [$\times 10^{-25}$ e.cm]	$\tilde{\chi}^2_{d_\mathrm{n}}$
7454	1.21	19.6	4.6	3.84243667(71)	11.2	-12.4 ± 11.6	-
7609	1.11	19.7	0.8	3.84247609(46)	3.8	-8.8 ± 4.3	2.32
7614	1.18	20.7	1.5	3.84243377(46)	4.2	0.5 ± 4.5	8.95
7639	1.20	15.6	2.4	3.84246715(15)	1.6	3.4 ± 1.6	6.37
7640	1.15	17.7	2.7	3.84245824(50)	4.5	0.4 ± 5.0	0.13
7643	1.00	17.4	2.8	3.84245882(31)	3.2	6.0 ± 3.5	5.74
7645	1.05	16.8	3.5	3.84243230(27)	3.2	5.8 ± 3.5	4.69
7647	1.27	17.1	3.1	3.84244399(38)	4.5	-1.7 ± 4.7	4.36
7648	1.09	17.5	3.2	3.84243225(30)	3.2	-3.8 ± 3.5	8.41
7650	1.23	18.6	3.4	3.84242684(19)	2.2	-5.3 ± 2.2	0.75
7666	1.29	17.2	0.7	3.84247139(34)	3.9	-0.7 ± 3.9	6.71
7673	0.99	18.3	0.9	3.84245125(23)	2.3	-1.6 ± 2.6	0.07
7674	1.21	19.3	1.2	3.84244439(35)	3.5	-0.9 ± 3.5	0.01

Table C.2: Summary of 2013 EDM precisions on the neutron and Hg Larmor frequencies. The nEDM statistical precision and the reduced χ^2 of the R vs high voltage fit have been added.

In addition to Tab. C.1, precisions obtained for the mercury and neutron Larmor frequencies as well as the precision on the nEDM for each run are summarised in Tab. C.2. $\sigma_{d_\mathrm{n}}^{\mathrm{exp}}$ is the expected nEDM sensitivity for the run. It is calculated using Eq (2.17) and takes into account the Hg frequency precision. In addition, it is scaled by the square root of the reduced χ^2 of the neutron Larmor frequency fit $\tilde{\chi}^2_{\mathcal{A}}$.

Bibliography

[1] C. A. Baker, D. D. Doyle, P. Geltenbort, K. Green, M. G. D. van der Grinten, P. G. Harris, P. Iaydjiev, S. N. Ivanov, D. J. R. May, J. M. Pendlebury, J. D. Richardson, D. Shiers, and K. F. Smith. Improved experimental limit on the electric dipole moment of the neutron. *Phys. Rev. Lett.*, 97:131801, 2006. (Cited on pages 3, 6, 9, 33, 41, 48, 59, 141, 143 and 147.)

[2] G. Taubes. Theorists nix distant antimatter galaxies. *Science*, 278:226, 1997. (Cited on pages 5 and 40.)

[3] A.D. Sakharov. Violation of CP invariance, C asymmetry, and baryon asymmetry of the universe. *JETP Letters*, 5:24–27, 1967. (Cited on pages 5, 33 and 40.)

[4] R.D. Peccei and H.R. Quinn. CP Conservation in the Presence of Pseudoparticles. *Phys. Rev. Lett.*, 38:1440, 1977. (Cited on pages 6 and 41.)

[5] CMS collaboration. Observation of a new boson at a mass of 125 GeV with the CMS experiment at the LHC. *Phys. Lett. B*, 716:30–61, 2012. (Cited on pages 6 and 41.)

[6] ATLAS collaboration. Observation of a new particle in the search for the Standard Model Higgs boson with the ATLAS detector at the LHC. *Phys. Lett. B*, 716:1–29, 2012. (Cited on pages 6 and 41.)

[7] E. Pierre. *Développement et optimisation d'un système de polarisation de neutrons ultra froids dans le cadre d'une nouvelle mesure du moment dipolaire électrique du neutron.* PhD thesis, Université de Caen/Basse-Normandie, 2012. (Cited on pages 9, 62, 63 and 71.)

[8] M.V. Berry. Quantal phase factors accompanying adiabatic changes. *Proc. R. Soc. London A*, 392:45–57, 1984. (Cited on pages 10 and 47.)

[9] F. Atchison, T. Bryś, M. Daum, P. Fierlinger, A. Fomin, R. Henneck, K. Kirch, M. Kuźniak, and A. Pichlmaier. The simulation of ultracold neutron experiments using GEANT4. *Nuclear Instruments and Methods in Physics Research A*, 552:513–521, November 2005. (Cited on page 11.)

[10] M. Burghoff, S. Knappe-Grüneberg, A. Schnabel, L. Trahms, and G. Ban *et al.* Progress Report. *PSI Proposal R-05-03.1*, 2011. (Cited on pages 13, 67 and 75.)

[11] I.S. Altarev, Yu.V. Borisov, N.V. Borovikova, A.B. Brandin, A.I. Egorov, V.F. Ezhov, S.N. Ivanov, V.M. Lobashev, V.A. Nazarenko, V.L. Ryabov, A.P. Serebrov, and R.R. Taldaev. A new upper limit on the electric dipole moment of the neutron. *Physics Letters B*, 102:13 – 16, 1981. (Cited on pages 13 and 75.)

[12] M. Burghoff, S. Knappe-Grüneberg, A. Schnabel, L. Trahms, and G. Ban *et al.* Progress Report. *PSI Proposal R-05-03.1*, pages 72–75, 2009. (Cited on pages 13 and 75.)

[13] G. Rogel. *Développement de détecteurs de neutrons ultra-froids et d'un système d'analyse de polarisation pour la mesure du moment dipolaire électrique du neutron.* PhD thesis, Université de Caen/Basse-Normandie, 2009. (Cited on pages 13, 68, 75 and 76.)

[14] G. Pignol *et al.* A measurement of the neutron to ^{199}Hg magnetic moment ratio. *submitted to Phys. Rev. C*, 2014. (Cited on pages 28 and 166.)

[15] M. Pospelov and A. Ritz. Electric dipole moments as probes of new physics. *Annals of Physics*, 318:119–169, 2005. (Cited on pages 33, 41 and 42.)

[16] Dirk Dubbers and Michael G. Schmidt. The neutron and its role in cosmology and particle physics. *Rev. Mod. Phys.*, 83:1111–1171, 2011. (Cited on pages 33 and 40.)

[17] K. Kirch and P. Harris. Edm world page. (Cited on pages 33 and 42.)

[18] V.V. Fedorov, M. Jentschel, I.A. Kuznetsov, E.G. Lapin, E. Lelièvre-Berna, Nesvizhevsky V., A. Pethoukov, Semenikin S.Yu., T. Soldner, Voronin V.V., and Yu.P. Braginetz. Measurement of the neutron electric dipole moment via spin rotation in a non-centrosymmetric crystal. *Phys. Lett. B*, 694:22–25, 2010. (Cited on pages 33 and 48.)

[19] P. Geltenbort. Private communication, 2014. (Cited on page 33.)

[20] A.P. Serebrov, E.A. Kolomenskiy, A.N. Pirozhkov, I.A. Krasnoschekova, A.V. Vassiljev, A.O. Polushkin, M.S. Lasakov, A.K. Fomin, I.V. Shoka, V.A. Solovey, O.M. Zherebtsov, P. Geltenbort, S.N. Ivanov, O. Zimmer, E.B. Alexandrov, S.P. Dmitriev, and N.A. Dovator. New measurements of the neutron electric dipole moment. *JETP Letters*, 99:4–8, 2014. (Cited on pages 33 and 49.)

[21] C A Baker, S N Balashov, V Francis, K Green, M G D van der Grinten, P S Iaydjiev, S N Ivanov, A Khazov, M A H Tucker, D L Wark, A Davidson, J R Grozier, M Hardiman, P G Harris, J R Karamath, K Katsika, J M Pendlebury, S J M Peeters, D B Shiers, P N Smith, C M Townsley, I Wardell, C Clarke, S Henry, H Kraus, M McCann, P Geltenbort, and H Yoshiki. CryoEDM: a cryogenic experiment to measure the neutron Electric Dipole Moment. *Journal of Physics: Conference Series*, 251:012055, 2010. (Cited on page 33.)

[22] I. Altarev, D. H. Beck, S. Chesnevskaya, T. Chupp, W. Feldmeier, P. Fierlinger, A. Frei, E. Gutsmiedl, F. Kuchler, P. Link, T. Lins, M. Marino, J. McAndrew, S. Paul, G. Petzoldt, A. Pichlmaier, R. Stoepler, S. Stuiber, and B. Taubenheim. A next generation measurement of the electric dipole moment of the neutron at the FRM II. *Il Nuovo Cimento*, pages 122–127, 2012. (Cited on page 33.)

[23] Yasuhiro Masuda, Koichiro Asahi, Kichiji Hatanaka, Sun-Chan Jeong, Shinsuke Kawasaki, Ryohei Matsumiya, Kensaku Matsuta, Mototsugu Mihara, and Yutaka Watanabe. Neutron electric dipole moment measurement with a buffer gas comagnetometer. *Physics Letters A*, 376:1347 – 1351, 2012. (Cited on pages 33 and 49.)

[24] T.M. Ito. Private communication, 2014. (Cited on page 33.)

[25] The nEDM@SNS collaboration. The nedm experiment at the spallation neutron source. (Cited on page 34.)

[26] B.W. Filippone. Private communication, 2014. (Cited on pages 34 and 49.)

[27] E.M. Purcell and N.F. Ramsey. On the possibility of Electric Dipole Moments for Elementary Particles and Nuclei. *Phys. Rev.*, 78:807, 1950. (Cited on page 39.)

[28] J.H. Smith, E.M. Purcell, and N.F. Ramsey. Experimental Limit to the Electric Dipole Moment of the Neutron. *Phys. Rev.*, 108:120–122, 1957. (Cited on pages 39 and 47.)

[29] T.D. Lee and C.N. Yang. Question of Parity Conservation in Weak Interactions. *Phys. Rev.*, 104:254, 1956. (Cited on page 39.)

[30] C.S. Wu and et al. Experimental Test of Parity Conservation in Beta Decay. *Phys. Rev.*, 105:1413, 1957. (Cited on page 40.)

[31] L. Landau. On the conservation laws for weak interactions. *Nuc. Rev.*, 3:127–131, 1957. (Cited on page 40.)

[32] N.F. Ramsey. Time Reversal, Charge Conjugation, Magnetic Pole Conjugation, and Parity. *Phys. Rev.*, 109:225, 1958. (Cited on page 40.)

[33] J.H Christenson and et al. Evidence for the 2π Decay of the K_2^0 Meson. *Phys. Rev. Lett.*, 13:138, 1964. (Cited on page 40.)

[34] K. Abe. Observation of large CP violation in the neutral B meson system. *Phys. Rev. Lett.*, 87:9, 2001. (Cited on page 40.)

[35] J.P. Lees. Observation of Time-Reversal violation in the B_0 meson system. *Phys. Rev. Lett.*, 109:21, 2012. (Cited on page 40.)

[36] R. Aaij. Evidence for CP violation in Time-Integrated $D^0 \to h^- h^+$ decay rates. *Phys. Rev. Lett.*, 108:11, 2012. (Cited on page 40.)

[37] Jonathan Engel, Michael J. Ramsey-Musolf, and U. van Kolck. Electric dipole moments of nucleons, nuclei, and atoms: The standard model and beyond. *Progress in Particle and Nuclear Physics*, 71:21 – 74, 2013. Fundamental Symmetries in the Era of the {LHC}. (Cited on page 40.)

[38] L. Canetti, M. Drewes, and Shaposhnikov M. Matter and Antimatter in the Univers. *New J. Phys.*, 14:095012, 2012. (Cited on page 40.)

[39] E. Komatsu, et al, and [WMAP collaboration]. Seven-year Wilkinson Microwave Anisotropy Probe (WMAP) observations: cosmological interpretation. *Astrophys. J. Suppl.*, 192:18, 2011. (Cited on page 40.)

[40] G. Steigman. Primordial Nucleosynthesis in the Precision Cosmology Era. *Annu. Rev. Nuc. Part. Sci.*, 57:463–491, 2007. (Cited on page 40.)

[41] D.V. Nanopoulos and et al. On the electric dipole moment of the neutron. *Phys. Lett.*, B 87:53–56, 1979. (Cited on page 40.)

[42] E.P. Shabalin and et al. *Sov. J. Nucl. Phys.*, 28:75, 1978. (Cited on page 41.)

[43] A. Czarnecki and B. Krause. Neutron Electric Dipole Moment in the Standard Model: Complete Three-Loop Calculation of the Valence Quark Contributions. *Phys. Rev. Lett.*, 78:4339, 1997. (Cited on page 41.)

[44] M. Pospelov and A. Ritz. The theta term in QCD sum rules and the electric dipole moments of the vector meson. *Nuclear Physics*, B 558:243–258, 1999. (Cited on page 41.)

[45] K. Kajantie, M. Laine, K. Rummukainen, and M. Shaposhnikov. The electroweak phase transition: a non-perturbative analysis. *Nuclear Physics B*, 466(1-2):189 – 258, 1996. (Cited on page 41.)

[46] M. Carena, G. Nardini, M. Quirós, and C.E.M. Wagner. MSSM electroweak baryogenesis and LHC data. *Journal of High Energy Physics*, 2013, 2013. (Cited on page 41.)

[47] S.J. Huber, M. Pospelov, and A. Ritz. Electric dipole moment constraints on minimal electroweak baryogenesis. *Phys. Rev. D*, 75:036006, 2007. (Cited on pages 41 and 43.)

[48] The Storage Ring EDM Collaboration. A Storage Ring proton Electric Dipole Moment experiment: most sensitive experiment to CP-violation beyond the Standard Model. *Proceedings of the DPF - 2011 Conference, Providence, RI*, 2011. (Cited on page 42.)

[49] The Storage Ring EDM Collaboration. Muon and Deuteron EDM Experiments. *Nucl. Phys. B - Proceedings Supplements*, 155:375–377, 2006. (Cited on page 42.)

[50] W. Ketterle and N.J. Van Druten. *Advances In Atomic, Molecular, and Optical Physics*, chapter Evaporative Cooling of Trapped Atoms, pages 181–236. B. Bederson and H. Walther, Academic Press, San Diego, 1996. (Cited on page 42.)

[51] L.I. Schiff. Measurability of Nuclear Electric Dipole Moments. *Phys. Rev.*, 132:2194, 1963. (Cited on page 42.)

[52] B. Regan, E. Commins, C. Schmidt, and D. DeMille. New limit on the electron electric dipole moment. *Phys. Rev. Lett.*, 88:18, 2002. (Cited on page 42.)

[53] J. J. Hudson, D.M. Kara, I. J. Smallman, B.E. Sauer, M.R. Tarbutt, and E.A. Hinds. Improved measurement of the shape of the electron. *Nature*, 473:493–496, 2011. (Cited on page 42.)

[54] The ACME Collaboration, J. Baron, W.C. Campbell, D. DeMille, J.M. Doyle, G. Gabrielse, Y. V. Gurevich, P.W. Hess, N.R. Hutzler, E. Kirilov, I. Kozyryev, B.R. O'Leary, C.D. Panda, M.F. Parsons, E.S. Petrik, B. Spaun, A.C. Vutha, and A.D. West. Order of Magnitude Smaller Limit on the Electric Dipole Moment of the Electron. *Science*, 343:269–272, 2014. (Cited on page 42.)

[55] W. C. Griffith, M. D. Swallows, T. H. Loftus, M. V. Romalis, B. R. Heckel, and E. N. Fortson. Improved Limit on the Permanent Electric Dipole Moment of ^{199}Hg. *Phys. Rev. Lett.*, 102:101601, Mar 2009. (Cited on pages 43 and 145.)

[56] J. Zenner. *The search for the neutron electric dipole moment.* PhD thesis, Johannes Gutenberg-Universität, Mainz, 2013. (Cited on pages 47, 61, 63 and 123.)

[57] W. B. Dress, P. D. Miller, J. M. Pendlebury, Paul Perrin, and Norman F. Ramsey. Search for an electric dipole moment of the neutron. *Phys. Rev. D*, 15:9–21, 1977. (Cited on page 48.)

[58] V.I. Lushchikov, Y.N. Pokotilovskii, A.V. Strelkov, and F.L. Shapiro. Observation of Ultracold Neutrons. *Sov. Phys. JETP*, 9:23, 1969. (Cited on pages 48 and 50.)

[59] B. Filippone. New searches for the neutron electric dipole moment. Physics of fundamental Symmetries and Interactions at low energies, 2013. (Cited on page 49.)

[60] M.G.D. Van Der Griten *et al.* CryoEDM: A cryogenic experiment to measure the neutron electric dipole moment. *Nucl. Instr. Methods A*, 611:129–132, 2009. (Cited on page 49.)

[61] J. Chadwick. The Existence of a Neutron. *Proc. Roy. Soc.*, A 136:692, 1932. (Cited on page 50.)

[62] E. Fermi and L. Marshall. Interference Phenomena of Slow Neutrons. *Phys. Rev.*, 71:666, 1947. (Cited on page 50.)

[63] Ya. B. Zel'dovich. Storage of cold neutrons. *Sov. Phys. JETP*, 36:1952–1953, 1959. (Cited on page 50.)

[64] R. Golub, D.J. Richardson, and S.K. Lamoreaux. *Ultra-Cold Neutrons*. Adam Hilger, Bristol, Philadelphia, and New York, 1991. (Cited on page 51.)

[65] E. Fermi. Motion of neutrons in hydronenous substances. *Ricerce Scientifica*, 7:13–52, 1936. (Cited on page 51.)

[66] P.J. Mohr, B.N. Taylor, and D.B. Newell. CODATA Recommended Values of the Fundamental Physical Constants: 2010. *Rev. Mod. Phys.*, 84, 2010. (Cited on page 52.)

[67] F. Atchison, T. Bryś, M. Daum, P. Fierlinger, P. Geltenbort, R. Henneck, S. Heule, M. Kasprzak, K. Kirch, A. Pichlmaier, C. Plonka, U. Straumann, C. Wermelinger, and G. Zsigmond. Loss and spinflip probabilities for ultracold neutrons interacting with diamondlike carbon and beryllium surfaces. *Phys. Rev. C*, 76:044001, Oct 2007. (Cited on page 52.)

[68] K.K.H. Leung and O. Zimmer. Proposed neutron lifetime measurement using a hybrid magnetic trap for ultra-cold neutrons. *Nuclear Instruments and Methods A*, 611:181 – 185, 2009. Particle Physics with Slow Neutrons. (Cited on page 52.)

[69] R.T. Robiscoe. A Spin-Flip Problem. *Am. J. Phys.*, 39:146–150, 1971. (Cited on pages 52 and 175.)

[70] F. Bloch. Nuclear Induction. *Phys. Rev.*, 70:460, 1946. (Cited on page 52.)

[71] H. Abele and H. Leeb. Gravitation and quantum interference experiments with neutrons. *New J. Phys.*, 14:055010, 2012. (Cited on page 53.)

[72] J. Beringer and et al. (Particle Data Group). *Phys. Rev.*, D86, 2012. (Cited on page 54.)

[73] N. Severijns and O. Naviliat-Cuncic. Symmetry Tests in Nuclear Beta Decay. *Annual Review of Nuclear and Particle Science*, 61:23–46, 2011. (Cited on page 54.)

[74] B. Plaster and et al.(UCNA collaboration). Measurement of the neutron β-asymmetry parameter A_0 with ultracold neutrons. *Phys. Rev.*, C86:055501, 2012. (Cited on page 54.)

[75] A. Steyerl. A "neutron turbine" as an efficient source of ultracold neutrons. *Nuclear Instruments and Methods*, 125:461–469, 1975. (Cited on page 54.)

[76] B. Lauss. Startup of the high-intensity ultracold neutron source at the Paul Scherrer Institute. *Hyperfine Interact*, 211:21–25, 2012. (Cited on page 60.)

[77] R. Golub and J.M. Pendlebury. Super-thermal sources of ultracold neutrons. *Physics Letters A*, 53:133–135, 1975. (Cited on page 60.)

[78] K. Bodek, M. Daum, R. Henneck, S. Heule, M. Kasprzak, K. Kirch, A. Knecht, M. Kuźniak, B. Lauss, M. Meier, G. Petzoldt, M. Schneider, and G. Zsigmond. Storage of ultracold neutrons in high resistivity, non-magnetic materials with high Fermi potential. *Nuclear Instruments and Methods in Physics Research A*, 597:222–226, December 2008. (Cited on page 64.)

[79] G. Pignol. Effect of Hg pulse on neutron frequency extraction. Internal Notes, 2010. (Cited on page 64.)

[80] B. Franke. *Investigations of the Internal and External Magnetic Fields of the Neutron Electric Dipole Moment Experiment at the Paul Scherrer Institute*. PhD thesis, ETH Zürich, 2013. (Cited on pages 65 and 66.)

[81] M. Burghoff, S. Knappe-Grüneberg, A. Schnabel, L. Trahms, and G. Ban *et al.* Progress report. *PSI Proposal R-05-03.1*, 2009. (Cited on page 65.)

[82] K. Green, P. G. Harris, P. Iaydjiev, D. J. R. May, J. M. Pendlebury, K. F. Smith, M. van der Grinten, P. Geltenbort, and S. Ivanov. Performance of an atomic mercury magnetometer in the neutron EDM experiment. *Nucl. Instr. Methods A*, 404:381–393, 1998. (Cited on pages 66 and 129.)

[83] S. Groeger, G. Bison, P.E. Knowles, R. Wynands, and A. Weis. Laser-pumped cesium magnetometers for high-resolution medical and fundamental research. *SENSORS AND ACTUATORS A: PHYSICAL*, 129:1–5, 2006. (Cited on page 67.)

[84] T. Lefort *et al.* A ^{6}Li doped scintillators based detector for ultracold neutrons. *To be submitted to European Physical Journal A*, 2014. (Cited on page 68.)

[85] G. Ban, K Bodek, T. Lefort, O. Naviliat-Cuncic, E. Pierre, C. Plonka, and G. Rogel. UCN detection with ^{6}Li-doped glass scintillators. *Nucl. Instr. Methods A*, 611:280–283, 2009. (Cited on page 68.)

[86] D. Etasse, B. Carniol, C. Fontbonne, J.M. Fontbonne, J. Hommet, H. Plard, J. Poincheval, T. Charentré, and D. Cussol. Faster web site. (Cited on page 69.)

[87] M. Burghoff, S. Knappe-Grüneberg, A. Schnabel, L. Trahms, and G. Ban *et al.* Progress report. *PSI Proposal R-05-03.1*, 2010. (Cited on page 69.)

[88] P. Fierlinger. *Loss and Depolarization Studies of Ultracold Neutrons Stored using Diamond-like Carbon*. PhD thesis, Universität Zürich, 2005. (Cited on page 75.)

[89] A.-J. Dianoux and G. Lander. Neutron data booklet, 2003. (Cited on page 76.)

[90] S.V. Grigoriev, A.I. Okorokov, and V.V. Runov. Peculiarities of the construction and application of a broadband adiabatic flipper of cold neutrons. *Nucl. Instr. Methods A*, 384:451–456, 1997. (Cited on pages 97, 99 and 175.)

[91] G. Quéméner. Private communication, 2013. (Cited on pages 98 and 99.)

[92] A. Abragam. *Principles of Nuclear Magnetism*. Oxford Science Publication, 1961. (Cited on pages 99 and 175.)

[93] J. Weibler. Properties of Metals used for RF shielding. *EMC Test and Design*, 1993. (Cited on page 100.)

[94] M. Burghoff, S. Knappe-Grüneberg, A. Schnabel, L. Trahms, and G. Ban *et al.* Progress Report. *PSI Proposal R-05-03.1*, 2013. (Cited on pages 101 and 103.)

[95] D. Goupillière and G. Quéméner. Private communication, 2013. (Cited on page 103.)

[96] T. Lefort and G. Quéméner. Private communication, 2013. (Cited on page 103.)

[97] G. Quéméner. Private communication, 2014. (Cited on page 103.)

[98] B. Lauss. Measured during UCN source test. Private communication, 2013. (Cited on page 106.)

[99] A.P. Serebrov, A.V. Alduschenkov, M.S. Lasakov, I.A. Kuznetsov, and I.V. Stepanenko. New method for precise determination of neutron beam polarization. *Nucl. Instr. Methods A*, 357:503 – 510, 1995. (Cited on pages 107 and 110.)

[100] G. Zsigmond. Private communication, 2013. (Cited on page 115.)

[101] K. Green, P. G. Harris, P. Iaydjiev, D. J. R. May, J. M. Pendlebury, K. F. Smith, M. van der Grinten, P. Geltenbort, and S. Ivanov. Performance of an atomic mercury magnetometer in the neutron EDM experiment. *Nucl. Instr. Methods A*, 404:381–393, 1998. (Cited on page 123.)

[102] D. J. R. May. *A High Precicion Comparison Of The Gyromagnetic Ratios Of The 199Hg Atom And The Neutron.* PhD thesis, University of Sussex, 1998. (Cited on page 124.)

[103] Y. Lemière. Private communication, 2014. (Cited on page 127.)

[104] Y. Kermaïdic. PhD thesis, Université de Grenoble 1, In preparation. (Cited on page 129.)

[105] Y. Chibane, S. K. Lamoreaux, J. M. Pendlebury, and K. F. Smith. Minimum variance of frequency estimations for a sinusoidal signal with low noise. *Meas. Sci. Tech.*, 6:1671, 1995. (Cited on page 129.)

[106] C.A. Baker, Y. Chibane, M. Chouder, P. Geltenbort, K. Green, P.G. Harris, B.R. Heckel, P. Iaydjiev, S.N. Ivanov, I. Kilvington, S.K. Lamoreaux, D.J. May, J.M. Pendlebury, J.D. Richardson, D.B. Shiers, K.F. Smith, and M. van der Grinten. Apparatus for measurement of the electric dipole moment of the neutron using a cohabiting atomic-mercury magnetometer. *Nucl. Instr. Methods A*, 736:184 – 203, 2014. (Cited on page 130.)

[107] Y. Kermaïdic. Private communication, 2014. (Cited on page 130.)

[108] Y. Kermaïdic. Master 2 internship report: ^{199}hg frequency extraction in the nedm experiment. Not published, 2013. (Cited on pages 131 and 145.)

[109] G. Pignol *et al.* A measurement of the neutron to ^{199}Hg magnetic moment ratio. *Submitted to Phys. Lett. B*, 2014. (Cited on pages 133 and 147.)

[110] M. Burghoff, S. Knappe-Grüneberg, A. Schnabel, L. Trahms, and G. Ban *et al.* Progress Report. *PSI Proposal R-05-03.1*, 2013. (Cited on pages 133, 138, 142 and 167.)

[111] E. Wursten. Private communication, 2014. (Cited on pages 133, 148 and 166.)

[112] S. Roccia. *La comagnétométrie mercure pour la mesure du moment électrique du neutron.* PhD thesis, Université Joseph Fourier, Grenoble I, 2009. (Cited on page 141.)

[113] J. M. Pendlebury, W. Heil, Y. Sobolev, P. G. Harris, J. D. Richardson, R. J. Baskin, D. D. Doyle, P. Geltenbort, K. Green, M. G. D. van der Grinten, P. S. Iaydjiev, S. N. Ivanov, D. J. R. May, and K. F. Smith. Geometric-phase-induced false electric dipole moment signals for particles in traps. *Phys. Rev. A*, 70:032102, 2004. (Cited on pages 142 and 143.)

[114] G. Pignol and S. Roccia. Electric Dipole Moment searches: re-examination of frequency shifts for particles in traps. *Phys. Rev. A*, 85:042105, 2012. (Cited on pages 142 and 143.)

[115] F. Bloch and A. Siegert. Magnetic Resonance for Nonrotating Fields. *Phys. Rev.*, 57:522–527, 1940. (Cited on page 143.)

[116] N.F. Ramsey. Resonance Transitions Induced by Perturbations at Two or More Different Frequencies. *Phys. Rev.*, 100:1191–1194, 1955. (Cited on page 143.)

[117] M. Horras. *A highly sensitive ^{199}Hg magnetometer for the nEDM experiment.* PhD thesis, ETH Zürich, 2011. (Cited on page 143.)

[118] G. Pignol. Physics Results, Systematics, Analysis, Planned Measurements. nEDM review, PSI, 2011. (Cited on page 143.)

[119] S. K. Lamoreaux and R. Golub. Comment on "Improved Experimental Limit on the Electric Dipole Moment of the Neutron". *Phys. Rev. Lett.*, 98, 2007. (Cited on page 146.)

[120] G. Quéméner. Notes on a new set of harmonic polynomial series expansions to parametrize a magnetic field. Internal Notes, 2011. (Cited on pages 153 and 154.)

[121] G. Quéméner. Private communication, 2013. (Cited on page 153.)

[122] G. Wyszyński. PhD thesis, Jagiellonian University / ETH, In preparation. (Cited on page 153.)

[123] G. Pignol. How to extract meaningfull gradient from Cesium magnetometers. Internal Notes, 2012. (Cited on page 156.)

[124] R.G. Miller. The Jackknife – A review. *Biometrika*, 61:1–15, 1974. (Cited on page 156.)

[125] G. Wyszyński. Private communication, 2012. (Cited on page 157.)

[126] M. Burghoff, S. Knappe-Grüneberg, A. Schnabel, L. Trahms, and G. Ban *et al.* Progress Report. *PSI Proposal R-05-03.1*, 2012. (Cited on page 161.)

[127] G. Quéméner. Notes on magnetic field harmonic polynomial series expansions and application to correcting coils currents optimization. nEDM Internal Notes, 2010. (Cited on page 161.)